STAB

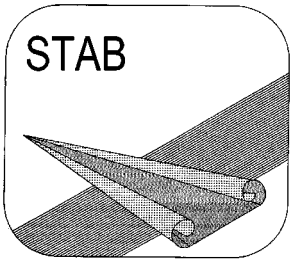

J A H R E S B E R I C H T

2022

zum

23. DGLR-Fachsymposium

9. - 10. November 2022

Berlin

„Deutsche Strömungsmechanische Arbeitsgemeinschaft, STAB“

INHALT

Mitteilungen der Geschäftsstelle

Die STAB-Jahresberichte werden bei den alternierenden Veranstaltungen Symposium und Workshop als Sammlung der Kurzfassungen der Vorträge an die Teilnehmer verteilt. Somit erscheint dieser STAB-Jahresbericht 2022 zum 23. DGLR-Fachsymposium, das am 9. und 10. November 2022 in Berlin stattfindet.

Der Bericht enthält 77 „Mitteilungen“ über Arbeiten aus den Fachgruppen, über die beim Symposium vorgetragen wird. Den „Mitteilungen“ vorangestellt ist ein Inhaltsverzeichnis (Seite 14 bis 19), das nach Fachgruppen gegliedert ist. Innerhalb der Rubriken ist alphabetisch nach Verfassern sortiert. Die Beiträge verteilen sich (bezogen auf den Erstautor) zu 1 % auf die Industrie, 40 % auf die Hochschulen und zu 59 % auf Forschungseinrichtungen (DLR, DNW, ISL). Auf Seite 174 sind die Autoren und Koautoren dieses Berichtes aufgelistet.

Die Jahresberichte werden nur an den tatsächlich daran interessierten Personenkreis verteilt und können zusätzlich von der Webseite (*https://www.dlr.de/as/desktopdefault.aspx/tabid-128/268_read-1678/*) heruntergeladen werden. Alle Teilnehmer des diesjährigen STAB-Symposiums erhalten zur Veranstaltung ein Exemplar. Weiterhin wird der Jahresbericht an die Mitglieder der STAB-Gremien und weitere Interessierte versandt.

Dieser Jahresbericht erscheint in einer Auflage von 110 Exemplaren. Einige Restexemplare sind erfahrungsgemäß bis zum Ende des jeweiligen Jahres verfügbar.

Aktualisierte Informationen über STAB finden Sie auch unter: www.dlr.de/agstab

Göttingen, im Oktober 2022

Zielsetzungen, chronologische Entwicklung und Organisation

Die Arbeitsgemeinschaft „Strömungen mit Ablösung“ (STAB) wurde auf Initiative der Deutschen Gesellschaft für Luft- und Raumfahrt (DGLR) - Lilienthal-Oberth, e.V. - 1979 von Strömungsforschern, Aerodynamikern und Luftfahrtingenieuren aus DLR, Hochschule und Industrie ins Leben gerufen.

Sie entstand aus „dem gemeinschaftlichen Bestreben, die Strömungsforschung in Deutschland generell zu fördern und durch Konzentration auf ein wirtschaftlich und forschungspolitisch zukunftsträchtiges Teilgebiet zu vertiefen“ (Auszug aus der Präambel der Verfahrensordnung der STAB).

In Zeiten knapper werdender Kassen bei gleichzeitig massiv erhöhtem Wettbewerbsdruck sind diese Ansätze notwendiger denn je. Die öffentlichen Finanziers setzen diese Kooperationsbereitschaft inzwischen aber auch voraus. Da dieser Leitgedanke der STAB dadurch inzwischen anderweitig verfolgt wird, konzentriert sie sich mehr auf fachliche Veranstaltungen.

STAB ist als ‚Kompetenznetzwerk’ der DGLR angegliedert. Auf der DGLR-Webseite findet man STAB unter: *https://www.dglr.de/vernetzen/fachbereiche/kompetenznetzwerk-stab/*

In der STAB sind alle wichtigen Gebiete der Strömungsmechanik - insbesondere die der Luft- und Raumfahrt - aus Grundlagenforschung, Großforschung und Industrie in Deutschland zusammengeschlossen. Bei der Gründung Ende der 70er Jahre stand die Idee dahinter, über ein hochaktuelles fachliches Thema - identifiziert wurde seinerzeit „Strömungen mit Ablösung“ - Forschungsverbünde aus der Industrie, den Hochschulen und der Großforschung zu organisieren. In den folgenden Jahren sind auch andere strömungsmechanische Fragestellungen aufgegriffen worden, womit die STAB sich in der Fachwelt einen wohlbekannten Namen erworben hat. Es sind aber nicht nur diejenigen angesprochen, die sich mit den traditionellen Themen der Strömungsmechanik beschäftigen, sondern es können auch Probleme aus dem Automobilbau, der Gebäudeaerodynamik, der Verfahrenstechnik, dem Motorenbau, usw. diskutiert werden.

Die Programmleitung hat im November 2000 entschieden, zukünftig das „AG“ im Namen wegzulassen.

Die öffentlichkeitsrelevanten wissenschaftlichen Aktivitäten spiegeln sich in der nachfolgenden chronologischen Entwicklung wider:

DGLR-Symposium „Forschung und Entwicklung auf dem Gebiet der Strömungsmechanik und Aerodynamik in der Bundesrepublik Deutschland“	Bonn, 29.11.-01.12.1978
„Gespräch über Strömungsforschung in Deutschland“	Ottobrunn, 30.01.1979
„Memorandum über zukünftige nationale Zusammenarbeit in der Strömungsforschung, insbesondere der Aerodynamik auf dem Gebiet der Strömungen mit Ablösung“	Oktober 1979
Programmpräsentation anlässlich der BDLI-Jahrestagung	Bonn, 01.07.1980

Programm der Arbeitsgemeinschaft „Strömungen mit Ablösung“	September 1980
Programmpräsentation im Bundesministerium für Forschung und Technologie	Bonn, 19.03.1981
Konstituierung des Kuratoriums und Neuorganisation der Arbeitsgemeinschaft „Strömungen mit Ablösung" (AG STAB)	Köln-Porz, 23.02.1982
Konstituierung von Programmleitung/Programmausschuss	Göttingen, 24.03.1982
Erfassung STAB-relevanter Aktivitäten in der Bundesrepublik Deutschland (Stand Mitte 1981)	April 1982
Fachtagung anlässlich der ILA '82 „Strömungen mit Ablösung“	Hannover, 19.05.1982
Neue Impulse für die Strömungsforschung- und Aerodynamik; Vortrag von H.-G. Knoche, DGLR-Jahrestagung	Hamburg, 01.-03.10.1984
DGLR Workshop „2D-Messtechnik“	Markdorf, 18.-19.10.1988

Symposium

1. DGLR-Fachsymposium	München, 19.-20.09.1979
2. DGLR- Fachsymposium	Bonn, 30.06.-01.07.1980
3. DGLR- Fachsymposium	Stuttgart, 23.-25.11.1981
4. DGLR- Fachsymposium	Göttingen, 10.-12.10.1983
5. DGLR- Fachsymposium	München, 09.-10.10.1986
6. DGLR-Fach-Symposium	Braunschweig,08.-10.11.1988
7. DGLR- Fachsymposium	Aachen, 07.-09.11.1990
8. DGLR- Fachsymposium	Köln-Porz, 10.-12.11.1992
9. DGLR- Fachsymposium	Erlangen, 04.-07.10.1994
10. DGLR- Fachsymposium	Braunschweig,11.-13.11.1996
11. DGLR- Fachsymposium	Berlin, 10.-12.11.1998
12. DGLR- Fachsymposium	Stuttgart, 15.-17.11.2000
13. DGLR- Fachsymposium	München, 13.-15.11.2002
14. DGLR- Fachsymposium	Bremen, 16.-18.11.2004
15. DGLR- Fachsymposium	Darmstadt, 29.11.-01.12.2006
16. DGLR- Fachsymposium	Aachen, 03.-04.11.2008

17. DGLR- Fachsymposium	Berlin, 09.-10.11.2010
18. DGLR- Fachsymposium	Stuttgart, 06.-07.11.2012
19. DGLR- Fachsymposium	München, 04.-05.11.2014
20. DGLR- Fachsymposium	Braunschweig,08.-09.11.2016
21. DGLR- Fachsymposium	Darmstadt, 06.-07.11.2018
22. DGLR- Fachsymposium	Aufgrund der Corona-Pandemie abgesagt
23. DGLR-Fachsymposium	Berlin, 09.-10.11.2022

Workshop

1. STAB-Workshop	Göttingen, 07.-08.03.1983
2. STAB-Workshop	Köln-Porz, 18.-20.09.1984
3. STAB-Workshop	Göttingen, 10.-11.11.1987
4. STAB-Workshop	Göttingen, 08.-10.11.1989
5. STAB-Workshop	Göttingen, 13.-15.11.1991
6. STAB-Workshop	Göttingen, 10.-12.11.1993
7. STAB-Workshop	Göttingen, 14.-16.11.1995
8. STAB-Workshop	Göttingen, 11.-13.11.1997
9. STAB-Workshop	Göttingen, 09.-11.11.1999
10. STAB-Workshop	Göttingen, 14.-16.11.2001
11. STAB-Workshop	Göttingen, 04.-06.11.2003
12. STAB-Workshop	Göttingen, 08.-09.11.2005
13. STAB-Workshop	Göttingen, 14.-15.11.2007
14. STAB-Workshop	Göttingen, 11.-12.11.2009
15. STAB-Workshop	Göttingen, 09.-10.11.2011
16. STAB-Workshop	Göttingen, 12.-13.11.2013
17. STAB-Workshop	Göttingen, 10.-11.11.2015
18. STAB-Workshop	Göttingen, 07.- 08.11.2017
19. STAB-Workshop	Göttingen, 05.-06.11.2019
20. STAB-Workshop	Göttingen, 16.-17.11.2021

Ein Kurs über „Application of Particle Image Velocimetry, PIV“
findet seit 1993 regelmäßig im DLR in Göttingen statt,
letztmalig am: 21. - 24.03.2022

Die STAB-Symposiums-Tagungsbände durchlaufen einen Begutachtungsprozess.
Die Bände der letzten Jahre finden Sie hier aufgelistet.

- Notes on Numerical Fluid Mechanics, Vol. 60; Ed.: H. Körner, R. Hilbig; Vieweg, Braunschweig/Wiesbaden, 1997
- Notes on Numerical Fluid Mechanics, Vol. 72; Ed.: W. Nitsche, H.-J. Heinemann, R. Hilbig; Vieweg, Braunschweig/Wiesbaden, 1999
- Notes on Numerical Fluid Mechanics, Vol. 77; Ed.: S. Wagner, U. Rist, H.-J. Heinemann, R. Hilbig; Springer, Berlin Heidelberg New York, 2002
- Notes on Numerical Fluid Mechanics and Multidisciplinary Design, Vol. 87; Ed.: Chr. Breitsamter, B. Laschka, H.-J. Heinemann, R. Hilbig; Springer, Berlin Heidelberg New York, 2004
- Notes on Numerical Fluid Mechanics and Multidisciplinary Design, Vol. 92; Ed.: H. J. Rath, C. Holze, H.-J. Heinemann, R. Henke, H. Hönlinger; Springer, Berlin Heidelberg New York, 2006
- Notes on Numerical Fluid Mechanics and Multidisciplinary Design, Vol. 96; Ed.: C. Tropea, S. Jakirlic, H.-J. Heinemann, R. Henke, H. Hönlinger; Springer-Verlag Berlin Heidelberg, 2007
- Notes on Numerical Fluid Mechanics and Multidisciplinary Design, Vol. 112; Eds.: A. Dillmann, G. Heller, M. Klaas, H.-P. Kreplin, W. Nitsche, W. Schröder; Springer-Verlag Berlin Heidelberg, 2010
- Notes on Numerical Fluid Mechanics and Multidisciplinary Design, Vol. 121; Eds.: A. Dillmann, G. Heller, H.-P. Kreplin, W. Nitsche, I. Peltzer; Springer-Verlag Berlin Heidelberg, 2013
- Notes on Numerical Fluid Mechanics and Multidisciplinary Design, Vol. 124; Eds.: A. Dillmann, G. Heller, E. Krämer, H.-P. Kreplin, W. Nitsche, U. Rist; Springer-Verlag Berlin Heidelberg, 2014
- Notes on Numerical Fluid Mechanics and Multidisciplinary Design, Vol. 132; Eds.: A. Dillmann, G. Heller, E. Krämer, C. Wagner, C. Breitsamter; Springer-Verlag Berlin Heidelberg, 2016
- Notes on Numerical Fluid Mechanics and Multidisciplinary Design, Vol. 136; Eds.: A. Dillmann, G. Heller, E. Krämer, C. Wagner, S. Bansmer, R. Radespiel, R. Semaan; Springer-Verlag Berlin Heidelberg, 2018
- Notes on Numerical Fluid Mechanics and Multidisciplinary Design, Vol. 142; Eds.: A. Dillmann, G. Heller, E. Krämer, C. Wagner, C. Tropea, S. Jakirlic; Springer-Verlag Berlin Heidelberg, 2019
- Notes on Numerical Fluid Mechanics and Multidisciplinary Design, Vol. 151, Eds.: A. Dillmann, G. Heller, E. Krämer, C. Wagner, Verlag Berlin Heidelberg, 2020

Vorschau:

23. STAB-Workshop	Göttingen, Herbst 2023
29. Kurs „PIV“	Göttingen, 20.03. – 24.03.2023

Programmleitung

Dipl.-Ing. R. Behr (Ariane Group, München)
roland.behr@ariane.group Tel.: 089 / 6000 25171

Prof. Dr. C. Breitsamter (Technische Universität München)
christian.breitsamter@aer.mw.tum.de Tel.: 089 / 289-16137

Prof. Dr. A. Dillmann (Sprecher) (DLR, Göttingen)
andreas.dillmann@dlr.de Tel.: 0551 / 709-2177

Prof. Dr. J. Fröhlich (TU Dresden)
jochen.froehlich@tu-dresden.de Tel.: 0351 / 463 37607

Dr. R. Höld (MBDA Deutschland GmbH,
roland.hoeld@mbda-systems.de Schrobenhausen)
Tel.: 08252 / 99 8845

Dr. G. Heller (Sprecher) (Airbus, Bremen)
gerd.heller@airbus.com Tel.: 0421 / 538-2649

Prof. Dr. E. Krämer (Sprecher) (Universität Stuttgart)
kraemer@iag.uni-stuttgart.de Tel.: 0711 / 685-63401

P. Noeding (Airbus, Bremen)
peter.noeding@airbus.com Tel.: 0421 / 539-4752

Prof. Dr. R. Radespiel (Technische Universität Braunschweig)
r.radespiel@tu-braunschweig.de Tel.: 0531 / 391-94250

Prof. Dr. C.-C. Rossow (DLR, Braunschweig)
Cord.Rossow@dlr.de Tel.: 0531 / 295-2400

Prof. Dr. U. Rist (Universität Stuttgart)
rist@iag.uni-stuttgart.de Tel.: 0711 / 685-63432

Dipl.-Ing. D. Schimke (Airbus, Helicopters)
dieter.schimke@airbus.com Tel.: 090 / 6718 511

Prof. Dr. W. Schröder (RWTH, Aachen)
office@aia.rwth-aachen.de Tel.: 0241 / 80 95410

Prof. Dr. L. Tichy (DLR, Göttingen)
lorenz.tichy@dlr.de Tel.: 0551 / 709-2341

Fachgruppen[1]	**Sprecher:**
Aeroelastik und Strukturdynamik*	Prof. Dr. L. Tichy (DLR, Göttingen) Tel.: 0551 709-2341 E-Mail: Lorenz.Tichy@dlr.de
Experimentelle Aerodynamik*	Prof. Dr. C. Breitsamter (Technische Universität München) Tel.: 089 289-16137 E-Mail: Christian.Breitsamter@aer.mw.tum.de
Fluid- und Thermodynamik*	NN
Hyperschallaerothermodynamik	Dr. T. Eggers (DLR, Braunschweig) Tel.: 0531 295-2436 E-Mail: Thino.Eggers@dlr.de und P. Nöding (Airbus, Bremen) Tel.: 0421 539-4752 E-Mail: Peter.Noeding@airbus.com
Multidisziplinäre Optimierung	Dr. M. Hepperle (DLR, Braunschweig) Tel.: 0531 295-3337 E-Mail: Martin.Hepperle@dlr.de und Dipl.-Ing. D. Reckzeh (Airbus, Bremen) Tel.: 0421 538-2136 E-Mail: Daniel.Reckzeh@airbus.com
Numerische Aerodynamik*	Dr. C. Grabe (DLR, Göttingen) Tel.: 0551 709-2628 E-Mail: Cornelia.Grabe@dlr.de
Strömungsakustik*	Prof. Dr. J. Delfs (DLR, Braunschweig) Tel.: 0531 295-2170 E-Mail: Jan.Delfs@dlr.de
Strömungsbeeinflussung	Dr. A. Büscher (Airbus, Bremen) Tel.: 0421 538-4268 E-Mail: Alexander.Buescher@airbus.com
Turbulenz und Transition	Prof. Dr. W. Schröder (RWTH, Aachen) Tel.: 0241 80 95410 E-Mail: office@aia.rwth-aachen.de und Prof. Dr. N. Adams (Technische Universität München) Tel.: 089 289-16120 E-Mail: Nikolaus.Adams@tum.de

*assoziierte DGLR-Fachkreise
[1]grundlagenorientiert

Fachgruppen[2]	**Sprecher:**
Allgemeine Strömungstechnik	Prof. Dr. Claus Wagner (DLR Göttingen) Tel.: 0551 709-2261 E-Mail: Claus.Wagner@dlr.de
Drehflügler	Dr. A. Gardner (DLR, Göttingen) Tel.: 0551 709-2267 E-Mail: Anthony.Gardner@dlr.de
Hochagile Konfigurationen	Dr. R. Höld (MBDA Deutschland GmbH, Schrobenhausen) Tel.: 08252 99 8845 E-Mail: Roland.Hoeld@mbda-systems.de
Transportflugzeugkonfigurationen	Dr. A. Seitz (DLR, Braunschweig) Tel.: 0531 295-2888 E-Mail: Arne.Seitz@dlr.de
Versuchsanlagen	NN
Wissenschaftlicher Koordinator	Prof. Dr. C. Wagner (DLR Göttingen) Tel.: 0551 709-2261 E-Mail: Claus.Wagner@dlr.de

[2]anwendungsorientiert

Stand: Oktober 2022

Verfassen von „Mitteilungen“:

Die Anmeldungen zum STAB-Symposium bzw. STAB-Workshop werden bei der jeweiligen Veranstaltung als Bericht/Proceedings an die Teilnehmer verteilt.

Die Mitteilung ist eine zweiseitige Kurzfassung des Beitrags, bei der nur der unten dargestellte Kopf vorgegeben ist.

Mitteilung

Fachgruppe:

Thema/Titel des Beitrags

Autor(en)
Institution
Adresse
E-Mail

Bitte halten Sie sich bei der Anmeldung zur STAB-Veranstaltung unbedingt an die vorgegebenen zwei Seiten pro „Mitteilung“.
Tragen Sie bitte keine Seitenzahlen ein.
Der Druck erfolgt weiterhin ausschließlich in schwarz/weiß.

Für Rückfragen steht Ihnen die Geschäftsstelle gerne zur Verfügung:

Tel.: 0551 709 - 2464
Fax: 0551 709 - 2241
E-Mail: stab@dlr.de

Mit freundlichen Grüßen
Ihre Fachgruppenleiter/innen und Ihre Geschäftsstelle

The **CEAS Aeronautical Journal** and the **CEAS Space Journal** have been created under the umbrella of CEAS to provide an appropriate platform for excellent scientific publications submitted by scientists and engineers. The German Aerospace Center (DLR) and the European Space Agency (ESA) support the journals.

CEAS Aeronautical Journal

An Official Journal of the Council of European Aerospace Societies
ISSN: 1869-5582 (Print), 1869-5590 (Online)
Springer Wien
http://www.springer.com/13272

The Journal is devoted to publishing results and findings in all areas of aeronautics-related science and technology as well as reports on new developments in design and manufacturing of aircraft, rotorcraft, and unmanned aerial vehicles. Of interest are also (invited) in-depth reviews of the status of development in specific areas of relevance to aeronautics, and descriptions of the potential way forward. Typical disciplines of interest include flight physics and aerodynamics, aeroelasticity and structural mechanics, aeroacoustics, structures and materials, flight mechanics and flight control, systems, flight guidance, air traffic management, communication, navigation and surveillance, aircraft and aircraft design, rotorcraft and propulsion.

The Journal publishes peer-reviewed original articles, (invited) reviews and short communications.

CEAS Space Journal

An Official Journal of the Council of European Aerospace Societies
ISSN: 1868-2502 (Print), 1868-2510 (Online)
Springer Wien
http://www.springer.com/12567

The Journal is devoted to new developments and results in all areas of space-related science and technology, including important spin-off capabilities and applications as well as ground-based support systems and manufacturing advancements. Of interest are also (invited) in-depth reviews of the status of development in specific areas of relevance to space, and descriptions of the potential way forward. Typical disciplines of interest include mission design and space systems, satellite communications, aerothermodynamics (including physical fluid dynamics), environmental control and life support systems, materials, operations, space debris, optics, optoelectronics and photonics, guidance, navigation and control, mechanisms, propulsion, power, robotics, structures, testing, thermal issues, and small satellites.

The Journal publishes peer-reviewed original articles, (invited) reviews and short communications.

1. Fachgruppe „Aeroelastik und Strukturdynamik“

2. Fachgruppe “Experimentelle Aerodynamik”

8. Fachgruppe „Turbulenz und Transition“

9. Fachgruppe „Allgemeine Strömungstechnik“

12. Fachgruppe „Transportflugzeugkonfigurationen“

Mitteilung

Fachgruppe: Aeroelastik und Strukturdynamik

Analysis of the Boundary Layer on a Highly Flexible Wing based on Infrared Thermography Measurements

Christoph Mertens[1], Adrián Grille Guerra[1], Bas W. van Oudheusden[1],
Michael Fehrs[2] and Markus Ritter[2]
[1] TU Delft, Faculty of Aerospace Engineering, Kluyverweg 1, 2629HS Delft, NL
[2] DLR, Institute of Aeroelasticity,Bunsenstraße 10, 37073 Göttingen
C.Mertens@tudelft.nl

The Pazy wing is a benchmark experimental model that was introduced as a reference geometry of a highly flexible wing to support the development of novel nonlinear aeroelastic prediction models with experimental validation data [1,2]. The Pazy wing was designed to sustain very large deformations in wind tunnel experiments, with wingtip deflections above 50% of the span width, which is $s = 550\ \mathrm{mm}$. To comply with this requirement, the wing is constructed from a 3D-printed chassis that forms the leading and trailing edges as well as the ribs, that have a NACA 0018 cross-sectional shape. The stiffness of the wing is mainly provided by an aluminum spar plate that is glued inside the chassis. A thin Oralight iron-on film is used as the skin and is applied to the chassis by thermal shrinking. This construction process fails to preserve the design airfoil shape in between the ribs, as illustrated in Figure 1.

Figure 1 : Side view of the TU Delft Pazy wing with detail of the sagging skin between ribs

In a recent study [3], high-fidelity CFD simulations were used to investigate the effect of the distorted shape between the ribs on the boundary layer state at a chord-based Reynolds number of $Re = 340\ 000$. The grid for the CFD simulations was generated from a shape scan of the actual TU Delft Pazy wing [2]. A complex boundary layer pattern was observed, where the flow separates locally and transitions to turbulence over a laminar separation bubble, with strong differences depending on the spanwise location, as demonstrated by the skin friction distributions shown in Figure 2. These differences between the design and actual shape could have a significant impact on the wing's aerodynamic performance in experiments.

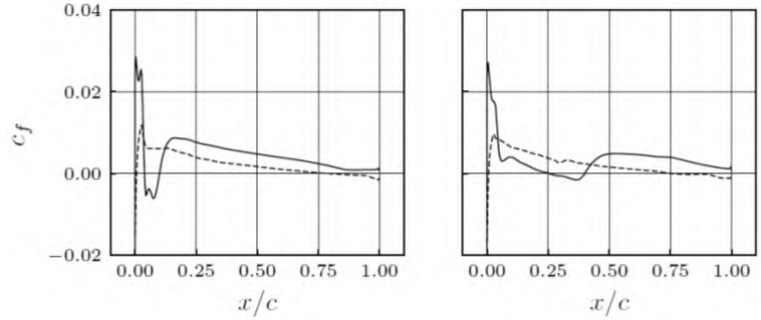

Figure 2 : Skin friction coefficient distributions from CFD simulations (dashed lines: pressure side, solid lines: suction side) [3], left: between ribs, right: on rib location

In the current study, the boundary layer on the Delft-Pazy wing is analyzed in a wind tunnel experiment. Measurements of the wing's surface temperature are acquired with an infrared camera, as shown in Figure 3. The surface temperature measurements can be used to infer the boundary layer state based on the relation between skin friction and heat transfer [4].

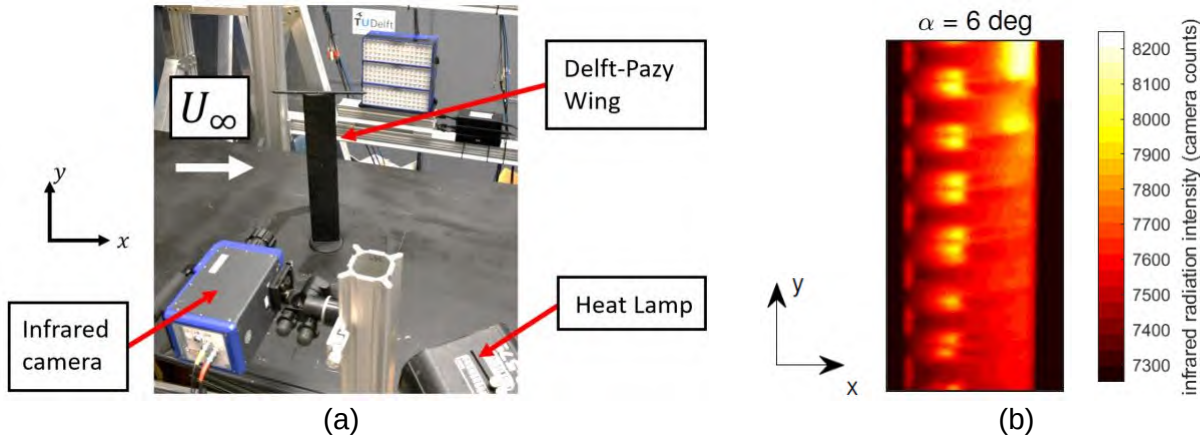

Figure 3: (a) Wind tunnel setup at TU Delft, (b) temperature distribution measured at $\alpha = 6°$

The high degree of flexibility of the Pazy wing makes it suceptible for experiencing vibrations and thus unsteady flow conditions. While the use of infrared thermography for detecting transition in steady and unsteady attached flows is established, the detection of unsteady laminar separation bubbles using differential infrared thermography (DIT) has only recently been explored [5]. A preliminary analysis to extract the boundary layer transition location from the temperatures and temperature difference distributions on the wing undergoing a motion with period T is shown in Figure 4. The full paper will provide a detailed experimental analysis of the boundary layer on the Pazy wing in steady and unsteady flow conditions.

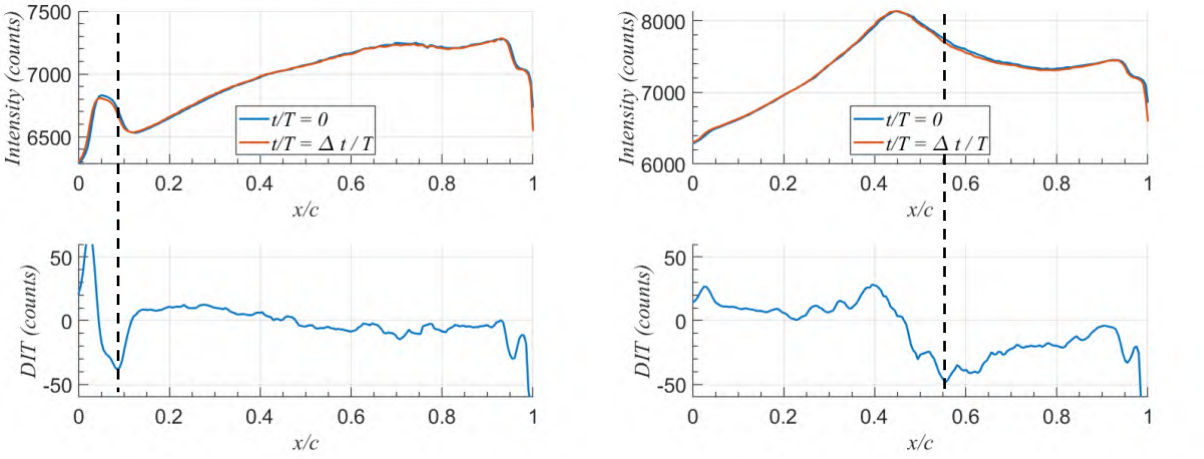

Figure 4: Temperature (top) and temperature difference (bottom) distributions during unsteady wing motion, black dashed lines indicates transition. Left: between ribs, right: on rib location

References

[1] Avin, O., Raveh, D. E., Drachinsky, A., Ben-Shmuel, Y., & Tur, M. (2022). Experimental Aeroelastic Benchmark of a Very Flexible Wing. AIAA Journal, 60(3), 1745-1768.

[2] Mertens, C., Sodja, J., Sciacchitano, A., & van Oudheusden, B. (2022). Experimental Aeroelastic Characterization of a Very Flexible Wing in Steady and Unsteady Inflow. In AIAA SCITECH 2022 Forum (p. 1344).

[3] Fehrs, M., Ritter, M., Helm, S., Mertens, C. (2022). CFD simulations of the Pazy wing in support of the third aeroelastic prediction workshop. In International Forum on Aeroelasticity and Structural Dynamics IFASD 2022.

[4] Wolf, C. C., Gardner, A. D., & Raffel, M. (2020). Infrared thermography for boundary layer transition measurements. Measurement Science and Technology, 31(11), 112002.

[5] Grille Guerra, A. (2022). Experimental Investigation of a Laminar Separation Bubble Subjected to Wing Structural Motion. Master Thesis, TU Delft.

Mitteilung

Fachgruppe: Aeroelastik und Strukturdynamik

Numerical Investigation of a Spoiler Effect on the Transonic Flutter Boundary

Martin Schmalz, David Quero
DLR Institute of Aeroelasticity, Bunsenstr. 10, 37073 Göttingen
Martin.Schmalz@dlr.de

Motivation: In the transonic flow regime, an aircraft typically encounters aerodynamic nonlinearities such as shock waves, which, for instance, are formed on the surface of the wing. Depending on the intensity of the shock wave, flow separation can occur behind the shock wave foot leading to large separation bubbles or even fully separated flow up until the trailing edge. These nonlinearities have a crucial impact on the stability of the aircraft as they lead to a sudden reduction in the flutter boundary known as the transonic dip. Nonetheless, flutter stability must be ensured in the design process of an aircraft. For safety reasons, stable conditions are required within a margin of 15% beyond the design dive speed of the aircraft, which limits the flight envelope [1]. Thus, the use of a flutter suppression device may be acceptable for the certification of an airplane, which is otherwise stable within its flight envelope, beyond the flight envelope limit (in the region between design dive speed and 15% above that) [2]. One possible option may exploit the use of a static spoiler deflection. In the literature, experimental results have been achieved by Dogget and Cole [3,4], who conducted wind tunnel tests with a symmetric rectangular wing model at transonic flow conditions. By deflecting a spoiler on both surfaces of the wing model, an increase in the flutter dynamic pressure could be achieved. However, as no systematic numerical investigations can be found in the literature, more information is still needed in order to fully understand the effectiveness of such flutter suppression device and, finally, to assess its potential for industrial applications on real aircraft configurations.

Objective: The present work aims at gaining more insight into the use of a statically deflected spoiler as a flutter suppression device. The concept is considered to be an on-off flutter suppression technology as the spoiler is deflected once into its static position at critical conditions. After the instability has been sufficiently damped the spoiler is retracted. Within the scope of this paper, only the effect of the statically deflected spoiler on the transonic flutter boundary is investigated. The intention is to give a first numerical assessment of this flutter suppression device in the transonic flow regime by investigating 2D airfoil models. Possible connections between the steady characteristics of the transonic aerodynamics and the flutter boundary due to the spoiler deflection are tried to be pointed out.

Methods: The effect of the spoiler on the transonic flutter boundary is studied with two different airfoil geometries, i.g. the NACA64A010 airfoil and a cross-section of NASA's Common Research Model (CRM). A variable generic spoiler geometry is added to the upper surface of the airfoils, which are all modelled as a three-degrees-of-freedom system in terms of their structural properties. These include heave, pitch and flap motion. CFD-methods are applied for all aerodynamic calculations. RANS-simulations are used for steady flow and linearized URANS-simulations in the frequency domain for unsteady flow. The motion induced aerodynamic forces from the URANS-simulations are combined with the structural model resulting in the flutter equation described by a nonlinear eigenvalue problem.

Results: From the steady-state results it can be seen that even with small spoiler deflection angles (SDA ≤10°) the spoiler has a great impact on the characteristics of the transonic flow. The spoiler achieves a flow redirection accompanied with a flow compression and deceleration in front of it. Due to this effect, it is possible to suppress supersonic regions and thus the for-

mation of a shock on the upper surface at particular flow conditions. However, the flow simultaneously accelerates on the lower surface, which increases the risk of a shock formation there (See Figure 1).

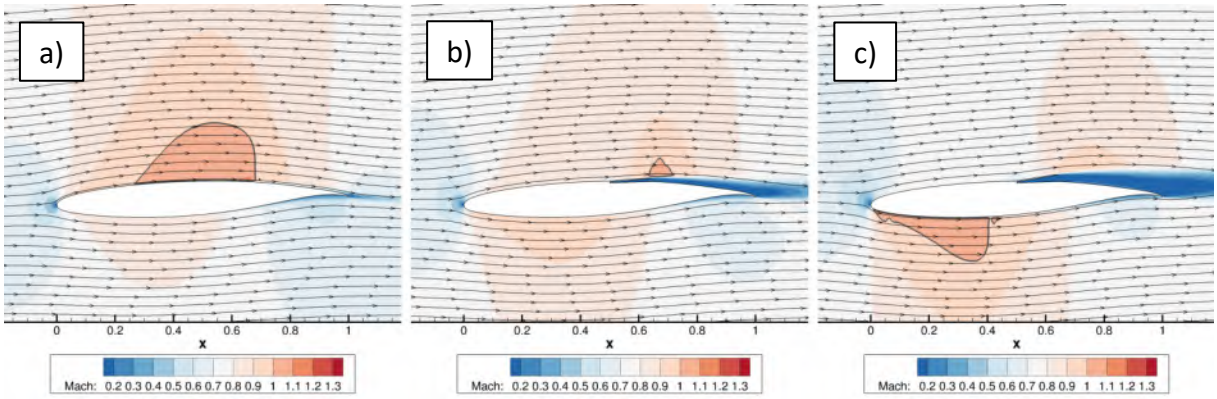

Figure 1: Local Mach number with isoline at Mach 1 around CRM airfoil configurations at Mach 0.74: a) 0° spoiler deflection b) 5° spoiler deflection c) 10° spoiler deflection.

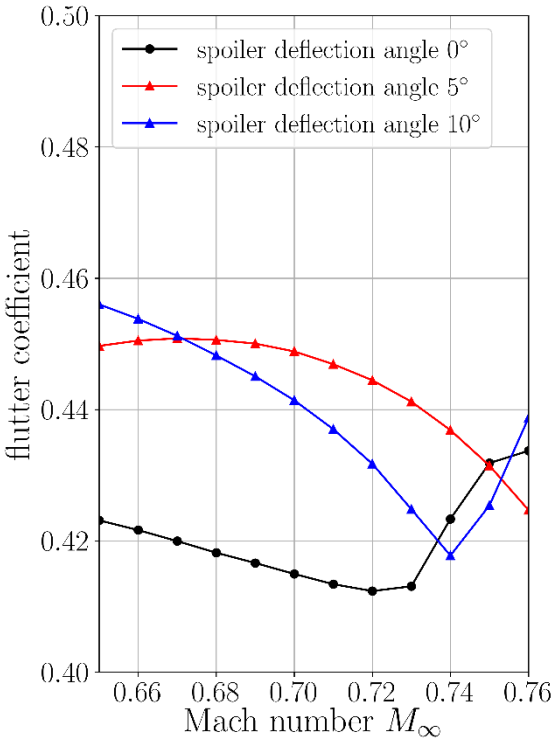

Figure 2: Flutter boundaries of the CRM airfoil configurations with 0°, 5° and 10° deflection angle.

As a result, changes in the flutter behavior of the airfoil configurations can be detected. Especially in the region of the transonic dip, increases in the flutter velocity are observed for both airfoil types due to a spoiler deflection. For example, an increase of 7.5% in the flutter coefficient is achieved for the CRM configuration with the smallest spoiler deflection angle of 5° at Mach 0.72, which is depicted in Figure 2. Despite these stability improvements, no overall robust behavior of this flutter suppression device can be demonstrated. At Mach numbers higher than the transonic dip region, a decline in the flutter stability boundary can be seen for some configurations. Also, some severe instabilities appear occasionally at these Mach numbers that could be traced back to the occurrence of buzz phenomena. This sensitivity towards Mach number and spoiler geometry indicates a careful use and a scheduling scheme dependent on the Mach number for the use of this flutter suppression technology.

References :

[1] Wright , J.R.; Cooper, J.E. Introduction to Aircraft Aeroelasticity and Loads, John Wiley, 2007.
[2] Livne, E. Aircraft Active Flutter Suppression: State of the Art and Technology Maturation Needs. J. Airc. 2017, 55, 1-41.
[3] Doggett, R. V. Some Effects of Aerodynamic Spoilers on Wing Flutter. NASA Technical Memorandum 101632, 1989.
[4] Cole, S. R. Aeroelastic Effects of Spoiler Surfaces on a Low-Aspect-Ratio Rectangular Wing. J. Aircr. 1992, 29, 768–773.

Mitteilung

Fachgruppe: Experimentelle Aerodynamik

Wind tunnel measurement of integral aerodynamic forces on a Flettner rotor using a low cost approach

H.T. Bartzsch, G. Brenner, A.D. Gardner, C.C. Wolf
Technische Universität Clausthal, Hauke.Bartzsch@dlr.de

A spinning cylinder in crossflow is the most fundamental example for the analogy between lift and circulation, and this principle is implemented by Flettner rotors.
The flow around a rotating cylinder and, therefore, its lift is highly dominated by flow separation and consequently by the Reynolds number. Eventhough the first successfull measurements of the resulting forces date back to 1853 [1], only few attemps have been made to quantify the relation between the lifting force and the Reynolds number, especially in the regime of Re<10 000. In the past decades, some numerical studies in this regime were conducted, while only two experimental studies are known [2-3], with the lowest Reynolds number being about 4 000 and thus leaving a huge gap of data being available for validation.
One major reason for this coarse data basis seems to be the particularly small magnitude of forces as a result of the obligatory small velocities and rotor diameters to achieve small Reynolds numbers. Another problem is the relatively high rotational rate being necessary for significant ratios of circumferential speed to freestream velocity, in the following refered to as α, caused by the small rotor diameters.
To fill the gap in validation data and to demonstrate the practical feasibility of experiments at Reynolds numbers being as small as 1 000, a low-cost approach was chosen to conduct measurements of the lifting force on a rapidly spinning cylinder of small diameter, using exclusively open source software and freely available off-the-shelf equipment.

The measurements took place in a small 300x200 mm wind tunnel of the Department of Fluid Mechanics of the Technical University Clausthal. The rotor diameter was as small as 10 mm, resulting in a Reynolds number of about 790 and a circumferential speed up to α = 4. To account for ground effect, the working section was chosen to be half-opened with sidewalls of acrylic glass hiding the apparatus for force measurement from the flowstream.

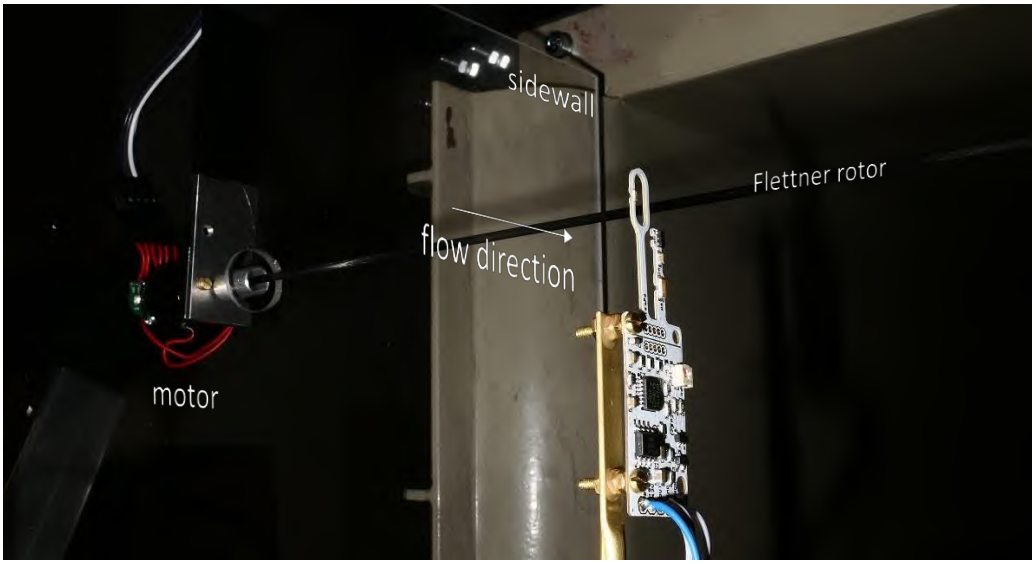

Fig. 1 : Test section with Flettner rotor made of carbon-fibre for structural stiffness and low-cost hot-wire anemometer

The lift force was measured by metallic strain-gauge incorporated loadcells for tiny wheigting applications, being able to measure forces in the range of millinewtons, while the freestream velocity was determined with the use of a low-cost hot-wire anemometer [4].
Actuator control and data acquisition were realized by use of a microcontroller.

Despite accounting for just a few millinewtons, the recorded forces show good agreement with both experimental and numerical studies at Reynolds numbers close to that of the current experiments. After an approximately linear growth of lift with the circumferential speed, a slight flattening of the lift curve is observated at an α of about three. As it has already been shown by several experiments [2-3], Prandtl's Postulate of a lift maximum at an α of two does not apply, nevertheless a reduction in lift slope beyond this point seems to take place. Interestingly the lift curve fits best to one computed on a three-dimensional model with a similar reynolds number [5] than to one being computed on a two-dimensional one [6], which predicted a lower lift at high circumferencial speeds. Vortices in the plane perpendicular to the flowstream, originating on the cylinder's surface and propagating with the flowstream, were observated numerically on three-dimensional models [5] and may be the reason for this discrepancy.

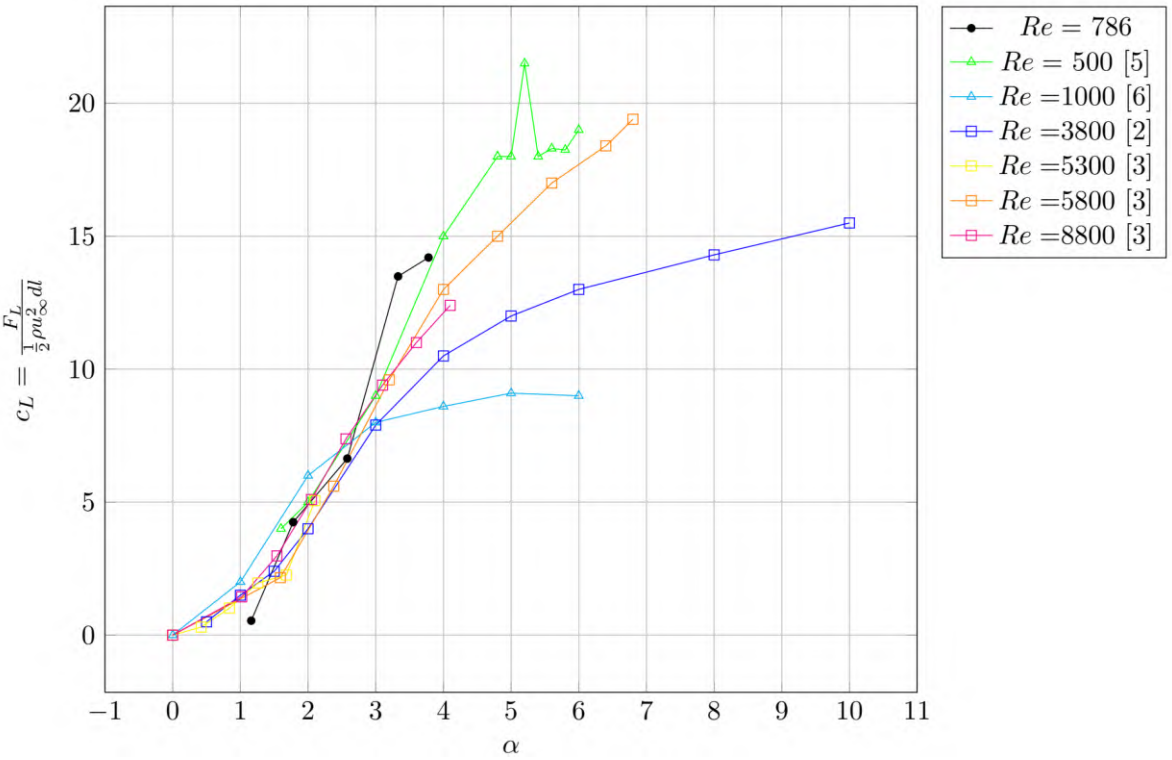

Fig. 2 : Lift coefficient, referenced to the diameter of the cylinder, versus ratio of circumferential speed to freestream velocity for small Reynolds numbers

[1] G. Magnus : "On the Deflection of a Projectile", *Abhandlungen der Akademie der Wissenschaften, Berlin, Germany*, 1852.

[2] P.T. Tokumaru, P.E. Dimotakis : "The lift of a cylinder executing rotary motions in a uniform flow", *Journal of fluid mechanics* 255, 1993, S.1-10.

[3] A. Thom : "Effect of discs on the air forces on a rotating cylinder", *Techn. Ber. HM Stationary Office*, 1934.

[4] D. Prohasky, S. Watkins : "Low cost hot-element anemometry versus the TFI Cobra", *19th Australasian Fluid Mechanics Conference*, 2014.

[5] A. Munir, M. Zhao, H. Wu : "Three-dimensional numerical simulations of flow past a rotating circular cylinder at a Reynolds number of 500", *International Journal of Offshore and Polar Engineering*, 2020, S. 105-111.

[6] Y.T. Chew, M. Cheng, S.C. Luo : "A numerical study of flow past a rotating circular cylinder using a hybrid vortex scheme", *Journal of fluid mechanics* 299, 1995, S. 35-35.

Mitteilung

Fachgruppe: Experimentelle Aerodynamik

Measuring the oncoming flow that operational freight-trains experience using the DLR FR8-LAB

James R. Bell*, Alexander Buhr, Arne Henning
German Aerospace Center (DLR), Institute of Aerodynamics and Flow Technology, Göttingen, Germany
*james.bell@dlr.de

Freight trains operate in a complex variety of conditions in the real-world: interaction with infrastructure, local topography and exposure to the environment. In spite of the relatively simple geometries in a freight-train consist – which can also be highly varied with a wide range of possible loading configurations – these operating conditions result in complex aerodynamics, that are critically important for a train's energy efficiency and safety of operation.

The DLR FR8-LAB is a 'swap-body' shipping-container (Fig 1, left), that can be loaded in different configurations. The FR8-LAB is self-contained, with an on-board power supply (rechargable by roof solar panels), data acquisition system and remote-access communication capability that has been transported on normal operating freight-trains in Europe.

The primary measurements are time-resolved (200-1000Hz) surface-pressure measurements at up to 330 positions on the container. Pressure on the front and rear surface can be integrated and provide insight into the pressure drag. Longitudinal rows and rings along the side and roof of the container provide insight into the side force, yaw and roll moments. A global navigation satellite system (GNSS) determines the location and the velocity over ground (VOG). Seven single-point LIDAR distance sensors with ~40m range are located on the container's sides, roof and front/rear surface to quantitatively characterize the physical environment. Two wide-angle 75° field-of-view (FOV)) thermal cameras (able to operate at night and in poor weather conditions) provide additional qualitative information on the local topography. Accelerometers and temperature sensors also measure the conditions inside the container.

In addition to measuring transient pressure and deriving transient forces and moments, the container can be utilized as a multi-hole dynamic-pressure probe, to measure the wide variety of oncoming-flow conditions freight-trains experience during real-world operation. The identified oncoming flow conditions can be used as input into aerodynamic/multi-body models to assess the risk of overturning (side-wind stability) as well as modelled in numerical simulations and replicated in wind-tunnel experiments. The inclusion of realistic oncoming flow can improve the accuracy of risk-assessment models, and enable any aerodynamic optimizations identified in simulations/experiments to be more transferable to real-world application.

Figure 1: Left: the FR8-LAB loaded on an operational freight train in Germany.
Right: the 1:15 scaled model of the FR8-LAB in the wind-tunnel experiment.

The oncoming flow can be derived from the surface pressure measurements on the FR8-LAB container's front/rear/side/roof surfaces (an example is illustrated in Fig. 2a) through a calibration developed in a 1:15 scaled closed-return wind-tunnel experiment (Fig 1, right). The wind-tunnel model of the container was statically yawed over a range of -90:90°, mapping the relationship between changing surface pressure characteristics and different yaw angles (i.e. the known oncoming flow conditions). This relationship (illustrated in Fig. 2b) can then be used to infer the oncoming flow characteristics the FR8-LAB experiences in real-world operation, through application of the calibration to the transient surface pressure measured. The calibration experiment was performed over a velocity and Reynolds-number range of 10-60m/s, Re=1-6x10^5 respectively, different freestream turbulence intensities of ~1,3 and 5% and with different loading configurations; upstream locomotives/containers resulting in full-scale equivalent gaps of 0.23-17.8m. These variables provide insight into the sensitivity of the calibration to conditions, as well as possible range of calibrations depending on the loading configuration.

With the calibration applied to the transient pressure measurements at key positions on the surface (that have strong characteristics that vary with yaw angle) the resultant wind magnitude V_R and direction (relative yaw angle) that the container experiences can be derived. Coupled with the velocity of the train over ground, V_T, measured by the GNSS, the atmospheric wind, V_W can be determined. An example of the derived velocity components is illustrated in Figure 2c.

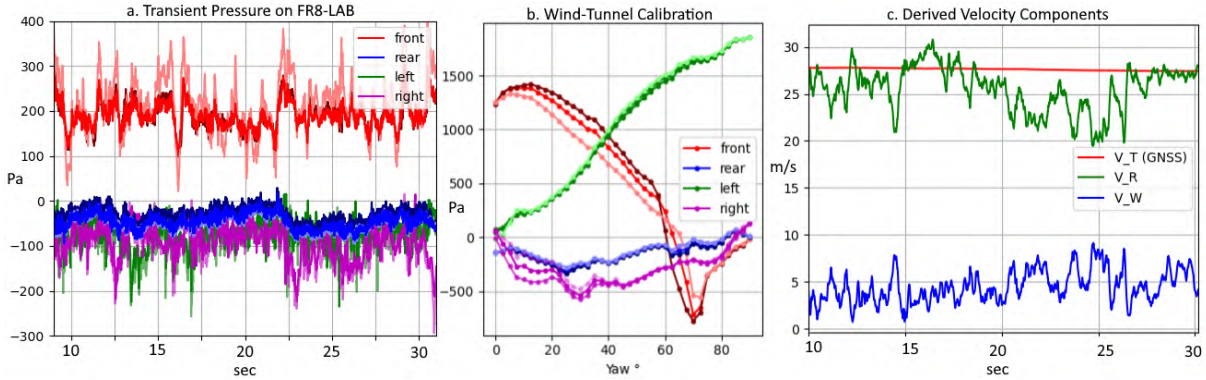

Figure 2: a. Example transient pressures at the front, sides, and rear (multiple shades of red, green, magenta and blue respectively) of the FR8-LAB during real-world operation. b. Corresponding pressure variation at the front, sides and rear at different discrete static yaw angles in the 1:15 scaled wind-tunnel experiment. c. Derived velocity components of the train V_T, resultant V_R and wind V_W.

The measurements obtained by the DLR FR8-LAB on operational freight trains have demonstrated the ability for the measurement, power and communication systems to successfully function in the challenging industrial conditions. The results show that the FR8-LAB can be used to not only determine peak pressure loads and subsequently derive forces and moments, but the entire container can also be used as a multi-hole dynamic pressure probe to infer the oncoming flow conditions that freight trains experience.

This work is part of FR8Rail IV project that has received funding from the ER-JU under the European Union's Horizon 2020 research and innovation programme GA 101004051

Mitteilung

Fachgruppe: Experimentelle Aerodynamik:

Separation detection inside a turbulent SBLI by means of a PVDF piezofoil array

Cosimo Corsi and Julien Weiss
Institut für Luft- und Raumfahrt, Technische Universität Berlin,Marchstraße 12,
10587 Berlin
cosimo.corsi@tu-berlin.de

Shockwave boundary layer interactions represent an ongoing topic of research, due to their complex flow structure and the rising interest in supersonic flow applications. This kind of phenomena is characterized by a natural unsteadiness, which is manifested by an oscillation of the shockwave at low frequencies, particularly evident when the boundary layer separates due to the incident shock. [1] Thus it is evident that the study of unsteadiness and the detection of separation within the SBLI is important for understanding the mechanism behind this type of phenomenon.

In a previous work we developed a novel cost-effective technique for SBLI unsteady wall-pressure measurement based on a piezo-film sensor array. [2] The film sensors are based on the organic polymer *polyvinylidene fluoride* (PVDF) and his piezoelectric proprieties (change in surface-charge caused by mechanical loading of the film) are due to the particular crystalline disposition that the polymer acquires after artificial polarization. The polymer layer is coated on both sides with a thin layer of metal, so that the 2 faces of the film act as collectors for the charges generated by the external forces through the piezoelectric effect of the material. The metal coating layer can be partially etched into custom shapes and patterns keeping only a wanted portion of the metal. In such a way it is possible to form specific active sensing areas with virtually as many sensors as required from a single foil.

In the present contribution we want to integrate the previous work, where only the unsteadiness of the flow was addressed, by gathering information about the separation point location. In this way we will have a thorough picture of the phenomenon for more in depth investigations.

The separation detection with the sensor array is possible thanks to the simultaneous acquisition of the time signals of various consecutive sensors. The phase shift of the signal can be derived in relation to the frequency from the cross correlation that takes place between two series of signals from adjacent sensors. The phase position allows then to determine the significant flow regions. When two sensors are installed in the region of a flow that is not subject to interference, their signals occur in the same phase, excluding the minimal time shift between the two sensors. When the point of separatceion or reattachment lies between two sensors, their signals have to be in opposite phases, sin the direction of the separated flow and, consequently, both the fluctuations in pressure and shear stresses have to be inversely proportional at these sensors. Here, the phase shift has to be close to ±180 deg.

The described behavior is presented in Figure 1 where on the left the cross correlated phase spectra are shown, and on the right, we can see an oil-flow visualization [3] of the studied flow with the position of the piezo sensors overlapped in red. Is evident how between position 5/6 and between positions 4/5 the signals are in phase (phase shift = 0°), indeed these sensors are all located under the separation bubble. Instead for position 2/3 we have out of phase signals (180° phase shift) and in fact the sensors straddle the detachment line (as shown in the oil-vis image). Eventually for position 1/2 we have an uncertain behavior since the sensor 2 is located really close to the separation line.

For the final version of the paper we will increase the spatial resolution of our piezo array in order to better detect the exact location of the separation.

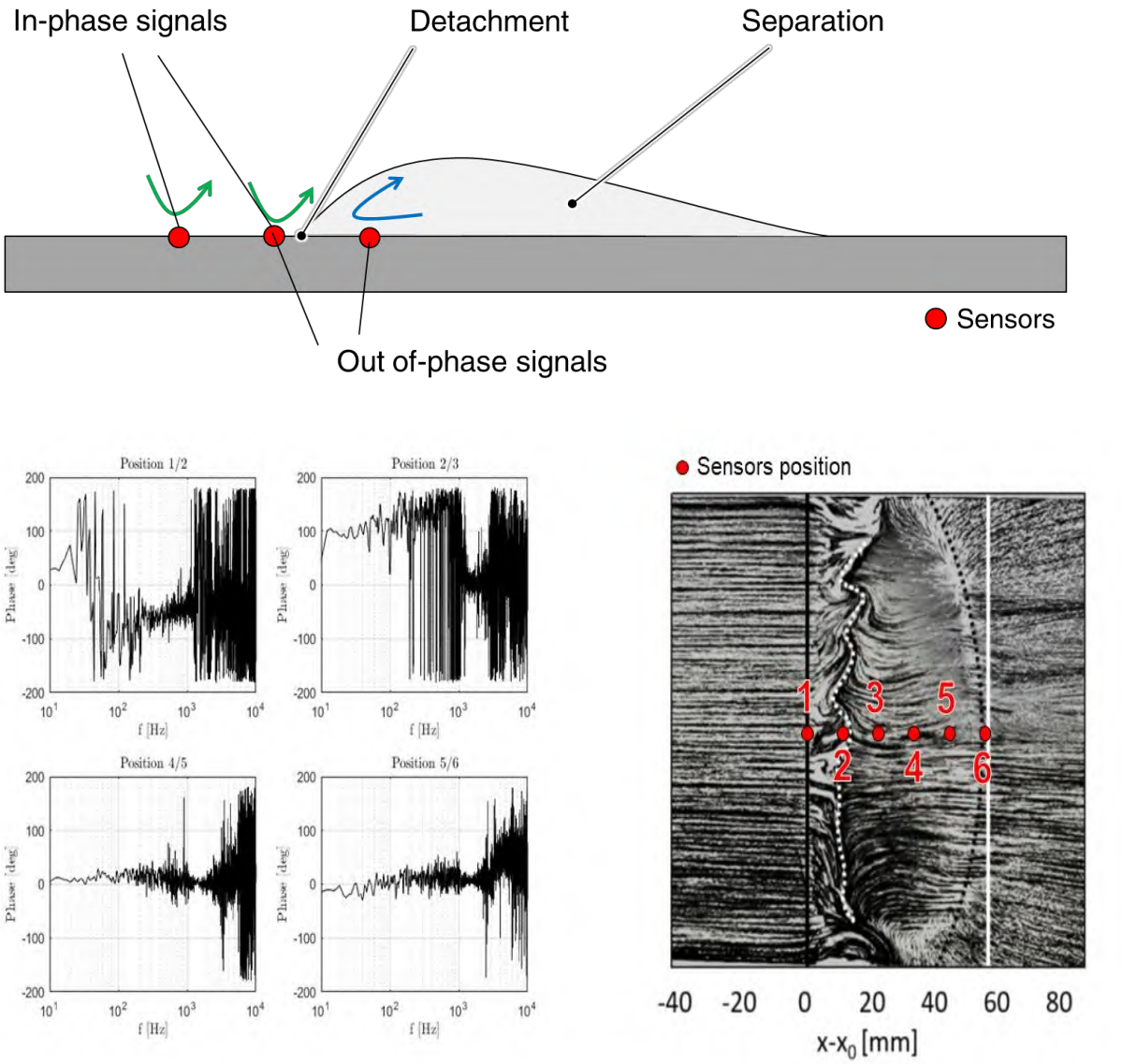

Figure 1: *Working principle for separation detection based on PVDF sensor array (top). Phase cross-spectra between adjacent piezoelectric sensors (left). Surface oil-flow visualization of the separation zone in a turbulent SBLI obtained with a 10° shock generator in a Mach 2 supersonic flow (right). [3]*

References:

[1] Harvey, J., and Babinsky, H., "*Shock Wave-Boundary-Layer Interactions"*, Cambridge University Press, 2013.

[2] Corsi, C., Rohlfs, L., Weiss, J., Wang, B., Kahf, M., Obloch, P. and Ngo, H. "*Development of a PVDF Piezo-Film Sensor Array for Unsteady Wall-Pressure Measurements in a Turbulent SBLI*" AIAA Aviation 2022 Forum, American Institute of Aeronautics and Astronautics, 2022

[3] Rohlfs, L., Stab, I., and Weiss, J., "*Experimental Investigations of Incident Shockwave Boundary Layer Interactions in a Continuously Operating Supersonic Wind Tunnel*," AIAA Aviation 2022 Forum, American Institute of Aeronautics and Astronautics, 2022

Mitteilung

Fachgruppe: Experimentelle Aerodynamik

Investigations on the effectiveness of passive aerodynamic manipulations at the leading edge of a wind turbine rotor blade airfoil to influence lift

Marten Danker∗ Maximilian Maigler+ Oliver Meyer∗ Jochen Schein+

∗Institut für Aerodynamik und Flugsimulation, +Institut für Plasmatechnik
Universität der Bundeswehr München, Werner-Heisenberg-Weg 39, 85579 Neubiberg
∗marten.danker@unibw.de +maximilian.maigler@unibw.de

Overview
Within the last decades, extensive efforts have been made to optimize high-lift airfoils for wind turbines in the incompressible flow regime based on a variety of optimization criteria. Modern wind turbine blades feature a diversity of modifications, both active and passive. On the passive side, vortex- generators may be attached on the upper airfoil surface in order to delay the flow separation at high Reynolds numbers. An example for active modification is the ability to rotate the blade along its tangential centerline in order to increase or decrease the angle-of-attack α based on the incoming wind velocity magnitude and direction.

Still, accidents are occurring that can lead to partial or complete destruction of the wind turbine caused by sudden gusts or high incoming wind velocities. For this reason, wind turbines are equipped with several safety mechanisms to prevent overloading. One approach is to limit the aerodynamic forces that are exerted on the blades due to the aerodynamic forces. The present work focuses on another approach by employing passive aerodynamic modifications to limit these forces without or only slightly decreasing the overall generated power. The main concept is to influence the local air flow at the leading edge of the blade airfoil. As a retrofit, motionless leading edges with a small radius can be added to the blades. This manipulation leads to a limitation of lift at a certain operation range, which is defined by a high power outcome without any threats of damage and can be seen as a local angle-of-attack of the airfoil against the leading edge air flow.

The present study is a continuation of the work of [1], but applies the methodology on a different blade airfoil that has a larger initial leading edge radius and less critical stall behaviour. In addition, we implemented novel techniques for finding an optimized design such as an analytical tool for adding various leading edge shapes to a given base airfoil. The reliability of the experimental results by using the additive manufacturing process like 3D-printing for manipulating the blade airfoil was assessed. Further validation work was carried out using computational fluid dynamics in two measures. The first step was to devise a numerical setup producing data for the lift and drag coefficients which deviates only slightly from the experimental results. The second step was to use the validated model for simulating many variations in order to find an optimized leading edge design. Finally, based on the described research, we devised an optimum design as a model for wind tunnel verifications.

Experimental and Numerical Methodology
The methodology of our approach can be summarized into 3 main parts:

1. Experimental analysis of the TEG2618 base profile at $Re = 8 \cdot 10^5$ and validation of the numerical model based on the produced reference data.
2. Numerical analysis of geometrical modifications for a range of α to determine the modification meeting our requirements.
3. The determined modification is manufactured and experimentally analyzed and compared with 3D printed leading edges that are glued to the base profile.

In the first instance, the base profile ($L = 0.35\mathrm{m}$) is analyzed at our in-house wind tunnel facility for $\alpha = -5 \text{ to } 12°$ at a Reynolds number of $Re = 8 \cdot 10^5$. Then, the generated polar and Lilienthal plots are used as the reference data to validate the numerical approach where the same wind tunnel conditions are simulated using CFD and the optimum settings such as the turbulence model and discretization are determined. After successful validation, various leading edge modifications are devised using the analytical approach.

A software tool was developed in order to automatically simulate all modifications for the entire range of α. Besides the lift and drag coefficients, characteristic quantities such as the static pressure and velocity fields are written out and analyzed for gaining understanding why certain modifications perform better than others. The modification closest to meeting our criteria is selected and the entire airfoil manufactured. To assess the necessity of having a completely smooth profile or if a slight non- tangency at the geometrical transition from the leading edge to the profile can produce similar results with acceptable deviation, the modified leading edge is 3D printed and glued to the base profile.

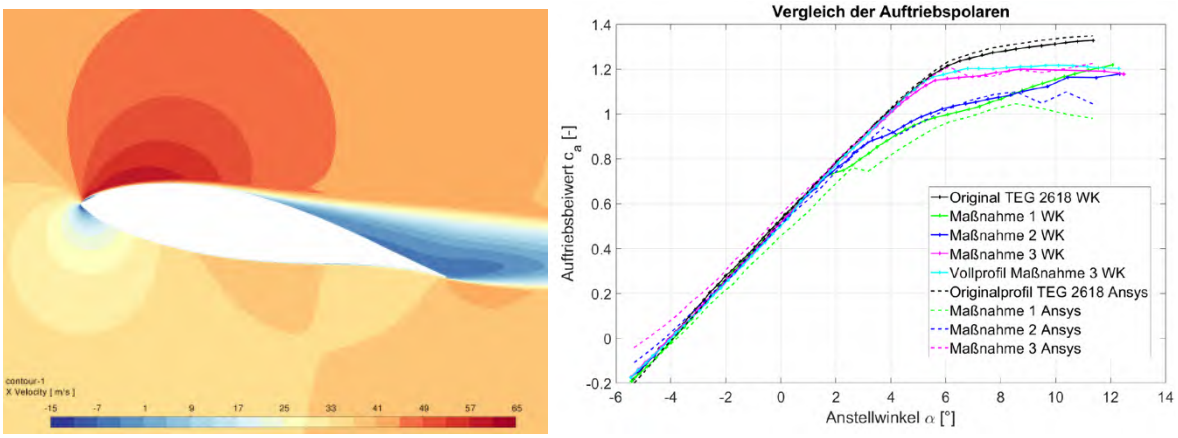

Figure 1: Comparison of base profile to modification wind tunnel and CFD [3]

Summary of Results

A sample CFD predicted velocity field of a modification and a polar c_l plot comparison is shown in fig. 1. The simulations for the same range of α could successfully be implemented for the entire range, even at high α it is able to match the shape of the experimental data plots compared to traditional inviscid Euler codes such as XFOIL [2] while maintaining feasible run times. With the validated CFD model the devised variants of leading edges were simulated for the same Reynolds number. We chose the one as our final modification that exhibits the combination of maximum c_l and longest constant lift after stalling. The leading edge of this modification was 3D printed and glued to the base airfoil in order to compare the experimental results between the glued leading edge and the fully smooth, manufactured airfoil modification. We discovered that the simple glued solution is able to provide satisfactory results in the wind tunnel compared to the manufactured modification, saving time and cost during future research on airfoil modifications. The coefficients predicted by the automated CFD simulations exhibit good agreement with the subsequent wind tunnel experiments and allow understanding of the flow field around the airfoil, particularly the boundary layer and flow separation, allowing us to analyze a large number of airfoil modifications without the need for the same number of wind tunnel experiments.

References

[1] O. Meyer, “On the effectiveness of retrofitted airfoil leading edge devices to limit lift,” in New results in numerical and experimental fluid mechanics XIII, vol. 151, G. K. Dillmann Andreas; Heller, Ed. Cham, Switzerland: Universität der Bundeswehr München, Springer Nature, 2021, pp. 729–738. doi: 10.1007/978-3-030-79561-0_69.
[2] Massachusetts Institute of Technology, “XFOIL - subsonic airfoil development system.” https://web.mit.edu/drela/Public/web/xfoil/ (accessed Jun. 17, 2022).
[3] C. Meichsner, “Validierung von Untersuchungen zur Wirksamkeit von Vorderkantenmaßnahmen zur Beeinflussung des Hochauftriebsverhaltens bei Flügelprofilen”, Studienarbeit, Universität d. Bundeswehr München, 2022

Mitteilung

Fachgruppe: Experimentelle Aerodynamik

Eine neuartige Strömungssonde zur Erfassung der zeitlich hochaufgelösten Wandschubspannung in Betrag und Richtung

Mario Eck, Dieter Peitsch
Technische Universität Berlin,
Institut für Luft- und Raumfahrt,
Fachgebiet Luftfahrtantriebe,
Marchstraße 12-14, D-10587 Berlin,
Mario.Eck@tu-berlin,de
Dieter.peitsch@tu-berlin.de

Christian Westphal
Technische Universität Berlin,
Institut für Strömungsmechnaik und Technische Akustik
Fachgebiet Numerische Fluiddynamik
Müller-Breslau-Straße 15, D-10623 Berlin
Christian.Westphal@tnt.tu-berlin.de

Die Wandschubspannung ist eine zentrale Größe in der Grenzschichttheorie und von außerordentlich großer Bedeutung für Auslegungs- und Optimierungsprozesse in der Aerodynamik. Per Definition beschreibt die Wandschubspannung eine tangential auf eine umströmte Wand wirkende Kraft pro Flächenelement. In vektorieller Form ist sie daher eindeutig durch den Betrag und die Richtung definiert. Für die experimentelle Bestimmung stehen unterschiedliche indirekte und direkte Messverfahren zur Verfügung, welche sich durch ihre Anwendungsfreundlichkeit und Robustheit unterscheiden. Die meisten beschränken sich auf den Einsatz in geraden 2D-Grenzschichtströmungen und erlauben meistens lediglich die Bestimmung zeitgemittelter Schubspannungen.
Das Fachgebiet Luftfahrtantriebe hat eine herkömmliche, druckbasierte Messtechnik, die Oberflächenzaunsonde, weiterentwickelt. Durch den Einsatz einer alternativen Sondengeometrie soll der Informationsgewinn erheblich gesteigert werden. Die besondere Eigenschaft der Sonde besteht darin, die zeitlich hochaufgelöste Wandschubspannung gleichzeitig in Betrag und Richtung zu erfassen. Darüber hinaus ist sie aufgrund der Verwendung piezoresistiver Drucksensoren vergleichsweise robust.
Der vorliegende Beitrag befasst sich mit der experimentellen Validierung des Auflösungsvermögens definierter Richtungsänderungen der Wandschubspannung. Zur Erzeugung periodischer Richtungsänderungen wird ein fluidischer Oszillator (Fluidik) in Form eines sog. Sweeping-Jet Aktuators verwendet. Mithilfe der High-Speed-Shadowgraph-Visualisierung wird zunächst der zeitlich hochaufgelöste Jetwinkel im engsten Düsenquerschnitt bestimmt und anschließend wird an dieser Position die Oberflächenzaunsonde platziert. Die zeitlichen Jetwinkel der Sonde und der High-Speed-Shadowgraph-Visualisierung werden jeweils ensemble-gemittelt und gegenübergestellt, um schließlich eine frequenzabhängige Dämpfung und Phasenverschiebung der Sondendaten zu ermitteln.
Das Ergebnis dieser Frequenzkalibrierung ist eine Übertragungsfunktion für die Oberflächenzaunsonde. Gleichzeitig dienen die Ergebnisse als vorläufige Demonstration der Funktionsfähigkeit dieser innovativen Sonde.

Mitteilung

Fachgruppe: Experimentelle Aerodynamik

Zu Druck und Strömungsgeschwindigkeit neben einem Zug im Tunnel

Klaus Ehrenfried und Daniela Heine

Institut für Aerodynamik und Strömungstechnik, DLR
Bunsenstraße 10, 37073 Göttingen
klaus.ehrenfried@dlr.de

Die numerische Simulation von Druckwellen, welche bei der Tunnelfahrt von Schienenfahrzeugen entstehen, hat eine lange Tradition. Die Ergebnisse werden zum Beispiel dazu verwendet, um die Lasten auf die Infrastruktur im Tunnel oder auf die Züge selbst abzuschätzen. Um die Druckwellenausbreitung im gesamten Tunnel einschließlich der Reflexion an den Enden und die komplexen Überlagerungen der hin- und herlaufenden Wellen zu berechnen, werden üblicherweise quasi-eindimensionale Verfahren verwendet (siehe z.B. [1]). Dabei werden Druck, Dichte und Geschwindigkeit in einem Querschnitt durch jeweils einen Wert repräsentiert. Abgesehen von den dreidimensionalen Strömungsfeldern am Bug und Heck des Zuges kann der Druck näherungsweise über den Querschnitt als konstant angenommen werden. Jedoch ist das Geschwindigkeitsfeld neben dem Zug mit den Grenzschichten an der Zugoberfläche und der Tunnelwand relativ komplex. In den verschiedenen Bereichen besitzt die Geschwindigkeit im allgemeinen unterschiedliche Vorzeichen. Es stellt sich die Frage, wie gut quasi-eindimensionale Verfahren die Strömung um den Zug überhaupt abbilden können, und ob mit den berechneten Werten zum Beispiel die Anströmgeschwidigkeit an einem Stromabnehmer im Tunnel vorhergesagt werden kann.

Reibungseffekte werden bei den eindimensionalen Berechnungen mit Hilfe von empirischen Parametern berücksichtigt. Dazu gehören Reibungsbeiwerte für Zug- und Tunnelwand sowie Koeffizienten, zur Berechnung der Verluste in den dreidimensionalen Strömungen am Bug und Heck. Die Parameter werden so eingestellt, dass die berechneten Druckverläufe mit in Testfahrten Gemessenen möglichst gut übereinstimmen. Allerdings zeigten Messungen der Strömungsgeschwindigkeit im Tunnel häufig größere Abweichungen zur Rechnung ([2]). Ein Problem dabei stellt die Positionierung der Sonde dar. Sie kann unter Umständen von der Grenzschicht am Zug oder an der Tunnelwand erfasst werden. So ist die Interpretation der gemessenen Geschwindigkeiten oft schwierig.

Um zu überprüfen, wie gut eindimensionale Rechnungen die Strömungsgeschwindigkeit im Tunnel nachbilden, wurden Modellversuche durchgeführt. Diese fanden an der Tunnelsimulationsanlage (TSG) des DLR in Göttingen statt. Dabei wurde die Tunnelfahrt mit einem bewegten Modell im Maßstab vom 1:25 nachgebildet. Das Modell wurde mit einem Katapult auf 31.5 m/s beschleunigt und fuhr dann auf Schienen durch einen 10 m langen Modelltunnel. Gemessen wurde die Strömungsgeschwindigkeit mit einem Pitot-Rohr am Modell 0.9 m (knapp eine Wagenlänge) hinter der Zugnase und 28 mm von Oberfläche entfernt. Die Position wurde so gewählt, dass an der Sonde die Geschwindigkeit außerhalb der Grenzschicht erfasst wird. Zusätzlich wurden der statische Druck und der Druckgradient entlang des Zuges gemessen. Das Zugmodell war dazu mit einer speziell entwickelten Datenerfassung ausgerüstet. Aufgezeichnet wurden neben den Strömungsgrößen auch die Beschleunigung des Modells und Positionsdaten von einem optischen Sensor unten am Zug. So ist eine Zuordnung der gemessenen Werte zur momentanen Position des Modells möglich.

In Abbildung 1 ist der Verlauf der Anströmgeschwindigkeit u an der Pitot-Sonde über dem Messort x aufgetragen (blau). Bei $x = 0$ befindet sich der Tunneleingang. Zu erkennen ist die Erhöhung der Anströmgeschwindigkeit im Tunnel. Diese wird auch in den Simulationen erfasst (rote Kurve). Bis auf Abweichungen am Tunnelein- und -ausgang, die sich durch drei-

dimensionale Effekte erklären lassen, ist die Übereinstimmung der Kurven relativ gut. In der Simulation ist die Geschwindigkeit etwas geringer als im Experiment, da es sich um den über den Querschnitt gemittelten Wert handelt. Dieser ist wegen der Anteile aus den Grenzschichten etwas niedriger als der in der Kernströmung gemessene Wert.

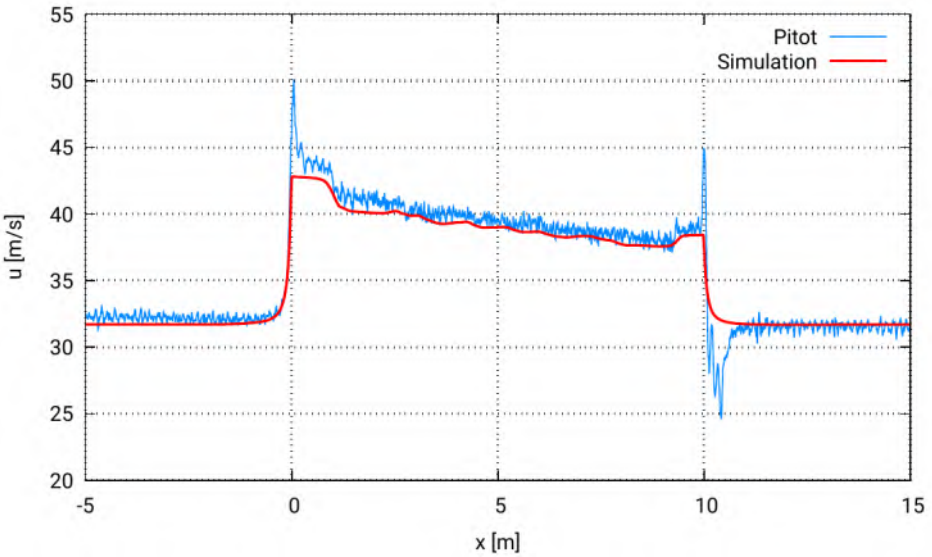

Abbildung 1: Anströmgeschwindigkeit der Pitot-Sonde als Funktion der Position; Blau: Gemessen; Rot: Quasi-eindimensionale Simulation.

Literatur

[1] Schultz, M., Sockel, H.: Pressure transients in short tunnels. In Proceedings of 7th International Symposium on Aerodynamics and Ventilation of Vehicle Tunnels (Ed. A. Haerter), Brighton, 27-29 November 1991, pp. 221-237 (BHR Group, Cranfield).

[2] Vardy, A.E., Reinke, P.: Estimation of train resistance coefficients in tunnels from measurements during routine operation. Proceedings of the Institution of Mechanical Engineers, Part F: Journal of Rail and Rapid Transit. 1999;213(2):71-87.

Mitteilung

Fachgruppe: *Experimentelle Aerodynamik*

Aufbau eines Prüfstandes zur Umströmung einer unstetig gekrümmten Kontour mit definiertem Grenzschichtverlauf und Anreicherung der Grenzschicht mit Sand

Uwe Fey*, Thomas Kowalski*, Torsten Gries* und Manuel Gageik**

*DLR-Göttingen, Bunsenstrasse 10, 37073 Göttingen, Uwe.Fey@dlr.de

**Siemens Mobility GmbH, Duisburger Str.145, 47829 Krefeld, Manuel.Gageik@siemens.com

Im Beitrag wird beschrieben, wie ein experimenteller Aufbau realisiert wurde der zur Untersuchung einer Gitterklappe dient, welche sich seitlich im Unterbodenbereich eines Schnellzuges befindet der in einer Wüste operieren soll. Beim Betrieb in einer Wüste wird durch den fahrenden Zug ein bestimmter Anteil des am Boden befindlichen Sandes aufgewirbelt (Korngrößen von ca. 50 bis 400 μm) und in die turbulente Grenzschicht im seitlichen Unterbodenbereich der Wagons eingetragen. Durch das betreffende Gitter wiederum wird während der Fahrt Luft eingesaugt um interne Aggregate zu versorgen. Ist die gitternahe Luft (d.h. die Grenzschicht am Zug die sich im Fahrbetrieb ausbildet) mit Sand angereichert, so wird zwangsläufig auch ein Anteil von Sand durch die Gitteröffnungen hindurch gesaugt werden. Zur Bestimmung dieses Sandanteils wurde ein Prüfstand aufgebaut (*Abb.1a*), der es erlaubt den durch das Gitter gesaugten Sand für verschiedene Gittervarianten, nachgeschaltete Sandfilter und verschiedene Methoden der Abdichtung eines umlaufenden Spaltes zu bestimmen. Dabei bestand folgende Zielsetzung:

1. Die am Zug in unterbodennähe montierte Gitterklappe soll im Maßstab 1:1 über die komplette Fläche mit Sand-angereicherter Luft wandparallel überströmt werden

2. Es ist eine geeigneter Sand zu finden, der hinsichtlich seiner Korngrößenverteilung in etwa dem realen Wüstensand entsprechen soll

3. Es ist über dem Gitter eine Grenzschicht herzustellen, die der realen Grenzschicht am fahrenden Zug entsprechen soll, und zwar für drei verschiedene Positionen im Zugverband (vorne, mitte, hinten) und für drei verschiedene Geschwindigkeiten (80, 160, 230 km/h). Dabei wird vereinfachend angenommen, dass die Wandgrenzschicht am realen Zug dem Verlauf des 1/7-Potenz Gesetztes entsprechen soll

4. Das Gitter besitzt eine spezielle, unstetig gekrümte Querschnittsform (*Abb.1b*) und in der Montage am Zug einen rundum laufenden Spalt. Die Gitter- und Spalt-nahe Strömungsgrenzschicht soll homogen mit Sand angereichert werden, wobei während der Versuchsläufe eine bestimmte Sandkonzentration (reproduzierbar) herzustellen ist

5. Der durch das Gitter (und den Spalt) hindurch gesaugte Sand soll nach dem Testlauf möglichst komplett aufgesammelt werden. Es soll sein Gewichtsanteil am gesamten, verbrauchten Sand sowie seine Korngrößenverteilung bestimmt werden. Exemplarisch sollen für eine Variante drei verschiedene Absaugraten untersucht werden

6. Die Versuche sind möglichst reproduzierbar zu gestalten um einen möglichts genauen Vergleich verschiedener Varianten von Gittern mit Filtern und Abdichtungen zu ermöglichen

Im hier vorgestellten Beitrag wird gezeigt, wie durch umfangreiche Vorversuche sämtliche o.g. Bedingen erfüllt werden konnten. Es wurde ein Prüstand neu aufgebaut, der im Wesentlichen aus einem Gebläse besteht, welches über eine neu gefertigte Spezialdüse die komplette Kontour des Gitters und die Spalte wandparallel überströmt. Die Grenzschichtform (*Abb.2a*) konnte durch eine Kombination von Zackenblechen am Düseneingang und zwei Stolperdrähten unterschiedlicher Dicke im Verlauf der Düsenkontraktion hergestellt werden. Die homogene Verteilung des Sandes (*Abb.2b*, unten) wurde durch Injektion an drei Positionen unterschiedlicher Höhe mittels Reservoirs am Düseneingang erzeugt, welche mit Druck beaufschlagt werden können (*Abb.1a*, ‘‘Sand-Reservoirs’’), sowie über ein Reservoir an oberen Düsenausgang ohne Druckbeaufschlagung.

Durch Regelung des Vordrucks konnte der Sand-Durchsatz der vorderen Reservoirs während der Testläufe synchronisiert und reproduzierbar auf einen gewünschten Wert eingestellt werden. Die spezielle Gestaltung der Kammer, die die Gitterklappe trägt (brauner Kasten in *Abb.1a*) und ein in der Kammer montiertes Filtervlies ermöglichten es, den angesaugten Sand mit sehr wenig Verlusten für die Analyse aufzusammeln. Die Simulation der Absaugung erfolgte durch ein weiteres Gebläse hinter der Kammer (*Abb.1a*, oben) und ein integrierter Sondenrechen erlaubte die instantane Bestimmung der Absaugrate und damit eine genau Regulierung des Volumenstroms auf 1% genau, was für den Vergleich verschiedener Varianten von Gittern/Filtern/Abdichtungen Voraussetzung ist. Da der komplette Prüfstand in einer Versuchshalle aufgebaut wurde, musste weiterhin eine Vorrichtung erstellt werden um den mit ca. 230 km/h am Gitter vorbei geblasenen Sand in geeigneter Weise wieder aufzufangen (der vordere Teil davon – in Form eines Trichters – ist in *Abb1a,* links unten zu sehen).

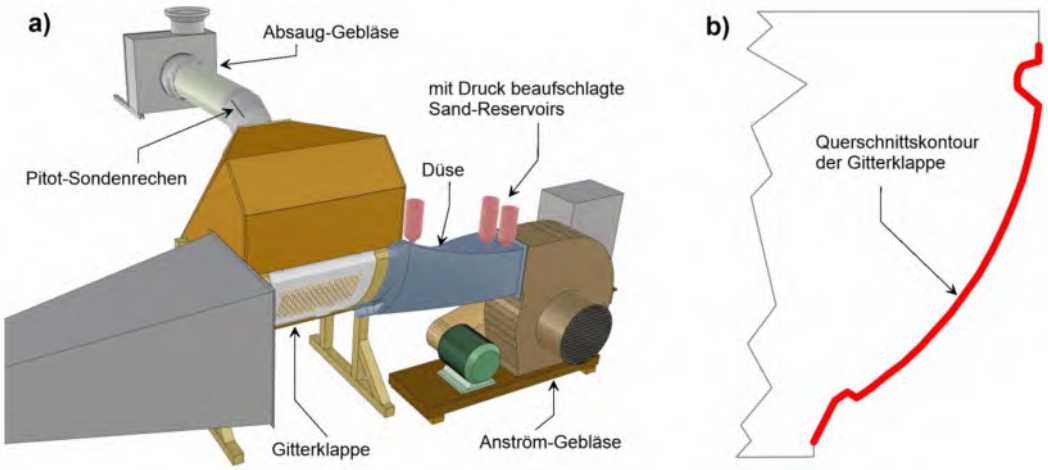

Abbildung 1*: a) Aufbau des Prüfstandes mit Gebläsen und Spezial-Düse. b) Vertikaler Schnitt der Gitterklappe*

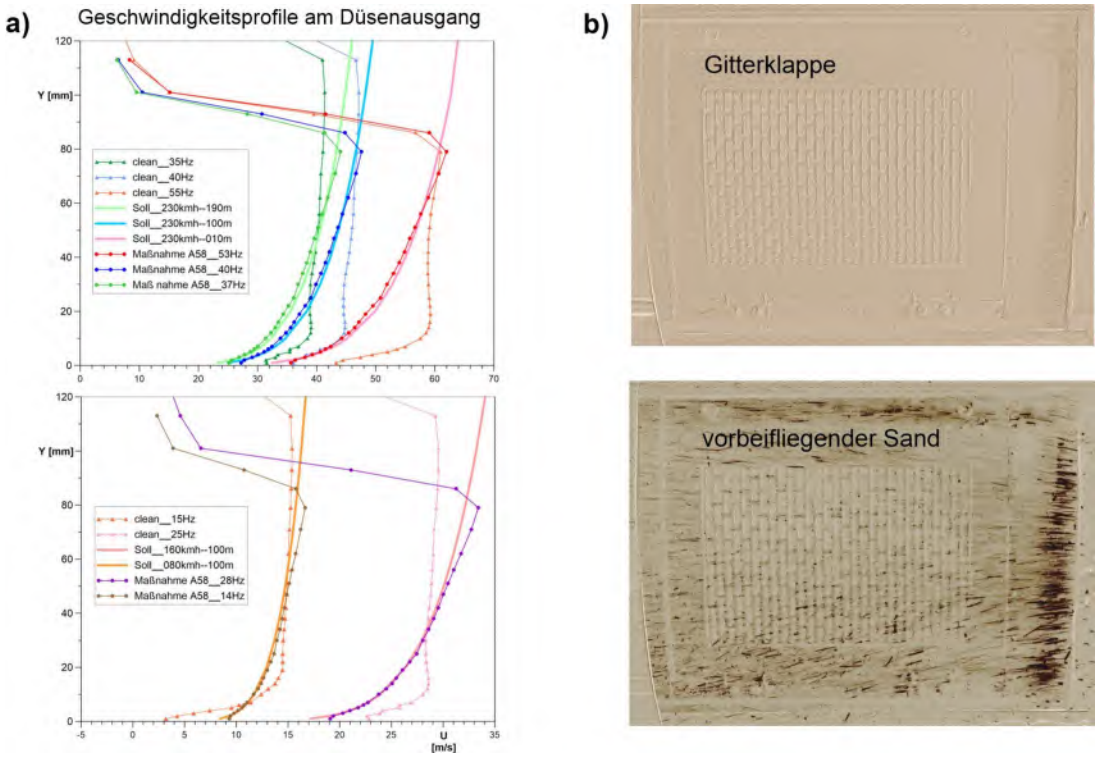

Abbildung 2 : *a) Grenzschichtverläufe am Düsenausgang für verschiedene Geschwindigkeiten und Positionen im Zugverband: ohne GS-Beeinflussung (clean), Verlauf nach dem 1/7-Potenz Gesetz (Soll) und per Zackenblech und Stolperdrähten erzeugter Verlauf (Maßnahme A58). Die Werte in Hz sind ein Maß für die Gebläsedrehzahl. b) Gitter ohne (oben) und mit Sand angereicherter Luft umströmt (unten).*

Mitteilung

Fachgruppe: Experimentelle Aerodynamik

Experimental investigation of the flow-physical effects of a **D**istributed **E**lectric **P**ropulsion configuration on a 2D wing model in high-lift configuration

Alex Gothow, Julien Weiss
Technische Universität Berlin, Institute of Aeronautics and Astronautics,
Marchstraße 12 10587 Berlin, a.gothow@tu-berlin.de

One approach to achieving climate-neutral aviation is to electrify the drivetrain. This opens up new possibilities for the overall airplane configuration. Distributing the propulsion system of an aircraft among several smaller electric propellers instead of a few large ones is one new concept that has a number of potential advantages, such as reducing the load on the wing structure, increasing reliability through redundancy and increasing efficiency, especially for the high lift system. [1] Recent studies have shown that an increase in the lift coefficient of up to 72% is possible in the high-lift system, especially for regional aircraft, which is relevant for short take-off and landing (STOL) configurations. [2] This results, for example, in potential savings for drag and weight in this class of aircraft by reducing the size of the wing and vertical stabilizer. [3] As technology advances, it can be assumed that this concept will also be transferable to medium- and long-range aircrafts.
The EU-funded project DISPROP deals with the validation of numerical methods of Distributed Electric Proplusors (DEP) by experimental parameter studies on a medium- and large-scale 2D wing model in a high-lift configuration. For a validation of the numerics an exact knowledge about the position of the laminar turbulent transition is indispensable. This study deals with the results for the medium-scale model and is focused on the flow-physical effect of a configuration with propellers compared to the isolated wing and the laminar turbulent transition.
The wing model used is based on a NACA65(3)-218 airfoil that is scaled to a chord length of 410mm with a wingspan of 1550mm. The high-lift system consists of a droop nose and a single slotted flap, where the droop nose is fixed and the angle of attack of the flap can be varied to three positions. Figure 1 and 2 representing the medium-scale wing model for the GroWiKa experiments.

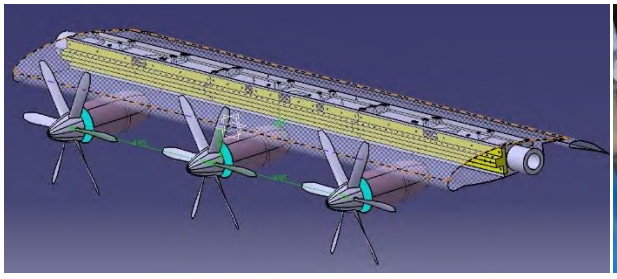

Figure 1:conceptional design of the model

Figure 2: wing model with propellers at GroWiKa

The propeller used is a scaled variant of the six blade XPROP research propeller from TU-Delft, that is well documented and variable in pitch. [4] For the experiments in the GroWiKa, the XPROP is scaled to a diameter of 13' and the pitch is adjusted so that a desired thrust coefficient ct of 0.3 is achieved. In the experiments at GroWiKa, the high-lift configuration is tested at an inflow velocity of 35m/s and a resulting reynolds number of about 960,000. Possible Reynolds number effects are investigated in the following studies at DNW-NWB on the large-scale model.

Results:
Initial results with hotfilms on the isolated wing have shown that a laminar flow is present on the upper surface in the front part of the wing and that a transition to a turbulent flow between the first and the second sensor occurs, see figures 3 and 4.

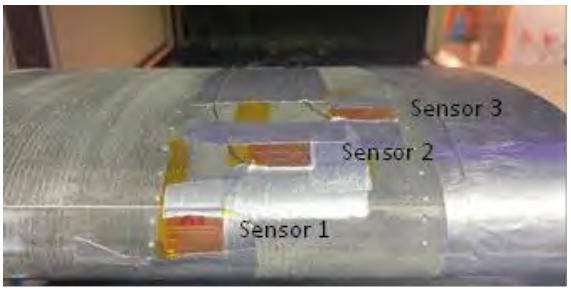

Figure 3: hotfilm sensors positions on the wing

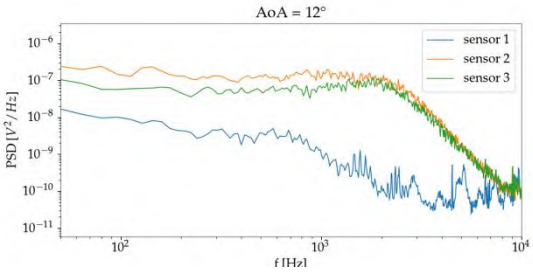

Figure 4: hotfilm for the isolated wing

Oil flow visualizations have additionally revealed the formation of a laminar detachment bubble in this area that can prevented with a turbulator placed in front of the first sensor, see figure 5.

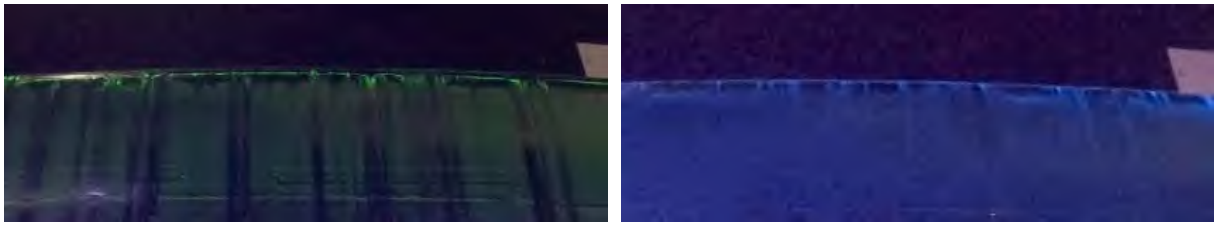

Figure 5: Oil flow visualization of the isoalted wing top view (green without tripping and blue with tripping)

Figure 6 shows an oil flow visualization for the configuration with propeller, in which no laminar detachment bubble is visible anymore, but very prominent detachment areas in the area of the side walls, which are caused by the propeller flow.

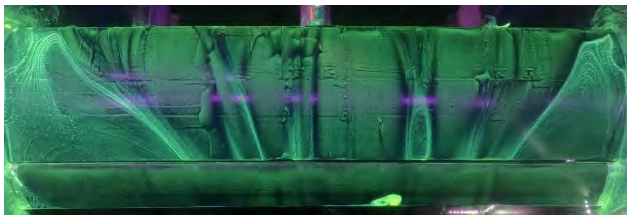

Figure 6: Oil flow visualization wing with propellers

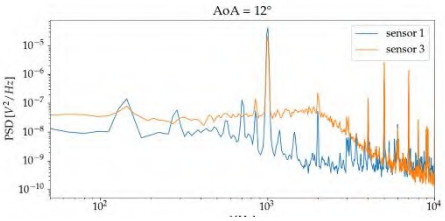

Figure 7: hot-wire for the wing with propeller

The hotfilms are still indicating an laminar turbulent transition between the first sensor and the third sensor.
In further investigations a constant position of the laminar turbulent transition is to be achieved by a suitable positioning of the turbulator.

References

[1] Hepperle, M.: Aspects of Distributed Propulsion Payloads. Symposium Elektrisches Fliegen. 2016.
[2] Keller, D. Towards higher aerodynamic efficiency of propeller-driven aircraft with distributed propulsion. *CEAS Aeronaut J* 12, 777–791 (2021). https://doi.org/10.1007/s13272-021-00535-5
[3] Biser, Filipenko, Boll, Kastner, Atanasov, Hepperle, Keller, Vechtel, Noe: Design Space Exploration Study and Optimization of a Distributed Turbo-Electric Propulsion System for a Regional Passenger Aircraft - AIAA Propulsion and Energy 2020 Forum, 2020
[4] Tom C. Stokkermans, Sebastiaan Nootebos and Leo L. Veldhuis. "Analysis and Design of a Small-Scale Wingtip-Mounted Pusher Propeller," AIAA 2019-3693. AIAA Aviation 2019 Forum. June 2019.

This project has received funding from the European Union's Horizon 2020 research and innovation programme under grant agreement No EC grant 101005232.

Mitteilung

Fachgruppe: *Experimentelle Aerodynamik*

Untersuchung der instationären Lasten auf ein Zugmodell im Windkanal

Daniela Heine, Klaus Ehrenfried, Torsten Gries, Gerrit Heine, Max Müller

DLR Göttingen, Bunsenstr. 10, 37073 Göttingen, daniela.heine@dlr.de

Die Aerodynamik von Fahrzeugen wird zumeist unter stationären Bedingungen untersucht. Eine Betrachtung unter instationären Anströmbedingungen ist nicht trivial und ist in den Normen, welche die Zulassung von Zügen regeln, nur als Abschätzung vorgesehen (siehe bspw. [1]). Für PKW jedoch wurde gezeigt, dass die mittleren instationären Lasten und Momente die stationären signifikant übersteigen können (vgl. [2]-[4]). Daher wurden die instationären Lasten auf Zugmodelle experimentell untersucht.
Am Deutschen Zentrum für Luft- und Raumfahrt in Göttingen wurde die Seitenwindanlage Göttingen (SWG) für die Studien zur Untersuchung instationärer Aerodynamik ertüchtigt. Ein Laufband samt Modellhalterung wurde installiert, zudem wurde eine Absaugeinrichtung erstellt. Ein System aus vier Flügeln mit jeweils separat anzusteuernden, beweglichen Klappen an der Hinterkante liefert die einstellbaren, instationären Störungen der Anströmung. Mithilfe des Flügelsystems können sinusförmige Böen verschiedener Frequenzen und Amplituden erzeugt werden. Zudem ist auch eine frei wählbare Klappenbewegung möglich.
Mithilfe der Versuchsanlage wurden zwei verschiedene Zugmodelle untersucht, welche in der folgenden Abbildung gezeigt sind. Das erste ist ein generischer Körper, welcher über einen superelliptischen Querschnitt und eine halbellispoide Nasenform verfügt. Das zweite Modell ist das des sog. NGT Cargo, eines Hochgeschwindigkeits-Cargozuges, welcher eine vom DLR entwickelte Studie darstellt. Das Zugmodell ist skaliert im Maßstab 1 :25 und wurde mittels des 3D-Druckverfahrens hergestellt.

Abbildung 1 : links : generisches Zugmodell, rechts : Modell des NGT Cargo

Beide Zugmodelle wurden in der SWG bei einer Geschwindigkeit von 30m/s untersucht. Die Strömung wurde mittels sinusförmigen Böen mit Frequenzen zwischen 20Hz und 50Hz gestört. Messungen ohne Klappenbewegung dienen als Referenz. Verschiedene Amplituden wurden bei der Frequenz von 30Hz untersucht. Diese Frequenz wurde gewählt, da die hier entstehenden, sinusförmigen Strömungsstrukuren in ihrer Ausdehnung den Abmessungen des Zugkopfes entsprechen und damit die größte Auswirkung auf die gemessenen Lasten und Momente zu erwarten ist.

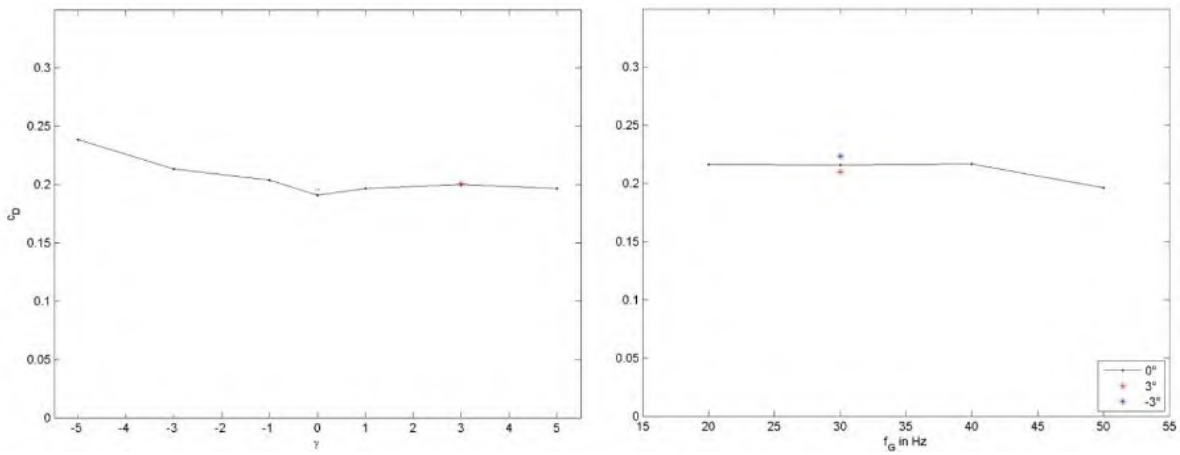

Abbildung 2 : links : stationär gemessener Widerstandsbeiwert des generischen Zugmodells bei versch. Anstellwinkeln, rechts : instationär ermittelter Widerstandsbeiwert über der Anregungsfrequenz (zusätzlich bei 30Hz : jeweils die Werte für die Anstellwinkel 3 ° und -3°)

Abbldung 2 zeigt exemplarisch die gemessenen Widerstandsbeiwerte für das generische Zugmodell bei den oben genannten Versuchsbedingungen. Es ist ersichtlich, dass beim Anstellwinkel von 0° die instationären Lasten über einen großen Frequenzbereich die stationären um mehr als 10% übersteigen. Dies zeigt sich hier auch bei den Anstellwinkeln 3° und -3°.

Die Messungen haben auch für die Seitenwindlasten sowie das Giermoment gezeigt, dass sich die instationäre Anströmung auf die Lasten und Momente auswirkt.

Es wurde gezeigt, dass die instationäre Anströmung die Lasten auf Züge, insbesondere den Zugkopf, erhöhen können. Erhöhte Lasten können für den Betrieb der Züge von Bedeutung sein, weshalb Sie Bestandteil der aerodynamischen Untersuchungen von Zügen sein sollten.

Quellenangaben :

[1] Europäische Kommission: EN 14067-6 Bahnanwendungen - Aerodynamik - Teil 6: Anforderungen und Prüfverfahren zur Bewertung von Seitenwind , 2020

[2] Wilhelmi, H., Jessing, C., Bell, J., Heine, D. et al., “Aerodynamic Characterisation of a Compact Car Overtaking a Heavy Vehicle,” in: Dillmann, A., Heller, G., Krämer, E., Wagner, C. et al. (eds.), New Results in Numerical and Experimental Fluid Mechanics XII, Notes on Numerical Fluid Mechanics and Multidisciplinary Design, Springer International Publishing, Cham, ISBN 978-3-030-25252-6:794–804, 2020

[3] Jessing, C., Wilhelmi, H., Wittmeier, F., Wiedemann, J. et al., “Characterization of the Transient Airflow Around a Vehicle on Public Highways,” 12th FKFS-Conference: Progress in Vehicle Aerodynamics and Thermal Management, Stuttgart, October 2019

[4] Schröck, D., Widdecke, N., and Wiedemann, J., “On-Road Wind Conditions Experienced by a Moving Vehicle,” in: Wiedemann, J. (ed.), Progress in Vehicle Aerodynamics and Thermal Management V, expert, Renningen, ISBN 978-3-8169-2771-6, 2008

Mitteilung

Fachgruppe: Experimentelle Aerodynamik

Low-order Modeling of Measured Bistable Sideforces on a Sphere in Transient Inflow

Max Müller[1], Klaus Ehrenfried[1] & Claus Wagner[1,2]
[1] Institut für Aerodynamik und Strömungstechnik – Bodengebundene Fahrzeuge, DLR, Bunsenstr. 10, 37073 Göttingen
[2] TU Illmenau – Fakultät Maschinenbau – FG Aerodynamik – Am Helmholtzring 1, 98693 Ilmenau
max.mueller@dlr.de

It is widely accepted that low-order models can pinpoint leading instability mechamism and are of potential use for optimization and control. Armin et al [1] developed for example a low order model to predict the force answers on two cylinders in proximity, where the wake interaction leads to vortex-induced vibration, using the Duffing equation, $\ddot{x} + \delta\dot{x} + \alpha x + \beta x^3 = \gamma\cos(\omega t)$, described by Jordan and Smith [2]. The first three terms represent a damped, harmonic oscillator, therafter is the cubic nonlinear (Duffing) term and on the right hand side is a driving force. Yang et al. [3] extended the driving term to three excitation frequencies, so that the driving force becomes $\sum_{n=1}^{3}\gamma_n\cos(\omega_n t + \theta_n)$. This adaption made it possible to include multiple frequencies in the prediction of the system response.
Although, the Duffing equation is often used for sinusoidal force responses, the equation is also capable of covering chaos, as shown by Jordan and Smith [2], who set the paramters to $\ddot{x} + 0.3\dot{x} - 1x + 1x^3 = \gamma\cos(1.2t)$ and were able to show that whether the behavior of the oscilator is chaotic depends on the amplitude of the driving force γ. For γ < 0.3, the system is stable and multiperiodic. In the range of 0.3 < γ < 0.36 however, there is no periodic regularity and hence the system is considered chaotic with two fix points in the phase plane.
Such a behavior is also known from bistable wakes, which can appear behind bluff bodies and are characterized by switching irregularly from one side to the other. Varon et al. [4] have proven that the bistable, low frequency behavior of the wake of an Ahmed body is weakly chaotic, in contrast to the raw signal, which is stochastic. To extract the low frequency behavior, they used a low pass filter with the cut-off Strouhal number of $St_w = 0.001$, which is connected to $f_{LP} \approx 0.11$ Hz.
Bistable side forces on long time scales have also been found by Müller et al. [5] in wind tunnel experiments with a a sphere mounted on a cross stream rod (CSR). Here, the vertical lateral CSR breaks the symmetry in a way that the wake has two different horizontal partially stable states. These bistable side forces also prevail in transient, sinusoidal inflow conditions. The unsteady inflow is induced with a gust generator consisting out of four wings, with active flaps. The amplitude of the flap movement was set to ψ = 5° at a frequency of f_{gust} = 40 Hz. The undisturbed wind speed was set to u_0 = 15 m/s. The sphere has a diameter of 100 mm and the forces were measured by an internal force balance.
Regarding the Duffing equation the chaotic bistable side force, the sinusoidal transient inflow and the gust generators wakes are multiple forcing sources. Thus, the aim of this work is to include the three effects into one low order model, based on the Duffing equation, since the latter can cover the chaotic behavior as well as simple oscillation.
In a first step the raw signal of the side force coefficient c_S was low-pass filtered with a cut off frequency of 5 Hz and normalized that the partially stable states are at $c_S = \pm 1$. The resulting signal is displayed in Figure 1 in black. and showing clear bistable behavior with different partially stable periods. Furthermore, eg. at t ≈ 11s, the system leaves one state, but instead of switching, it falls back into the same state. Because chaotic systems are sensitive to minor changes, a representation of this behavior was found by adapting the parameters of the Duffing equation manually. The equation was altered to $\ddot{x} + \delta\dot{x} - {\omega_0}^2(x - x^3) = \gamma\cos(\omega t)$ as it is known from the harmonic oscillator that $\alpha = -\omega_0^2$ and from Jordan and Smith [2] that α=-β is a choice that allows chaotic behavior. The fitting results for the parameters are shown in Table 1. The eigenfrequency ω_0^2 was set in accordance with the frequency of the low pass filtered signal, which is slightly higher than 4 Hz. The frequency of the driving force was set to the cut off frequency of the low pass filter. The ratio of the two frequencies is close to the one used by

Jordan and Smith [2] for their example. The damping and the amplitude of the driving force are then adapted manually to achieve a similar behavior of the Duffing oscillator.

Table 1 Set of parameters for the Duffing equation

δ	ω_0^2	γ	ω
0.001	675	65	2π 5 Hz

Hereby, similarity is achieved, when there is bistability with comparably long periods of partial stable times and amplitude in the oscillations around the partially stable states, as well as occasions where the system leaves one state without switching. The Duffing oscillator was simulated using an Euler Scheme and is dsiplayed in Figure 1 in blue. Here, the same number of partially stable periodes leads to the same mean stable time, as for the low pass filtered signal. Also there are occasions, where the system leaves a state without switching like at $t \approx 12$ s. Changes of the state, without logging in the other state, see $t \approx 4$ s appear in the Duffing simulation, but are also known from other measurements not shown here and are consequently not considered as an issue concernig similarity. The oscillation around the partially stable states is affected from the closeness of ω_0 and ω and results in some sort of beating, which in this case is inevitable. The comparison of the phase plots reveals that although the time derivate is in the same order of magnitude, the oscillation around one partially stable state is over all narrower for the low-pass filtered signal than for the simulation. For both however, there is a narrow and a wide oscillation around the partially stable state, which again contributes to the similarity concerning the behavior.

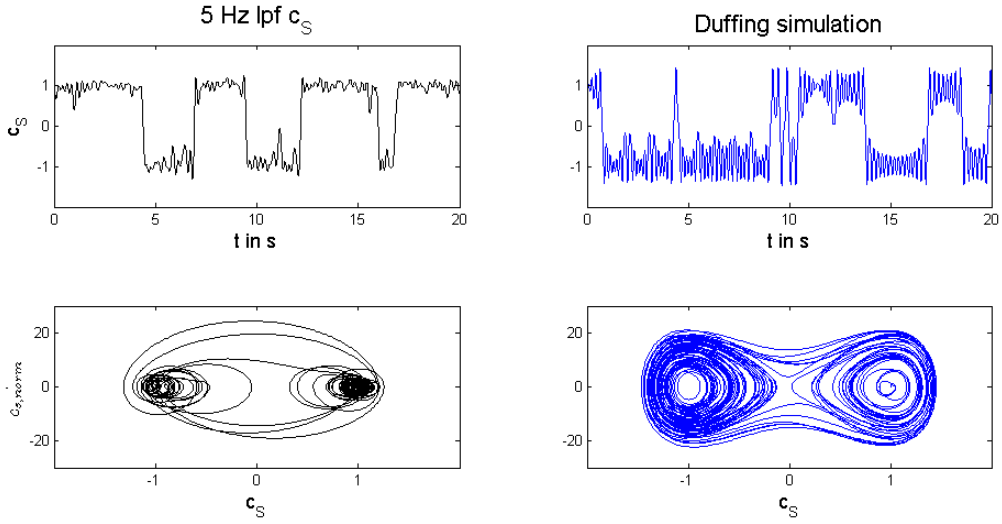

Figure 1 Normalized sideforces on a sphere at u_0 = 15 m/s, ψ = 5° and f_{gust} = 40 Hz; left timeline and phase plot of the 5 Hz low pass filtered signal; right time line and phase plot of the simulated Duffing oscillator with the parameter setting of table 1

After achieving a similar low frequency behavior, the next step is to add the further forcing from the transient inflow, to obtain a low order model for the side forces acting on a sphere with sinusoidal transient inflow, which will be presented at the symposium.

Literatur

[1] Armin, M., Day, S., Karimirad, M., Khorasanchi, M., (2021) On the development of a nonlinear time-domin numerical method for describing vortey-induced vibration and wake interference of two cylinders using experimental results, Nonlinear Dyn 104:3517-3531

[2] Jordan, D.W., Smith, P. (2007) Nonlinear Ordinary Differential Equations, Fourth Ed. Oxford University Press, ISBN 978-0-19-920824-1

[3] Yang, S. Nayfeh, A.H., Mook, D.T. (1998), Combination resonances in the response of the Duffing oscillator to a three-frequency excitation, Acta Mechanica 131, 235-245

[4] Varon, E., Eulalie, Y., Edwige, S., Gilotte, P., Aider, J.L., (2018) The chaotic dynamics of large-scale structures in a turbulent wake, Phys. Rev. Fluids 2, 034604

[5] Müller M. Ehrenfried, K. Bell, J. Wagner, C. (2020) Analysis of Model Mount Configurations with Regard to Force Measurements with Transient Inflow New Results in Numerical and Experimental Fluid Mechanics XII, volume 142, pages 684–694

Mitteilung

Fachgruppe: Experimentelle Aerodynamik

Effects of jet orifice shape on the flow-control effectivess of air-jet vortex generators

Deepak Prem Ramaswamy & Anne-Marie Schreyer
Institute of Aerodynamics, RWTH Aachen University, 52062 Aachen
d.ramaswamy@aia.rwth-aachen.de

Shock-wave / turbulent-boundary-layer interactions are complex flow phenomena, commonly encountered in many high-speed aerospace applications like transonic air-foils, supersonic air-breathing-engine inlets, rocket-engine nozzles, external surfaces of supersonic and hypersonic vehicles et cetera. A strong shock-wave imposes a large adverse pressure gradient on the incoming boundary-layer and can lead to a large-scale flow separation and a subsequent recirculation region [1]. In order to alleviate the associated detrimental effects, several flow-control techniques have been proposed and studied in literature [2]. One effective approach is to use air-jet vortex generators (AJVGs) [3]. In this technique, small jets of air are injected onto the incoming crossflow in order to generate streamwise vortices [4]. These vortices redistribute the momentum within the boundary layer, bringing high momentum fluid close the wall and making the boundary layer more resistant to separation. However, the flow-control effectiveness of AJVGs depends on several geometrical and flow parameters [5] [6]. To improve the overall understanding of AJVG control mechanisms, we investigate one such parameter – the jet-orifice shape – in this study and assess its influence on the mean and turbulent quantities using oil-flow visualisations and PIV.

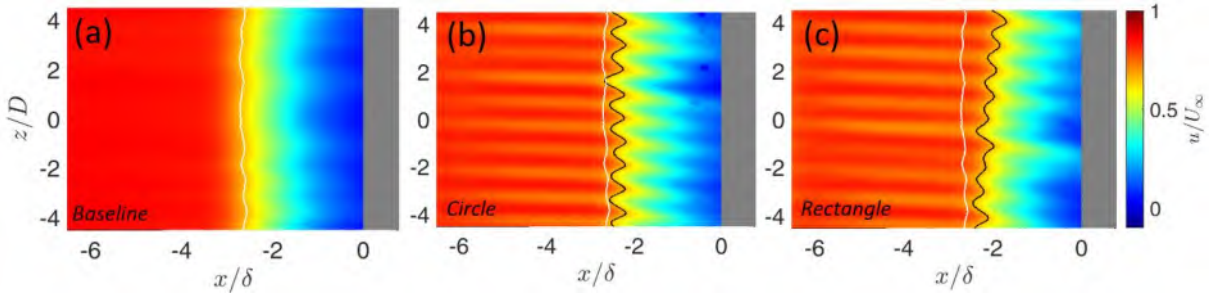

Fig 1. Mean streamwise velocity for the (a) Baseline, (b) Circular AJVG, and (c) Rectangular AJVG cases at y = 0.24δ

The experiments for this investigation were conducted on a 24° compression-ramp model in the trisonic wind tunnel facility at RWTH Aachen University at Mach 2.52 and Re_θ = 8225. The incoming boundary-layer thickness (δ) at x = -4.5δ (upstream of the ramp corner at x=0) is 10.4mm. A single array of purely spanwise-injecting jets with a pitch angle of φ = 45° was placed at x = -7.69δ. We chose a jet-to-jet spacing of D = 0.76δ and a jet-injection pressure equal to the wind tunnel stagnation pressure. In addition to traditional circular orifices, non-circular AJVG arrays were manufactured by means of an laser abalation technique using short-pulse lasers. One rectangular AJVG array with an aspect ratio of 2, and four triangular AJVG arrays, each oriented at 0°, 90°, 180° and 270° with respect to the crossflow were tested to assess the influence

of sharp corners and jet-orifice orientation on the flow-control effectiveness. All geometries were characterised by the same hydraulic diameter (hd_{jet} = 0.1δ). For the PIV analysis, a wall-parallel setup was used with the laser light sheet illuminating the streamwise/spanwise plane at two wall-normal locations: (a) y = 0.24δ and (b) y = 0.69δ. Illumination was provided by a Quantronix Darwin-Duo 100 Nd:YLF laser operated at 1000 Hz with a maximum pulse energy of 30 mJ per oscillator. The laser was synchronised with a Photron SA.5 highspeed camera (with a resolution of 1024 px × 1024 px) placed above the wind tunnel, using an ILA high-speed synchronizer. The acquired images were processed with an adaptive PIV algorithm with final interrogation-window sizes of 16px by 16px at 50% overlap. For further details on the 24° compression-ramp model and the wall-parallel PIV setup, see Ref. [5].

The mean streamwise velocity contour at y = 0.24δ for the uncontroled case is presented in Fig. 1a. The white line depicts the location of the surrogate separation line, identified using the measured streamwise velocities. As the flow approaches the ramp corner, it undergoes a strong deceleration due to the separation shock and separates from the surface. The resulting large region of reverse flow is visible in Fig. 1a. Nevertheless, the flow and surrogate separation shock are nearly 2D for the baseline case.

With the injection of jets from circular AJVGs (see Fig. 1b), a spanwise series of streamwise vortices is generated, visible as streaks of low and high-speed regions in the mean streamwise velocity contour. Consequently, the surrogate separation line is corrugated (black lines in Fig. 1b). The favourable momentum exchange brought about by the streamwise vortices results in a downstream movement of the mean separation line and an overall reduction of the reverse flow region.

In comparison, the injection of jets from rectangular AJVGs (see Fig. 1c), leads to a measurable improvement in control effectiveness, with a further downstream movement of the mean separation line.

In the full article, we will systematically discuss the results of the rectangular and triangular AJVGs in comparison to both the baseline and circular AJVG cases and explain the differences in control mechanism. We thus improve the understanding of AJVGs, in particular of non-circular air jets, to control shock-induced flow separation.

References

[1] P. Dupont, C. Haddad and F. Debieve, “Space and time organization in a shock-induced separated boundary layer,” *Journal of Fluid Mechanics,* pp. 255-277, 2006.

[2] D. V. Gaitonde, “Progress in shock wave/boundary layer interactions,” *Progress in Aerospace Sciences,* vol. 72, pp. 80-99, 2015.

[3] R. A. Wallis, “The use of air jets for boundary layer control,” Aeronautical Research Lab, Melbourne, 1952.

[4] R. Sebastian and A.-M. Schreyer, “Flow field around a spanwise-inclined jet in supersonic crossflow,” *Aerospace science and technology,* vol. 106, p. 106209, 2020.

[5] D. P. Ramaswamy and A.-M. Schreyer, “Effects of Jet-to-Jet Spacing of Air-Jet Vortex Generators in Shock-Induced Flow-Separation Control,” *Flow, Turbulence and Combustion,* vol. 109, pp. 35-64, 2022.

[6] S. B. Verma and C. Manisankar, “Shockwave/Boundary-Layer Interaction Control on a Compression Ramp Using Steady Micro Jets,” *AIAA Journal,* vol. 50, no. 12, pp. 2753-2764, 2012.

Mitteilung

Fachgruppe: Experimentelle Aerodynamik

Discovering Latent Physical Variables from Experimental Data in Supersonic Flow using Physics-Informed Neuronal Networks (PINNs)

Lennart Rohlfs and Julien Weiss
Institut für Luft- und Raumfahrt, Technische Universität Berlin,
Marchstraße 12, 10587 Berlin
l.rohlfs@tu-berlin.de

When performing wind-tunnel experiments on any object, it is of high interest to aquire as many information about the flow field as possible. However usually due to spatial-, time- and financial constraints it is only possible to perform a limited amount of measurements with a couple of different methods.
On the other hand, traditional CFD simulations provide all physical quantities simultaneously, but depending on the complexity of the setup can take a very long time to prepare and the models have to be validated with experimental data as well to make sure they are accurate and can be trusted.
In between those two classic departments recent advancements in machine learning and especially the development of so called Physics-Informed Neural Networks (PINNs) have opened up new possibilities to process data and combine any data with computational methods. By implementing the underlying differential equations such as the Euler equations or even the full Navier Stokes equations into the framework of a classical NN, it is possible to, for example, discover pressure and density from velocity fields or even purely qualitative data [1].
While these new methods have been proven to work in many different publications using synthetical or CFD data [2, 3], there have been very few attempts to actually use them with experimental data.
For this reason the objective of our contribution is to use PINNs to infer pressure and density fields from PIV data of supersonic flow features. The original dataset features time averaged velocity data of a turbulent shockwave-boundary layer interaction at Ma = 2 that has been tested in the high-speed wind tunnel at TU Berlin [4]. From this snapshot multiple subsets were extracted and used to train the neural network. In this contribution we investigate the networks ability to accurately predict shock- and expansion waves and compare the results with theoretical values. Additionally we limit the amount of training data to demonstrate extrapolation capabilities and impose several boundary conditions to modify the predictions.

Figure 1 shows the results of such a training process. The training velocity fields (Top row) include two shocks and one expansion fan that were created due to the incident shockwave boundary layer interaction. This part of the flow field is well outside of the separation bubble interaction zone and thus the assumption of inviscid flow is valid.
The training data was put into a neural network that takes x and y coordinates as input and outputs u, v, p and ρ. During the training process the output velocities are compared with the training velocities and the error is minimized as part of the loss function. For the second part of the loss function the output variables and their derivatives are put into the Euler equations and the equation of state and the resulting residuals are minimized as well. This part makes the regular neural network « physics informed » . In addition total temperature as well as static and total pressure were imposed as boundary on the left side of the domain. These values can all be measured during a single wind tunnel run without introducing much complexity or interfer with the PIV measurements.
The middle row of Figure 1 shows the predicted pressure and density fields. As expected both variables increase over the shocks and decrease in the expansion. In the final contribution a comparison with classical shock-expansion theory will be shown to quantify the uncertainty of the network predictions. The bottom row shows temperature and Mach number

fields. These variables were not predicted directly by the network but can be derived from the given data using ideal gas relations and the speed of sound.
The final dataset has information on all state variables which allows a much more comprehensive analysis of the flow field in comparison to just using the velocity data.

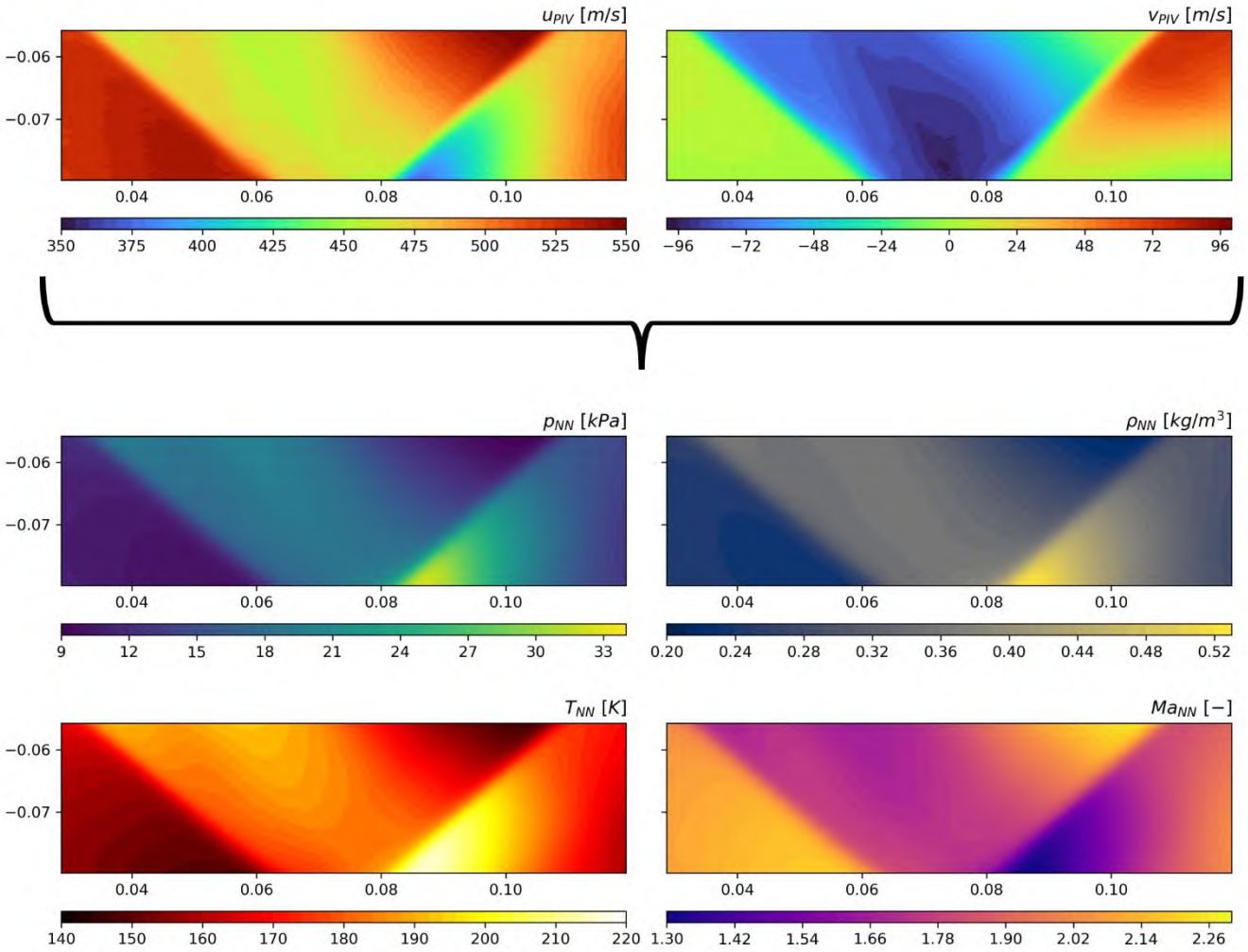

Figure 1: Input and output data from the training process. Top: Streamwise (left) and normal (right) velocity fields from PIV; Middle: Pressure (right) and density (left) fields discovered by the network during the training process; Bottom: Derived Quantities after the training process. Temperature (left) and Mach number (right) fields.

References:

[1] Raissi, M., Yazdani, A., & Karniadakis, G. E. (2020). Hidden fluid mechanics: Learning velocity and pressure fields from flow visualizations. Science, 367(6481), 1026–1030.

[2] Cai, S., Mao, Z., Wang, Z., Yin, M., & Karniadakis, G. E. (2022). Physics-informed neural networks (PINNs) for fluid mechanics: a review. Acta Mechanica Sinica, 1–12.

[3] Jagtap, A. D., Mao, Z., Adams, N., & Karniadakis, G. E. (2022). Physics-informed neural networks for inverse problems in supersonic flows, 1–19

[4] Rohlfs, L., Stab, I., and Weiss, J. (2022). Experimental Investigations of Incident Shock-wave Boundary Layer Interactions in a Continuously Operating Supersonic Wind Tunnel. AIAA Aviation 2022 Forum, American Institute of Aeronautics and Astronautics

Mitteilung

Fachgruppe: Experimentelle Aerodynamik

Super-resolution-enhanced computation of time-dependent finite-time Lyapunov exponent fields

Ben Steinfurth & Julien Weiss
Technische Universität Berlin, Fachgebiet Aerodynamik
10587 Berlin, ben.steinfurth@freenet.de

The finite-time Lyapunov exponent (FTLE) has recently gained prominence as an objective Lagrangian diagnostic that helps to uncover dominant material surfaces organizing the flow into ordered patterns. Being derived from the flow map, which governs the advection of passive tracer particles over time, it is directly linked to the skeleton of Lagrangian particle dynamics. After obtaining this flow map by numerically integrating the velocity field under consideration, Lagrangian Coherent Structures can be identified as ridges in the FTLE field. Since the FTLE gradient in ridge normal direction is relatively large, the accuracy of feature extraction depends on the spatial resolution of the FTLE field. In other words, the flow map needs to be determined at a large number of points inside the flow field. This leads to a substantial numerical effort, especially in the case of three-dimensional velocity fields.
While many previous studies striving for a more efficient computation were based on grid refinement schemes, the idea presented in this paper relies on an enhancement of the spatial resolution using Machine Learning techniques. To this end, super-resolution (SR) will be applied, essentially deriving the non-existent information statistically from a training database. Two approaches will be pursued: the first based on an example dictionary, the second by employing a generative adversarial network (GAN).

SR based on example dictionary

In this rudimentary implementation, a training database of patches containing example textures is generated at first; for each patch, there is a downscaled pendant with the same resolution as the image (= scalar field) to be processed. Next, this image is subdivided into areas of the same dimension as the downscaled patches. By minimizing a cost function, e.g. the mean square deviation, the low-resolution elements in the training database that are most similar to the areas of the image are identified. Finally, a reconstruction is performed using the corresponding high-resolution patches. It is immediately apparent that the accuracy of this approach is only ensured when the training database contains similar textures as the image.
To examine the capabilities of example-based SR, we applied this method to the FTLE field in the symmetry plane of a vortex ring. The high-resolution ground truth is shown in the right of figure 1. To obtain a low-resolution image (left in figure 1), the ground truth was downscaled by a factor of five in both dimensions. The low-resolution image was then divided in $i = 1, \dots, 390$ quadratic patches I^i with edge lengths of three pixels (= scalar entries) that were then compared with downscaled patches J^j of two example dictionaries by evaluating the cost function

$$\mathcal{L}_{ij} = \left\| I^i - J^j \right\|_2^2.$$

The first dictionary (top in figure 1) contains approximately 14,000 patches taken from FTLE fields obtained prior/subsequent to the timestep of the ground truth. The second dictionary was composed of 27,000,000 patches taken from the database DIV2K containing everyday pictures (but no FTLE fields). Despite the much larger number of sample patches, the reconstruction using the second dictionary arguably does not enhance the level of detail of the input image. The reconstruction achieved with the first dictionary, on the other hand, leads to a result that cannot be distinguished from the ground truth. This can be explained by the example patches being almost identical to the reference FTLE field because the vortex structure does not change substantially once the formation process is completed.

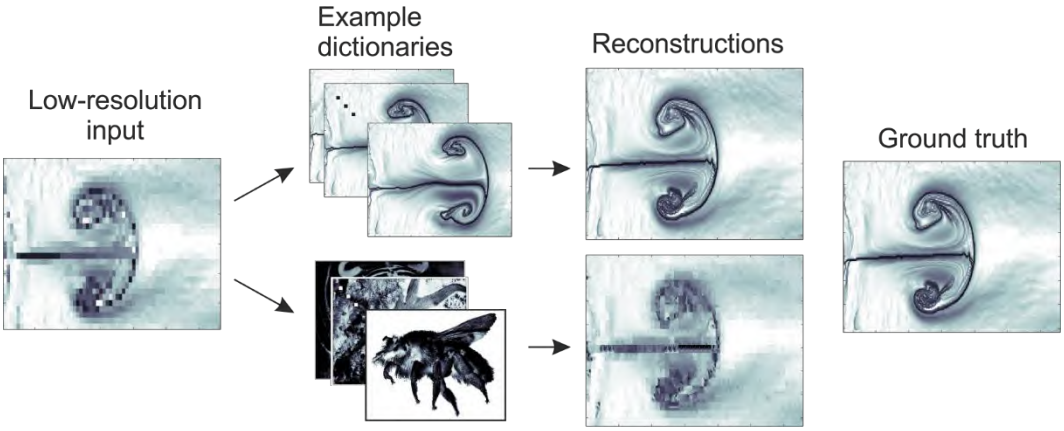

Figure 1. Reconstruction of FTLE field using example patches with similar textures (top) and DIV2K database (bottom)

This demonstration confirms the great importance of an appropriate example database. At the same time, it leads us to believe that a more efficient computation of FTLE time series is feasible by employing example-based SR and only compute a limited number of high-resolution FTLE fields to process low-resolution fields at the remaining timesteps. This approach will be examined in detail in the full paper.

SR based on GAN

In the second technique presented in the full paper, two “competing” convolutional neural networks (CNN) will be employed. The first network (generator) is supplied with low-resolution patches of an FTLE field. It then generates high-resolution counterparts that are assessed by the second CCN (discriminator). The discriminator compares the patches with a high-resolution ground truth and classifies the output of the generator: either the patches are sufficiently similar to the ground truth or not. If generated patches fail this test, the generator keeps producing patches until sufficient similarity is achieved. After a certain number of training cycles, the GAN learns how to assign high-resolution patches to the low-resolution input. Now, the computation efficiency may be enhanced as high-resolution scalar fields will be reconstructed based on low-resolution computations.

In the full paper, we will compare the capabilities of the two techniques introduced above and assess whether they may be used to enable more efficient FTLE computations in the future.

Mitteilung

Fachgruppe: Experimentelle Aerodynamik

Feedforward Neural Network based prediction of 2D Car wake

Mathis Thieme, Technische Universität Berlin, mathis.thieme@tu-berlin.de
Stephan Löffler, Technische Universität Berlin, stephan.loeffler@tu-berlin.de
Julien Weiss, Technische Universität Berlin, julien.weiss@tu-berlin.de

The positioning of a car rear wing and its effect on the car's wake requires computationally intensive numerical simulations or time-consuming experiments. By using machine-learning algorithms such as neural networks (NN) [1], the effort can be reduced by taking only a data set for training and validation and performing further design exploration by the prediction of the NN [3]. The main goal of this study is to predict the wake of a generic vehicle model (DrivAer) [2] faster, through a trained NN, with only the spoiler position specification. Here, the deep learning algorithm is trained with experimental data. Furthermore, the aim is to train the NNs with the smallest feasible data set.
The training and test data sets are generated in a low-speed wind tunnel at a freestream velocity of 13m⁄s. Fig. 1 shows the experimental setup. The 15% scaled DrivAer model is equipped with a traversable rear wing, which is variable in the *x*- position, *z*- position and in the angle of attack. Depending on the posi -tioning of the rear wing, the wake is modified. 130mm behind the model a wakerake is mounted, which is traversable in height. The pressure probes are distrib-uted equidistantly along a line with 20mm spacing. Furthermore, stereo PIVmeasurements of the center section of the DrivAer wake are performed. TheDrivAer model was installed elevated in the test section so that a splitter plateseparates the model from the bottom wind tunnel boundary layer.

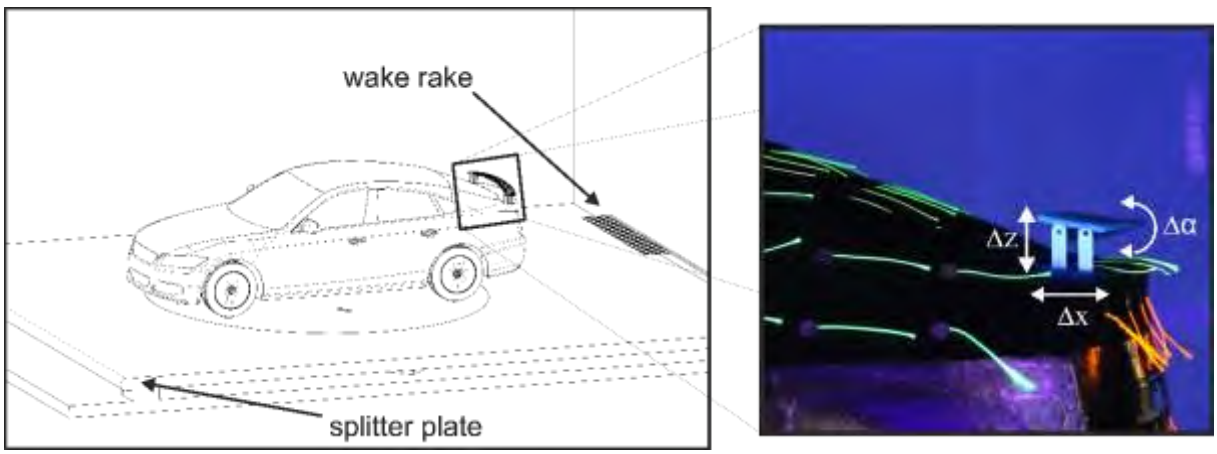

Figure 1: Experimental setup of the DrivAer model with a traversable rear wing.

A feed-forward neural network (FNN) has been successfully trained for predicting the wake pressure distribution given the spoiler positioning. Figure 2 shows the wake prediction of the FNN and the corresponding measured pressure distribution of the validation dataset. Different neural network architectures were tried to perform the results with the smallest possible training data set. Furthermore, another FNN is built to predict the flow field of the PIV measurements.

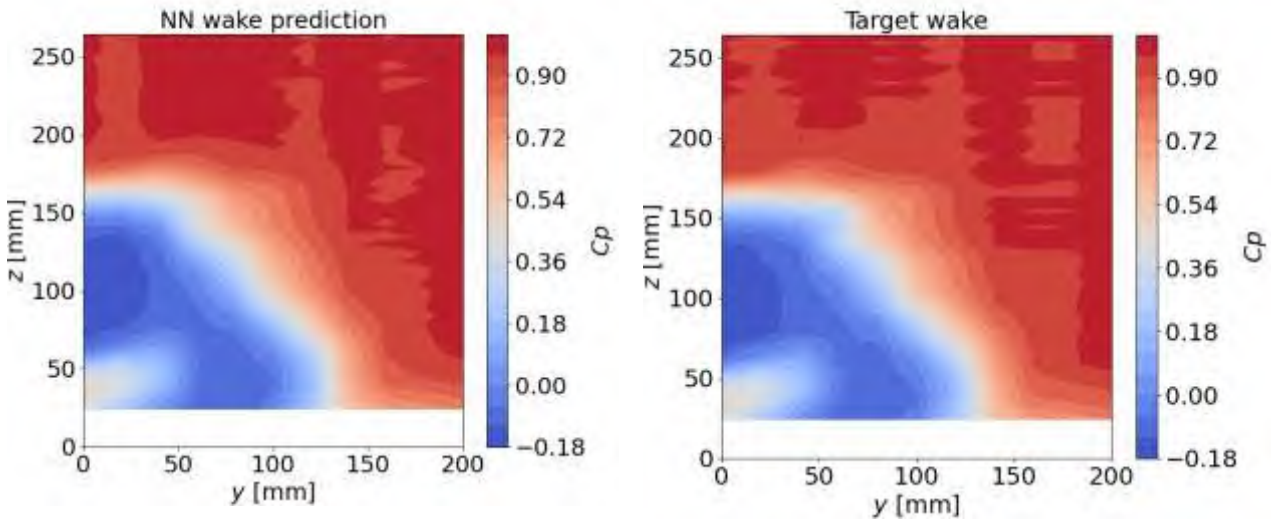

Figure 2: FNN wake pressure prediction (left); measured wake pressure distribution (right)

[1] Heft, Indinger & Adams. (2011) : *Investigation of Unsteady Flow Structures in the Wake of a Realistic Generic Car Model*. 29th AIAA Applied Aerodynamics Conference 2011. 10.2514/6.2011-3669.

[2] Rosenblatt, Frank: *The perceptron: a probabilistic model for information storage and organization in the brain*. Psychological review 65 6 (1958), pages: 386-408.

[3] White, Ushizima & Farhat: *Fast Neural Network Predictions from Constrained Aerodynamics Datasets*. AIAA Scitech 2020 Forum (2020). 10.2514/6.2020-0364.

Mitteilung

Fachgruppe: Hyperschallaerothermodynamik

Advances in the development of the Fokker-Planck method for simulation of rarefied gases

Leo Basov[1], Martin Grabe[2]
[1,2]DLR, Bunsenstraße 10, D-37073 Goettingen,
[1]l.basov@dlr.de

Flows encountered in space applications, like atmospheric reentry or jet plume interactions, are characterized by a wide range of the Knudsen number. The well-known Boltzmann equation describes the evolution of a distribution function f in such rarefied flows due to intermolecular collisions:

$$\frac{\mathrm{D}f}{\mathrm{D}t} = S_{Boltz}. \tag{1}$$

A common approach to numerically solve Eq. (1) is the Direct Simulation Monte-Carlo (DSMC) method pioneered by Bird [1]. The method is very efficient for high Knudsen numbers but becomes computationally intensive when approaching the continuum limit. Approximations of the collision operator S_{Boltz} in Eq. (1) can greatly reduce this computational cost. One such approximation is the Fokker-Planck collision operator S_{FP} [2]:

$$S_{Boltz} \approx S_{FP} = -\frac{\partial}{\partial v_i}(A_i f) + \frac{\partial^2}{\partial v_j \partial v_j}(D^2 f) \tag{2}$$

where the drift coefficient A_i and the diffusion coefficient D of Eq. (2) are model parameters chosen in such a way that moments calculated using the Boltzmann collision operator are reproduced in the continuum limit.

The resulting Fokker-Planck equation can be solved through stochastic motion which in turn can be modelled using a particle method. Due to the similarity in their formulation a hybrid method based on DSMC and FP can be derived which allows the computationally efficient simulation of flows with a broad range of Knudsen numbers [3].

For the application of the FP model to engineering problems the simulation of complex gases and gas mixtures must be possible. The FP model has been extended from monatomic to diatomic gas for single species [4, 5] as well as for mixtures [6, 7]. However, the extension of the model to polyatomic gases for single and multispecies applications is still a research topic.

This paper discusses how the recently developed FP models for diatomic gases can be extended to allow modeling of polyatomic molecules using the Master-equation ansatz.
The extension for polyatomic species is done by allowing energy transfer inside all 3 modes of rotational as well as an arbitrary number of vibrational modes. The probability of energy transfer is calculated using Landau-Teller and Larsen-Borgnakke based rate coefficients which were originally derived in [5]. A validation of the approach is performed using code to code comparisons with the LasVegas DSMC software [10]. A simple heat bath experiment as well as a more complex hypersonic flow problem are investigated. It is shown, that the results agree very well for the heat bath test case but show differences for the hypersonic case in areas of strong thermal non-equilibrium. An argumentation for the differences is provided and potential improvements discussed.

In this paper we will additionally point out why the current multi-species formulations [6, 7] do not contain the special case of a single-species gas [8]. To establish consistency, we will propose a modification based on a potential ansatz for the drift coefficient A_i where the potential function itself is defined as an expansion of Hermite polynomials. This approach was already applied for the single species case where it was used to prove the H-theorem [9].

REFERENCES

[1] G. A. Bird, Molecular Gas Dynamics and the direct Simulation of Gas Flows (Oxford University Press, New York, 1994).
[2] P. Jenny, M. Torrilhon, S. Heinz, Journal of Computational Physics 229, 1077–1098 (2010).
[3] M. H. Gorji, P. Jenny, Journal of Computational Physics 287, 110–129 (2015).
[4] M. H. Gorji, P. Jenny, Physics of Fluids 25, 062002 (2013).
[5] C. Hepp, M. Grabe, K. Hannemann, Journal of Computational Physics 418, 109638 (2020).
[6] C. Hepp, M. Grabe, K. Hannemann, Physics of Fluids 32, 027103 (2020).
[7] C. Hepp, M. Grabe, K. Hannemann, AIP Advances 10, 085219 (2020).
[8] M. H. Gorji, M. Torrilhon, P. Jenny, Journal of Fluid Mechanics 680, 574–601 (2011)
[9] M. H. Gorji, M. Torrilhon, Journal of Computational Physics 430, 110034 (2021)
[10] M. Pfeiffer, P. Nizenkov, and S. Fasoulas, AIP Conference Proceedings 2132, 100001 (2019)

Mitteilung
Fachgruppe: Hyperschallaerothermodynamik

Numerical Assessment of Aerothermodynamic Loads of a Generic 3D Hypersonic Glide Vehicle Including Radiation

Dominik Hauger[1] and Christian Mundt[2]
Institut für Thermodynamik, Fakultät für Luft- und Raumfahrt, Universität der Bundeswehr München
Werner-Heisenberg-Weg 39, 85577 Neubiberg, dominik.hauger@unibw.de

Interest in maneuverable hypersonic vehicles is surging around the world. In comparison to ballistic missiles, their trajectory after atmospheric reentry is not easily predictable which complicates interception. Assessing their aerothermodynamic loads is therefore critical to understand their capabilities. For this purpose, a model of a generic 3D hypersonic glide vehicle (HGV) was designed and numerically investigated. In this work, results of a coupled Euler-boundary layer method are presented for different inflow conditions. The influence of radiation is computed via a Photon Monte Carlo Method and taken into account during flow field calculations as a source term.

I. Introduction

The race is on for maneuverable hypersonic vehicles. China has declared its DF-17 HGV operational in 2019 [1]. The National Defense Authorization Act 2022 makes hypersonics a top priority in the US [2]. In March 2022 a hypersonic cruise missile (HCM) was used for the first time in history in the armed conflict between Russia and Ukraine [3]. In contrast to predominant ballistic missiles, HGVs and HCMs are maneuverable after atmospheric reentry. The trajectory is thus not easily predictable and interception is more complicated than with a ballistic missile.

The performance characteristics of such a vehicle are needed to understand its capabilities. Aerodynamic loads, i.e. lift and drag coefficients, are needed to predict the vehicles trajectory. The surface heat flux must be tolerable for the heat shield. Extreme temperatures behind the shock lead to a strong infrared (IR) signature. This signature can be used to detect an incoming vehicle, e.g. via a satellite-based sensor (Figure 1a). Experiments on a real test vehicle to determine these performance characteristics are unrealistically expensive. Hence, this work provides answers using computational fluid dynamics simulations.

II. Methodology

Despite tremendous progress in understanding flow features of blunt bodies in hypersonic flow, the generation of high-quality 3D results is still a challenge. General approaches like Reynolds-averaged Navier Stokes (RANS) simulations or Large Eddy Simulations (LES) have long computation times. A specialized coupled Euler-boundary layer method can achieve similar accuracy at a much shorter computation time. The coupled Euler-boundary layer code used in this work, KEGS, has recently generated 2D numerical solutions for a generic triple cone [4] and the Fire II experiment [5]. Now, the code is being used to generate a 3D numerical solution for a generic HGV.

KEGS uses a shock-fitting approach that computes the flow state immediately behind the shock via the Rankine-Hugoniot conditions. This serves as boundary condition (BC) to compute an inviscid (Euler) solution for the flow field behind the shock. The boundary layer (BL) around the vehicle is then computed via the second-order boundary layer equations [6]. These are iterated until the BL profile fits the inviscid solution. Once converged, a new Euler solution is computed with an equivalent source distribution representing the BL solution as new BC at the vehicle surface. Then, a new BL solution is computed with the updated Euler solution. This concludes the flow field computations.

The radiation heat flux is important as it affects the temperature distribution and thus the IR signature. It is computed with a Photon Monte Carlo Method and fed back to the Euler-boundary layer method as a source term. In the first iteration, the radiation heat flux was assumed to be zero. This is iterated for only a few iterations as convergence is established rapidly. The gas is modeled as an equilibrium real gas. A thermal non-equilibrium model is currently being implemented to expand the validity of generated results to higher altitudes. Chemical non-equilibrium is already implemented in the 2D version of the code.

[1] Research associate, [2] Full professor, head of institute

III. Interim Results

Numerical results for the front part of the vehicle were already obtained successfully for angles of attack between $-5°$ and $+10°$, see Figure 1b, and Mach numbers between 6 and 18. The glide ratio for the generic HGV is low, but in line with an estimation of 2.6 for a test flight of the US-american HTV-2 [7]. The lift coefficient increases linearly for increasing angles of attack as expected. The drag coefficient has the overall shape of a parabola with a minimum around $2.5°$.

Figure 1a shows a typical result. The shock is very close to the tip of the vehicle (distance on the order of mm). The temperature peak is at the tip as well and reaches several thousand Kelvin. For a non-equilibirum solution the temperature immediately behind the shock is expected to be even higher [4]. Higher positive angles of attack lead to a lower shock distance on the lower side and a greater shock distance on the upper side. Higher Mach numbers lead to a smaller shock distance overall, and higher temperatures.

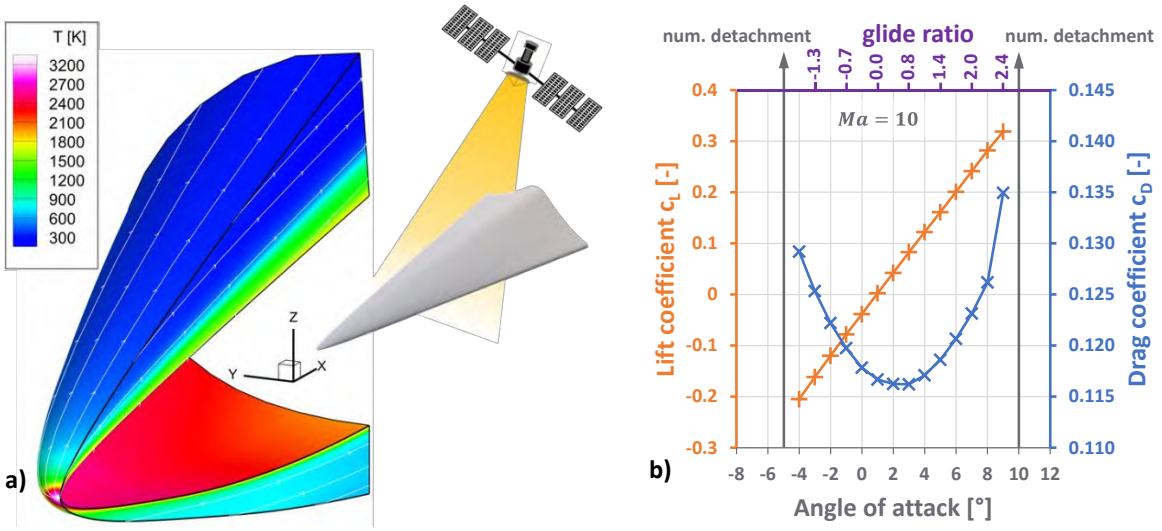

Figure 1. a) Temperature distribution from an Euler solution for the tip of the generic HGV geometry at Mach 10, $10°$ angle of attack, and 30km altitude; streamlines are in white. b) Aerodynamic loads from the Euler-boundary layer method for varying angles of attack at 30km altitude and Mach 10.

IV. Outlook

Calculations shown in the interim results section shall be expanded to the entire geometry of the HGV, not just the tip. Results for the aerodynamic loads can then be compared and differences pointed out. Additionally, a thermal non-equilibrium implementation of the gas shall be compared with the equilibrium gas model. It is expected that for high altitudes the thermal non-equilibrium model will give more accurate answers.

References

[1] US military news website, " DF-17", accessed in June 2022. https://www.military-today.com/missiles/df_17.htm

[2] US news channel, "Defense spending act makes hypersonic a top priority, calling for billions in investment", accessed in June 2022. https://www.cnbc.com/2021/12/29/defense-act-makes-hypersonic-top-priority-calls-for-investing-billions.html

[3] CNN (US-american television channel), "What to know about hypersonic missiles fired by Russia at Ukraine", accessed in June 2022. https://edition.cnn.com/2022/03/22/europe/biden-russia-hypersonic-missiles-explainer-intl-hnk/index.html

[4] J. Bonin, “Untersuchung der optischen Abstrahlung von ballistischen Flugkörpern unter Berücksichtigung der Kopplung von Strömung und Strahlung“, Dissertation UniBwM (2019). https://athene-forschung.unibw.de/133244

[5] J. Bonin, Ch. Mundt, “Full Three-Dimensional Monte Carlo Radiative Transport for Hypersonic Entry Vehicles". In: Journal of Spacecraft and Rockets 56.1 (2019), p. 44-52. https://arc.aiaa.org/doi/full/10.2514/1.A34179

[6] Ch. Mundt, M. Pfitzner, M. A. Schmatz, “Calculation of viscous hypersonic flows using a coupled Euler / second order boundary layer method”, Notes on Numer. Fluid Mech. 29 (1990), p. 419-429. https://link.springer.com/chapter/10.1007/978-3-663-13975-1_42

[7] J. M. Acton, “Hypersonic Boost-Glide Weapons”, Science & Global Security, Volume 23 (2015), v. 23 no. 3. https://scienceandglobalsecurity.org/archive/2015/09/hypersonic_boost-glide_weapons.html

Mitteilung

Fachgruppe: Hyperschallaerothermodynamik

Uncertainty Quantification of Expanding High-Enthalpy Air Flows

Georgii Oblapenko[1], Hannemann Volker[2]
[1,2]DLR, Bunsenstraße 10, D-37073 Goettingen,
[1]georgii.oblapenko@dlr.de

Numerical simulation is one of the main means of studying high-speed high-enthalpy flows relevant to re-entry problems. Due to the large number of different physical phenomena occuring in such flows, such as excitation of internal energy modes of molecules, chemical reactions, and ionization, the modeling has to account for these thermochemical relaxation processes [1]. However, data on the rates of these processes often suffers from a high degree of uncertainty, which in turn leads to uncertainty in the computed flow quantities of interest. Thus, in the recent years, there has been a growing interest in quantification of the effects of these uncertainties, along with uncertainties in the free-stream conditions, on high-speed re-entry flows [2,3].
Yet the main focus of such studies has remained on post-shock flows, whereas high-enthalpy expanding flows have received less attention, despite their relevance to operations of various experimental facilities for re-entry investigations. Moreover, computational models developed for and validated against re-entry flows may not be directly applicable to conditions occuring in expanding flows. Some studies have been carried out to estimate the impact of vibrational relaxation modeling [4,5,6] and variation in the reservoir conditions [7] on flows in hypersonic nozzles, but only these particular effects were investigated. Thus, a full uncertainty quantification and global sensitivity analysis of expanding flows, along with an assessment of the impact of choice of model remains a relevant topic for numerical simulation.

In the present work, we perform uncertainty quantification and sensitivity analysis studies of expanding air flows, accounting for uncertainties in the reservoir conditions, thermal and chemical relaxation rates, for conditions relevant to the operation of the High-Enthalpy Shock Tunnel Göttingen (HEG) [8]. The uncertainty quantification and sensitivity analysis approach is based on the generalized Polynomial Chaos Expansion method. In order to reduce the model parameter space, a parametrization method for quantifying variations in the vibrational relaxation times and chemical reaction rates is developed. In addition, preliminary studies in binary flows of nitrogen and oxygen are carried out to provide estimates of the sensitivities of the flow quantities in a simplified setup and further reduce the parameter space by determining model uncertainties which have negligible impact on the flow.

An example of such a preliminary study (in a binary flow of nitrogen) is shown on Fig. 1, where black lines show the computed mean values (over multiple simulations with varying thermal and chemical relaxation rates) and variation of flow quantities of interest (temperatures, speed, pressure, and molecular molar fraction).

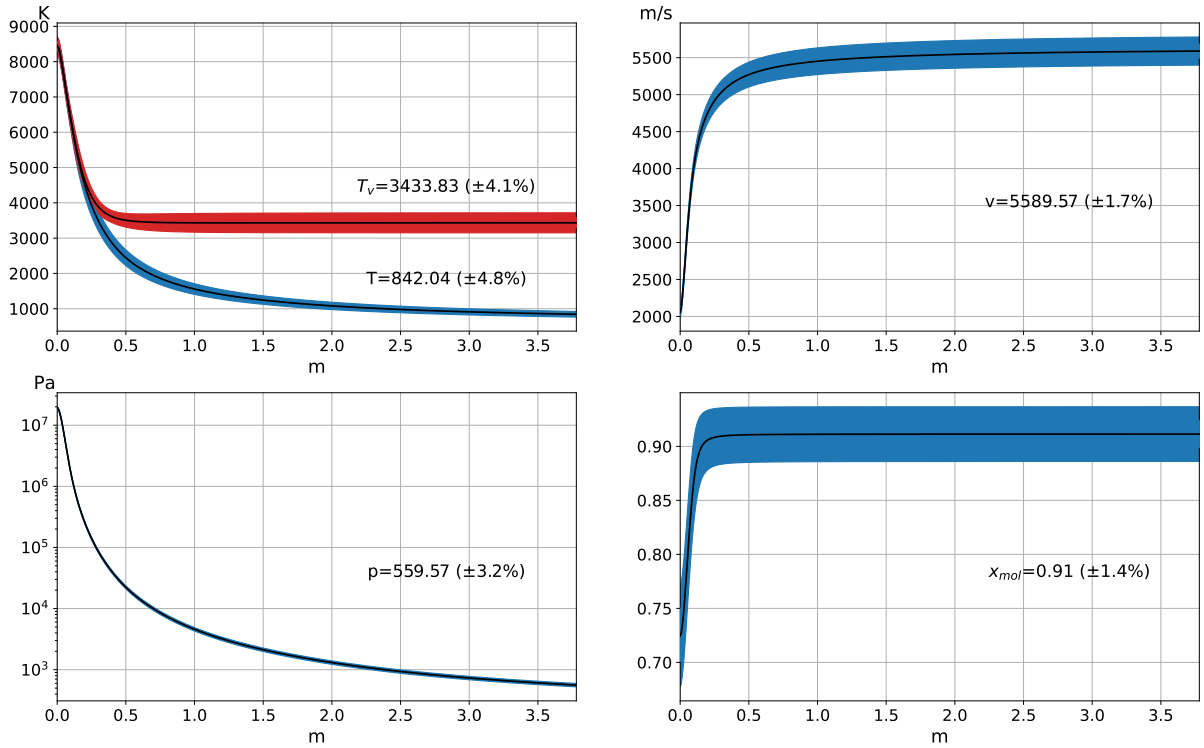

Figure 1: Flow properties (mean values and variation due to model uncertainties) along nozzle axis for binary flow of nitrogen in HEG Nozzle V for reservoir condition H22R0.20.

The results are planned to include simulations of expanding air flows for various HEG conditions, analysis of uncertainty in the flow parameters and their sensitivities to different vibrational and chemical relaxation pathways.

Georgii Oblapenko acknowledges the funding provided by the Alexander von Humboldt foundation for his stay as a guest researcher at the German Aerospace Center (DLR).

[1] Candler, G., and R. MacCormack. Computation of weakly ionized hypersonic flows in thermochemical nonequilibrium. J. Thermophys. Heat Transfer, 5(3):266–273, 1991.
[2] Weaver, A., A. Alexeenko, R. Greendyke, and J. Camberos. Flowfield uncertainty analysis for hypersonic computational fluid dynamics simulations. J. Thermophys. Heat Transfer, 25(1):10–20, 2011.
[3] West IV, T., and S. Hosder. Uncertainty quantification of hypersonic reentry flows with sparse sampling and stochastic expansions. J. Spacecr. Rockets, 52(1):120–133, 2015.
[4] Sharma, S., S. Ruffin, W. Gillespie, and S. Meyer. Vibrational relaxation measurements in an expanding flow using spontaneous Raman scattering. J. Thermophys. Heat Transfer, 7(4):697–703, 1993.
[5] Chikhaoui, A., E.A. Nagnibeda, E.V. Kustova, and T.Yu. Alexandrova. Modeling of dissociation–recombination in nozzles using strongly non-equilibrium vibrational distributions. Chem. Phys., 263(1):111–126, 2001.
[6] Gu, S., J. Hao, and C. Wen. State-specific study of air in the expansion tunnel nozzle and test section. AIAA Journal, pages 1–15, 2022.
[7] Gimelshein, S., and I. Wysong. Nonequilibrium effects in high enthalpy gas flows expanding through nozzles. Phys. Fluids, 33(10):106104, 2021.
[8] Hannemann, K., J. Martinez Schramm, A. Wagner, and G. Ponchio Camillo. The high enthalpy shock tunnel Göttingen of the German aerospace center (DLR). Journal of large-scale research facilities JLSRF, 4(A133):1–14, 2018.

Mitteilung

Fachgruppe: Hyperschallaerothermodynamik

On the Operation and Diagnostics of an ECR Thruster with Magnetic Nozzle

Clara Schäfer

AS-RFZ Göttingen, Bunsenstraße 10, 37073 Göttingen, clara.schaefer@dlr.de

This work aims to document the operation of an electron cyclotron resonance plasma thruster with magnetic nozzle. Its purpose is to identify operating parameters in order to develop an expertise. This is intended to improve the process of designing and developing of a new electric propulsion system. Furthermore, the purpose of the reported campaign is to achieve competences regarding diagnostics and therefore the determination of plasma and beam characteristics, as well as influence factors on the diagnostics in use.

The operation and measurement campaign of the electron cyclotron resonance thruster with magnetic nozzle MINOTOR is performed at the Justus-Liebig-University Giessen in February 2022. The thruster under investigation was developed within the project MINOTOR (Magnetic Nozzle Electron Cyclotron Resonance Thruster) [1] under the lead of ONERA (fr. Office national d'études et de recherches aérospatiales). This thruster concept realises electrode-less plasma generation, by electron cyclotron resonance (ECR). The plasma is accelerated by means of a magnetic nozzle (MN). To ionise the gaseous fuel gas, electrons gyrating around the magnetic field lines of a permanent magnet are resonantly excited with an electromagnetic wave in the microwave regime. The acceleration of the plasma follows then from the divergent character of the magnetic field of the permanent magnet [1].

The diagnostics documented in this report are the double Langmuir probe, parallel plate analyzer and Faraday cup. Langmuir probes are used to determine plasma parameters. The basic operating principle of Langmuir probes is the application of a voltage, i.e. the establishment of a potential difference between plasma and a reference potential [2]. Following its parameters, the plasma reacts to this voltage and a current can be measured [2]. The interpretation of the current-voltage characteristic leads to the determination of these plasma parameters (density, temperature,...) [2]. The probe used in this work is a double Langmuir probe. This double Langmuir probe has the advantage that neither the determination of the local plasma potential nor a stable ground potential is necessary, since a potential difference between the two probe ends can be applied [2]. To determine influencing factors such as magnetic

fields, different orientations of the probe are carried out. To be able to make statements about the MN, two measurement methods are chosen.

A Faraday cup (FC) with an electron repeller is used to determine the ion density in the beam. This determines the current flow due to the impact of ions, proportional to their number, hence the ion current density of the beam [3]. The energy of the ions is determined with an electrostatic analyzer, a parallel plate analyzer (PPA) [4]. In a PPA the ions are directed by an electric field onto a detector, depending on their energy. In this way, an ion velocity distribution can be detected [4]. The normal operation conditions are found with xenon as propellant at a volume flow of 1 sccm and a microwave input power of 30 W at a frequency of 2.45 GHz. An additional mass shock is found necessary for plasma ignition. The gas inlets are sensitive in handling and show significant material fatigue. It is observed that a variation of mass flow has an impact on the floating potential of the thruster, in such a way, that with decreasing mass flow, an increase in potential is observed. There is no significant change in the ratio of inflow power and reflected power in dependency of the magnitude of the signal observed. A plasma density of $10^{17} m^{-3}$and an electron temperature of 15 eV are determined with Langmuir probe measurements. There is no observable saturation of the ion current and assumptions made for the derivation of the interpretation for the data, such as Maxwell-distributions, cold ions and no collisions within the sheath layer remain to be confirmed. The maximum ion energy is determined with PPA measurements as 117 eV. A decrease in energy can be observed with a stronger volume flow, while an increase in microwave power has no effect on the peak position of the velocity distribution. The ion current density in the beam is determined as 86 $\mu A/cm^2$ by FC measurements.

This work allows the identification operating factors for ECR thruster with MN. Plasma and beam measurements are performed and the evaluation of the data is presented. The values determined are critically examined for their validity. Taking into account any false assumptions or influencing factors, the results are used for plasma and acceleration characterization. This work gives an outview in what needs to be further understood or investigated in order to allow the development of an improved electric propulsion system, based on ECR and MN concepts. In addition, future measurement methods for ECR thrusters are presented, which can be used to identify or circumvent factors influencing diagnostics.

References

[1] Denis Packan et al. “The” MINOTOR” H2020 project for ECR thruster development”. In: 36th International Electric Propulsion Conference (Atlanta, USA). 2017.
[2] Robert B Lobbia and Brian E Beal. “Recommended practice for use of Langmuir probes in electric propulsion testing”. In: Journal of Propulsion and Power 33.3 (2017), pp. 566–581.
[3] CE Sosolik et al. “A technique for accurate measurements of ion beam current density using a Faraday cup”. In: Review of Scientific Instruments 71.9 (2000), pp. 3326–3330.
[4] TS Green and GA Proca. “A parallel plate electrostatic spectrograph”. In: Review of Scientific Instruments 41.10 (1970), pp. 1409–1414.

Mitteilung

Fachgruppe: Hyperschallaerothermodynamik

Calibration of Heterodyne Dual Frequency Comb Laser Absorption Spectroscopy for *NO* and H_2O Detection

Leni Schmidt und Jan Martinez Schramm
Deutsches Zentrum für Luft- und Raumfahrt e.V.
Institut für Aerodynamik und Strömungstechnik, Abteilung Raumfahrzeuge
Bunsenstraße 10, 37073 Göttingen
Leni.Schmidt@dlr.de, Jan.Martinez@dlr.de

The progressing climate change and its consequences for everyone necessitate to reduce the environmental impact of civil aviation. At once, an improvement in performance of spacecraft regarding their efficiency and flight time is an economic as well as a social desire. A possibility for hypersonic passenger flights is the use of scramjets that are powered by hydrogen combustion. While this combustion has zero carbon dioxide output, water vapor and *NO* are formed inthe process. Both are believed to have an strong influence on the atmospheric chemistry [1].

Therefore, a precise experimental determination of both *NO* and H_2O production during thehydrogen combustion is necessary for the evaluation of environmental effects caused by hydro-gen fueled vehicles. To test these models in the future in the High Enthalpy Shock TunnelGöttingen (HEG), one of the major European hypersonic test facilities where the test time forexperiments is typically in the ms range, the employed diagnostic techniques need to offer highacquisition rates.

A novel experimental approach to study the development of gas concentrations at rapid rates is the absorption spectroscopy with quantum cascade lasers (QCLs) in the infrared regime [2]. The used spectrometer (Iris-F1, IRsweep AG) is based on the frequency comb technology. In contrast to conventional laser systems that emit at one single wavelength at a given time, the Nobel prize awarded technology generates an optical spectrum with many discrete equidistant lines in the frequency domain [3]. The frequency comb sources are quantum cascade lasers. The two included QCLs have slightly different repetition rates $f_{rep,1}$ and $f_{rep,2}$. When both are combined, they generate a heterodyne beating signal as radiofrequency comb spectrum with $\Delta f_{rep} = f_{rep,1} - f_{rep,2}$ (fig. 1, left). The repetition rates are chosen for Δf_{rep} to be on the order of 1 to 5 MHz, so that the heterodyne beating pattern can be recovered from a high-bandwidth detector. To conduct the spectrometric measurements, two beams are needed. The reference beam reaches the detector undisturbed, while the sample beam passes through the sample and inter-

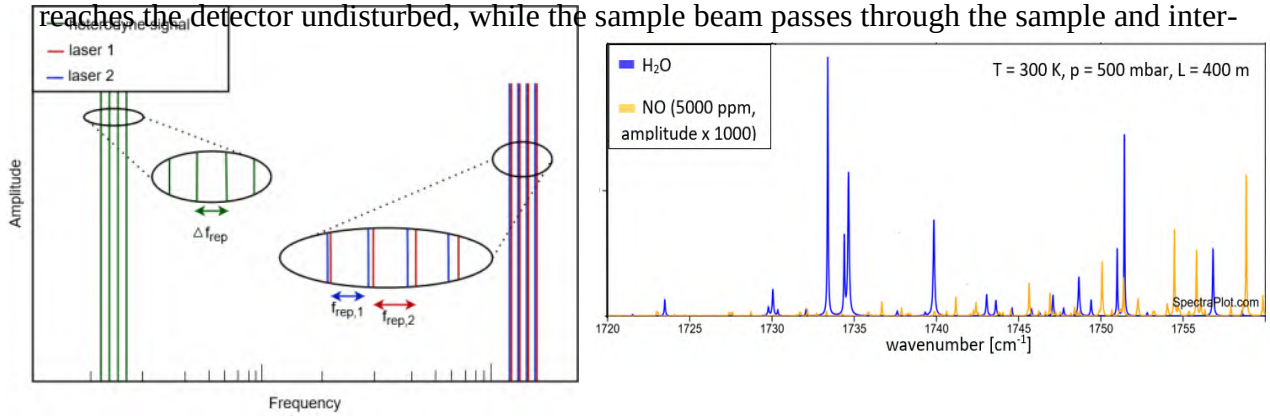

Figure 1: Frequency combs and heterodyne beating signal as RF spectrum (left). Simulated spectra of NO and H_2O via Hitran (right).

acts via absorption. The absorption attenuates the heterodyne signal and is characteristic for each gas species. The spectrometer covers a spectral region of 1720 to 1760 cm^{-1}. As simulated with HITRAN in figure 1, *NO* and H_2O lines are present in this region which allows to study the production of these during hydrogen combustion experiments.
The applicability of the spectroscopic technique was demonstrated and it could be applied to a test case of hydrogen combustion in HEG [4], but the measurements also showed the urge of more sophisticated calibration procedures for the spectrometer. Thus, part of the current work is the establishment of these procedures. The set-up is presented in figure 2. A multipass absorption cell is placed inside the spectrometer's sample compartment. The so called Herriott cell consists of mirrors that reflect an incoming light beam several times to increase the path length before coupling the beam out again. In this case, the cell has a circular design with individually curved mirror segments that achieve a path length of 4 meters within a compact volume of 31 ml. After evacuating, the cell is filled either with 200 ppm *NO* in N_2 or with ambient air to detect the amount of water for a range of pressure between 0 and 1000 mbar which is monitored with a manometer. The spectrometer is continuously purged with N_2 to remove disturbing water molecules from ambient air. As expected, the amount of water increases with a rising pressure. The measurements for water are in good agreement with the theoretical spectra that are plotted using the HITRAN database as figure 2 presents. The detection of *NO* came along with various challenges. A major issue were the used plastic tubings that pulled water from the surrounding. The tubings needed to be replaced with flexible metal tubings. A long evacuation time of the cell has to be attended to ensure a complete absence of water inside it. So far, the tests were conducted as long term measurements, but the spectrometer offers also a times resolved mode. This limits the acquisition time to around 33 ms, but enables time resolutions of 1-4 µs which is suitable for experiments at HEG. In a next step, a bigger Herriott cell creating a longer path length is used externally to study the weakening influence of fibers on the intensity signal. An outcoupling optical unit directs the sample light beam from the spectrometer into the fiber that leads towards the external setup. The same is done for the path back to the detector. After these measurements, experiments with a small shock tube employing the spectroscopy technique will be performed. The results will be reported in the paper.

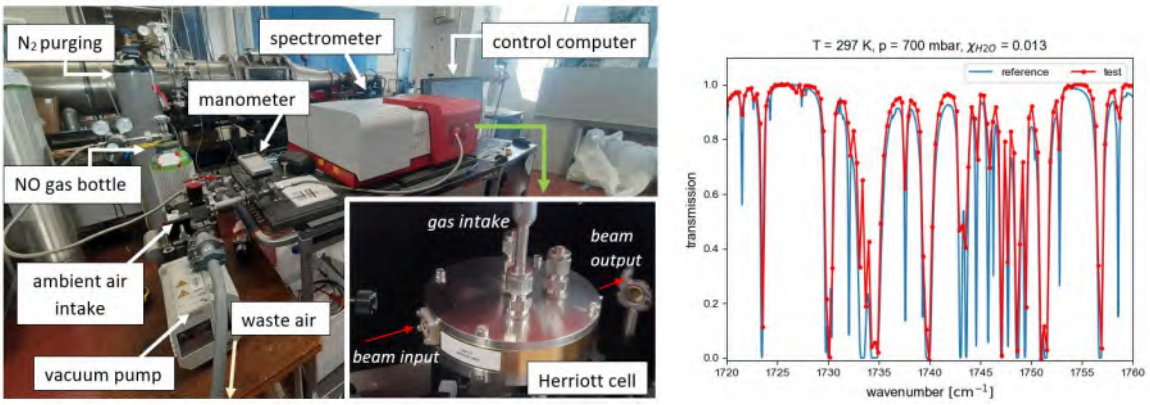

Figure 2: experimental set-up including the Herriott cell and gas connections (left). Results from spectroscopic water measurements in comparison with reference HITRAN data (right).

References

[1] B. Khandelwal, A. Karakurt, P. R. Sekaran, V. Sethi, and R. Singh, "Hydrogen powered aircraft : The future of air transport," *Prog. Aerosp. Sci.*, vol. 60, pp. 45–59. (2013)

[2] G. Zhang, R. Horvath, D. Liu, M. Geiser, and A. Farooq, "QCL-Based Dual-Comb Spectrometer for Multi-Species Measurements at High Temperatures and High Pressures," *Sensors*, vol. 20, no. 12, p. E3602. (2020)

[3] T. Fortier and E. Baumann, "20 years of developments in optical frequency comb technology and applications," *Commun. Phys.*, vol. 2, no. 1, Art. no. 1. (2019).

[4] J. Martinez Schramm and D. Luís, "Experimental Approach on Concentration Measurements of NO in Hydrogen Combustion Based on Heterodyne Laser Absorption Spectroscopy Using Quantum Cascade Lasers," in *New Results in Numerical and Experimental Fluid Mechanics XIII*, vol. 151, A. Dillmann, G. Heller, E. Krämer, and C. Wagner, Eds. Cham: Springer International Publishing, 2021, pp. 110–120. (2021)

Mitteilung

Fachgruppe: Multidisziplinäre Optimierung

Schleppdrohne Spin-Off des Schubklappenprojektes SKA
1. Schritt Segelflug-Schleppdrohne

Georg Emanuel Koppenwallner
DLR Göttingen, AS-HEL,
Bunsenstr. 10
37073 Göttingen
georg.koppenwallner@dlr.de

Problem des Elektrofluges ist die geringe Energiedichte der Batterien im Vergleich zu fossilen Brennstoffen. Eine technisch und ressourcenschonende Anwendung des Elektrofluges muss den Energieverbrauch von Elektroflugzeugen gering halten.
Dies kann durch verbesserte Aerodynamik und durch neue Antriebskonzepte geschehen.

Das SKA-Projekt im DLR untersucht die Anwendung einfahrbarer E-Antriebe am Beispiel der sogenannten Schubklappe. Dabei werden E-Triebwerke in Spannweitenrichtung - vergleichbar zur Schempp-Hirth Klappe an der Flügeloberseite aus-/ eingefahren. Es handelt sich dabei um eine "over the wing" OTW-Propeller Konfiguration, die bereits 1926 von Seiferth in Göttingen untersucht wurde.
An einem 1 :1 Modell wurde dieser Antrieb 2021 in der SWG (Seiten-Wind-Versuchsanlage-Göttingen) untersucht. Die Ergebnisse der Messungen zeigen erneut, dass diese Konfiguration Vorteile, u.a. bezüglich des Auftriebsbeiwertes und insbesondere in der Start – und Steigphase, bietet.

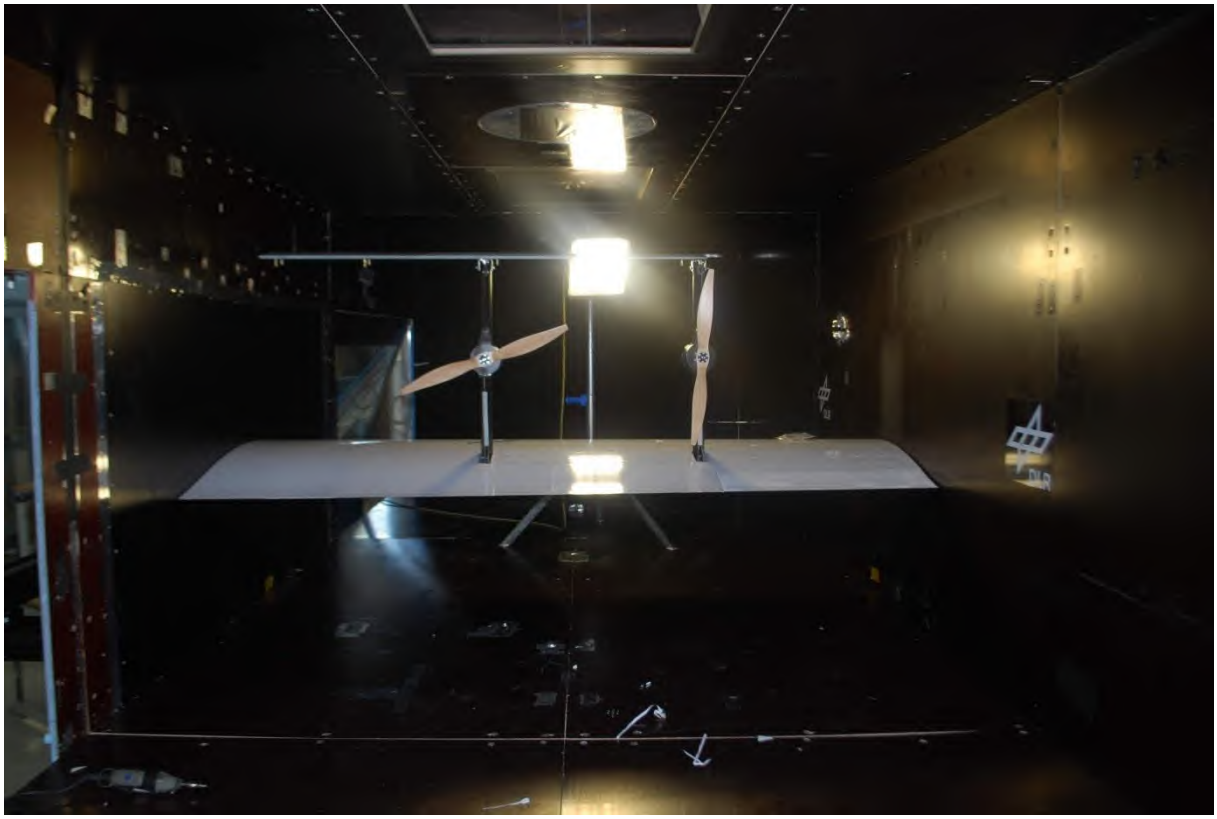

Abb. 1 SKA-WKM in der Seitenwindversuchsanlage-Ansicht von hinten

Das Einfahren der Antriebe beim SKA-Projekt resultiert aus dem Ausgangspunkt dieser Entwicklung eine neue Motorseglerkonfiguration für den Segelflug zu entwickeln.
Übertragen auf ”größere Flugzeuge“ kann man mit der Schubklappe die Anzahl der ausgefahrenen Triebwerke für Reiseflug und Start besser anpassen.

Statt die „überflüssige“ Triebwerke im Reiseflug einzufahren kann man diese auch einfach nach dem Start vom Flugzeug „entfernen“.
Das ist auch die Grundidee das F-Schlepps, DE 491 456 1927, der 1927 von Raab und Katzenstein in Kassel entwickelt wurde. "Drohnenschlepp" ist für die Modellflieger seit langem eine Selbstverständlichkeit. Es werden die verschiedenen Startarten für Segelflugzeug energetisch abgeschätzt und besonders der Energieaufwand für den Schlepp mit einem UL mit Verbrennungsmotor und einer Schleppdrohne basierend auf den im SKA-Projekt vermessenen Antrieben verglichen. Dazu wird eine Schleppdrohnen-Konfiguration mit verteilten Antrieben in OTW-Konfiguration vorgeschlagen. Diese Schleppdrohne im Gewichtsbereich von 25 kg – 150 kg kann als Erprobungsträger für den Segelflugzeugschlepp und als Sub-Scale Testing Demonstrator für größere Schleppdrohnen für die künftige E-Flug Luftfahrt dienen.

Mitteilung

Fachgruppe: Multidisziplinäre Optimierung

Gust and Maneuver Load Alleviation in Conceptual Aircraft Design

Markus D. Krengel Martin Hepperle

DLR Institut für Aerodynamik und Strömungstechnik, Lilienthalplatz 7, Braunschweig
Markus.Krengel@dlr.de

Introduction

The lift distribution of a wing depends on its shape. It is usually a compromise between the aerodynamically driven cruise performance and the capability of the structure to withstand the maximum loads. While these maximum loads are single events, the cruise performance influences the fuel burn during the entire flight. Load alleviation control laws for maneuver and gust loads are able to alter the load distribution temporarily. This reduces the maximum structural loads and as a consequence the compromise between aerodynamic and structural requirements can potentially be shifted towards the cruise performance. A multidisciplinary wing and overall aircraft design with load alleviation technologies therefore requires the combination of three disciplines: aerodynamics, structures and flight dynamics in a coupled approach.

Xu and Kroo [7] for example assessed a short-range aircraft including a flexible wing based on conceptual methods. A physics-based aeroservoelastic model was included but the design did not contain take-off weight iterations. They showed a fuel burn reduction of 11 %. In the early design stage so-called ''high fidelity'' approaches based on unsteady Reynolds-Averaged Navier-Stokes equations coupled with structural finite element methods can usually not be applied because the required detailed geometric shapes are not yet defined. Once the geometry is detailed enough, the available design space is already narrowed significantly. A recent “high fidelity” approach applying the DLR TAU software is presented in Wunderlich et al. [6] for a long range aircraft. The massive computational effort only allowed for some major overall aircraft geometry constraints rather than a full feedback of the wing sizing into the overall aircraft design. The optimization resulted in a combined block fuel reduction of 12.9 %.

The approach here is to include the full overall aircraft design loop for take-off weight as well as a more detailed unsteady aerodynamic approach and more relevant load cases in the design process than Xu and Kroo. On the other hand, the approach is simplified compared to Wunderlich et al. [6] to reduce the computational effort and enable a larger design study in a reasonable simulation time frame.

Methodology

This investigation utilizes a physics-based framework for conceptual aircraft design with a flexible wing structure sizing. It is based on the DLR overall aircraft design environment OpenAD [5] and the CPACS data scheme [1]. Figure 1 shows the data flow of the framework, starting from a set of Top Level Aircraft Requirements and constraints. The global output is a converged aircraft design with a more detailed wing.

Within the process, two major loops for the overall aircraft design and the detailed wing design cascade into each other. ASWING from Drela [2, 3] is included as a physics-engine, integrating the flexible aircraft into the design framework. It is based on unsteady lifting-line calculations combined with non-linear Euler beam theory. The load cases are based on design mission points. The process is demonstrated for a generic long-range transport aircraft. Maneuver and gust load alleviation will be included via deployed flaps. It is not a full loads process including the entire load envelope which on the other hand usually cannot consider the design perspective. The process is

based on previous activities [4]. In addition, a better model for transonic aerodynamics is included as well as dynamic gust load cases, a pitch damper and gust load alleviation. The design parameters for the optimization with and without load alleviation are also given in Figure 1. They contain planform parameters, stations for twist optimization and stations for the adaption of the airfoil thickness distribution. As a simplification the wing structure topology will not be optimized. This reduces the design space.

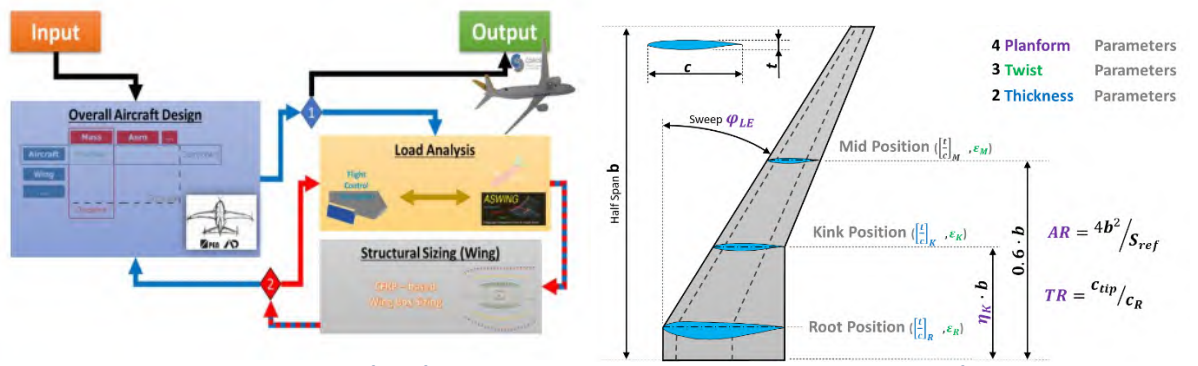

Figure 1: Overview over the process flow for dynamic aeroelastic wing sizing and illustration of the design parameters.

Outlook on Final Paper

This research will reflect a wing shape optimization in conceptual aircraft design. The optimization is performed in four cases: without load alleviation, with maneuver load alleviation, with gust load alleviation and with both. Figure 2 shows selected results of an initial sensitivity study with the revised framework. Geometrical constraints like a wing span limit or the space allocation for the main landing gear integration can be applied to filter the designs for practical feasibility at aviation infrastructure.

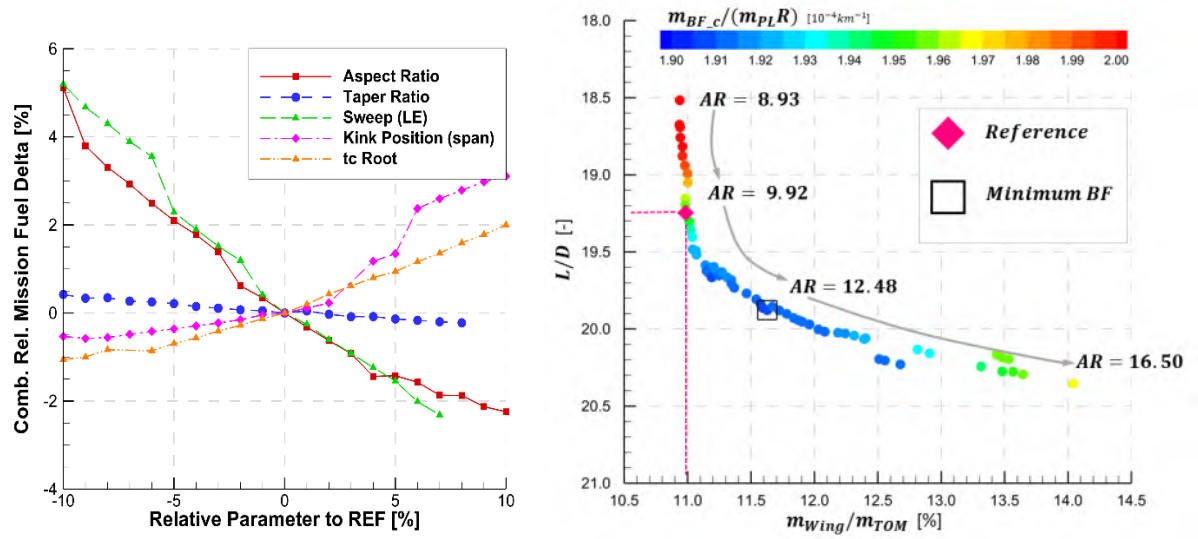

Figure 2: Gradient of most sensitive parameters around the reference and aspect ratio study.

References

[1] **Alder**, M., Moerland, E., Jepsen, J., and Nagel, B., Recent Advances in Establishing a Common Language for Aircraft Design with CPACS, Aerospace Europe Conference 2020, Bordeaux, Frankreich, 2020.

[2] **Drela**, M., ASWING 5.99 Technical Description - Steady Formulation, Massachusetts Inst. of Technology, Cambridge, MA, 2015, Chaps. 1, 8.

[3] **Drela**, M., ASWING 5.99 Technical Description - Unsteady Extension, Massachusetts Inst. of Technology, Cambridge, MA, 2015, Chaps. 1, 15.

[4] **Krengel**, M. D., Hepperle, M., Effects of Wing Elasticity and Basic Load Alleviation on Conceptual Aircraft Designs. AIAA SCITECH 2022 Forum, 2022, p. 0126. doi:10.2514/6.2022-0126

[5] **Woehler**, S., Atanasov, G., Silberhorn, D., Fröhler, B., and Zill, T., Preliminary Aircraft Design within a Multidisciplinary and Multifidelity Design Environment, Aerospace Europe Conference 2020, Bordeaux, Frankreich, 2020.

[6] **Wunderlich**, T. F., Dähne, S., Reimer, L., and Schuster, A., Global Aerostructural Design Optimization of More Flexible Wings for Commercial Aircraft, Journal of Aircraft, 2021, pp. 1, 18. doi:10.2514/1.C036301

[7] **Xu,** J., and Kroo, I., \textit{Aircraft Design with Active Load Alleviation and Natural Laminar Flow}, Journal of Aircraft, Vol. 51, No. 5, 2014, pp. 1532, 1545. doi:10.2514/1.C032402.

Mitteilung

Fachgruppe: Multidisziplinäre Optimierung

Digital Design of Moveables at DLR Virtual Product House

Fabian Lange-Schmuckall
German Aerospace Center (DLR), Institute of Aerodynamics and Flow Technology, Lilienthalplatz 7, 38108 Braunschweig, Germany, Fabian.Lange@dlr.de

Alexander Zakrzewski
German Aerospace Center (DLR), Institute of Aerodynamics and Flow Technology, Lilienthalplatz 7, 38108 Braunschweig, Germany, Alexander.Zakrzewski@dlr.de

Martin Rädel
German Aerospace Center (DLR), Institute of Composite Structures and Adaptive Systems, Lilienthalplatz 7, 38108 Braunschweig, Germany, Martin.Raedel@dlr.de

René Hollmann
German Aerospace Center (DLR), Institute of Flight Systems, Lilienthalplatz 7, 38108 Braunschweig, Germany, Rene.Hollmann@dlr.de

Abstract. This work presents the virtual design activities performed within the Virtual Product House (VPH) start-up project. In this project a multi-disciplinary process for virtual design, manufacturing and testing is developed. The VPH acts as integration plateau where the assessment capabilities of multiple partners from research, industry and certification authority are combined and applied to use cases. The multi-disciplinary analysis setup enabled the investigation and improvement of aircraft designs and allows the impact assessment of modifications on a existing configurations. As starting point, three disciplines are considered: aerodynamic, structural and system design. This paper presents results for selected modifications on trailing edge moveable devices of a representative research aircraft, including variations of the applied structural constituent and design, actuation system as well as number of flap tracks.

Keyword: VPH, Digital Design, Moveables

The development of innovative and complex technologies requires a collaborative work of various stakeholders to solve multi-disciplinary problems. The DLR project VicToria (Görtz, et al., 2020) is to be emphasized with respect to the latest developments of multi-disciplinary process chains for transport aircraft configurations. Additional disciplines, like engine sizing or systems design, have been added to the already established coupling between aerodynamic and structural design. Therefore, new methods were implemented and existing tools extended to improve the interfaces and collaboration between disciplines. The biggest challenge within this and many other MDO projects is the coordination and implementation of interfaces between disciplines and the availability of a common research environment. In consequence, the DLR Virtual Product House (VPH) was established in the ECOMAT in Bremen to improve the exchange and collaboration of research facilities, aircraft manufacturer, suppliers and certification authority.
In the course of the VPH start-up project the initial use case “Multifunctional moveables” was selected together with the industry partners (Airbus, FFT, IABG, Liebherr-Aerospace).
Up to this date, the main focus of most MDO processes was on clean wing configurations. Therefore, the application and especially extension of available methods in regards to

takeoff and landing configurations was required to enable the evaluation of the essential parts of a state of the art high lift system and associated requirements.
Finally, a digital continuous End-to-End process chain was established ranging from virtual design (Lange, 2021) over virtual manufacturing (Rädel, et al., 2021) up to virtual testing .

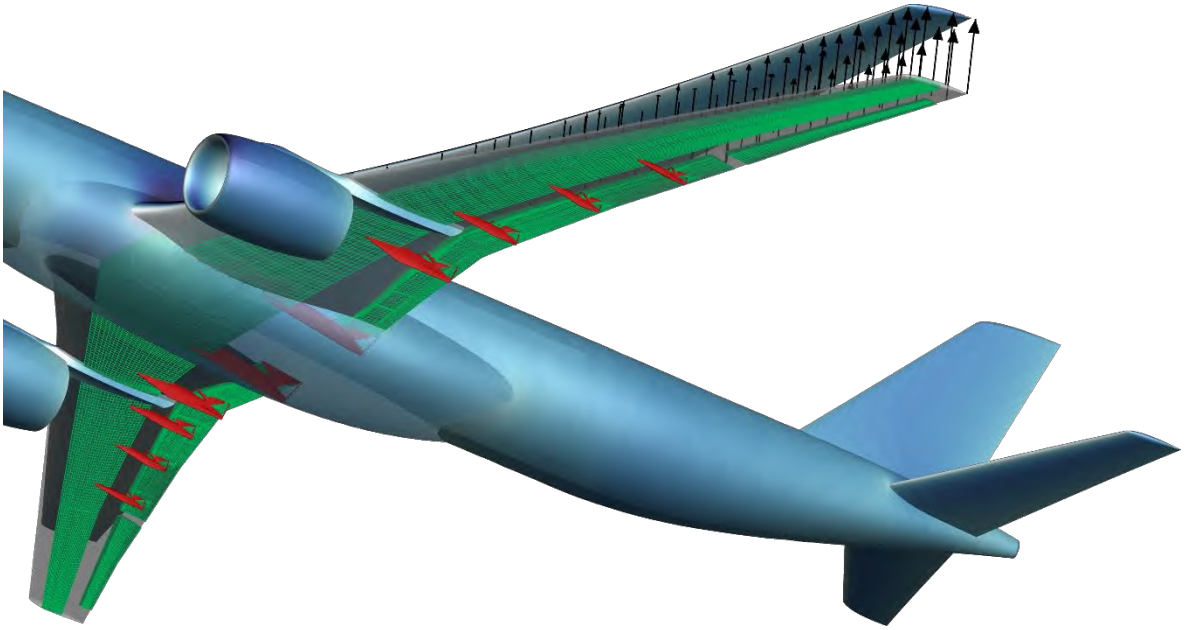

Within this article, results obtained by applying the virtual design process (Lange, 2021) on the aircraft configuration shown above will be presented covering selected investigations. These comprise the modification of the structural constituent from metal to composite, a change of the structural concept of the flap from a classical differential concept to a composite multi-spar concept with integral load introduction (CMFIL), the modification of the high lift kinematic from Track-Rear-Link kinematic to an Adaptive Dropped Hinge Flap (ADHF) as well as a study regarding the number of flap tracks.

The Virtual Product House start-up project is funded by the German federal state of Bremen and the European Regional Development Fund (ERDF).

European Union
Investing in Bremen's Future
European Regional
Development Fund

References

Görtz, S., Abu-Zurayk, M., Ilic, C., Wunderlich, T., Keye, S., Schulze, M., . . . Petsch, M. (2020). Overview of Collaborative Multi-Fidelity Multidisciplinary Design Optimization Activities in the DLR Project VicToria. *AIAA Aviation Forum 2020.* Virtual Event. doi:10.2514/6.2020-3167

Hollmann, R. W., Schäfer, A., & O. Bertram, M. (2021). Virtual Testing of Multifunctional Moveable Actuation Systems at Virtual Product House. *Deutscher Luft- und Raumfahrtkongress.* Online.

Lange, F. Z. (2021). Digital Multi-Disciplinary Design Process for Moveables at Virtual Product House. *Deutscher Luft- und Raumfahrtkongress.* Online.

Rädel, M., Delisle, D., Krombholz, C., Bertling, D., Hein, R., & Wille, T. (2021). Towards Robustness Assessment in Virtual Testing. *Deutscher Luft- und Raumfahrtkongress.* Online.

Mitteilung

Fachgruppe: Multidisziplinäre Optimierung

Optimierung von Steuerflächenausschlägen am hochgestreckten Flügel zur Steigerung der Gleitzahl im Reiseflug

Tobias Wunderlich und Florian Siebert
DLR Institut für Aerodynamik und Strömungstechnik,
Lilienthalplatz 7, 38108 Braunschweig, tobias.wunderlich@dlr.de

Einleitung: Mit dem Ziel die CO_2-Emmisionen beim Langstreckenverkehrsflugzeug deutlich zu reduzieren, gilt es die Gleitzahl im Reiseflug weiter zu steigern, leichtere Werkstoffe einzusetzen und das Triebwerk zu verbessern. Um dies zu erreichen, ist der hochgestreckte adaptive Flügel Gegenstand der aktuellen Forschung. Dieser Flügel passt seine Geometrie optimal an den aktuellen Flugzustand an, um die dimensionierenden Lasten zu reduzieren und die Flugleistung zu verbessern. Zusätzlich ist durch den Einsatz des Getriebefans von einer Reduzierung des schubspezifischen Kraftstoffverbrauchs auszugehen.

Vorgehen: Im Rahmen des LuFo-VI Verbundvorhabens INTELWI wird ein hochgestreckter adaptiver Flügel für ein Langstreckenverkehrsflugzeug untersucht. Der vom DLR entwickelte Flügelgrundriss liegt mit einer Streckung von 12.4 deutlich über den Werten moderner Verkehrsflugzeuge und erfüllt die geometrischen Randbedingungen für die Unterflügelanordnung eines zukünftigen Getriebefans. Ausgehend von diesem Flügelgrundriss erfolgte ein multidisziplinärer Flügelentwurf mit der im DLR-Projekt VicToria (Virtual Aircraft Technology Integration Platform) weiterentwickelten und erfolgreich angewendeten Prozesskette [1], [2]. Diese Prozesskette wurde hier für die Optimierung von Steuerflächenausschlägen eingesetzt, wobei das vorher dimensionierte Strukturmodell unverändert blieb. Die Flugleistung im Reiseflug wird unter Verwendung einer numerischen Strömungssimulation durch Lösung der Reynolds-gemittelten Navier-Stokes-Gleichungen (RANS) ermittelt. Das elastische Verhalten des Flügels folgt aus einer numerischen Struktursimulation unter Verwendung der Finite-Elemente-Methode (FEM). Dabei werden die Verformungen des elastischen Flügels durch eine Strömungs-Struktur-Kopplung berücksichtigt. Hier werden die Ergebnisse der numerischen Optimierung von Steuerflächenausschlägen zur Steigerung der Gleitzahl im Reiseflug vorgestellt. Dabei werden die statischen aeroelastischen Verformungen des Flügels und die Trimmung des Flugzeugs unter transsonischen Reiseflugbedingungen berücksichtigt. Als Zielfunktion der Optimierung wird die Minimierung des kombinierten Kraftstoffverbrauchs verwendet. Dabei resultiert der kombinierte Kraftstoffverbrauch aus drei unterschiedlichen Flugmissionen („multi-mission design“). Dabei werden die Kraftstoffverbräuche der betrachteten Flugmissionen unterschiedlich gewichtet.

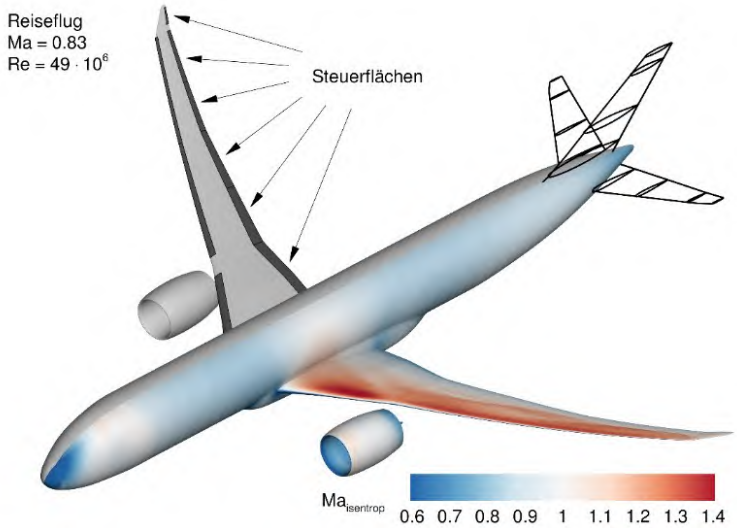

Ergebnis: Als zentrales Ergebnis sollen hier das Flugzeug ohne die Verwendung der Steuerflächen dem Flugzeug mit optimierten Steuerflächenausschlägen gegenübergestellt werden. Für den kombinierten Kraftstoffverbrauch und die daraus resultierenden CO_2-Emissionen pro Passagierkilometer konnte eine Reduzierung von 0.9% erzielt werden. Den Erwartungen entsprechend konnte die größte Verbesserung bei der Flugmission mit der höchsten Mach-Zahl erreicht werden, weil die dort vorliegenden Strömungsverhältnisse sich am stärksten von den

Verhältnissen bei der am höchsten gewichteten Bewertungsmission unterscheiden [3]. In der Tabelle sind die optimalen Ausschläge der verwendeten Steuerflächen für die Bewertungsmission und die daraus resultierenden Kenngrößen angegeben. Im gezeigten Bild erfolgt eine detaillierte Gegenüberstellung der aerodynamischen Ergebnisse für das Referenzflugzeug ohne und mit optimierten Steuerflächenausschlägen. Die entsprechenden Ergebnisse zeigen die Oberflächenlösung der numerischen Strömungssimulation in Form der isentropen Mach-Zahl und die spannweitige Auftriebs- und Auftriebsbeiwertverteilung.

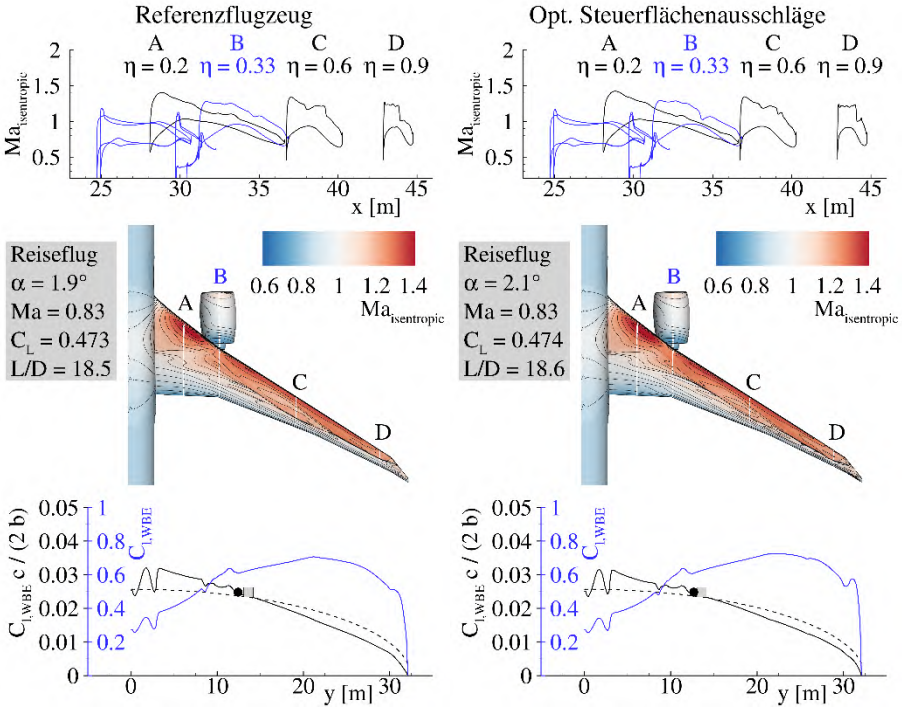

			Ohne Steuerflächen-ausschläge	Optimierte Steuerflächen-ausschläge	Differenz
Bewertungs-mission mit Ma = 0.83	Steuerflächen-ausschläge	$\delta_{Flap,in}$	0.0°	−1.5°	-
		$\delta_{Flap,mid}$	0.0°	+0.0°	-
		$\delta_{Flap,out}$	0.0°	+0.2°	-
		$\delta_{Aileron,in}$	0.0°	+1.3°	-
		$\delta_{Aileron,out}$	0.0°	+2.1°	-
		$\delta_{Tip\ device}$	0.0°	+5.9°	-
	Anstellwinkel	α	1.9°	2.1°	+11.9 %
	Gleitzahl	L/D	18.52	18.62	+0.5 %
	Druckpunkt	$2\,y_{CoP}/b$	0.382	0.390	+2.1 %
	Kraftstoffverbrauch	$m_F/(R\,m_P)$	$1.435 \times 10^{-4}\,\mathrm{km}^{-1}$	$1.428 \times 10^{-4}\,\mathrm{km}^{-1}$	−0.5 %
Zielfunktion	Kombinierter Kraftstoffverbrauch	$m_F/(R\,m_P)$	$1.563 \times 10^{-4}\,\mathrm{km}^{-1}$	$1.549 \times 10^{-4}\,\mathrm{km}^{-1}$	−0.9 %
	CO_2 Emissionen pro Passagierkilometer[a]	$m_{CO2}/(R\,m_P)$	$51.7\,g_{CO2}$/pkm	$51.2\,g_{CO2}$/pkm	−0.9 %

[a] Annahmen: $3.15\,kg_{CO2}/kg_{Fuel}$ für Turbofantriebwerk [21] und 105 kg pro Passagier mit Gepäck

Literatur:

[1] T. F. Wunderlich und L. Reimer, „Integrated Process Chain for Aerostructural Wing Optimization and Application to an NLF Forward Swept Composite Wing," in *AeroStruct: Enable and Learn How to Integrate Flexibility in Design.*, Bd. 138, R. Heinrich, Hrsg., Cham, Springer International Publishing, 2018, p. 3–33.

[2] T. F. Wunderlich, S. Dähne, L. Reimer und A. Schuster, „Global aero-structural design optimization of composite wings with active manoeuvre load alleviation," *CEAS Aeronautical Journal,* May 2022.

[3] Z. Lyu und J. R. R. A. Martins, „Aerodynamic Shape Optimization of an Adaptive Morphing Trailing-Edge Wing," *Journal of Aircraft,* Bd. 52, p. 1951–1970, November 2015.

Mitteilung

Fachgruppe: Numerische Aerodynamik

Towards Scalable Framework Integration of the Next-Gen CFD Software *CODA* for Multidisciplinary Nested MPI-Parallel Matrix-Free Newton-Krylov

S. Ehrmanntraut, A. Büchner, S. Gottfried, A. Stück
German Aerospace Center (DLR), Institute of Software Methods for Product Virtualization, Zwickauer Straße 46, Dresden, Germany, simon.ehrmanntraut@dlr.de

Motivation Scalable solution algorithms for coupled multiphysics problems are a key enabler towards large-scale design analyses and optimizations of future aircraft configurations in conjunction with high-fidelity simulations. Coupling partitioned single-disciplinary solvers for multidisciplinary problems by straightforward nonlinear block-Gauß-Seidel or block-Jacobi methods has severe limitations regarding algorithmic scalability and convergence: the methods converge linear at best and diverge if interdisciplinary coupling becomes too dominant. We aim to circumvent said issues by employing Newton-Krylov-type methods: the methods converge asymptotically quadratic and may also converge for problems with dominant coupling. Effective hierarchical preconditioning techniques may further increase robustness. Key aspect is the integration of the next-generation CFD solver *CODA* [1] – a joint development of DLR, ONERA and Airbus – into a scalable nested MPI-parallel framework for multidisciplinary problems.

Methodology We pursue a partitioned framework approach that relies on the multidisciplinary HPC ecosystem *FlowSimulator* [2] and the open-source *Python* framework *OpenMDAO* [3]. Via the *FlowSimulator* infrastructure, the single-disciplinary solvers provide their nonlinear residuals, their directional derivatives by algorithmic differentiation, and their linear solution/preconditioning routines to *OpenMDAO* as *Python* access points. From *OpenMDAO*, a multidisciplinary Newton-Krylov method is executed by concatenating the single-disciplinary problems to one multidisciplinary residuals vector

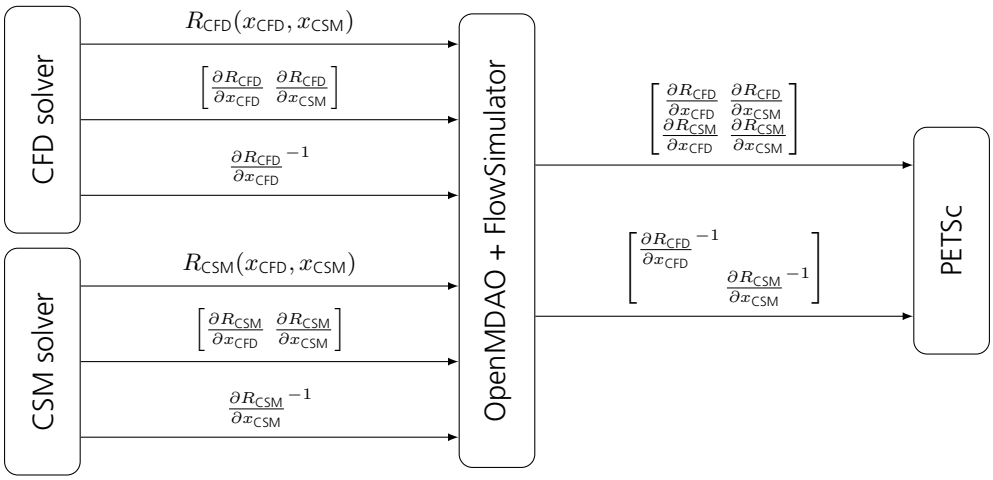

Figure 1: Simplified schematic overview of shared operators for an aeroelastic problem. The CFD/CSM solvers provide their nonlinear residuals, their Jacobians by algorithmic differentiation and their linear solvers to *OpenMDAO* as matrix-free linear operators. Running Newton's method, *OpenMDAO* provides the concatenated Jacobian and the block-'inverses' to *PETSc* for matrix-free block-Jacobi preconditioned Krylov methods.

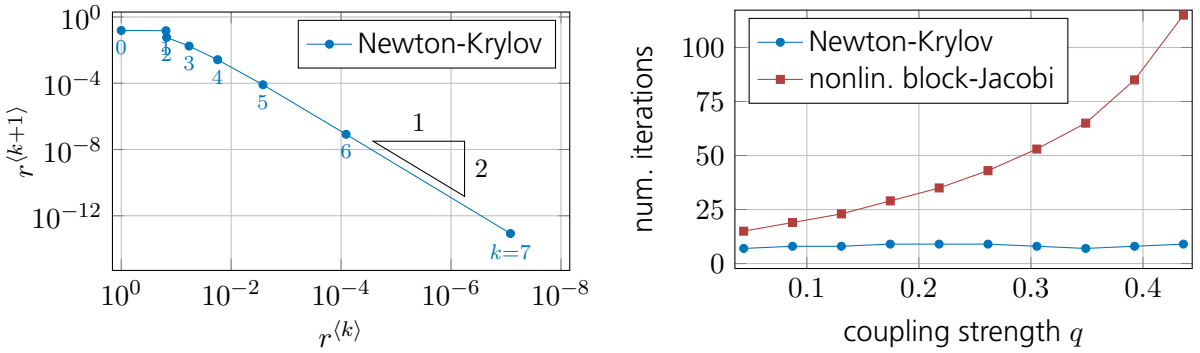

Figure 2: NACA 0012 airfoil in viscous flow ($Ma := 0.3$, $Re := 1{\cdot}10^4$) with torsional spring attachment. Left: Iteration history of the multidisciplinary nonlinear relative residual norm $r^{\langle k \rangle}$ in the k-th iteration. Right: Number of nonlinear iterations to relative residual norm $1{\cdot}10^{-13}$ against coupling strength q (i. e. aerodynamic forces over spring stiffness).

and matrix-free Jacobi operator (see Fig. 1). The linearized system is preconditioned via the single-disciplinary solvers by linear block-Jacobi, and solved by flexible GMRES from *PETSc* . This approach is implemented such that the disciplines run matrix-free in different parallel MPI processes.

Preliminary results As proof of concept, we implemented a simple problem from static aeroelasticity: a rigid NACA 0012 with torsional spring attachment in viscous flow. The aerodynamic unknowns – the fluid variables and the coefficient of moment – are handled by *CODA*. The structural unknown – the twist angle, resp. the angle of attack – is handled by a simple solver equating the moments of the spring and the airfoil. As intended, the Newton-Krylov method converges asymptotically quadratic (see Fig. 2 left), implying *CODA* provided its derivatives with sufficient accuracy and MPI communication was done properly. As expected, the Newton-Krylov method requires less iterations than the baseline method, nonlinear block-Jacobi (see Fig. 2 right). Further, while the latter method requires increasingly more iterations for tightly coupled cases, the former requires a roughly constant amount of iterations (see Fig. 2 right).

Full-paper Outlook In ongoing work, we aim to improve the stability of Newton's method in the transient phase by implementing both a multidisciplinary variant of pseudo-transient continuation [4] and Armijo-Goldstein backtracking line search [5]. The approach shall be tested with multidisciplinary problems involving a industry-scale aircraft configuration. To further challenge the multidisciplinary solution capabilities of the framework approach, we intend to solve multidisciplinary problems with hundreds of solvers via different solution hierarchies.

References

1. LEICHT, T. et al. *DLR-Project DIGITAL-X – Next Generation CFD Solver FLUCS* [DLRK]. 2016. Available also from: `https://elib.dlr.de/111205/`.
2. BACKHAUS, T.; GOTTFRIED, S.; MERLE, A.; HWANG, J.; STÜCK, A. *Modularization of High-Fidelity Static Aeroelastic MDO Enabling a Framework-based Optimization Approach for HPC* [AIAA 2021-1236]. 2021. Available from doi: `10.2514/6.2021-1236`.
3. GRAY, J. S.; HWANG, J. T.; MARTINS, J. R. R. A.; MOORE, K. T.; NAYLOR, B. A. OpenMDAO: An open-source framework for multidisciplinary design, analysis, and optimization. *Structural and Multidisciplinary Optimization*. 2019, vol. 59, no. 4, pp. 1075–1104. Available from doi: `10.1007/s00158-019-02211-z`.
4. KELLEY, C. T.; KEYES, D. E. Convergence Analysis of Pseudo-Transient Continuation. *SIAM Journal on Numerical Analysis*. 1998, vol. 35, no. 2, pp. 508–523. Available from doi: `10.1137/S0036142996304796`.
5. ARMIJO, L. Minimization of functions having Lipschitz continuous first partial derivatives. *Pacific Journal of Mathematics*. 1966, vol. 16, no. 1, pp. 1–3. Available from doi: `10.2140/pjm.1966.16.1`.

Mitteilung

Fachgruppe: Numerische Aerodynamik

Time-spectral extension to the next-generation CFD software CODA with hierarchical, implicit solution methods

Erik Gros and Arthur Stück

German Aerospace Center (DLR)
Institute of Software Methods for Product Virtualization
Zwickauer Straße 46, 01069 Dresden, Germany
erik.gros@dlr.de, arthur.stueck@dlr.de

Motivation

The Time Spectral Method (TSM) has a huge potential for the time-accurate prediction of flows that are predominantly time-periodic, e.g. for periodic excitations such as rotor or propeller configurations. However, by construction the TSM leads to large coupled, nonlinear equation systems that need to be solved efficiently in order to benefit from the tailored ansatz in time. Therefore, we aim for strong implicit solution techniques for the non-linear TSM-problem, composed of a Newton-like (pseudo-time) approach and appropriate block-preconditioning methods for the resulting linear problems [1]. Unlike other time-discretization methods based on a spectral approach such as the Harmonic Balance (HB) [2], the TSM leads to real-valued equation systems. Accordingly, it allows for an implementation that reuses huge portions of the steady-state implementation of existing CFD solvers. The TSM method has been implemented in the next-generation CFD software CODA [3] developed by Onera, DLR and Airbus with its key features being presented and discussed in this paper.

Methodology

The TSM employs a temporal discretization approach assuming time-periodic responses of the flow. The Fourier ansatz:

$$q_n = q(t_n) = \sum_{k=-H}^{H} \hat{q}_k \, e^{-i\omega \, k \, t_n}$$

is applied to a periodic function of time denoted $q(t)$ with values sampled at equidistant points in a period *T*. The sampling points $t_n, n = 1, \ldots, N$ are also called time instances and their total number is related to the number of harmonics H by $N = 2H + 1$. The TSM employs a collocation matrix to discretize the time derivative leading to a large non linear equation system coupling all time instances involved. The collocation matrix replaces the time-operators known from classical time stepping methods, which are often of finite-difference type in time.

The numerical solution of coupled TSM problems tend to become more challenging with increasing number of time instances in the ansatz. This is addressed by a nested solution strategy in this study: all time instances per element (or control volume) are block-inverted by means of a direct LU decomposition that is embedded in a block-Jacobi method, which in turn is used as a preconditioner to a relaxed Newton-Krylov (GMRES) scheme. Exact derivatives computed by algorithmic differentiation (AD) are available to drive the Newton-Krylov method.

First Results

A 2D NACA0012 airfoil that undergoes a forced plunging oscillation in compressible, laminar flow ($Ma = 0.3$) was considered as a test case for the described TSM implementation. The unstructured computational mesh used for all time-instance is shown in Figure 1.

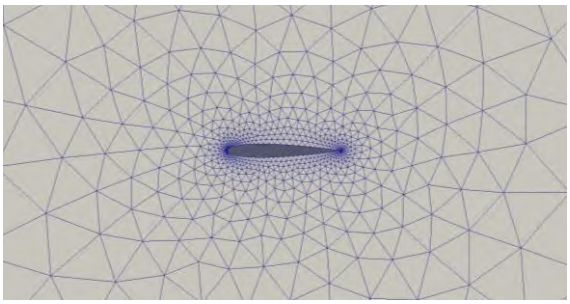

Fig. 1. Snapshot of the NACA0012 airfoil mesh.

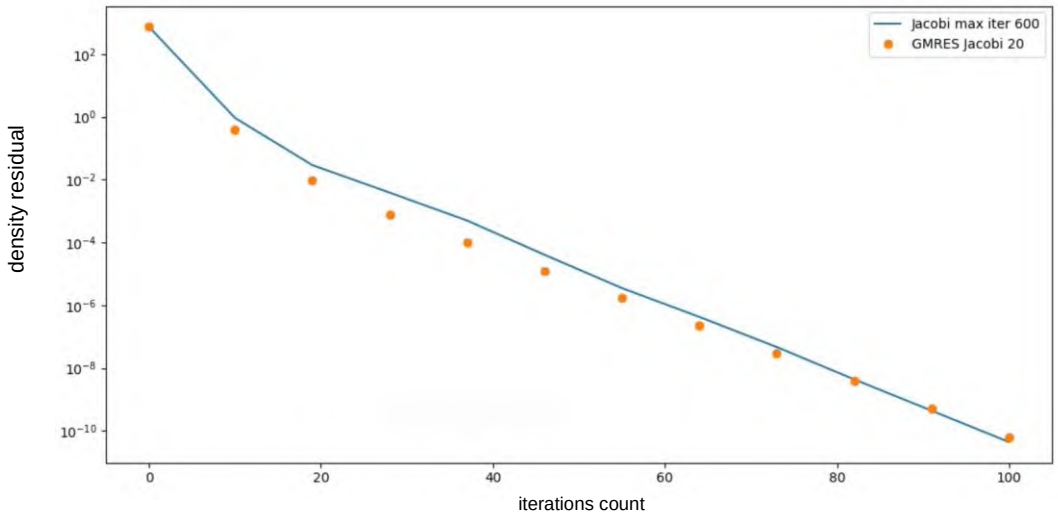

Fig. 2. Convergence of the density residual magnitude for the TSM solution Vs. non-linear (pseudo-time) iterations.

Using a moving mesh approach, the plunging motion of the airfoil was achieved by translating all coordinates of the computational mesh up and down following the equation $z = V \frac{T}{2\pi} \cos\left(2\pi\, t/T\right)$. The mesh velocity is homogeneous across the mesh and its amplitude (V) was chosen such that an effective angle of attack α is enforced $V = U_\infty \sin(\alpha)$ with respect to the free stream U_∞. With a few harmonics only, the TSM simulations match time-accurate time stepping reference results. The solution history is depicted in Figure 2 for two variants of the nested solution scheme: up to 600 block-Jacobi iterations are required per Newton-step when a block-Jacobi is used to solve the linear system, whereas for the Krylov-solver up to 20 GMRES sweeps were used each preconditioned by 4 block-Jacobi iterations. A convergence behavior similar to Figure 2 was obtained for RANS simulations at $Re = 1.4\ 10^7$ with the SA-neg model.

Outlook

An implicit TSM method was implemented in CODA and verified for a plunging airfoil configuration. In the next steps, the scalability of the approach with increasing number of time instances will be investigated. Moreover, the implementation will be applied to 3D configurations and higher-order Discontinuous-Galerkin (DG) discretizations in space.

References

1. Mundis, N.L, Mavriplis, D.J.: *Toward an optimal solver for time-spectral fluid-dynamic and aeroelastic solutions on unstructured meshes.* J. Comp. Phys. 345: 132-161 (2017).
2. Krack, M., Gross, J.: *Harmonic Balance for Nonlinear Vibration Problems.* Springer (2019).
3. Leicht, T. et al. *DLR-Project DIGITAL-X – Next Generation CFD Solver FLUCS*, DLRK (2016).

Mitteilung

Fachgruppe: Numerische Aerodynamik

Fortschritte und Weiterentwicklung von Body Force Methoden zur Verwendung in Auslegung und Nachrechnung von Fan Intake Systemen

Jonas Grubert und Jens Friedrichs
Institut für Flugantriebe und Strömungsmaschinen, TU Braunschweig
Hermann-Blenk-Str. 37, 38108 Braunschweig
j.grubert@ifas.tu-braunschweig.de

Der stetige Bedarf an Effizienzsteigerungen im Bereich der Flugzeugpropulsoren führt neben der Erforschung neuartiger Triebwerkskonzepte auch zur anhaltenden Weiterentwicklung bestehender Technologien. Im Bereich der etablierten Konfiguration der Triebwerksanordnung unterhalb des auftrieberzeugenden Flügels ist das Potenzial des Vortriebwirkungsgrades von Turbofan Triebwerken noch nicht ausgeschöpft. Derzeitige Entwicklungstrends sehen eine weitere Steigerung des Nebenstromverhältnisses vor. Hiermit einher geht zum einen der Bedarf an Getrieben zur Entkopplung der Niederdruckturbinendrehzahl von der Fan-Drehzahl. Zum anderen entsteht durch die steigenden Nebenstromverhältnisse der Bedarf an gewichts- und widerstandsarmen Triebwerkseinläufen.

Ein Nebenprodukt der Erhöhung der Nebenstromverhältnisse ist die Zunahme der Triebwerksdurchmesser, was gleichbedeutend mit einer Gewichts- und Widerstandszunahme ist. Um diesem Nebenprodukt des aktuellen Entwicklungstrends entgegenzuwirken, bedarf es aggressiverer Einlaufdesigns (1). Aggressiv bedeutet in diesem Kontext Einläufe mit möglichst geringer axialer Länge. Die Minimierung der axialen Länge des Triebwerkeinlaufs benötigt jedoch eine intensive Betrachtung der Wechselwirkungen der Einlaufaerodynamik und der Fan-Aerodynamik. Eine isolierte Betrachtung beider Komponenten ist nicht ausreichend, um das Potenzial vollständig ausschöpfen zu können. Eine gekoppelte Betrachtung ist somit bereits während der Auslegungsphase essenziell.

Da während der Auslegung hochauflösende, detaillierte Betrachtungen der beiden Komponenten im Sinne von herkömmlichen RANS bzw. uRANS Methoden ressourcentechnisch nur schwierig umsetzbar sind, sind hierfür reduzierte Methoden notwendig.

Eine mögliche reduzierte Methode ist der sogenannte Body Force Ansatz. Dieser Ansatz konnte in der Vergangenheit für diesen Anwendungsfall vielversprechende Ergebnisse, bei deutlich reduziertem Ressourcenbedarf, liefern (1–3)

Bei der Body Force Methode werden die diskreten Schaufeln einer Fan-Stufe durch ein Volumen ersetzt, in welchem die Schaufelkräfte als Quellterme den Impuls- und Energiegleichungen hinzugefügt werden, um so die gleichen umfangsgemittelten Daten zu erhalten. Hiermit ist somit eine Bewertung integraler Parameter, wie z. B. des Wirkungsgrades, des Fan-Druckverhältnisses und des Massenstroms möglich. Lokale Phänomene wie beispielsweise Nachläufe, Sekundärströmungen, etc. sind durch dieses Modell hingegen nicht abbildbar.

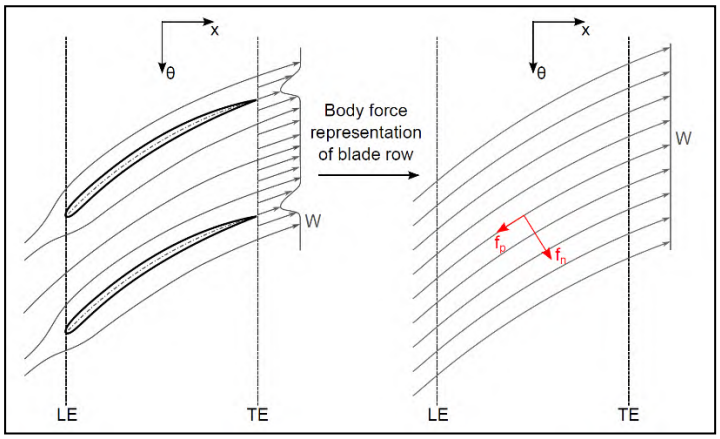

Abbildung 1: Prinzip der Body Force Methode aus (1)

Die notwendigen Eingabeparameter für ein Body Force Modell können entweder Single Passage RANS Rechnungen der Fan-Stufe sein oder aber lediglich die Geometrieparameter der Schaufel, z. B. der lokale Metallwinkel, die Dickenverteilung, etc. Die zweitgenannte Möglichkeit bietet den Vorteil, dass diese Parameter aus einer Auslegung heraus direkt verfügbar sind und somit für eine weitere Verwertung in einer mit dem Einlauf gekoppelten Betrachtung zur Verfügung stehen. Das Potenzial zur Einbindung der Body Force Methode in eine Optimierungskette sowohl für den Fan, als auch für den Triebwerkseinlauf ist somit vorhanden, um erste Abschätzungen bzgl. der Performance beider Komponenten unter diversen Betriebsbedingungen treffen zu können.

Um in Zukunft bessere Aussagen über die integralen Größen geben zu können, bedarf es der Berücksichtigung diverser Aspekte der Fan-Aerodynamik innerhalb des Body Force Modells. Dies ist zum einen die Berücksichtigung der durch die Schaufeln erzeugten Blockagewirkung, welche durch den Body Force Ansatz prinzipiell nicht berücksichtigt wird. Zum anderen werden Sekundäreffekte wie die Schaufelspitzenspaltströmung, oder der nabenseitige Eckenwirbel nicht inhärent vom Body Force Modell behandelt. Außerdem stellen die Betriebsbereichsgrenzen des Fan-Kennfeldes noch eine Herausforderung für den Body Force Ansatz dar.

Hinsichtlich der qualitativen und quantitativen Güte von Body Force Modellen, beschäftigt sich das Institut für Flugantriebe und Strömungsmaschinen (IFAS) aktuell mit der Weiterentwicklung dieser Ansätze. Das IFAS ist darüber hinaus in der Lage, mithilfe des Propulsorprüfstandes, in welchem die Fan-Einlauf-Interaktionen zukünftig experimentell untersucht werden sollen, eine direkte experimentelle Validierungsgrundlage der weiterentwickelten Body Force Ansätze zu bieten.

Die Ansätze zur Weiterentwicklung und erste numerische Validierungen des hier angewandten Body Force Modells, sollen im Rahmen des vollständigen Manuskripts diskutiert werden.

Literatur

1. Peters A. Ultra-Short Nacelles for Low Fan Pressure Ratio Propulsors [Dissertationsschrift]. Cambridge: Massachusetts Institute of Technology; 2014.
2. Hall DK, Greitzer EM, Tan CS. Analysis of Fan Stage Conceptual Design Attributes for Boundary Layer Ingestion. Journal of Turbomachinery 2017; 139(7):74.
3. Thollet W. Body Force Modeling of Fan-Airframe Interactions [Dissertationsschrift]. Toulouse, France: ISAE-SUPAERO; 2017.

Mitteilung

Fachgruppe: Numerische Aerodynamik

Parametric Surrogate Modelling of Integral Aerodynamic Force Coefficients for a Transonic Transport Aircraft Wing

Mauricio M. Jentys, Chrstian Breitsamter
Chair of Aerodynamics and Fluid Mechanics, Technical University of Munich
Boltzmannstraße 15, 85748 Garching b. München, mauricio.jentys@tum.de

Introduction

Within the LuFo VI-1 project CATeW (Coupled Aerodynamic Technologies for Aircraft Wings), the potential for aerodynamic drag reduction through a synergetic application of a variable camber (VC) and a hybrid laminar flow control (HLFC) system to the wing of a mid-range transonic transport aircraft is investigated.
The project consortium consists of two partners, which use tools of different fidelity levels for the investigations. The „low-fidelity“ (LowFi) aspect is covered by the Institute of Aerospace Systems (ILR) of RWTH Aachen University, performing using the overall aircraft design toolchain MICADO, which features a number of implementations for aerodynamic modelling of the technology coupling [1]. The „high-fidelity“ (HiFi) complement is provided by the Chair of Aerodynamics and Fluid Mechanics (AER) of the Technical University of Munich, performing aerodynamic analyses in the context of computational fluid dynamics (CFD). As for MICADO, different extensions for modelling of the technology coupling in the context of CFD computations have been implemented at AER in the course of CATeW [2].
A major goal of the project is to couple the analyses on both fidelity levels, namely by introducing results of HiFi CFD analyses into MICADO in a computationally effective manner through surrogate models or model order reduction, respectively. The latter requirement arises due to the structure of the OAD toolchain’s aerodynamic module, querying for parametrized aerodynamic results (essentially the drag coefficient C_D) in a near real-time manner.
For introduction of HiFi results into the aerodynamic module of MICADO, potential surrogate output of different abstraction levels has been derived, in line with the module’s code structure. With decreasing abstraction level, these encompass introduction of:

A: Total wing drag coefficients C_D, covering all aerodynamic (interaction) effects (see Figure 1) of the technology coupling into one scalar output and circumventing the application of the aerodynamic module within MICADO

B: Reconstruction of surface pressure or skin friction coefficient distributions, partially replacing computation steps in MICADO’s aerodynamic module and enhancing the modules’ fidelity with HiFi data

While approach B additionally offers the opportunity for calibration or derivation of correction factors of LowFi-routines and conservation of the structure of MICADO’s aerodynamic module, the contribution at hand aims at assessing possibilities and presenting results for surrogate architectures complying with category A.

Methodology

The different input parameters and their corresponding ranges for the envisaged surrogate model for prediction of the wing’s aerodynamic drag coefficient are summarized in Table 1.

Table 1: Designated parameter set to be covered by the surrogate model

Parameter			Range
Lift Coefficient	C_L	[-]	[0.4; 0.6]
Height	h	[ft]	[33000; 39000]
ADHF Deflection Angle	δ_{ADHF}	[°]	[-2; 4]
Suction Coefficient	C_q	[-]	$-12 \cdot 10^{-4}$
Mach Number	Ma	[-]	0.83

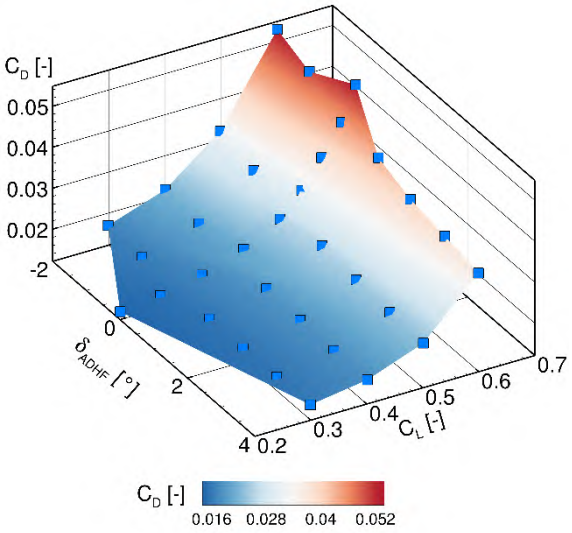

Figure 1: C_D characteristic for preliminary CFD computations to be expanded by the surrogate for higher dimensional parameterspaces

For the construction of the surrogate, machine learning approaches from the domain of kernel based methods, namely application of Gaussian process regression is envisaged [3]. These approaches are characterized by their beneficial regression properties for sparse data-sets and provide for a simple possibility of introduction of adaptive sampling strategies [4] due to their inherent formulation allowing for a quantification of the most uncertain parameter combinations. Additionally, models of this domain are chosen due to their computational efficiency, given the relatively low number of input dimensions and their beneficial scaling properties with respect to problem complexity [5]. Furthermore, surrogates built via Gaussian process regression possess the capability of inclusion of datasets from different sources, enabling construction of a Multi-Fidelity model via inclusion of computationally inexpensive LowFi data.
Lastly, the implementations and characteristics derived from the models serve as prerequisite for surrogate models within the approach denoted as B previously, when being connected for instance to a dimensionality reduction technique as the proper orthogonal decomposition.

Acknowledgments

Funding of the investigations within the LuFo VI-1 project CATeW (Coupled Aerodynamic Technologies for Aircraft Wings, FKZ : 20E1917B) by the German Federal Ministry for Economic Affairs and Climate Action (BMWK) is gratefully acknowledged.

References

[1] T. Effing, V. Schmitz, F. Schültke, F. Peter und E. Stumpf, „Combined Application of Hybrid Laminar Flow Control and Variable Camber in Preliminary Aircraft Design," in *33rd Congress of the International Council of the Aeronautical Sciences*, Stockholm, Sweden, 04.-09.09.2022.

[2] M. Jentys und C. Breitsamter, „Transitional Flow Modelling of a Hybrid Laminar Flow Control and Variable Camber Transonic Transport Aircraft Wing," in *33rd Congress of the International Council of the Aeronautical Sciences*, Stockholm, Sweden, 04.-09.09.2022.

[3] C. E. Rasmussen und C. K. I. Williams, Gaussian Processes for Machine Learning, Cambridge, MA: MIT Press, 1006.

[4] N. Karcher und T. Franz, „Adaptive sampling strategies for reduced-order modeling," *CEAS Aeronautical Journal,* Bd. 13, Nr. 2, pp. 487-502, 2022.

[5] S. Schuet, C. Malpica und J. Aires, „A Gaussian Process Enhancement to Linear Parameter Varying Models," in *AIAA Aviation 2021 Forum*, 2021.

Mitteilung

Fachgruppe: Numerische Aerodynamik

Development of a Coupled Implicit Incompressible Flow Solver

Deepak Kunhappan, Johannes Löwe
DLR, Institut für Aerodynamik und Strömungstechnik,
Bunsenstraße 10, 37073 Göttingen, deepak.kunhappan@dlr.de

Introduction

The discretization of the incompressible Navier-Stokes equations leads to a saddle-point problem in which the discrete equations for the pressure and momentum are decoupled. Traditionally, this decoupling is solved by segregated methods in which separate equations for momentum and pressure are solved with the constraint of obtaining a divergence free velocity field. In the coupled approach a single block system of equations for the momentum and pressure is formulated and solved simultaneously. Furthermore, solving such a coupled system has been shown to improve robustness and convergence properties [1]. In the present work, a coupled approach for solving the incompressible Navier-Stokes and RANS equations have been developed in the finite volume framework of the CFD software CODA. The implementation is verified and validated with various test cases.

Conducted Work and Results

Thanks to the modern software design of CODA, the incompressible solver re-uses the existing finite volume framework originally designed for compressible solver with minimal modifications, this includes the reconstruction schemes, time discretization schemes and the turbulence models. Developments specific to the incompressible solver include implementation of upwind and central differencing convection schemes. A pressure-stabilization scheme inspired from Rhie and Chow [2] and SUPG/PSPG stabilization scheme [3] was implemented in order to overcome the issue of pressure checkerboarding. Appropriate boundary conditions required for the incompressible solver were also implemented. The Spalart-Allmaras negative (SA-neg) and the SST2003 turbulence models from the compressible solver was interfaced with the incompressible solver. Several test cases were run in order to validate and benchmark the turbulence models.
As a first test case, simulations of the two-dimensional flow over the backward facing step [4] (2D BFS) at Re = 36000 using the SA-neg model were performed. Figure 1 shows the comparison of the obtained results with the experimental data Driver & Seegermiller and NASA's CFL3D code.
Reasonable agreement in the skin friction coefficient (Fig 1a), pressure coefficient (Fig 1b) and the velocity profile (Fig 1c) has been observed.

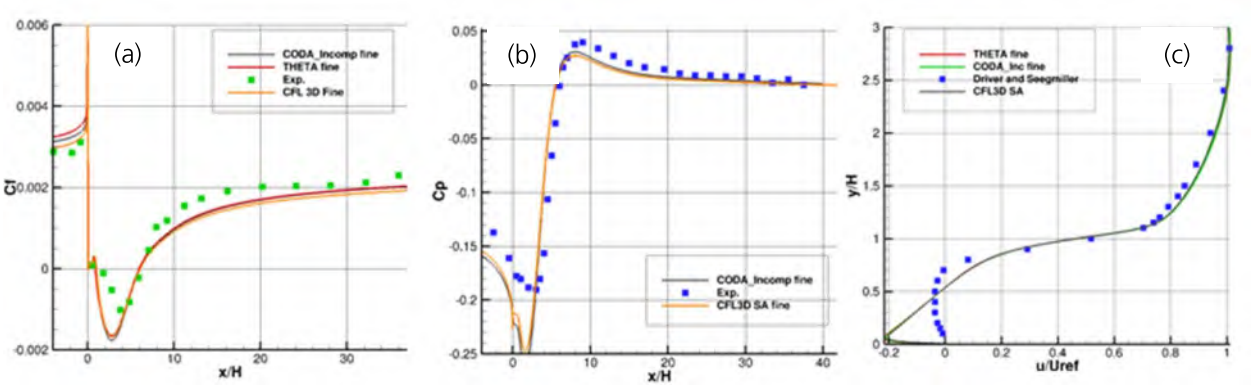

Fig. 1 : Validation of the SA-neg turbulence model, 2D BFS case. (a) skin friction profile, (b) pressure coefficient profile, (c) velocity profile at x/h = 1

For the validation of the SST-2003 turbulence model with the incompressible solver, computations on the turbulent flow over a 2D flat plate [5] (2DZPG) at Re = 5 x 10^6 were performed. Figure 2 shows the skin friction obtained for various grid resolutions, the results are in good agreement with the results obtained from CFL3D and FUN3D.
Figure 3 demonstrates the application of the incompressible flow solver for external aerodynamic

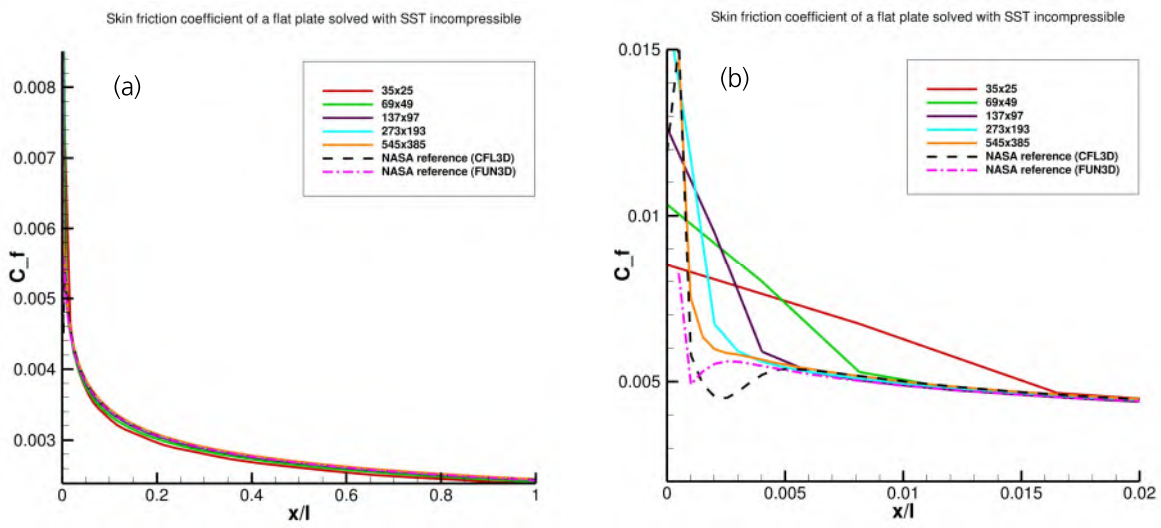

Fig. 2 : Validation of the SST-2003 turbulence model, 2DZPG case. (a) skin friction profile, (b) skin friction profile at leading edge.

flows, both the turbulence models : SA-neg and SST-2003 were used to perform the computations. The figure shows the contours of the velocity flow-field (a. SA-neg, b. SST-2003) and pressure coefficient (c) and skin friction coefficient (d) for the flow over the DLR-F15 three element airfoil at Re ~ 2 x 10^6 at 6^o AoA. The results are in agreement with the DLR TAU code when using the same model.

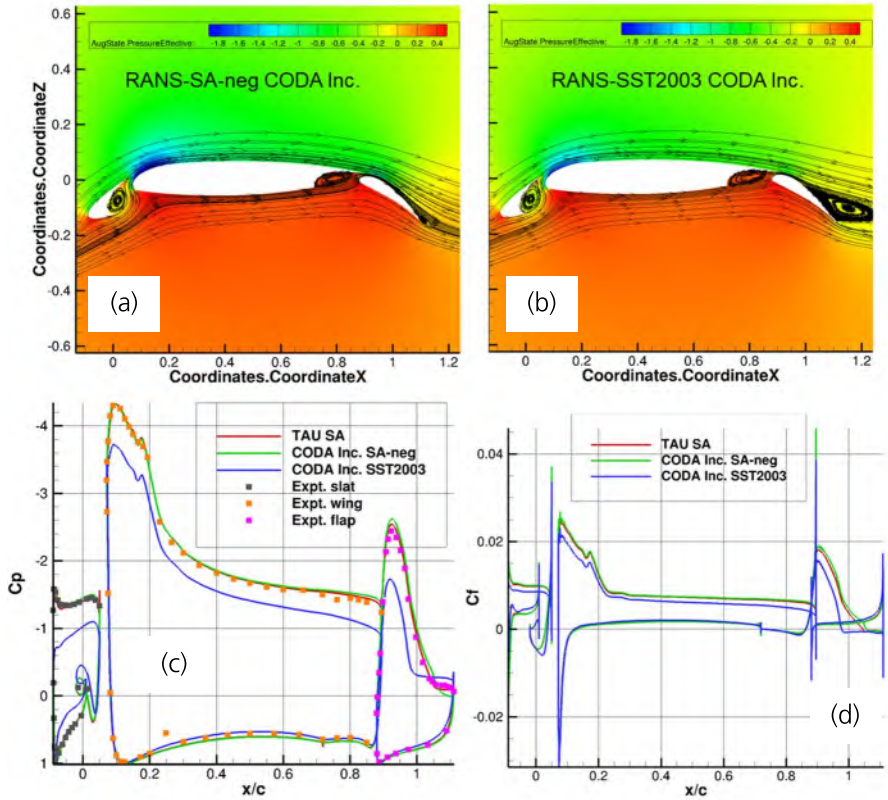

Fig. 3 : Flow around 3 element DLR F-15 airfoil. Velocity contours + streamlines : (a) SA-neg, (b) SST-2003. (c) Pressure coefficient profile. (d) Skin friction coefficient profile.

The final paper will also present validation studies with a 3D geometry (e.g. Ahmed Body), as well as performance investigations of the coupled incompressible solver (compared to existing solvers) including the effect of preconditioning by a linear multigrid method on the linear solver efficiency.

[1] Darwish, M., Sraj, I., & Moukalled, F. (2009). A coupled finite volume solver for the solution of incompressible flows on unstructured grids. Journal of Computational Physics, 228(1), 180-201.

[2] Rhie, C. M., & Chow, W. L. (1983). Numerical study of the turbulent flow past an airfoil with trailing edge separation. AIAA journal, 21(11), 1525-1532.

[3] Lube, G. (2006). Stabilized FEM for incompressible flow. Critical review and new trends. ECCOMAS CFD 2006: Proceedings of the European Conference on Computational Fluid Dynamics

[4] https://turbmodels.larc.nasa.gov/backstep_val.html

[5] https://turbmodels.larc.nasa.gov/flatplate.html

Mitteilung

Fachgruppe: Numerische Aerodynamik

An analytical view on data-driven turbulence modeling and a realization via a regularized Newton method

Stefan Langer
Institute of Aerodynamics and Flow Technology, DLR (German Aerospace Center)
Lilienthalplatz 7, 38108 Braunschweig,
stefan.langer@dlr.de

Formally, the RANS equations for a linear turbulence model differ from the Navier-Stokes equations by the additional unknown eddy viscosity μ_t. For closure, a turbulence model given by an additional set of equations is used to determine μ_t, such that

1. a steady-state solution of the RANS equations exists and it is unique,
2. this steady-state solution represents important features compared to a solution of the original Navier-Stokes equations,
3. it is possible to compute numerically an approximation to this steady-state solution.

To adapt a given turbulence model for one or several flow cases, a Field Inversion and Machine Learning (FIML) approach can be leveraged to obtain a closed-form correction for the given turbulence model to improve the predictions. For example, for the Spalart-Allmaras turbulence model the main idea, which can be found in the literature, is, to manipulate a field parameter weighting the production term in the turbulence model. Such an approach has been applied successfully for several examples (see for example [2]).

To approximate this field parameter using the FIML ansatz different approaches and regularization techniques are proposed. In order to clarify basic properties of this approach, in this work, instead of trying to modify a given turbulence model, we directly try to reconstruct an eddy viscosity field from given data. To do so, we consider the eddy viscosity field as a parameter in the RANS equations, which needs to be identified, such that the criteria mentioned above are satisfied. Formally, the problem is formulated as follows:
We consider $\mathbf{R}$ to be the residual operator corresponding to the set of equations for a boundary value problem for the RANS equations, μ_t is the field parameter of interest and $\mathbf{W}$ a state vector. Then these are linked via the equation $\mathbf{R(W;\ \mu_t) = 0.}$ The solution of this state equation for a given, fixed parameter μ_t can be interpreted as the direct problem.

For the inverse problem, we are not interested in solving the state equation for a given parameter, but instead, to determine the field parameter μ_t with respect to observed data related to a given state $\mathbf{W} = \mathbf{W}(\mu_t)$. This observation operator could be, for example either the identity (distributed measurement), or a trace operator to boundary values of the solution (boundary measurements). In CFD, these are often the C_p-distribution on the surface of the geometry and / or the skin friction coefficient C_f on the surface of the geometry. Such viewpoint is for example discussed in [1].

In this work, to have a sufficient amount of data, we consider a distributed measurement. To avoid an inverse crime, the data is generated from a finer mesh and then projected. That is, the complete field state $\mathbf{W}(\mu_t^{ref})$ is given, and μ_t^{ref} is the field parameter to be reconstructed.

We will show, in which way under these conditions this parameter identification problem for the eddy viscosity μ_t can be written as an equation $\mathbf{F}(\mu_t) = \mathbf{y}$, and $\mathbf{y}$ represents the given data, for example the C_p- and C_f-distributions or the distributed measurement $\mathbf{W}(\mu_t^{ref})$. The operator $\mathbf{F}$ will be explicitly stated.

It is shown by a numerical example that the operator equation $\mathbf{F(\mu_t) = y}$ may represent a severely ill-posed problem. As a confirmation, in Figure 1 the singular values of the linearized equation are shown, and they exhibit decay at an exponential rate. As a conclusion, the problem to reconstruct an eddy viscosity formulated as a parameter identification for the RANS equations, can be severely ill-posed. Since the operator **F** involves the solution of the RANS equations, heuristic arguments are given that this assertion may hold in general, also for the FIML approach. Moreover, it is shown that this general approach presented carries over to the FIML method.

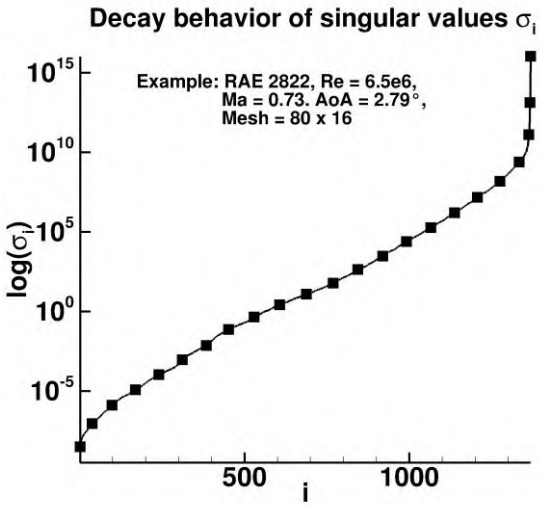

Figure 1: Decay behavior of singular values

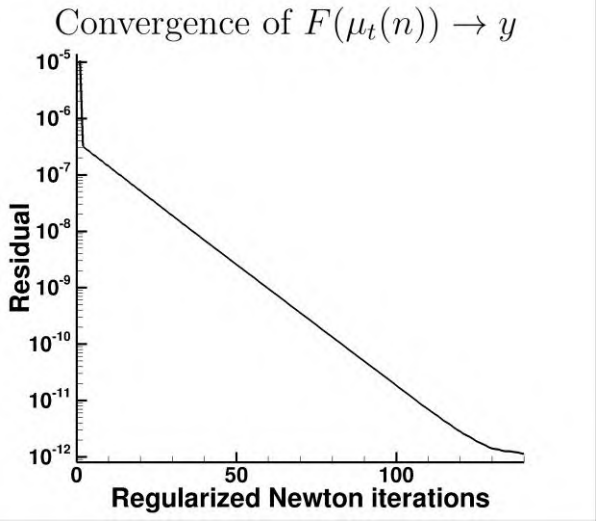

Figure 2: Convergence of eddy viscosity

To further demonstrate the ill-posed character of the problem, an example is shown that two different eddy viscosity fields yield almost exactly the same C_p and C_f-distributions of an airfoil. As a consequence, for this example the eddy viscosity is not determined uniquely by surface data.

To approximate a solution of the equation $\mathbf{F(\mu_t) = y}$, an algorithm based on a regularized Newton's method is proposed. First, very simple numerical results are shown as a "proof of concept" that the basic idea can be implemented and an eddy viscosity can be determined by providing enough data. A corresponding convergence history is shown in Figure 2.

Finally, as an outlook the following question is discussed: Given a sufficient amount of data, in which way can one learn an eddy viscosity field that is valid for more than one example?

.

Bibliography

[1] Stefan Langer and R.C. Swanson, On Boundary-Value Problems for RANS Equations and Two-Equation Turbulence Models, Journal of Scientific Computing, 2020, 85:20

[2] Florian Jäckel, A Closed-form Correction for the Spalart-Allmaras Turbulence model for Separated Flows, AIAA 2022-0462, https://doi.org/10.2514/6.2022-0462, 2022

Mitteilung

Fachgruppe: Numerische Aerodynamik

Comparison and unification of finite-volume discretization strategies
for the unstructured node-centered and cell-centered grid metric in TAU and CODA

Stefan Langer, Axel Schwöppe, Tobias Leicht
Institute of Aerodynamics and Flow Technology, DLR (German Aerospace Center)
Lilienthalplatz 7, 38108 Braunschweig,
stefan.langer@dlr.de, axel.schwoeppe@dlr.de, tobias.leicht@dlr.de

Numerical simulation is a key technology for designing aircraft in industry. To accurately predict aerodynamic properties of an aircraft the Euler and Reynolds averaged Navier-Stokes (RANS) equations are in focus. The effort for these high-precision calculations is very high and still increases, in particular with regard to the further growing complexity of the tasks to be solved. In addition, the further use of the data obtained in connection with other disciplines is becoming increasingly important. It is therefore of great practical importance to provide a software that determines a sufficiently accurate numerical solution of the underlying equations corresponding to the needs of other disciplines with the smallest possible computational effort. This interaction of Computational Fluid Dynamics (CFD) with other disciplines and the affordability of such an overall system are an important prerequisite for success of the numerical simulation applied in aircraft industry.

2nd order finite-volume discretization schemes generally offer a good compromise between computational effort and accuracy. The use of higher-order discretizations for the RANS equations is often regarded as excessively expensive, since the modelling error introduced by the turbulence model generally dominates the (low) numerical error of these discretizations, while the design order of a method is rarely achieved in practice, due to both the properties of the chosen discretization and the character of the underlying solution.
It is well-known that the accuracy of an approximate solution obtained by a 2nd order finite-volume scheme depends significantly on the discretization applied to the underlying grid. Therefore, the discretization has to be adapted to the chosen grid metric, including the types of elements present in the mesh. This is of no surprise, since the integral operators are discretized using geometrical data from the grid, for example cell-centers and normal vectors. Looking at the history of CFD, structured discretization methods exploited and still exploit these properties to achieve good accuracy on structured grids with little effort. While this is sufficient for many applications, e.g. 2-D airfoils or wings in 3-D, it is difficult to fulfill industrial needs for automatic grid generation of complex geometries, such as a complete helicopter or the landing gear of an aircraft.
Hence, unstructured meshes allowing the use of additional types of elements such as triangles, tetrahedra, pyramids and prisms are of high interest, and corresponding mesh generators with a high level of automation are meanwhile established. Unfortunately, it has often been observed, that for high Reynolds number turbulent flows, the accuracy of solutions obtained on these mixed-element grids using unstructured discretization schemes was not satisfactory. As a necessity, it is clear that in regions of the grid, where steep gradients need to be resolved (such as the boundary layers around a body), quadrilateral, hexahedral or prismatic elements with an extreme cell-stretching are required, to keep the number of degrees of freedom acceptable. As a result, one is now forced to develop unstructured discretizations that reliably produce accurate solutions for mixed grids with elements of high anisotropies.

In this work we review and demonstrate in which way these anisotropies can be meaningfully incorporated into the discretization scheme for unstructured grids in order to achieve good quality solutions. This is particularly true for the convection part of the equations.

Therefore, in this work we restrict ourselves to the Euler equations. This consideration is important, to separate effects on accuracy arising from the discretization of the full RANS equations from effects coming only from the inviscid part, if the source of inaccuracies in the solution is related to the discretization of the convection terms.
To this end, we present results of solutions to the Euler equations on meshes that are actually designed for solutions of the RANS equations and high Reynolds number turbulent flows. Total pressure losses are shown as a measure of accuracy in order to illustrate the influence of extreme cell-stretching. The behavior of different upwind and central schemes, some of which contain terms that take cell-stretching into account, is investigated. The baseline investigated discretization schemes are the Roe-scheme and the central scheme with matrix valued artificial dissipation.
In addition, we carry out our considerations for two different grid metrics. On the one hand, we consider a node-centered (sometimes called cell-vertex) dual grid metric, and on the other hand a cell-centered primary grid metric. It is further demonstrated in which way this choice of metric may influence the selection of a gradient computation to obtain accurate results.

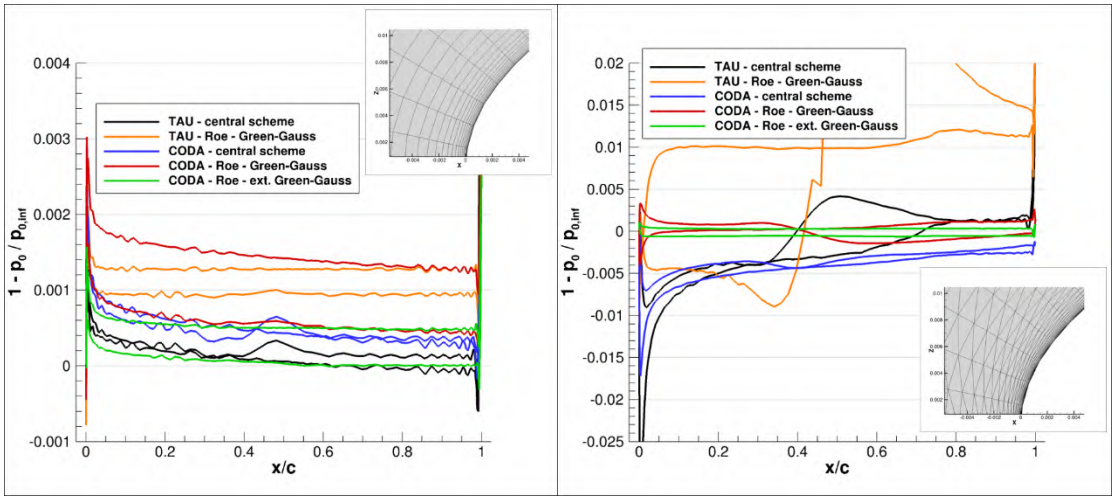

Figure 1: RAE2822 subsonic Euler - Comparison of total pressure losses of different discretizations on a structured and an unstructured grid

Numerical examples for both 2-D and 3-D will be shown in the full paper to demonstrate the different levels of accuracy of the different discretization schemes. The results are computed using the legacy finite-volume software TAU [1] based on a node-centered grid metric, and the newly developed software CODA [2] using its finite-volume scheme based on a cell-centered grid metric. Exemplarily, Fig.1 shows total pressure losses for 2nd order designed Roe- and matrix-valued artificial dissipation discretizations based on a cell-centered (CODA) and a node-centered (TAU) grid metric. The left picture of Fig.1 plots results obtained on a structured grid with highly stretched quadrilaterals resolving the boundary layer. The right picture plots the results obtained on an unstructured grid where the quadrilaterals of the structured grid are divided into triangles. The distinct differences in total pressure losses between the different discretizations suggest that the choice of the discretization of the convective terms has significant impact on the accuracy of the overall solution, in particular on grids with highly-stretched elements.

Bibliography

[1] Stefan Langer, Axel Schwöppe, and Norbert Kroll, The DLR Flow Solver TAU - Status and Recent Algorithmic Developments, In Proc. 52nd Aerospace Sciences Meeting, January 2014, number 2014-0080 in Conference Proceeding Series. AIAA, 2014.

[2] Leicht, T. el al.: DLR-Project Digital-X – Next Generation CFD Solver ‚Flucs'. Deutscher Luft- und Raumfahrtkongress 13-15 Sept, 2016, Braunschweig, Germany, 2016

Mitteilung

Fachgruppe: Numerische Aerodynamik

Deformation von CFD-Netzen mit anisotropen Zellen in der viskosen Randschicht mithilfe von Linien-impliziten Verfahren

Arne Rempke
Deutsches Zentrum für Luft- und Raumfahrt, Institut für Softwaremethoden zur Produktvirtualisierung, Zwickauer Straße 46, 01069 Dresden, arne.rempke@dlr.de

Verschiedene Verfahren zur numerischen Strömungssimulation (computational fluid dynamics, CFD) wie etwa die Finite Volumen Methode (FVM) oder Discontinuous Galerkin (DG) Verfahren basieren auf Simulationsnetzen der zu untersuchenden Geometrie. Um physikalische Phänomene wie etwa starke Gradienten einer turbulenten Strömung im Randbereich sinnvoll auflösen zu können, kommen häufig Netze zum Einsatz, die in dieser Randschicht besonders anisotrope Zellen enthalten. Diese Gitterzellen charakterisieren sich durch eine besonders kleine Länge in Wandnormalenrichtung bei gleichzeit großer Länge in Wandtangentialenrichtung. Das Verhältnis der Seitenlängen solcher anisotropen Zellen kann, je nach konkreter Strömungssituation, ein Verhältnis von mehr als 1000:1 betragen, siehe Abb.1(a). Das Generieren entsprechender Netze für die CFD ist eine anspruchsvolle Aufgabe, für die häufig spezielle Gittergeneratoren zum Einsatz kommen.
Bei einer multidisziplinären Simulation wird die Simulation der Aerodynamik mit anderen Disziplinen gekoppelt, etwa der Strukturmechanik oder der Flugmechanik. Diese Interakion beinhaltet eine Rückkopplung, bei der die Ausgangsgeometrie des Flugkörpers verändert wird, etwa das elastische Durchbiegen eines Flügels durch auf ihn wirkende Lasten oder das Ausschlagen einer Klappe. Bei einer multidisziplinären Optimierung kann sich die Geometrie zusätzlich noch verändern, weil z.B. nach einem verbesserten Flügelprofil gesucht wird. Um mit dieser veränderten Geometrie weitere Strömungssimulationen durchführen zu können, ist eine etablierte Technik die Anpassung des ursprünglichen Berechnungsnetzes an die neue Geometrie durch Netzdeformation. Dabei sollten die Charakteristiken des Netzes, wie etwa die oben beschriebene besondere Randschicht, möglichst gut erhalten bleiben.
Eine verbreitete Methode zur Netzdeformation von CFD-Netzen ist die Elastizitätsanalogie (EA) [3,7], die im Kern die lineare partielle Differentialgleichung zur elastischen Verformung des Berechnungsnetzes löst. Bei ihrer Anwendung werden die Verschiebungen der Randknoten as Randbedingungen vorgegeben und nach den dazu passenden Verschiebungen der inneren Gitterknoten gelöst. Die Differentialgleichung wird dabei auf dem Berechnungsgitter diskretisiert, denn für jeden dieser Knoten ist eine Deformation gesucht. Das bedeutet, dass auch die numerischen Eigenschaften der anisotropen Zellen übernommen werden. Bei besonders anisotropen Zellen kann es dazu führen, dass die numerische Lösung des Gleichungssystems sehr schwer wird.
Diese numerischen Schwierigkeiten bei Berechnungen auf stark anisotropen Zellen sind bereits aus der CFD bekannt. Hier gibt es spezielle Lösungsverfahren, die linien-impliziten Methoden, die stabilisierend auf diese Umstände wirken. Sie wurden bereits erfolgreich in verschiedenen numerischen Verfahren (FVM, DG, FEM) für Navier-Stokes- oder Euler-Gleichungen angewendet [1,2,4,5,6]. Dennoch gibt es wesentliche Unterschiede zwischen der CFD und der EA, etwa die konvektiven Anteile der Strömungsgleichungen oder die volumen- bzw. knotenzentrierte Freiheitsgrade und dadurch veränderte Konnektivität, die sich auch wesentlich auf eine Verwendung der linien-impliziten Methode bzw. der zugehörigen Liniensuche auswirken.
Im vorliegenden Beitrag wird die Anwendung der linien-impliziten Methoden auf die lineare Elastizitätsanalogie demonstriert, siehe Abb. 1(a)-(d). Es wird gezeigt, mit welchen Modifikationen der Übergang gelingt, und welche Ergebnisse durch die Anwendung erzielt werden können. Es stellt sich heraus, dass die Anwendung wesentliche Verbesserungen für die Stabilität des Lösers bringt und bisher divergierende Probleme nun gelöst werden können. In

anderen Fällen kann die Simulation signifikant beschleunigt werden. Die Untersuchungen werden anhand von verschiedenen 2d und 3d-Netzen demonstriert.

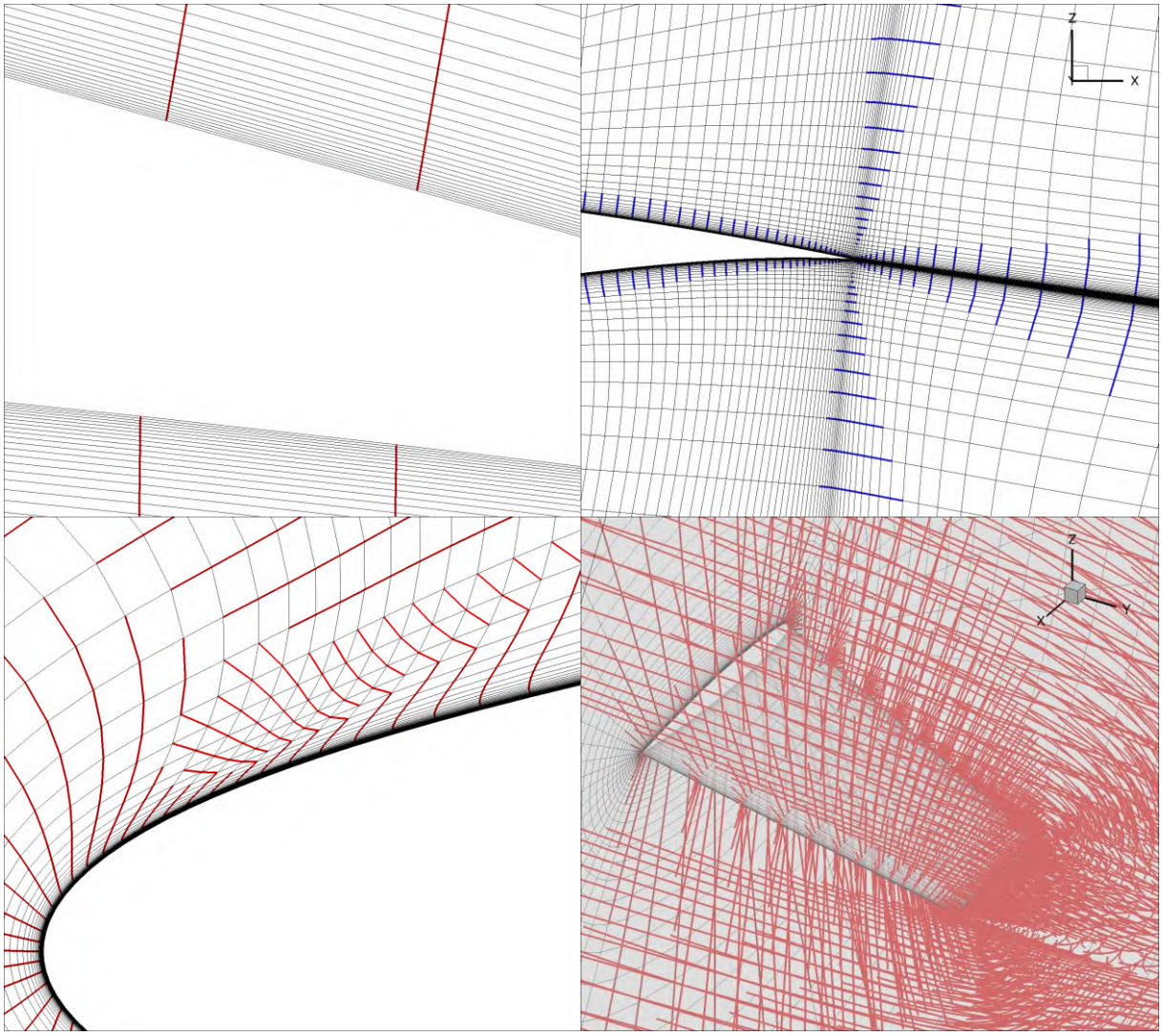

Abb.1: (a) Typische Zellen mit großem Seitenverhältnis in der CFD-Randschicht (b) Linien in Netzbereichen mit Zellen hoher Anisotropie (c) Detailansicht mit sowohl isotropen und aniisotropen Zellen, deren Knoten allesamt zu Linien zusammengefasst wurden (d) Linien in einem 3d Netz des Onera M6 Flügels

Literatur

[1] Mavriplis, D. J.: Multigrid strategies for viscous flow solvers on anisotropic unstructured meshes. In: Journal of Computational Physics 145 (1998), pp. 141–165.
[2] Okusanya, T. O.: Algebraic Multigrid for Stabilized Finite Element Discretizations of the Navier-Stokes Equations. PhD dissertation, M.I.T., Department of Aeronautics and Astronautics, 2002.
[3] Stein, K., Tezduyar, T., Benney, R.: Mesh Moving Techniques for Fluid-Structure Interactions with Large Displacements. In: Journal of Applied Mechanics 70:1 (2003), pp. 58-63.
[4] Fidkowski, K. J: A High-Order Discontinuous Galerkin Multigrid Solver for Aerodynamic Applications. Master's thesis, Massachusetts Institute of Technology, 2004
[5] Eliasson, P., Weinerfelt, P., Nordström, J.: Application of a line-implicit scheme on stretched unstructured grids. In: Proc. 47th AIAA Aerospace Sciences Meeting, 2009.
[6] Langer, S.: Application of a line implicit method to fully coupled system of equations for turbulent flow problems. In: International Journal of Computational Fluid Dynamic 27:3 (2013), pp. 131–150
[7] Rempke, A.: Netzdeformation mit Elastizitätsanalogie in multidisziplinärer FlowSimulator-Umgebung. In: Jahresbericht 2016 zum 20. DGLR-Fach-Symposium der STAB (2016)

Mitteilung

Fachgruppe: Numerische Aerodynamik

Numerical Simulation of Vortex-Dominated Flows Using Advanced Physical Models

V. Togiti
DLR-Institute of Aerodynamics and Flow Technology
Department: $C^2A^2S^2E$, Braunschweig
vamshi.togiti@dlr.de

Introduction

Significant enhancements in computational fluid dynamics (CFD) have led to the use of numerical simulation in the design process of both civil and military aircraft, especially for nominal cruise performance where flows are generally characterized by attached flows. However, military vehicles routinely operate well outside of the steady, attached flow regimes often dominated by separated vortex flows. State-of-the-art CFD methods lack the ability to predict onset and progression of separated vortex-dominated flows, especially from smooth surfaces. Investigations carried out in several AVT task groups of the NATO Science and Technology Organization (STO) [1] indicate that the shortcomings for these predictions mainly stem from deficiencies of the models of turbulence. In most numerical investigations for slender wings with low sweep angle and blunt leading edges [2] linear eddy-viscosity turbulence models are employed. These models tend to deliver acceptable predictions at moderate incidence angles. However, at higher incidence angles, force coefficients and pitching moments were observed to be off compared to experiments. Due to this, in this work advanced turbulence models such as a full differential Reynolds stress model (RSM) and Scale-resolving simulations (SRS) are employed and their capabilities for the prediction of vortex separated flows are discussed.

As the objective is to demonstrate the capabilities of RSM and SRS methods for vortex separated flows, the predictions are compared to the experimental data and to the predictions delivered by the SA eddy-viscosity turbulence model coupled with rotational correction (RC) [3] and the Quadratic Constitutive Relation (QCR) [4]. In the present investigations, the SSG/LRR-ln(ω) [5] Reynolds stress model is employed. Concerning the SRS, the delayed-detached eddy simulation [6] coupled with RC and QCR is applied.

Results

In this study, the flow over a delta wing and a diamond wing with a round leading edge are investigated. For the delta wing, investigations are conducted at a freestream Reynolds number based on the mean aerodynamic chord (c_{mac}) of $3x10^6$ and Mach number of 0.4 and the incidence angle of 13.3° with a medium radius rounded leading edge of r/c_{mac} = 0.15%. While for the diamond wing, studies are conducted at a free stream Mach number of 0.15 and Reynolds number based on the mean aerodynamic chord of $2.7x10^6$ and the incidence angle range of 12°. At these conditions, both configurations demonstrate separation from smooth surface and subsequent vortex formation.

Predictions obtained using the RSM and the SA-RC-QCR and the SA-RC-QCR-DDES for the delta and diamond wing are shown in Figure 1. As it can be seen, for the delta wing, improved predictions with RSM compared to the other models can be observed. In this case, the RSM shows improvement with respect to the separation location and outer primary vortex strength by delivering almost similar experimental cp peak. While the SA-RC-QCR and SA-RC-QCR-DDES predict flow separation earlier than in the experiments, which lead to earlier formation of inner and outer primary vortices. In the case of diamond wing, the SA-RC-QCR-DDES delivers improved predictions by yielding experimental cp associated with the outer primary vortex. In this case, the RSM predicts the flow separation downstream of the experimental separation location and delivers a weaker vortex. The reasons for the improved performance of RSM and DDES for the delta wing and diamond, respectively, are discussed in detail in the

final paper. Additionally, the shortcomings and the challenges involved for advanced turbulence models in the prediction of vortex separated flows will be presented.

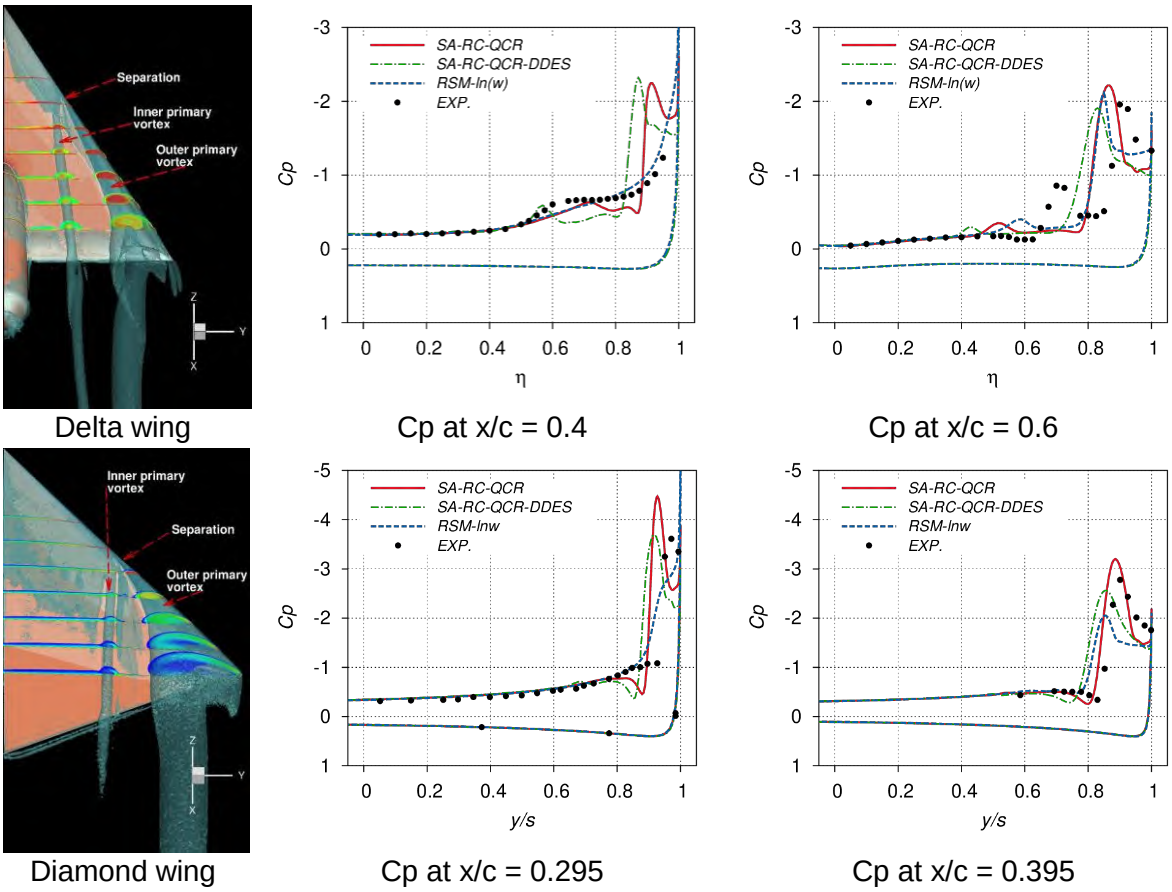

Figure 1. Comparison of sectional pressure distribution for delta and diamond wing.

References

[1] N. Frink, M. Tomac and A. and Rizzi, "Collaborative study of incipient separation on 53° swept diamond wing," *Aerospace Science and Technology,* vol. 57, pp. 76-89, 2016.

[2] M. Ghoreyshi, K. Ryszka, R. Cummings and A. Lofthouse, "Vortical flow prediction of a diamond wing with rounded leading edges," *AerospaceScienceandTechnology,* pp. vol. 57, pp. 103-117, 2016.

[3] M. L. Shur, M. K. Strelets, A. K. Travin and P. R. Spalart, "Turbulence Modeling in Rotating and Curved Channels: Assessing the Spalart-Shur Correction," *AIAA journal,* pp. Vol. 38, No. 5, pp. 784-792, 2000.

[4] M. Mani, D. A. Babcock, C. M. Winkler and P. R. and Spalart, "Predictions of a Supersonic Turbulent Flow in a Square Duct," in *AIAA Paper 2013-0860*, 2013.

[5] S. Braun, U. A., B. Eisfeld and E. Stumpf, "Numerical Simulation of Vortex Roll-Up Processes Using the SSG/LRR-w," *New Results in Numerical and Experimental Fluid Mechanics X Notes on Numerical Fluid Mechanics and Multidisciplinary Design ,* vol. 132, pp. 481-491, 2016.

[6] P. Spalart, S. Deck, M. Shur, K. Squires, M. K. Strelets and A. Travin, "A New Version of Detached-Eddy Simulation, Resistant to Ambiguous Grid Densities," *Theoretical and Computational Fluid Dynamic,* Vols. 0935-4964, pp. 181-195, July 2006.

Mitteilung

Fachgruppe: Numerische Aerodynamik

Instationäre Untersuchungen zur Flatterstabilität am Beispiel eines Nur-Flügel-Windkanalmodells

Guido Voß
Deutsches Zentrum für Luft- und Raumfahrt e.V.
Institut für Aeroelastik, Bunsenstraße 20, 37073 Göttingen
guido.voss@dlr.de

Im Rahmen des DLR-Projekts DIABOLO wurden umfangreiche Untersuchungen zur numerischen Modellierung von Windkanalmesskampagnen durchgeführt. Diese experimentellen Untersuchungen wurden in den DLR-Projekten FaUSST und MEPHISTO vorgenommen. Die Ergebnisse der Vorarbeiten zu den Untersuchungen sowie die Ergebnisse der Windkanalmessungen sind in mehreren Journalbeiträgen und in einer Dissertation veröffentlicht [1,2,3].

Bei dem Windkanalmodell handelt es sich um die IWEX-Geometrie (IWEX - Instationäres Wirbelexperiment), welche einen Ableger der bekannten DLR-F17/SACCON-Geometrie darstellt [1,2,3,4,5]. Mit Hilfe von RANS-CFD-Simulationsrechnungen sollen die Generalisierten Aerodynamischen Luftkräfte (GAF) für Flattern ermittelt werden [4]. Diese Rechnungen sind sehr aufwändig, da auf Grund der Strömungscharakteristik (Wirbel, Ablösungen) keine niederwertigen Verfahren wie beispielsweise DLM verwendet werden können.

Mit sogenannten instationären Pulsrechnungen werden die jeweiligen Eigenformen der Modellgeometrie angeregt. Mit dieser Methodik kann ein definierter Frequenzbereich abgedeckt werden, so dass es nicht notwendig ist, mit einer Vielzahl monofrequenter Anregungen die jeweiligen Systemantworten des Modells zu berechnen. Man erspart sich somit in erheblichem Ausmaß Rechenzeit.

Aus den Antwortsignalen jeder Pulsrechnung werden die Übertragungsfunktionen gebildet und in eine Matrix der Generalisierten Aerodynamischen Luftkräfte eingetragen, die wiederum als Eingabe für einen geeigneten Flatterlöser verwendet wird. Daraus werden die jeweils auftretenden Flattermechanismen berechnet, deren Ergebnisse in Form von Frequenz und Dämpfung in Abhängigkeit der Anströmgeschwindigkeit dargestellt werden.

Für diese Untersuchungen wurden zunächst eine Reihe von Testrechnungen durchgeführt, um einen geeigneten Satz von instationären Parametern zu finden, die einen guten Kompromiss hinsichtich Rechengenauigkeit und Rechenzeit darstellen. Diese Parameter sind die Zeitschrittweite *dt*, die Anzahl inner Iterationen pro Zeitschritt *N*, die maximale (reduzierte) Frequenz k_{max} sowie die Frequenzauflösung *dk*. Die Abwandlung einzelner Parameter im Vergleich zu Rechnungen mit Referenzparametern ist beispielhaft in unten stehender Abbildung aufgezeigt.

Daregstellt sind hier die komplexwertigen Diagonalelemente der GAF-Matrix in Realteil (grün) und Imaginärteil (rot). Variiert wird die Frequenzauflösung *dk*. Beim Referenzfall beträgt die Frequenzauflösung *dk* = 0.1, beim Vergleichsfall wird dieser Wert um den

Faktor 5 erhöht. Die Zeitschrittweite beträgt in beiden Fällen *dt* = 0.000089 s. Die Anzahl innerer Iterationen ist in beiden Fällen im Bereich des Pulses auf *N* = 4000 festgelegt um die Zeitschrittkonvergenz zu garantieren und wird im weiteren Verlauf (nach dem Puls) auf *N* = 400 zur Einsparung von Rechenzeit reduziert. Die gesamte Rechenzeit verringert sich dadurch im Vergleich zur Referenz um etwa neun Tage.

In dieser Abbildung zeigt sich eine gute Übereinstimmung beim Vergleich zwischen Referenzrechnung und Rechnung mit variiertem Parameter, so dass sich ein Hinweis ergibt, mit welchem Satz von instationären Parametern zukünftig gerechnet werden kann.

In dem Beitrag sollen die Ergebnisse weiterer Parametervariationen sowie die jeweilgen Auswirkungen auf das Flatterverhalten gezeigt werden.

[1] Wiggen, Stefan und Voß, Guido (2014) *Development of a wind tunnel experiment for vortex dominated flow at a pitching Lambda wing.* CEAS Aeronautical Journal, Seiten 1-10. Springer. doi: 10.1007/s13272-014-0121-4. ISSN 1869-5582

[2] Wiggen, Stefan und Voß, Guido (2014) *Vortical flow prediction for the design of a wind tunnel experiment with a pitching lambda wing.* CEAS Aeronautical Journal, Seiten 1-13. Springer. doi: 10.1007/s13272-014-0120-5. ISSN 1869-5582

[3] Wiggen, Stefan (2016) *Bewegungsinduzierte instationäre Luftkräfte bei wirbeldominierter Strömung.* DLR-Forschungsbericht. DLR-FB-2016-50. Dissertation. Technische Universität Braunschweig

[4] Voß, Guido und Schäfer, Dominik und Vidy, Cyrille (2018) *Investigation on flutter stability of the DLR-F19/SACCON configuration.* In: 36th AIAA Applied Aerodynamics Conference 2018. AIAA AVIATION Forum 2018, 25.-29. Jun. 2018, Atlanta, GA (USA). ISBN 978-162410559-3

[5] Voss, Guido (2021) *Numerical modelling of a wind tunnel experiment to investigate vortex-dominated flow at medium and high angles of attack.* In: 22nd STAB/DGLR Symposium on New Results in Numerical and Experimental Fluid Mechanics XIII. Springer International Publishing. STAB 2020 - 22. DGLR-Fachsymposium der STAB, Nov. 2020, Göttingen, Deutschland. ISBN 978-3-030-79560-3. ISSN 1612-2909

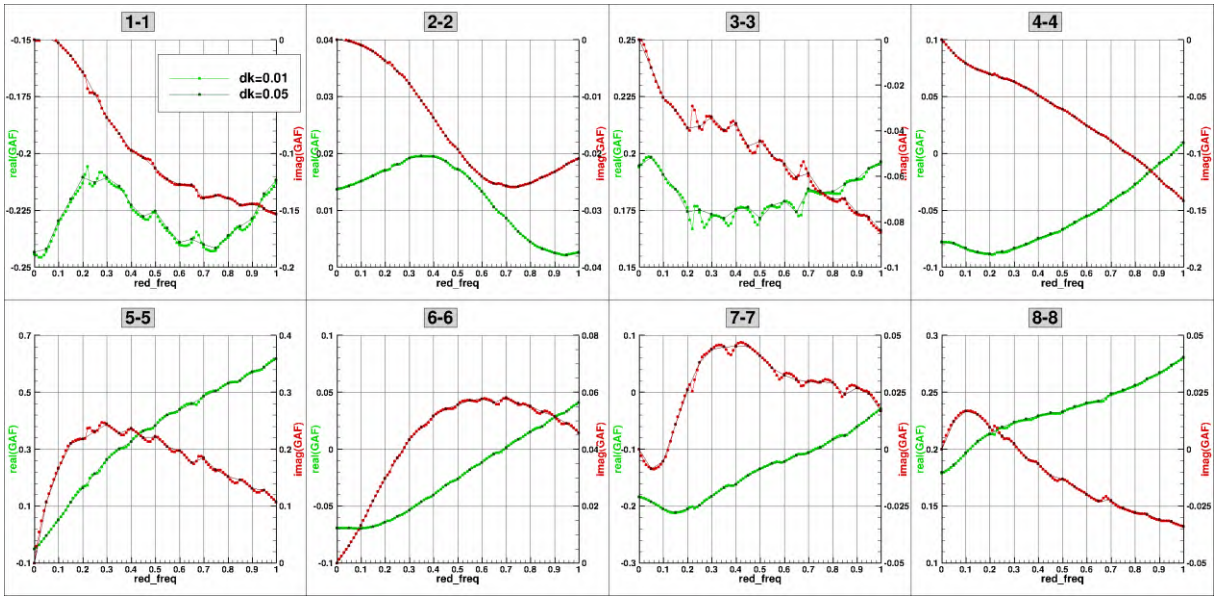

Abb. 1 : Vergleich zwischen Referenzrechnung (helle Farben) und Rechnung mit variiertem Parameter (dunkle Farben); gezeigt sind die Diagonalelemente der GAF-Matrix in Realteil (grün) und Imaginärteil (rot) unter Berücksichtigung von acht strukturellen Eigenformen

Mitteilung

Fachgruppe: Numerische Aerodynamik

Computational Assessment of the Aerodynamic Loading on the NGT-Cargo Vehicle

K. Weinman[1*], K. Ehrenfried[1]
[1]DLR Göttingen, Institute of Aerodynamics and Flow Technology
Bunsenstr. 10, 37073 Göttingen, Germany

.

The DLR NGT-Cargo concept is designed to increase the rail share of the European freight traffic market. High speed operations are a component of this concept for which a detailed understanding of the aerodynamic forces acting on a vehicle is needed. Computational Fluid Dynamics (CFD) provide an attractive tool for this purpose and the use of computational methods to assess aerodynamic loading on trains is recognized for full-scale or reduced model geometries. For example EN 14067-6 provides guidelines for CFD assessments at cross wind conditions using RANS (Reynolds-averaged Navier-Stokes) equations. A major challenge in satisfying these guidelines is due to the multi-scale nature of a flow characterized by a large range of energetically significant flow scales. This aspect challenges the numerical methods used in today's industrial environment.

Wind-tunnel measurements are being currently performed in the cross-wind facility *Seitenwindversuchsanlage* Göttingen (SWG) located at the DLR Göttingen. Inconjunction with these experiments a CFD study has been undertaken. This study, which is the subject of the paper, assesses the ability of CFD approaches to reproduce both the observed on-flow conditions as well as the aerodynamic drag of the vehicle. The CFD calculations shown in this work utilize the framework of the OpenFOAM computational library and use the Spalart-Allmaras turbulence model.

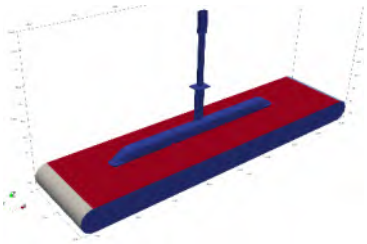

Fig. 1. The 1:25 scale model is mounted on a moving belt system which mimics the relative ground speed in the wind canal reference system.

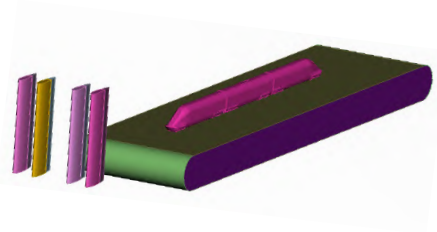

Fig. 2. An array of vertically mounted flaps which are used to generate controlled upstream flow disturbances (gusts).

Figure 1 illustrates the NGT-Cargo model mounted inside the wind-tunnel on a moving belt system to simulate ground effects. The model consists of the train head, the middle wagon section, and a rear section (the head section rotated by 180°). Upstream flow disturbances are generated by a set of oscillating flaps shown in figure 2. The use of this flap system allows an accurate control of unsteady onflow

gusts. Figure 3 provide an illustration of the flow-field about the model obtained by imposing periodic upstream oscillations through the flap system.

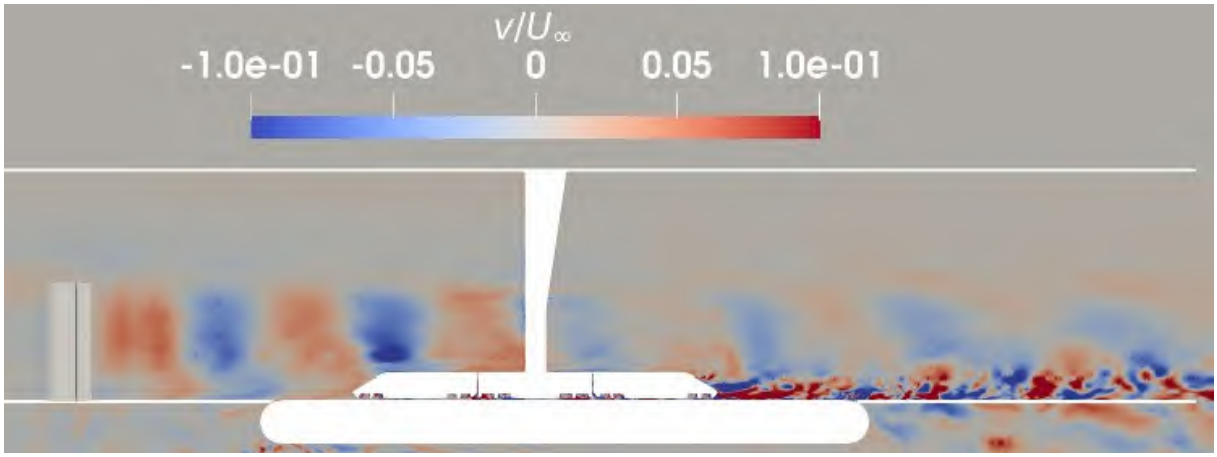

Fig. 3. Contour plot of the y velocity component on the symmetry plane (x-z) of the model. Flap oscillation amplitude/frequency is 3° / (0 0 30) Hz.

The aerodynamic forces acting on a train play a significant role in determining the operating costs for the vehicle. It is therefore of interest to study the development of the aerodynamic forces acting on the train under both steady and unsteady conditions. These and other details, including the frequency characteristics of the flow, will be overviewed in the paper, which will overview the methodology implemented and discuss the advantages/disadvantages of the CFD approach used.

Mitteilung

Fachgruppe: Numerische Aerodynamik

HyperCODA -- Towards high-performing time-resolving flow simulations

Johannes Wendler, Immo Huismann, Ronny Tschüter
German Aerospace Center (DLR),
Institute of Software Methods for Product Virtualization,
Dresden
Johannes.Wendler@DLR.de, Immo.Huismann@DLR.de, Ronny.Tschueter@dlr.de

Stefan Fechter
German Aerospace Center (DLR),
Institute of Aerodynamics and Flow Technology,
Göttingen
Stefan.Fechter@DLR.de

While steady-state RANS simulations are the state of the art for flow simulation in industry, they often mispredict the resulting flow patterns [1]. Scale-resolving and, to a lesser extent, time-resolving simulations offer a way out of the predicament at the expense of resources. Not only does the flow have to be resolved on a per-timestep basis, but low diffusivity is also required. This is where high-order methods can shine with their inherent low diffusivity.
Of the available high-order methods, the nodal discontinuous Galerkin spectral-element method (DG-SEM) offers speed and scalability while allowing for shock capturing and coupling with finite-volume methods [2, 3]. The speed results from two factors: On the one hand, tensor-product operators can be well optimized such that the code stays compute-bound, not memory bound [4]. On the other hand, well-crafted DG-SEM methods can scale up to one element per core [5].
In order for these methods to jump the gap from academia to industry, CODA - a CFD solver for aircraft aerodynamics jointly developed by DLR, ONERA, and Airbus - implements a DG-SEM method. Yet while the method allows for reaching peak performance, it is often not reached in practice. Meticulous performance engineering is essential here [6]. In this publication, time-resolving DG-SEM test cases are shown for HyperCODA [7] - the extensions to CODA towards multi-species flows. Their performance is investigated using the performance tools Likwid [8] and Score-P [9]. Performance bottlenecks are pinpointed (Figure 1) and optimizations for critical kernels are proposed. These suggestions will improve the performance of CODA and HyperCODA for unsteady flow simulations, such as the Depres test case [10], which is investigated as an example test case for base buffeting within the Collaborative Research Center Transregio 40 [11] as illustrated in Figure 2.

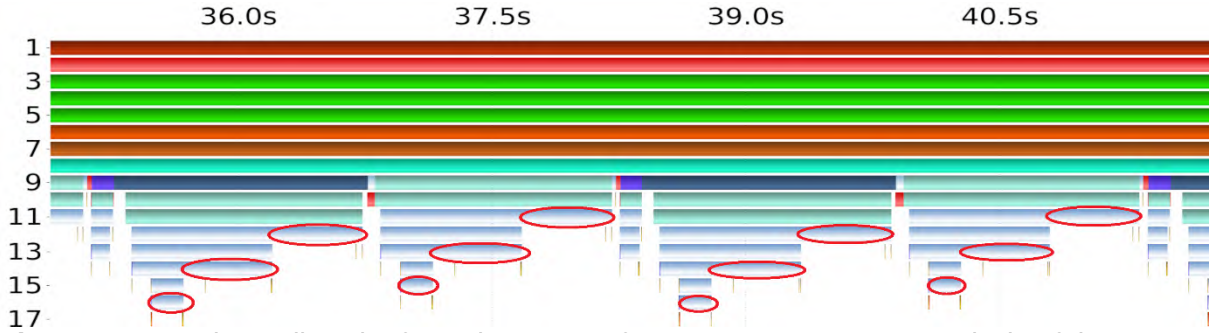

Figure 1 : Function-callstack of two timesteps of a DG-SEM test case: Analysis of the runtime behavior and identification of performance critical kernels (red ellipses).

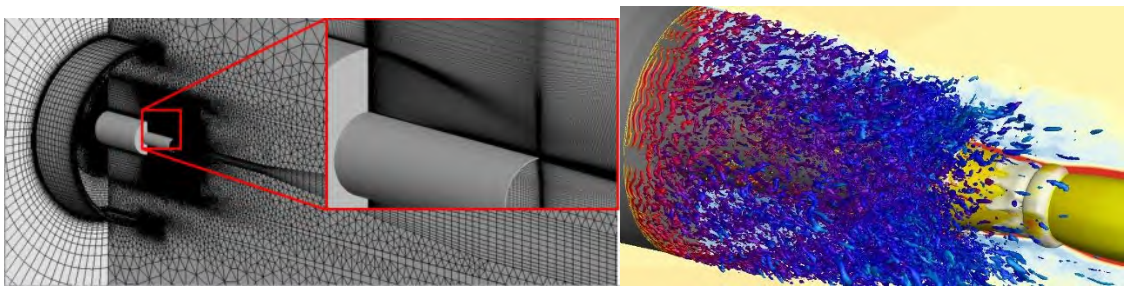

Figure 2 : TR40 test case. Left :Grid configuration, right: Turbulent vortex shedding.

Acknowledgements
This work is supported by Fabio Naddei (ONERA) and his work on DG-SEM methods in CODA.

Bibliography :

1. C. Grabe et.al., HPCN 2022
2. Krais, Nico, et al. "FLEXI: A high order discontinuous Galerkin framework for hyperbolic–parabolic conservation laws." Computers & Mathematics with Applications 81 (2021): 186-219.
3. Marmignon, C., Naddei, F., and Renac F. "Energy relaxation approximation for compressible multicomponent flows in thermal nonequilibrium." Numerische Mathhematik, 151 (2022), pp. 151-184.
4. Cantwell, Chris D., et al. "From h to p efficiently: Strategy selection for operator evaluation on hexahedral and tetrahedral elements." Computers & Fluids 43.1 (2011): 23-28.
5. Beck, A. D., et al. "Underresolved Turbulence Simulations with Stabilized High Order Discontinuous Galerkin Methods." Direct and Large-Eddy Simulation IX. ERCOFTAC Series, vol 20 (2015): 103-108.
6. Huismann, Immo, Fechter, Stefan, and Leicht, Tobias. "HyperCODA–extension of flow solver CODA towards hypersonic flows." STAB/DGLR Symposium. Springer, Cham, 2020.
7. Huismann, Immo, Stiller, Jörg, and Fröhlich, Jochen. "Efficient high-order spectral element discretizations for building block operators of CFD." Computers & Fluids 197 (2020): 104386.
8. Treibig, Jan, Hager, Georg, and Wellein, Gerhard. "LIKWID: Lightweight performance tools." Competence in High Performance Computing 2010. Springer, Berlin, Heidelberg, 2011. 165-175.
9. Knüpfer, Andreas, et al. "Score-P: A joint performance measurement run-time infrastructure for Periscope, Scalasca, TAU, and Vampir." Tools for High Performance Computing 2011. Springer, Berlin, Heidelberg, 2012. 79-91.
10. Deprés, D., Reijasse, P., and Dussauge, J. P. "Analysis of unsteadiness in afterbody transonic flows." AIAA journal 42.12 (2004): 2541-2550.
11. Schumann, Jan-Erik, et al. "Numerical Investigation of Space Launch Vehicle Base Flows with Hot Plumes." Future Space-Transport-System Components under High Thermal and Mechanical Loads. Springer, Cham, 2021. 179-191.

Mitteilung

Fachgruppe: Numerische Aerodynamik

Vortex Topology Mode Alternation in Hybrid RANS-LES Simulations of Transonic Flow over the DLR-F23 Combat Aircraft Wind Tunnel Model

J. Zastrow[1] & A. Probst[2]
1 : DLR – Institute of Aeroelasticity, Göttingen, jonas.zastrow@dlr.de
2 : DLR – Institute of Aerodynamics and Flow Technology, axel.probst@dlr.de

The large-scale unsteadiness of vortical flow topologies is a common characteristic of modern combat aircraft at moderate angle of incidence. Main drivers of the unsteadiness are topological features such as vortex-breakdown, vortex-vortex-interaction and vortex-shock-interaction. In particular, this affects aircraft planforms with multiple leading edges comprising several vortices, which yield a mixture of the phenomena mentioned before. Consequently, the global unsteadiness of the aerodynamic forces and moments is reflected by local flow structures. However, the dynamics of the flow topologies, and consequently the response of the aerodynamic system evolves manifold throughout the Mach-number and angle-of-incidence range. Additionally, even for steady boundary conditions the flow state may experience topological instabilities. In particular, the vortex-system dynamics on combat aircraft planforms with multiple leading-edge sweep angles can alternate between several topological modes [1]. Consequently, planform and control system design require knowledge of not only the local flow topologies, but also of the occurrence of global topological instabilities, which lead to an alternation of the dynamic system.

In order to apply this research field to multi-swept combat aircraft aerodynamics, the semi-span DLR-F23 wind tunnel model was developed and experimentally investigated in the Transonic Wind Tunnel Göttingen (TWG) [1]. These experiments comprise a Mach-number range in-between 0.5 and 1.2 and an angle-of-incidence range in-between 0° and 30°. As can be expected, this Mach-number and angle-of-incidence envelope yields many flow cases, which show the desired instabilities as described above. Hence, the DLR-TAU code flow solver is employed to investigate on these phenomena numerically. In a first step, the validity of the simulation set-up needs to be proven by comparison to the experimental data. This means that the computed flow field yields comparable results in its spatial and temporal characteristics. Only then, analysis of the flow topology dynamics can lead to profound control design suggestions. However, the fluid dynamics of interest are very demanding and challenge the capabilities of most current flow solvers, even with large computing resources. In order to address this subject, this work presents a feasible approach to compute the underlying phenomena of the DLR-F23's unsteady flow.

One of the flow states, at which the DLR-F23 shows very unique topological instabilities, is at Mach-number 0.85 and $\alpha = 21°$. Besides an inherent unsteadiness of the local flow features, a topological mode alternation between two states is apparent. A driving flow topology is the main-wing vortex, which alternates between complete burst and a locked breakdown. This can be seen by the standard deviation of the pressure coefficient $\sigma(c_p)$ as presented in Fig.1. Also, an oscillating shock is linked to this burst-breakdown alternation. Further inboard the fillet- and forebody vortices interact strongly and alter their position in relation to the dynamics of the main wing vortex. All three vortices are connected by the same oscillating shock.

To achieve an accurate representation of the flow, a hybrid RANS-LES approach based on the Improved Delayed Detached Eddy Simulation (IDDES) [2] is chosen and

numerically solved using a low-dissipation low-dispersion scheme (LD2) [3]. The numerical grid is locally adapted to the solution by TAU's adaptation module. An impression of the computed flow field is presented in Fig. 2. The chosen adaptation sensors are the statistically-converged values of the mean turbulent viscosity, the mean pressure coefficient and the standard deviation of pressure. Additionally, the time-step was chosen to satisfy a CFL-condition based on the vortex-core velocity, which is approximately three times the free stream velocity. As an outcome, the CFD-simulation represents the measured flow to an adequate extent in its spatial and temporal aspects.

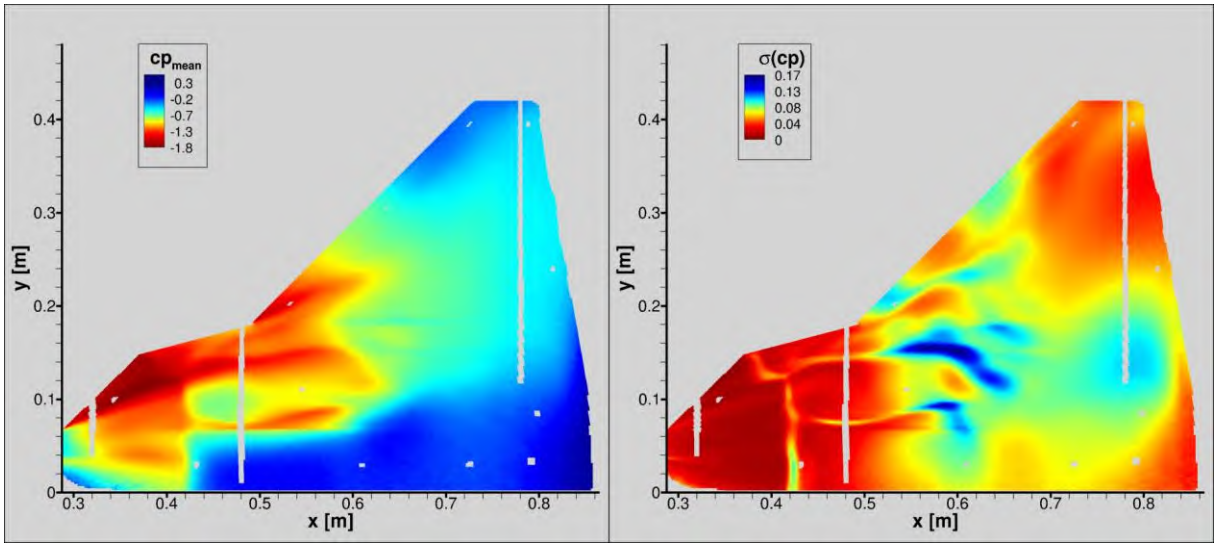

Figure 1: Time-resolved pressure sensitive paint shows mean and root-mean-square of c_p on DLR-F23's suction side at Mach-number 0.85 and $\alpha = 21°$

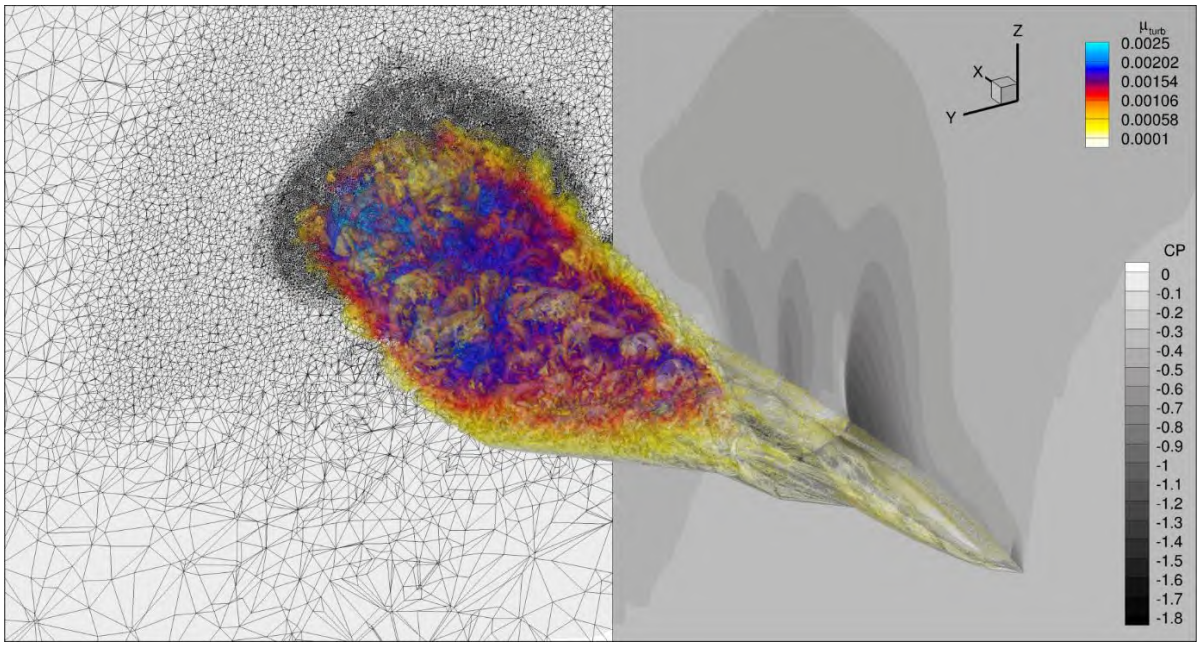

Figure 2: Hybrid RANS-LES simulation on adapted grid; instantaneous λ_2-criterion reflects unsteady vortical flow and is coloured by modelled turbulent viscosity; also, c_p at the symmetry plane outlines the shock system.

[1] Zastrow, J., Oberdieck, F., Henne, U., Klein, C., "Numerical and Experimental Investigations on the DLR-F23 Combat Aircraft Wind Tunnel Model", ICAS Congress, 2022

[2] Shur, M. L., Spalart, P. R., Strelets, M. K., & Travin, A. K., "A Hybrid RANS-LES Approach with Delayed-DES and Wall-Modelled LES Capabilities", International Journal of Heat and Fluid Flow, 29(6), 406–417, 2008

[3] Probst, A., Löwe, J., Reuß, S., Knopp, T., & Kessler, R., „Scale-Resolving Simulations with a Low-Dissipation Low-Dispersion Second-Order Scheme for Unstructured Flow Solvers", AIAA Journal, 54(10), 2972–2987, 2016

Mitteilung

Fachgruppe: Strömungsakustik

Numerical study of individuals exposure to road-noise in urban environments

A. Nabikhani, T. S. Müller, Arne Henning

Deutsches Zentrum für Luft- und Raumfahrt e.V. (DLR), Institut für Aerodynamik und Strömungstechnik
Bunsenstraße 10, 37073 Göttingen
Amin.Nabikhani@dlr.de

The adverse impact of environmental noise on individuals are of interest to many medical and behavioral studies addressing insomnia, cognitive performance and even cardiovascular diseases. Civil noise caused particularly by transportation means are among the most significant sources. According to an estimation of the World Health Organization (WHO), at least one million healthy disability-adjusted life-years (DALYs) are lost annually due to environmental noise [1]. An accurate method for simulating the exposure of individuals to road-noise during a typical working day in urban environments can help to investigate the physiological impact of noise pollution on the population. It can also be used as an efficient means for planing urban environments with optimal balance between traffic flow efficiency and noise pollution.

The present work combines three state-of-the-art simulation tools in order to provide an accurate account for the noise level perceived by a portion of the inhabitants of Berlin during a typical working day. The first tool in the simulation chain is the Travel Activity Pattern Simulation (TAPAS) which determines the traffic demand on the basis of a synthetic population of individuals [2]. This synthetic population is divided into different socio-economic and socio-demographic groups and daily activity plans are constructed for each individual. It is worth mentioning that the activity plans are not constructed randomly, but they are based on 35.000 diaries of 12.600 people who participated in a survey of the Federal Statistical Office of Germany in 2001/2002. After the traffic demand has been determined by TAPAS in form of origin, destination and arrival time for each individual, the second stage is the microscopic simulation of the traffic flow using SUMO (Simulation of Urban Mobility) [3]. As input to SUMO we provide the true-to-scale road network and the corresponding schedules of the traffic-light systems for the considered region in the center of Berlin. On the basis of this data SUMO simulates the traffic flow in the considered region during a full day. The output of SUMO is composed of the trajectories of all vehicles inside the considered region with a temporal resolution of one second. The last step in the simulation chain is the generation of a time-resolved noise map for which we provide the street network, the vehicle trajectories and a level-of-detail 1 (LOD1) representation of the buildings as input. Our method is based on the CNOSSOS-EU directive for strategic noise mapping [4] in combination with a ray-tracing technique that considers reflections on building facets and diffraction on horizontal and vertical building edges. Finally, the resulting time-resolved noise map is combined with the results of TAPAS in order to generate a personal noise diary for every individual in the simulated population.

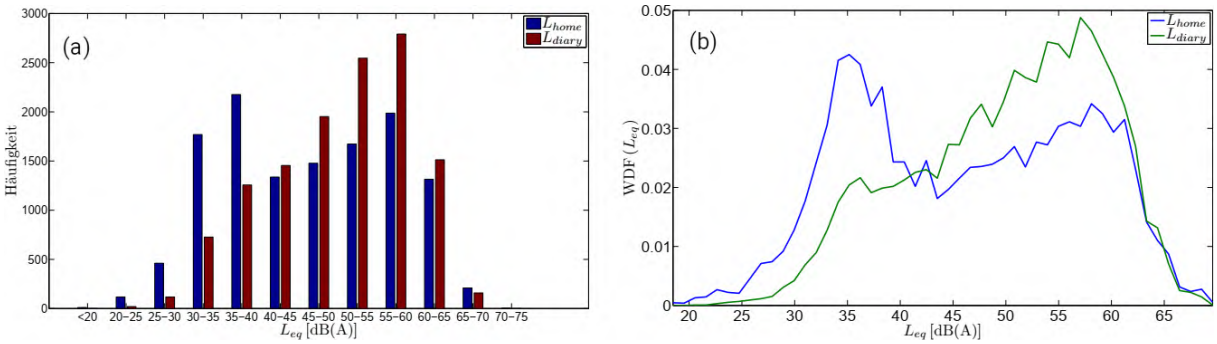

Figure 1: (a) *Occurrence distribution and* (b) *probability density function for the average sound level perceived by stationary (L_{home}) and vagrant agents (L_{diary}) in a span of a day.*

In the present work we consider a population of 12.538 agents during a period of 24 hours. Two location-based sound level scales, L_{home} and L_{diary} , are introduced in order to investigate the effect of changing agents' whereabouts on the average noise exposure throughout the day. L_{home} is defined as the average sound level on the facade of agents' residence while actual time-resolved agents' locations are used to calculate the average sound level L_{diary} . The results for the occurrence distribution of the equivalent sound levels in the two different situations are shown in Fig. 1 (a). Comparing the two distributions L_{home} and L_{diary} allows to infer the influence of agents' movements on their perceived average noise level. It suggests that non stationary agents are in comparison more likely to experience higher noise levels. Furthermore, one observes that L_{home} resembles a bimodal distribution with a lower peak at 35–40 dB(A) and a higher peak at 55–60 dB(A), while L_{diary} shows only a single maximum at 55–60 dB(A). These observations are also confirmed by the probability density function of the noise levels which is presented in Fig. 1 (b). The two peaks forming the bimodal distribution L_{home} can intuitively be explained considering the orientation of the buildings as well as the location of the individual probes with respect to the road. Probes placed on building facades located on the roadside experience higher noise levels and thus give rise to the higher peak, while the lower peak is associated with probes placed on the facades facing away from the roadside.

We conclude that the present combination of tree state-of-the-art simulation tools allows us to account very accurately for the noise level perceived by citizens in urban environments. We were able to reproduce the general trends in the noise-level distribution for stationary and vagrant agents and we quantified the impact on the exposure to road noise caused by traveling throughout the city or living in a road-side apartment. Further developments in this field could help to optimize the development of road networks and building blocks in urban environments which allow for a reduced noise pollution in critical areas and thus give rise to a higher overall quality of life.

References:

[1] L. Fritschi, B. AL, R. Kim, D. Schwela, and S. Kephalopoulos, Burden of disease from environmental noise (World Health Organization, Bonn, 2011).

[2] M. Heinrichs, in Next Generation Forum 2011, edited by P. Verkehr (Deutsches Zentrum für Luft und Raumfahrt e.V., 2011), pp. 74–74.

[3] P. A. Lopez, M. Behrisch, L. Bieker-Walz, J. Erdmann, Y.-P. Flötteröd, R. Hilbrich, L. Lücken, J. Rummel, P. Wagner, and E. Wießner, in The 21st IEEE International Conference on Intelligent Transportation Systems (IEEE, 2018).

[4] G. Forschungsstelle, I. G. für und Verbraucherschutz, F. Anfosso-Lédée, M. Paviotti, and S. Kephalopoulos, Common noise assessment methods in Europe (CNOSSOS-EU) (Publications Office, 2012).

Mitteilung

Fachgruppe: Strömungsakustik

Modelling mixing noise in low Mach number turbulent jets: reduced order modelling using one dimensional turbulence

Sparsh Sharma[a], Juan A. Medina Méndez, Marten Klein, and Heiko Schmidt
BTU Cottbus-Senftenberg, 03046 Cottbus, Germany
[a]: Corresponding author; E-mail: sparsh.sharma@b-tu.de

Jet noise is a significant source of aircraft noise, particularly during takeoff and landing. It has three components: turbulent mixing noise, broadband shock-associated noise, and screech tones [1], which are extensively studied using theoretical, semi-empirical, experimental, and computational techniques. Large-eddy simulations (LES) and direct numerical simulation (DNS) coupled with acoustic analogies are usually considered as state-of-the-art to evaluate the jet noise since both methods can predict more realistic turbulence [2]. With DNS still restricted to academic cases, LES has become the method of choice for jet noise prediction. In a typical LES, about 80% of the turbulent kinetic energy are resolved and 20% are modelled by a subgrid-scale (SGS) averaging approach due to which fine-scale information has been filtered out. Fine-scale turbulence, however, is considered as the dominant noise source component of turbulent mixing noise in subsonic jets because of the absence of Mach wave radiation [3]. Bres & Lele [4] in their recent review of jet noise mention that the estimation of the missing noise from the unresolved scales is one of the remaining challenges in modelling of jet noise. Here, we address the challenge mentioned by formulating a lower-order stochastic modeling strategy, which does not rely on the use of filtering operators, unlike LES. This strategy aims to resolve turbulent noise sources on all relevant scales in the acoustic near field with the aid of the one-dimensional turbulence (ODT) model [5]. ODT achieves numerical cost reduction by resolving the flow on a quasi-one-dimensional computational domain, that is, a notional line-of-sight. Along this line, turbulent advection is modeled stochastically, but molecular diffusion is directly resolved.

For this study, the modeling strategy is as follows: the near-field acoustic sources of a turbulent subsonic round jet are resolved with ODT as a stand-alone tool. After that, an ODT surrogate for pressure fluctuations is defined, with which we estimate the far-field noise using the Ffowcs-Williams and Hawkings (FW-H) approach [6]. The novelty is the coupling of established methods by the surrogate pressure fluctuations, which allows the study of fine-scale turbulence on jet noise. The stand-alone ODT formulation selected is a spatial ODT formulation as in [7], S-ODT. We utilise S-ODT in a configuration similar to that sketched in Fig. 1a. For the case of a low-Mach number flow with almost constant fluid density and viscosity, the ODT streamwise momentum equation for a round jet may be written as

$$u\frac{\partial \vec{u}}{\partial x}+\frac{1}{r}\frac{\partial r v\vec{u}}{\partial r}+\sum_{x_e}\mathscr{E}(\vec{u})\,\delta(x-x_e)=\frac{1}{r}\frac{\partial}{\partial r}\left(r\frac{\mu}{\rho}\frac{\partial \vec{u}}{\partial r}\right), \qquad (1)$$

where u is the streamwise component of $\vec{u}(r,x)$, but v is a distinct auxiliary variable that is evaluated when needed using conservation laws. x is the axial and r the radial coordinate, r is the dynamic fluid viscosity, and $\mathscr{E}(\vec{u})$ represents the stochastic ODT eddy events. The numerical solution procedure involves a fully-adaptive finite-volume discretisation on a Lagrangian grid [7]. The model employs a conservative mapping and a kernel mechanism in order to allow energy redistribution among the components of the velocity vector [7]. These operations aim to model the effects of turbulent advection and fluctuating pressure forces, respectively, which may be written as

$$\mathscr{E}(\vec{u}): \qquad \vec{u}(r,x)\rightarrow\vec{u}^{n}\left(f(r),x\right)=\vec{u}\left(f(r),x\right)+\vec{c}K(r)+\vec{b}J(r). \qquad (2)$$

In the above equation, the sources for mixing noise are contained in $\vec{c}$ and $\vec{b}$. These coefficients are localised, that is, effective only for the volume fraction of the ODT domain that is occupied by an eddy event. In order to estimate mixing noise, we collect the sources in terms of $\vec{c}$ and $\vec{b}$ for all eddy events that cross a predefined control surface. In shear flow, eddies need not be isotropic. We therefore attribute streamwise (axial) extend to the eddy events by a time-to-space transformation for the streamwise eddy size, $\Delta x_e = \tau_e u_e$, where u_e denotes a streamwise eddy velocity obtained by averaging $u(x_e,r)$ over the radial interval that is occupied by an eddy event at current downstream location x_e. By this procedure, an effective kinematic (specific) pressure fluctuation, $\pi\prime$, can be calculated based on dimensional grounds from the eddy turnover time τ_e, for stochastically sampled eddy length scale l_e, as surrogate estimator for the nominal acoustic sources that would be given by the actual specific pressure fluctuation, p'/ρ. An ensemble of independent ODT realisations is used to obtain a synthetic but statistically representative time history of the fluctuating surrogate pressure on the predefined control surface. This time-dependent surrogate pressure is then used to predict the acoustic pressure using the FW-H approach [7]. We also note that, due to the displacement of the jet under constant bulk velocity, a similar time-to-space transformation can be used to generate time-series of flow quantities, which in turn allow the evaluation of spectra for sources of sound radiation. An alternative in this context is the utilisation of the 2-D asymptotic Mach limit derived in [8] for the inhomogeneous wave equation. We note that in [8], the evaluation of dipole sources of sound radiation in turbulent channel flows only requires the knowledge of a time-series for the wall-shear stress; the evaluation of quadrupole sources, as in free-stream turbulence, requires the knowledge of the streamwise and spanwise velocity components along the wall-normal direction (ODT domain direction).

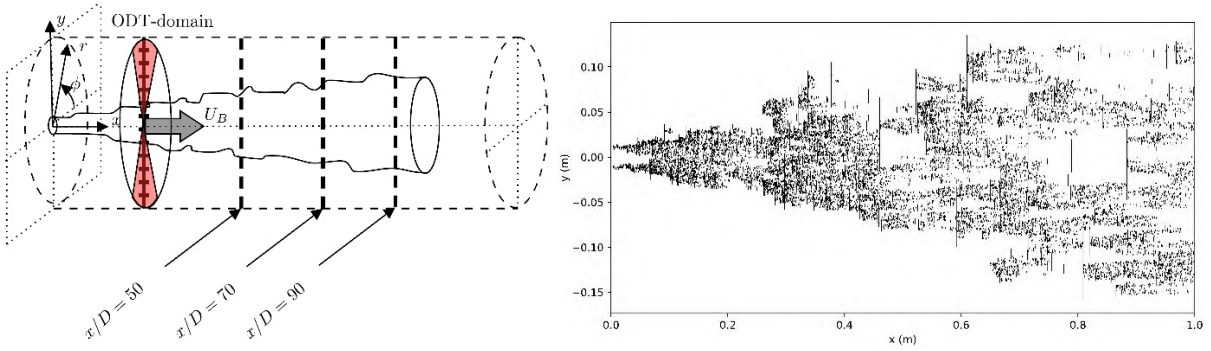

Fig. 1 (a) Schematic of the round jet (not to scale) that issues at location $x = 0$ into a slow co-flow; (b) Graphical representation of the sequence of eddy events during an S-ODT simulation of a spatially developing turbulent round jet with co-flow. Every eddy event is represented as vertical bar with finite size in radial (cross-stream y) direction but infinitesimal azimuthal and axial (x) extent.

Fig. 1b shows the ODT representation of the spatially developing turbulent round jet and indicates some of the flow features captured by the model. It is worth noting that the implemented eddy events shown in the figure encompass a broad range of scales and transient turbulent fluctuations. This is crucial for future model applications to turbulent jet noise modelling, which demands the simultaneous resolution of regions with zero and high turbulence intensity.

References

[1] Morris, P. J., and Viswanathan, K. (2013), In *CISM Int. Cent. Mech. Sci. Courses Lect.*, 545:119–96.
[2] Lyrintzis, A. S., and Coderoni, M. (2020), AIAA J. **58**, 4, 1620–38.
[3] Tam, C. K. W., Viswanathan, K., Ahuja, K. K., and Panda, J. (2008) J. Fluid Mech **615**, 253–92.
[4] Bres, G. A., and Lele, S. K. (2019), Philos. Trans. R. Soc. A Math. Phys. Eng. Sci. **377**, 2159.
[5] Kerstein, A. R (1999), J. Fluid Mech **392**, 277–334.
[6] Ffowcs Williams, J. E., and Hawkings, D. L. (1969), Philos. Trans. R. Soc. London A Math. Phys. Eng. Sci. **264**, 1151.
[7] Ashurst, W. T., and Kerstein, A. R. (2005), Phys. Fluids **17**, 025107.
[8] Hu, Z., Morfey, C., and Sandham, N. (2003), *J. Fluid Mech.* **475**, 269-302.

Mitteilung

Fachgruppe: Strömungsakustik

Physikalische Mechanismen der turbulenzinduzierten Generierung von Breitbandschall

Florian Wachter
Lehrstuhl für Strömungsmechanik, Universität Erlangen-Nürnberg,
Cauerstr. 4, 91058 Erlangen,
flo.wachter@fau.de

Eman Bagheri
Lehrstuhl für Strömungsmechanik, Universität Erlangen-Nürnberg,
Cauerstr. 4, 91058 Erlangen,
eman.m.bagheri@fau.de

Stefan Becker
Lehrstuhl für Strömungsmechanik, Universität Erlangen-Nürnberg,
Cauerstr. 4, 91058 Erlangen,
stefan.becker@fau.de

In zahlreichen technischen Anwendungen spielt der strömungsmechanisch induzierte Breitbandschall eine dominierende Rolle. Die Anwendungen reichen von der Tragflügelumströmung über die Fahrzeugakustik bis hin zum gesamten Ventilatorbereich. Die hier vorgestellten Forschungsarbeiten erlauben es, einen Zusammenhang zwischen der Physik der Turbulenz und den strömungsakustischen Quelltermen herzustellen. Als Referenzfall wurde die strömungsinduzierte Schallgenerierung an einer vorwärtsspringenden Stufe herangezogen. Dieser häufig verwendete Benchmarktestfall eignet sich besonders zur Untersuchung der strömungsinduzierten Generierung von Breitbandschall.

Ausgangspunkt der kürzlich durchgeführten Untersuchung bildet die Energiekaskade der Turbulenz. Aus Analogiebetrachtungen lässt sich ableiten, dass die strömungsakustischen Quellterme in proportionaler Beziehung zur Kaskadenrate stehen. Eine Erkenntnis, die aus der Analyse gewonnen werden konnte, ist, dass der Energietransfer der Turbulenzkaskade den primären Mechanismus der Breitbandschallerzeugung darstellt. Es lässt sich zeigen, dass die Erzeugung von Breitbandschall nicht von der lokalen Turbulenzintensität abhängt, sondern vom Wirbelzerfall. Damit ist die Zeitskala, die mit dem Wirbelzerfall verbunden werden kann, die relevante Zeitskala für den Breitbandschall und kann zur Abschätzung der Gittergrenzfrequenz (grid cut-off frequency) genutzt werden, welche bei einer effizienten numerischen Berechnung von strömungsakustischen Quellen eine entscheidende Rolle spielt.

Durch einen alternativen Ansatz kann ebenfalls gezeigt werden, dass sich die Erzeugung von Breitbandschall auf den Zerfall der turbulenten Wirbel zurückführen lässt. Hierbei wird eine Verbindung zwischen der inkompressiblen Formulierung des strömungsakustischen Quellterms der Lighthill-Analogie, dem Q-Kriterium und der turbulenten Dissipation hergestellt.

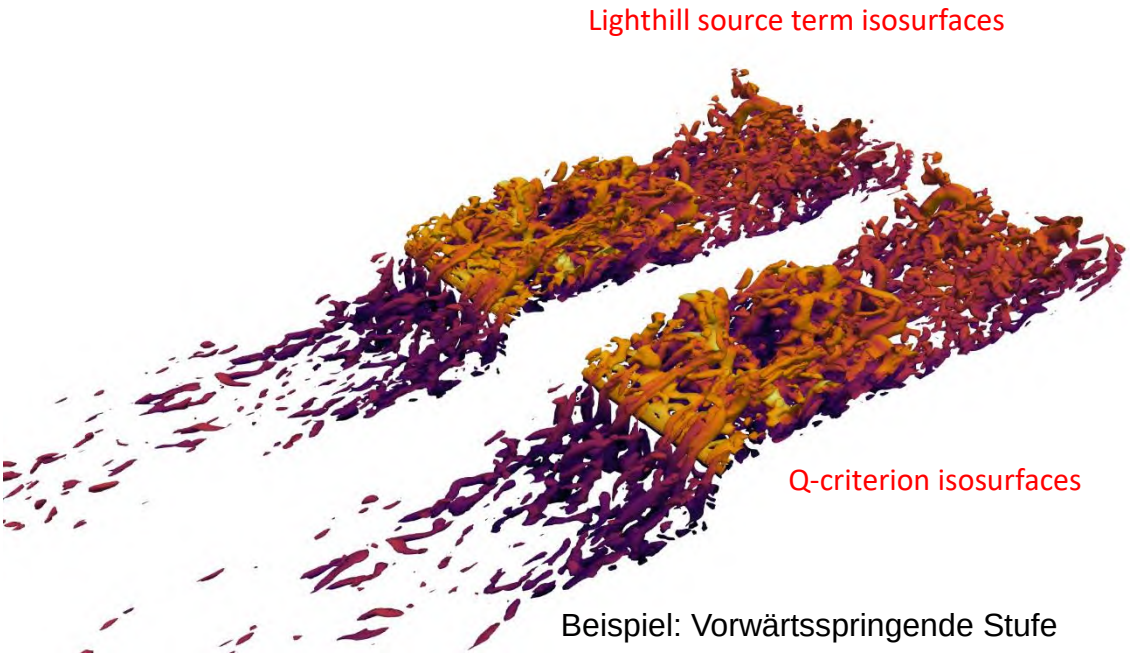

Beispiel: Vorwärtsspringende Stufe

Diese Erkenntnisse ermöglichen eine gute Übertragung der physikalischen Mechanismen der Schallgenerierung für ein verbessertes akustisches Design.

Mitteilung

Fachgruppe: Strömungsakustik

Aeroacoustics of High Fidelity URANS Simulations of Distributed Electric Propellers

Robin Wickersheim, Manuel Keßler and Ewald Krämer
Institute of Aerodynamics and Gas Dynamics (IAG), University of Stuttgart,
Pfaffenwaldring 21, 70569 Stuttgart, Germany
robin.wickersheim@iag.uni-stuttgart.de

Introduction

Since the aviation industry moves increasingly towards electric propulsion, distributed propellers have shown several aerodynamic advantages. Beside the aerodynamic improvement, acoustic effects due to propeller-propeller and propeller-wing interactions have to be considered. A numerical study is necessary to investigate a wide range of configurations by using a CFD/CAA calculation with an integration surface including all acoustic source terms. Therefore, the placement of the integration surface is crucial to examine interaction phenomena. Within the LuFo project VELAN, the University of Stuttgart ‘s electric technology demonstrator eGenius-Mod was equipped with distributed propellers as well as with an aeroacoustic measurement system and will be used for in-flight measurements in the near future.

Methodology

In this work the finite volume solver FLOWer is used to provide the CFD flow field results. Accordingly, the unsteady Reynolds-averaged Navier-Stokes (URANS) equations are solved within a structured mesh. Moving parts, like propeller blades, can be placed in a background grid using an overset chimera technique. FLOWer was originally developed by DLR [1] and further extended at the Institute of Aerodynamics and Gas Dynamics of the University of Stuttgart [2]. The acoustic extrapolation to far field observers is carried out with IAG’s FW-H solver ACCO [3]. Furthermore, a coupled approach consisting of ACCO and a Boundary Element Method (BEM) is used to give more insights into shielding effects [4]. The numerical setup includes three propellers with a diameter of 25.5 cm in tractor configuration mounted in front of the infinite elongated eGenius-Mod wing, see Figure **1**. The effects of propeller-propeller and propeller-wing interactions are investigated by using different FW-H integration surfaces. In this study two integration surfaces are implemented, one only enclosing the propellers and the other by taking the entire setup into account. A validation with the BEM solution only enclosing the propellers and therefore considering propeller noise and scattering on the wing, shows good agreement between the numerical results.

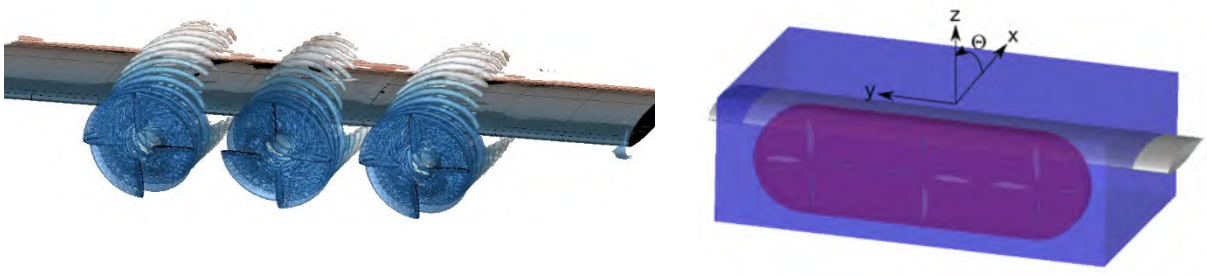

Figure 1 – Vortices visualization by λ_2 – value (left) and integration surfaces (right) to obtain acoustic interaction phenomena (blue FW-H 1 and red FW-H 2)

Preliminary results and discussion

Two flight states are examined, the takeoff state and the cruise flight state. Additionally, in each flight state the distance between the propellers and the rotation direction of the enclosed propeller are varied. As reference for the flight states the thrust requirements of the eGenius-Mod are prescribed. First results show the angular directivity of the Overall Sound Pressure Level (L_P). The two toolchains CFD+ACCO with fully enclosed structures and the CFD+ACCO+BEM approach show slight discrepancies at 330° as well as in the direction of the vertical axis. At the 30° direction the coupled ACCO+BEM approach agrees well with the FW-H 1 integration surface. In Figure **2** the directivity of the OASPL is presented for both integration surfaces and the BEM approach. Supplementary, the acoustic evaluation using the physical blade surface is given.

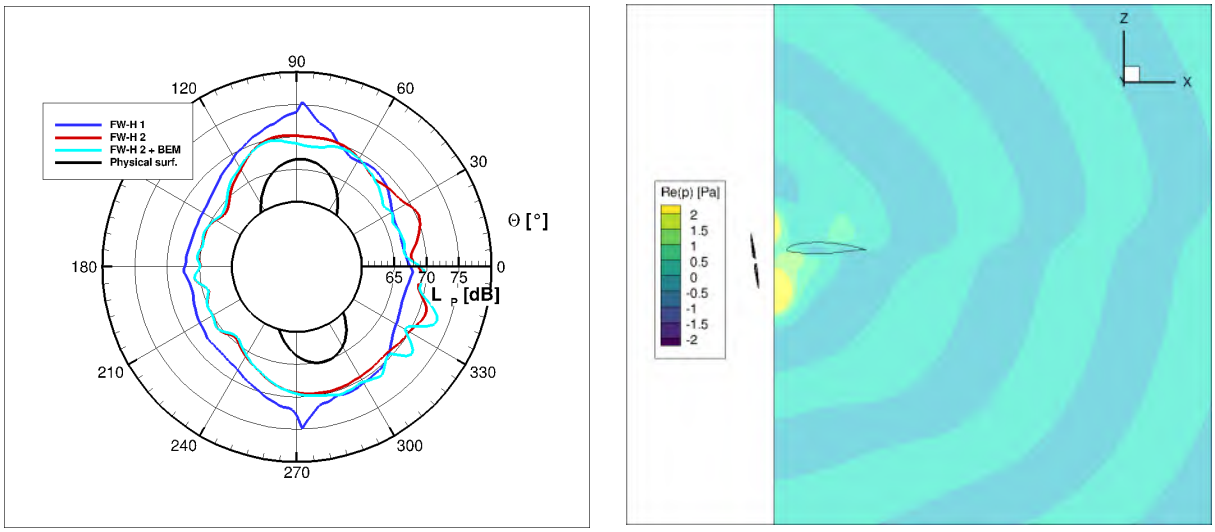

Figure 2 – Polar directivity of the integration surfaces and the coupled ACCO+BEM approach (left) and the scattering field of the first Blade Passing Frequency (right)

Using the scattering field of the wing, the directivity of the acoustic field can be observed. Furthermore, in Figure **2** the scattering effect of the acoustic waves can be found. The wing reflects the acoustic waves of the propellers and influences the directivity of the sound emission. Therefore, the final paper will include further propeller positions to investigate the effect and the acoustically most beneficial configuration for distributed propellers. The discrepancy between the integration surfaces will be explained and compared to each other. Finally, the tradeoff between acoustic and aerodynamic advantage will be discussed and set in relation.

Acknowledgement

The authors gratefully acknowledge the Federal Ministry for Economic Affairs and Climate Action (BMWK) for funding this work in the framework of the research project VELAN (FKZ: 20E1919).

Gefördert durch:
Bundesministerium für Wirtschaft und Klimaschutz
aufgrund eines Beschlusses des Deutschen Bundestages

References

[1] **Kroll N., Eisfeld B., Bleecke H.**: The Navier-Stokes code FLOWer. In: A. Schüller (Ed.), Portable Parallelization of Industrial Aerodynamic Applications (POPINDA), Notes on Numerical Fluid Mechanics, Vol. 71, pp. 58-71 (1999)

[2] **Kowarsch U., Oerhle C., Hollands M., Keßler M., Krämer E.**: Computation of Heli-Copter Phenomena Using a Higher Order Method. In: Nagel W.E., Kröner D.H., Resch M. M., High Performance Computing in Science and Engineering '13, pp. 423-438 (2013)

[3] **Keßler M., Wagner S.**: Source-Time Dominant Aeroacoustics. Computers & Fluids. Vol. 33, No. 5-6, pp. 791-800 (2004)

[4] **Dürrwächter L., Keßler M., Krämer E.**: Numerical Assessment of Open-Rotor Noise Shielding with a Coupled Approach. AIAA Journal. Vol. 57, No. 5, 2019

Mitteilung

Fachgruppe: Strömungsbeeinflussung

A New Approach of Using Porous Bleed Boundary Conditions - Application of Local Porosity

Julian Giehler, Pierre Grenson, Reynald Bur
DAAA, ONERA, Université Paris Saclay, 92190 Meudon, France
julian.giehler@onera.fr

The application of a porous bleed is a proven technology to mitigate the boundary layer separation caused by shock-boundary layer interactions (SBLI) in various applications. Currently, there is a renewed interest in supersonic transport, which makes this control technique more important also for civil applications. Although the working principle of a porous bleed is well understood, the effect on the flow is still difficult to estimate. Full simulations, including the porous bleed, are too cost- and time-consuming for industrial cases since a typical bleed region consists of hundreds or thousands of tiny holes. Therefore, multiple researchers adressed the problem to develop a simple model which can be applied as a boundary condition in CFD simulations [1] [2] [3] [4] [5].

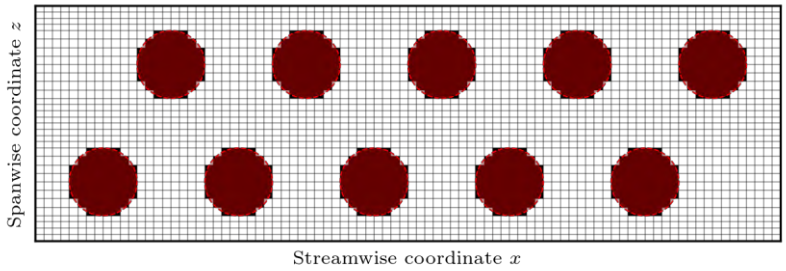

Figure 1: Local porosity applied on mesh; black cells illustrate porosity and red circles the hole geometry

In a previous study, existing bleed models have been investigated and evaluated with the aim of demonstrating advantages, disadvantages, and differences [6]. The findings concluded a significant impact of the implementation approach on the performance of the boundary conditions. Regardless of the model, the wall shear stress is significantly overestimated, especially in regions where the flow should detach in reality.
The current study presents a new method to implement the bleed boundary conditions into the ONERA-Safran finite-volume solver elsA by utilizing a local porosity level in contrast to a constant value for the whole boundary surface. An orthogonal mesh is used instead of considering the hole contour in the mesh, as done by Wukie et al. [7]. Thus, the plate geometry is modeled discretely, and suction/blowing is only locally applied, as illustrated in Figure 1.
Figure 2 compares a reference simulation with the different methods of applying the bleed boundary conditions. Therefore, the model of Slater [3] is used. In the reference simulation (Figure 2a), several expansion fans and shock waves provoked by the holes are apparent. These phenomena have a crucial effect on the boundary layer as they induce a pressure gradient. Contrary to reality, only one expansion fan is apparent if the uniform bleed boundary condition is applied, as shown in Figure 2b. Consequently, the boundary layer thinning is more efficient than in reality. The application of the local porosity is illustrated in Figure 2c. The locally distributed suction causes similar to the reference simulations with holes several expansion fans and shock waves. Also, the thicking of the boundary layer between the holes is apparent.

For the final proceeding, the use of the local porosity will be investigated for different hole diameters to define the minimum resolution required to obtain accurate results. Moreover, the bleed mass flow rate obtained by the different methods will be compared, as well as the boundary layer profiles on the porous bleed and downstream of the bleed.

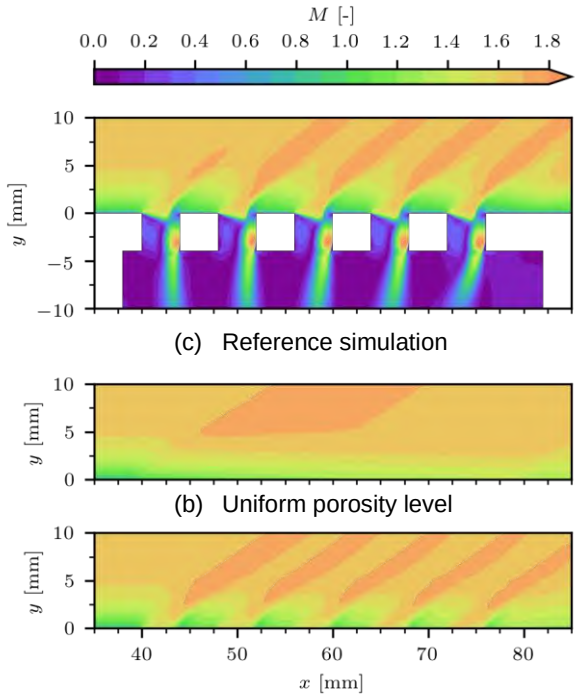

Figure 2: Mach number contours for the different simulation procedures

Bibliographie

[1] Gary J. Harloff and Gregory E. Smith, "Supersonic-inlet boundary-layer bleed flow," *AIAA Journal*, vol. 34, 1996.

[2] Piotr P. Doerffer and Rainer Bohning, "Modelling of perforated plate aerodynamics performance," *Aerospace Science and Technology*, vol. 4, 2000.

[3] John W. Slater, "Improvements in Modeling 90-degree Bleed Holes for Supersonic Inlets," *Journal of Propulsion and Power*, vol. 28, 2012.

[4] Yohan Choe, Chongam Kim, and Kwanghyun Kim, "Effects of Optimized Bleed System on Supersonic Inlet Performance and Buzz," *Journal of Propulsion and Power*, vol. 36, 2020.

[5] J. Grzelak, Piotr P. Doerffer, and Tomasz Lewandowski, "The efficiency of transpiration flow through perforated plate," *Aerospace Science and Technology*, vol. 110, 2021.

[6] Julian Giehler, Pierre Grenson, and Reynald Bur, "Porous Bleed Boundary Conditions for Shock-Induced Boundary Layer Separation Control," in *56th 3AF International Conference on Applied Aerodynamics*, Toulouse, 2022.

[7] Nathan A. Wukie, Paul D. Orkwis, Mark G. Turner, and Sean Duncan, "Simulations and Models for Aspiration in a Supersonic Flow Using OVERFLOW," *AIAA Journal*, vol. 53, 2015.

Mitteilung

Fachgruppe: Strömungsbeeinflussung

Simulation von Absaugkammern mit variabler spannweitiger Druckverteilung für HLFC Anwendungen

Heinrich Lüdeke
DLR, Institut für Aerodynamik und Strömungstechnik,
Lilienthalplatz 7, 38108 Braunschweig
Heinrich.Luedeke@dlr.de

Für einfache, effektive Kammer-Konzepte zur hybriden laminaren Strömungskontrolle (HLFC) von Grenzschichten wird das Strömungsfeld innerhalb von Absaug-Kammern unter Berücksichtigung spannweitiger Druckgradienten simuliert, um Einflüsse der Kammerströmung auf Absaugcharakteristiken abzuschätzen. Das ALTTA-Konzept einer äußeren porösen Oberfläche mit einer Unterstruktur aus Stringern und einer zweiten inneren Wand mit Drosselbohrungen zu einem Plenum bei kontantem Plenumsdruck wird im Folgenden ebenso untersucht, wie moderne Konzepte von HLFC-Segmenten mit Absaugrippen an einer Flügelkonfiguration (Siehe Fig. 1).

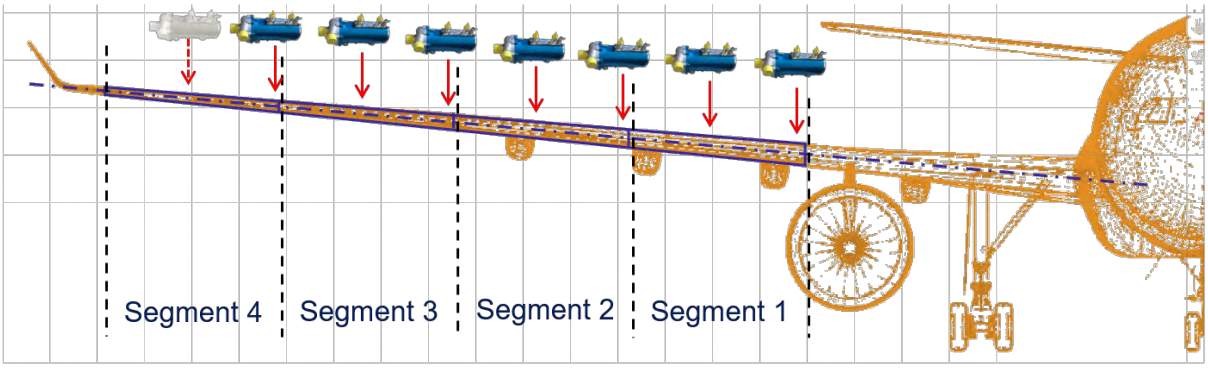

Fig. 1: HLFC segmente und Kompressor Verteilung entlang des Flügels (aus CleanSky 2 project HLFCWin [2]).

Entscheidend für die einzelnen Kammern, ist eine Vorhersage der Absaug-Geschwindigkeiten entlang der Außenwand. Dazu wird in der durchgeführten Studie das Strömungsfeld der Kammer unter Annahme von spannweitigen Wanddruck-Gradienten simuliert. Zur Überprüfung des implementierten Ansatzes werden zunächst zweidimensionale CFD-Simulationen der Kammer mit einem hochgenauen strukturierten CFD-Code durchgeführt. Die kreisförmigen Drosselbohrungen lassen sich durch Schlitze gleichen hydraulischen Durchmessers modellieren, so dass sich ein konstanter Massenstrom ergibt. Die Absaugung durch die poröse Wand wird bei diesem Ansatz durch eine analytische Beziehung zwischen dem Druckabfall über der Wand und der Absaug-Geschwindigkeit modelliert [1] und im Rahmen dieser Randbedingung ein tangentialer Druckgradient entlang des Absaugrandes hinzugefügt.

Die zweidimensionalen Simulationen der Kammer mit Drosselbohrung und externem Druckgradienten erfordern im Gegensatz zu bisherigen Modellierungen eine spezielle periodische Behandlung zwischen den Außenrändern, da der Druckgradient eine Abweichung von der spannweitigen strengen Periodizität dieser Ränder darstellt. Soll also nur der Bereich zwischen je zwei Drosselbohrungen simuliert werden, ist der Sprung im Wanddruck und den Absauggeschwindigkeiten zu berücksichtigen.

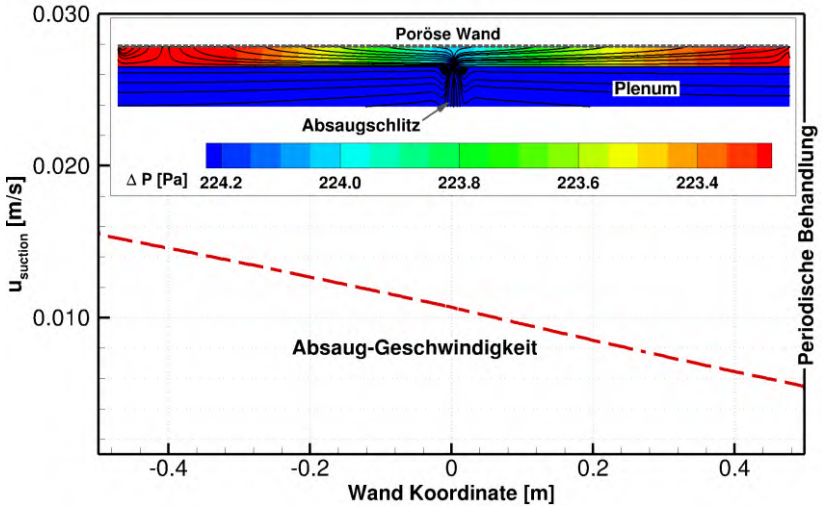

Fig. 2: Geschwindigkeitsverteilung und Differenzdruck einer Absaugkammer mit tangentialem Wanddruckgradienten. Die Konturansicht der Kammer wurde der Übersicht halber in Wandnormalen-Richtung um den Faktor 3 skaliert.

Eine solche periodische Randbedingung, die auch zu einer Verdoppelung des Rechenbereichs um den Drosselschlitz führt, wurde für die gezeigten Studien implementiert. Bei den betrachteten vorgegebenen Druckgradienten spielen die erwähnten Effekte zunächst noch eine untergeordnete Rolle, wie man am Verlauf der Absaug-Geschwindigkeit im Diagramm (Fig. 2) gut erkennen kann.

Neben den erwähnten periodischen Randbedingungen mit Drucksprung werden auch 3D Kammer-Simulationen mit tangentialem Druckgradienten betrachtet, die im Gegensatz zum ALTTA Konzept keine Drosselbohrungen zur Modifikation von Kammerdrücken erfordern.

Schließlich werden vergleiche mit gemessenen Drücken an einem vereinfachten Kammermodell mit Druckaufnehmern und unterschiedlichen Pumpendrehzahlen sowie Ansaugoberflächen gezeigt [2].

[1] G. Schrauf, K.H. Horstmann: Simplified hybrid laminar flow control. ECCOMAS 2004, Jyväskylä, Finland, 24-28 July 2004. CD-Proceedings 2004.

[2] T. Kilian, et.al., The influence of high spanwise chamber extent on HLFC performance. DLRK2021, Bremen und online, 31.08.-02.09.2021

Mitteilung

Fachgruppe: Strömungsbeeinflussung

Some specific challenges of HLFC design on a long-range wing

Geza Schrauf[1], Thomas Kilian
DLR, Lilienthalplatz 7, 38108, Braunschweig, Germany
contact@schrauf.de, thomas.kilian@dlr.de

The European project HLFC-WIN is developing a hybrid-laminar-flow-control (HLFC) system for the wing of a long-range aircraft as part of Clean Sky 2. The wing is based on the turbulent XRF1 research configuration. For the purpose of this study, the wing planform was not altered, only the airfoil sections were changed to favor laminar flow [1,2], while limiting the wave drag penalty. The wing has a pressure distribution with a high suction peak, which differs from previously considered HLFC applications, as, for example, for the A320 HLFC VTP [3] or the wing considered within the ELFIN II project in the nineties and tested in the ONERA S1MA wind tunnel [4] as can be seen in Figure 1.

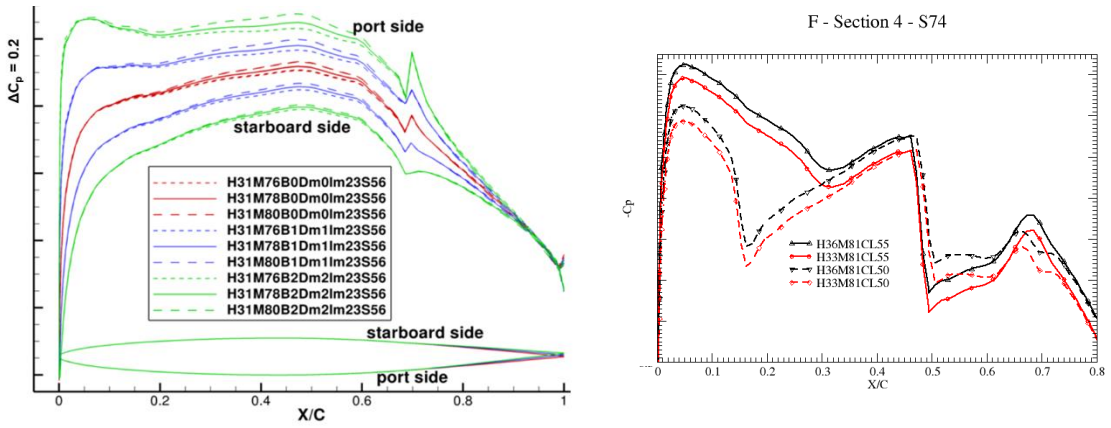

Fig. 1: Comparison of two pressure distributions. Left A320 VTP, right the HLFC wing.

One important difference between the pressure distribution of this wing and the previous ones considered is the large pressure increase at the leading edge for X/C>0.05 (property P1). The design idea is that this pressure increase allows for larger pressure decrease resulting in a boundary layer with larger flow acceleration, which is beneficial to delay the Tollmien-Schlichting (TS) transition. Furthermore, the shocks become weaker. On the other hand, the suction applied at the leading edge before the front spar must be strong enough not only to avoid cross-flow transition but also to suppress laminar separation on the suction panel.

The extent of the above-mentioned pressure increase varies strongly throughout the HLFC envelope and for some cases even exceeds the front spar datum (property P2), which usually limits the suction area.

[1] Retired from DLR

Other important design-relevant differences of suction systems on the wing compared to the VTP are the higher Mach number, the lower leading-edge sweep, and, correspondingly larger attachment line Reynolds numbers:

	XRF1 Wing	A320 VTP
Mach number	0.83±0.02	0.78±0.02
Leading edge sweep	32^{o} degree	40^{o} degree

For the aerodynamic design of this HLFC system, we have the following requirements:

R1 Enough suction to keep the attachment line laminar
R2 Enough suction to suppress crossflow (CF) transition
R3: Enough suction where the boundary layer is close to separation
R4: Enough suction to suppress Tollmien-Schlichting (TS) transition

To keep the attachment line laminar, i.e. for R1, we have to satisfy the K-criterion [5]. For the A320 VTP this criterion is automatically satisfied, if we apply sufficient suction to avoid CF-transition. We do not need to apply any additional suction to satisfy R1. The requirement R3 is caused by property P1 and is unique for this wing. Because of property P2, we need somewhat stronger suction at the end of the suction panel to delay transition up to the shock.

In the presentation, we will show how we designed the HLFC system. In contrast to the VTP, which is a classical ALTTA design with twenty-three suction chambers, we work with a single large chamber and apply different porosities of the micro-perforation to adjust the local suction strength.

References

[1] T. Streit et al: "Aerodynamic design and analysis of HLFC wings within the European project HLFC-WIN." 33rd ICAS Congress, Stockholm, Sweden, 2022.
[2] T. Kilian: "Aerodynamic design of an HLFC system for a long range wing." DLRK, Dresden, 2022.
[3] G. Schrauf, H. von Geyr: “Hybrid Laminar Flow Control on A320 Fin: Retrofit Design and Sample Results.” AIAA Journal of Aircraft (2021), Vol. 58, No. 6, November-December 2021, pp. 1272-1280.
[4] G. Schrauf: “Large-Scale Laminar-Flow Tests Evaluated with Linear Stability Theory.” AIAA Journal of Aircraft, Vol. 41, No. 2, March-April 2004, pp. 224 - 230.
[5] D. Arnal, J. C. Juillien, J. Reneaux, G. Gasparian: “Effect of wall suction on leading edge contamination.” Aerospace Science and Technology No. 8 (1997), pp. 505-571.

Mitteilung

Fachgruppe: Strömungsbeeinflussung

Numerische Simulationen aktiver Wirbelgeneratoren

Björn Selent, Ulrich Rist
Institut für Aerodynamik und Gasdynamik, Universität Stuttgart
Pfaffenwaldring 21,70569 Stuttgart
bjoern.selent@iag.uni-stuttgart.de

Aktive Wirbelgeneratoren sind strömungsmechanische Apparate, die durch das Einbringen eines transversalen Strahls in eine Grenzschichtströmung dazu führen, dass ein sekundäres Wirbelsystem in dieser Grenzschicht entsteht. Diese Wirbel können dabei für unterschiedliche Anwendungen erwünschte Effekte erzielen, z.B. in Brennkammern zur Vermischung von Treibstoff und Oxidans, zur Kühlung von Turbinenschaufeln in Gasturbinen, zur Steuerung von Flugzeugen mittels Schubvektordüsen oder zur Verhinderung von Ablösung auf Auftriebshilfen. Die Parameter, die die resultierende Strömung dabei maßgeblich bestimmen, sind u.a. die Winkel, unter denen der Strahl in die Querströmung eingebracht wird (s. Skizze).

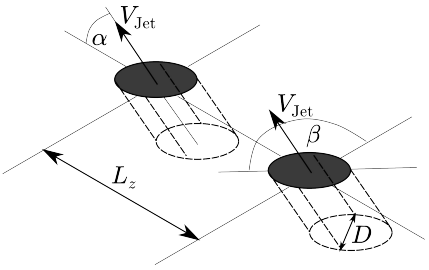

Definition Anstellwinkel α und Drehwinkel β

Um Aussagen über den Einfluss dieser Parameter treffen zu können, werden direkte numerische Simulationen für generische Anstell- und Drehwinkelvariationen durchgeführt.

Ausgehend von einer beispielhaften Anwendung in Form eines Wirbelgenerators zur Verhinderung von Ablösung werden die Zielgrößen Wandreibungskoeffizient Δc_f und Impulsgewinnbeiwert $\Delta I/b$ betrachtet. In Kombination mit weiteren Strömungsgrößen wie z.B. der Strahl-Trajektorie lassen sich Winkelkombinationen bestimmen, die die gewünschten Effekte erreichen.

Um den Einfluss weiterer Parameter der Konfiguration gering zu halten, werden Laborskalen für die Dimensionen der Grenzschicht- und Rohrströmungs-Reynoldszahl gewählt: $Re = \frac{U_{Jet}D}{\nu} = 742$ mit $U_{Jet} = 3U_\infty$. Dieses Vorgehen erlaubt es, die Konfiguration ohne weitere numerische Modelle zu simulieren und detaillierte Informationen über integrale Größen wie auch über lokale und transiente Strukturen zu erhalten. Für die Simulationen wird der Open-Source Strömungslöser OpenFOAM verwendet.

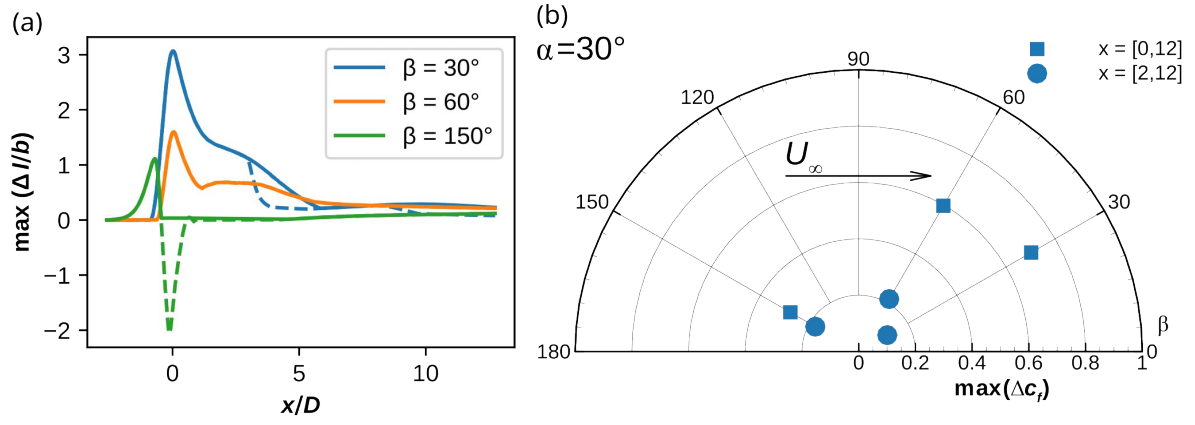

Abbildung 1: (a) Maximum des Impulsgewinnbeiwertes; (-) Strahl eingeschlossen, (--) nur Grenzschicht, (b) Maximum der Änderung des Wandreibungskoeffizient

Exemplarisch für die bisherigen Ergebnisse stellt Abbildung 1 den Verlauf des maximalen Impulsgewinnbeiwertes über die Stromabrichtung und das Maximum der Änderung des Reibungskoeffizienten dar. Die Werte wurden für unterschiedliche Drehwinkel von $\beta = 30°, 60°, 150°$ bei einem Anstellwinkel von $\alpha = 30°$ berechnet. Aus diesen lässt sich die Kombination von $\alpha = 30°$ und $\beta = 60°$ als effektivste ermitteln, da damit keine Impulsverluste auftreten und die Grenzschicht stromab des Wirbelgenerators am stärksten angereichert wird.

Weitere Simulationen sollen das Bild vervollständigen und idealerweise dabei unterstützen ein Modell aufzustellen, dass die Wirkung der Winkelvariation ausreichend genau beschreibt.

Literatur:

[1] Godard, G.; Foucaut, J.M.; Stanislas, M.; Control of a Decelerating Boundary Layer. Part 3: Optimization of Round Jets Vortex Generators, Aerospace Science and Technology 10 (3), 455 - 464

[2] Scholz, P.; Ortmanns, J.; Kähler, C.J.; Radespiel R.; Performance Optimization of Jet Actuator Arrays for Active Flow Control. CEAS/KATnet Conference on Key Aerodynamic Technologies, Bremen, 2005

[3] Selby, G.V.; Lin, J.C.; Howard F.G.; Control of Low-Speed Turbulent Separated Flow using Jet Vortex-Generators. Exp. Fluids 12, S.394 - 400

[4] von Stillfried, F. ; Wallin, S.; Johannson A.V. ; Casper M.; Ortmanns J.; Evaluation and Parameterizing Round Vortex-Generator Jet Experiments for Flow Control. AIAA J. 50 (11), S. 2508 - 2524

Mitteilung

Fachgruppe: Strömungsbeeinflussung

Control of laminar-turbulent transition using counter-rotating cylindrical roughness pairs

Yongxiang Wu, Ulrich Rist
Institut für Aerodynamik und Gasdynamik, Universität Stuttgart
Pfaffenwaldring 21,70569 Stuttgart
wu@iag.uni-stuttgart.de

In the roughness element induced streaky boundary layer, the spanwise modulation of the baseflow results in inflection points in either wall-normal or spanwisedirections. As found by Andersson *et al.* [1], inflectional instability is encounteredwhen the streak amplitude reaches 26% of the free-stream velocity. A global LSTinvestigation by Loiseau et al. [4] revealed that a varicose instability is associated with the three-dimensional shear around the central low-speed streak, while a sinuous instability has its root in the near wake and in particular the lateral shear around the separation bubble. Alongside the amplification of this inviscid secondary instability, higher harmonics can be activated which lead to the generation of turbulent spots and subsequently turbulence. On the other hand, roughness-induced streaks may also stabilize the boundary layer, of which the theoretical prediction and experimental validation have been provided by Cossu & Brandt [2] and Fransson *et al.* [3], respectively. The mechanism is that a negative spanwise production of perturbation kinetic energy is brought in by the velocity streaks, which together with the viscous damping outweighs the positive wall-normal production, thus resulting in an overall stabilization effect. In our previous study [5], a special case with rotating cylindrical roughness elements is found capable of stabilizing the TS-wave effectively as well. Whereas, the mechanism is the reduction of the wall-normal production. The goal of the present study is to confirm that the rotating wall-normal cylindrical roughness pair arrays can indeed stabilize the boundary-layer and even delay laminar-turbulent transition in a direct numerical simulation.

In this investigation, the H-type transition scenario over a flat-plate with and without counter-rotating cylindrical roughness pair arrays are investigated. Based on the distance from the leading edge x, the Reynolds number at the inlet of the integration domain is $Re_x = \frac{u_\infty x_0}{\nu} = 0.8 \times 10^5$. Here, free-streamwise velocity is $u_\infty = 15(m/s)$ and the kinematic viscosity is $\nu = 1.5 \times 10^{-5}(m^2/s)$. The integration domain has a dimension of $0.8 \leq \frac{Re_x}{10^5} \leq 8$ in the streamwise direction and $0 \leq \frac{Re_y}{10^5} \leq 4$ in the wall-normal direction while $-1.5 \leq \frac{Re_z}{10^3} \leq 1.5$ in the periodic spanwise direction. Following the setup in Wu *et al.* [5], five pairs of positive-counter-rotating cylinders with height $k = 0.00075(m)$ and aspect ratio $\eta = \frac{D}{k} = 0.5$ which are spaced by $\frac{\lambda}{k} = 2$ (between cylinders within a pair) and $\frac{\Lambda}{k} = 8$ (between pairs) are placed at $Re_x = 1.2 \times 10^5$. At the cylinder station, the boundary layer displacement thickness is $\frac{\delta^*}{k} = 0.779$, and the roughness-height-based Reynolds numbers are $Re_k = 750$ and $Re_{kk} = 540.9$. To excite the H-type transition, a blowing & suction strip located at $1.42 \leq \frac{Re_x}{10^5} \leq 1.58$ is used to generate the TS and oblique waves. The non-dimensional fundamental and subharmonic frequencies are $F_1 = 1.24 \times 10^{-4}$ and $F_{1/2} = 0.62 \times 10^{-4}$, respectively. Here the dimensionless frequency parameter is $F = \omega\upsilon/{u_\infty}^2$. The wave amplitudes

are $\frac{A_1}{u_\infty} = 0.001$ and $\frac{A_{1/2}}{u_\infty} = 0.0001$. The wavelength of the oblique wave is $1/2$ of the computation spanwise dimension.

Following case C1 in Wu *et al.* [5], three rotation speeds are investigated, i.e., $\Omega_u = 0, 0.1, 0.2$. The overall effect of TS-instability attenuation can be well illustrated by the instantaneous vortical structures as shown by the Q-criterion in figure 1 and the evolution of the skin-friction coefficients C_f versus Re_x in figure 2. For the H-type transition on a flat plate, its skin friction in figure 2 deviates from the laminar correlation at $Re_x = 4 \times 10^5$, where the characteristic staggered Λ vortices begin to evolve, see figure 1(a). Prior to this location, the 2D TS wave in the form of a spanwise vortex gradually evolves into 3D Λ vortices. For the rotating cases in figure 1(b)(c)(d), their instantaneous vortices' evolutions are all modulated by the streamwise vortices that are induced by the counter-rotating cylindrical arrays. In both figures, a transition delay effect is distinct even with a complete stabilization or relaminarization for case $\Omega_u = 0.2$ in the investigated domain, which confirms the LST prediction in Wu *et al.* [5]. In the final paper, a Fourier analysis of the spatial evolution of the instabilities and perturbations will be presented.

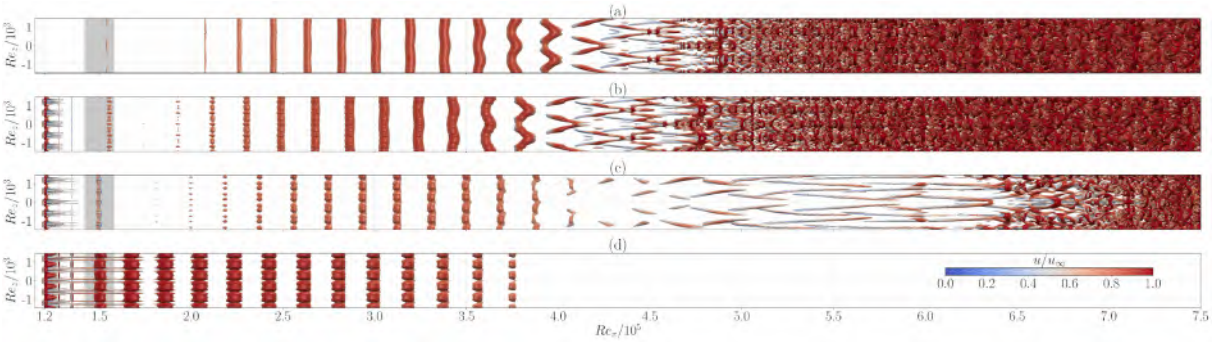

Figure 1. Iso-surfaces of the Q-criterion with $Q = 8 \times 10^4$ for (a): Flat plate reference, (b): $\Omega_u = 0$, (c): $\Omega_u = 0.1$ and $Q = 8 \times 10^3$ for (d): $\Omega_u = 0.2$. Color represents the streamwise velocity u/u_∞. Shaded region at around $Re_x = 1.5 \times 10^5$ marks the location of the TS generator.

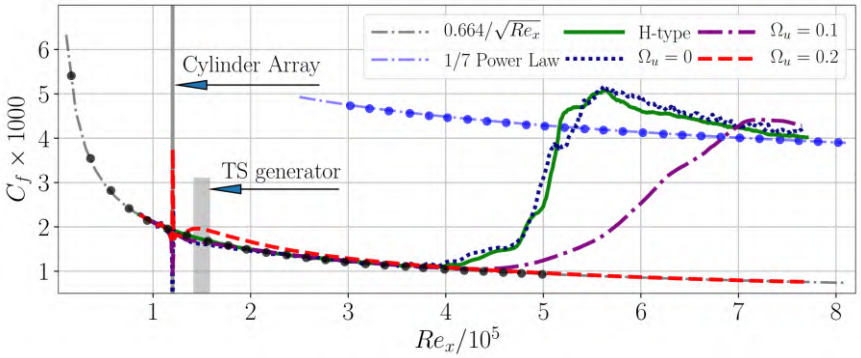

Figure 2. Local skin friction versus Re_x on flat plate.

References

1. Andersson, P., Brandt, L., Bottaro, A., & Henningson, D. S. (2001). On the breakdown of boundary layer streaks. *Journal of Fluid Mechanics*, *428*, 29-60.
2. Cossu, C., & Brandt, L. (2004). On Tollmien–Schlichting-like waves in streaky boundary layers. *European Journal of Mechanics-B/Fluids*, *23*(6), 815-833.
3. Fransson, J. H., Talamelli, A., Brandt, L., & Cossu, C. (2006). Delaying transition to turbulence by a passive mechanism. *Physical review letters*, *96*(6), 064501.
4. Loiseau, J. C., Robinet, J. C., Cherubini, S., & Leriche, E. (2014). Investigation of the roughness-induced transition: global stability analyses and direct numerical simulations. *Journal of Fluid Mechanics*, *760*, 175-211.
5. Wu, Y., Axtmann, G., & Rist, U. (2021). Linear stability analysis of a boundary layer with rotating wall-normal cylindrical roughness elements. *Journal of Fluid Mechanics*, *915*.

Mitteilung

Fachgruppe: Turbulenz und Transition

Modellierung von Turbulenzkeilen in korrelationsbasierten Transitionsmodellen

Michael Fehrs, Sebastian Helm
DLR, Institut für Aeroelastik, Bunsenstr. 10, 37073 Göttingen, michael.fehrs@dlr.de

Hintergrund

Die passive Laminarhaltung der Grenzschichtströmung auf Flügeln durch eine geeignete Konturgebung (Natural Laminar Flow Design) ist ein wichtiger Baustein, um den Reibungswiderstand zukünftiger Flugzeugkonfigurationen zu senken. Die Auslegung der Druckverteilung ermöglicht es hierbei, Anlegelinien-, Querströmungs- und Tollmien-Schlichting-Transition zu verhindern. Dennoch bleibt die laminare Grenzschicht anfällig für Störungen, die zu einem direkten Umschlag in den turbulenten Zustand führen. Beginnend bei der Störung bildet sich stromab ein Turbulenzkeil. Hierbei kann sich die lokal turbulente Strömung auf die Druckverteilung, das Ablöseverhalten und die Stoßposition auswirken. Dieser Effekt tritt gerade auch bei Windkanaltests von Laminarflügeln bei hohen Reynolds-Zahlen auf. Durch die enge Verzahnung von Winkanaltests und numerischer Modellierung im Entwurfsprozess ist es daher sinnvoll, Turbulenzkeile modellieren zu können, da nur so eine vollständige Beschreibung des experimentellen Grenzschichtzustands möglich ist.

Ziel

Dieser Artikel zeigt die Implementierung einer Turbulenzkeilfunktion in ein lokales, korrelationsbasiertes Transitionsmodell (γ-CAS-Modell, [1]) im DLR TAU-Code. Hierbei soll lediglich der Ort der Störung auf der Oberfläche des umströmten Körpers durch den Nutzer vorgegeben werden. Das Ziel ist, die Modellierung von Turbulenzkeilen sowohl in stationären als auch instationären CFD-Simulationen zu ermöglichen. In letzteren ergäbe sich ein fester Turbulenzkeil in einer ansonsten instationären Strömung – ein Effekt, der auch in instationären Windkanaltests zu finden ist.

Ansatz

Im DLR TAU-Codes existiert innerhalb des TAU-Transitionsmoduls [2] bereits die Möglickeit laminare Strömungsbereiche und einen Umschlag der Grenzschicht in Kombination mit Turbulenzmodellen vorzugeben. Helm et. al [3] zeigen auf diese Weise für die CRM-NLF-Konfiguration, dass bei Berücksichtigung der Turbulenzkeile auf dem Windkanalmodell eine bessere Modellierung der Aerodynamik und Aeroelastik gelingt. Eine ähnliche Funktionalität soll für das γ-CAS-Modell implementiert und getestet werden. Durch den Anwender soll hierbei die Koordinate einer Störung vorgeben werden, an der die Grenzschicht in den turbulenten Strömungszustand umschlägt. Hierbei ist es erforderlich, dass der Umschlag innerhalb eines weiten Reynoldszahlbereich robust funktioniert und sich ein Turbulenzkeil mit physikalisch richtigen Proportionen bildet.

Ergebnisse

Abbildung 1 zeigt die Verteilung des Wandschubsspannungsbeiwerts auf dem Flügel der CRM-NLF-Konfiguration und die Druckverteilung in einem ausgewählten Schnitt. Es ist hierbei ersichtlich, wie sich der frühere Umschlag der Grenzschicht auf die Druckverteilung und die Position des Stoßes auswirkt. Die laminaren und turbulenten Strömungsbereiche wurde mit dem TAU-Transitionsmodul definiert. Für die Strömung bei $RRee = 15 \cdot 10^6$, $MMaa = 0.856$,
$\alpha = 1.448°$ soll eine ähnliche Modellierung mit dem γ-CAS Transitionsmodell erfolgen.

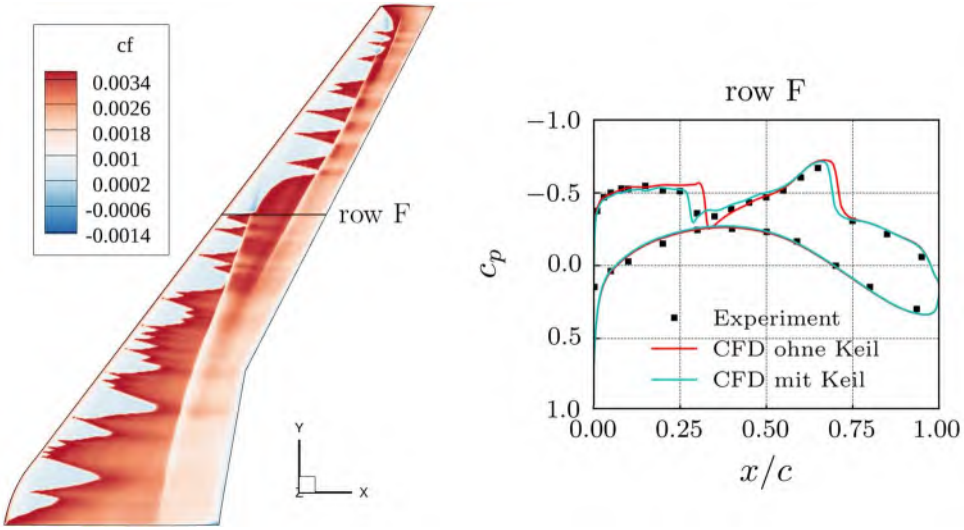

Abbildung 1 Wandschubsspannungsbeiwert und Druckschnitt an einer spannweitigen Position

Abbildung 2 zeigt das Ergebnis einer Machbarkeitsstudie mit einem einzelnen Turbulenzkeil an einem generischen Laminarflügel mit dem γ-Transitionsmodell [4]. Dargestellt ist die Verteilung des Wandschubspannungsbeiwerts c_f. Das Erreichen des Transitionskriterium wurde lokal erzwungen und es bildet sich ein Turbulenzkeil. Stromab des Turbulenzkeils kommt es am Stoß zu keiner Ablösung der Grenzschicht. Die Erfassung eben solcher Effekte ist zur Modellierung von Experimenten und zur Bewertung von Laminarkonfigurationen wichtig.

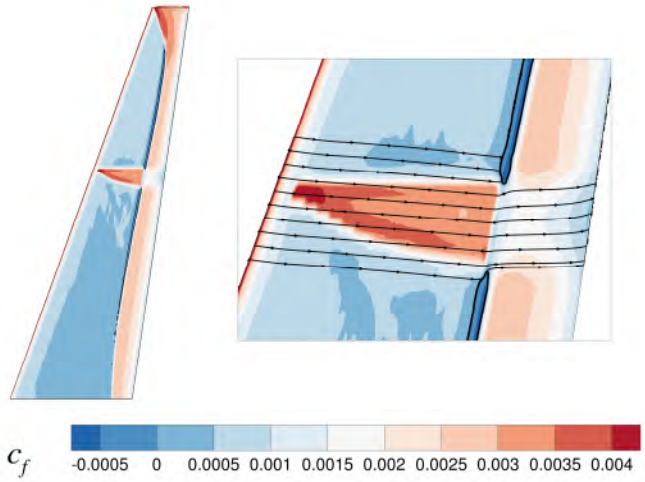

Abbildung 2 Turbulenzkeil und Wandschubspannungslinien an einem Laminarflügel mittels c_f-Verteilung dargestellt. Die zusätzliche schwarze Linie zeigt $c_f = 0$ an.

Literatur

1. Francois, D. G., Krumbein, A., Krimmelbein, N., Grabe, C. : Simplified Stability-Based Transition Transport Modeling for Unstructured Computational Fluid Dynamics. AIAA SciTech Forum (2022)
2. Krumbein, A., Krimmelbein, N., Schrauf, G.: Automatic Transition Prediction in Hybrid Flow Solver, Part 1: Methodology and Sensitivities. Journal of Aircraft, 46(4), 1176–1190 (2009)
3. Helm, S., Fehrs, M., Kaiser, C., Krimmelbein, N., Krumbein, A. : Towards CFD-based Aeroelastic Analysis of the CRM-NLF wing. AIAA Aviation Forum (2021)
4. Fehrs, M.: Boundary Layer Transition in External Aerodynamics and Dynamic Aeroelastic Stability. Dissertation, TU Braunschweig, ISSN 1434-8454, ISRN DLRFB–2018-11, also NFL-FB 2017-27, Braunschweig (2018)

Mitteilung

Fachgruppe: Turbulenz und Transition

First Comparison of CFD Simulation and Wind Tunnel Test of the Forward-Swept Natural Laminar Flow Model NLF-ECOWING-FSW

[1]Sebastian Helm, [1]Kristopher Davies, [1]Michael Fehrs
[1]DLR, Institut für Aeroelastik, Bunsenstr. 10, 37073 Göttingen, sebastian.helm@dlr.de

Background

The forward-swept NLF-ECOWING-FSW model is designed to facilitate extensive natural laminar flow (NLF) at a relatively high Mach number of 0.78. A wing-fuselage half model with a half-span of 1.25m was tested in the European Transonic Windtunnel (ETW). A first comparison of the experimental data with CFD simulations is presented in this paper.

Objective

CFD results shall be compared to wind tunnel data acquired at the ETW. The effect of turbulent wedges will be considered. The objective is to understand the steady aerodynamics of the NLF-ECOWING-FSW configuration. Eventually, this work aims at building the foundation for future unsteady investigations of this model.

Approach

The NLF-ECOWING-FSW model is a forward-swept NLF wing model designed as an advanced derivative of the TuLam configuration [1]. A CFD grid of the wing-body half model is generated using the commercial software CENTAUR. The DLR TAU-Code is used for RANS simulations. Transition prediction is based on the linear stability code LILO and the e^N method [2]. The transition location is determined by incompressible N-factors exceeding the critical value $N_{crit}=8$ for both crossflow and Tollmien-Schlichting transition. The CFD simulations are performed as a blind test at the Reynolds number of $Re_{MAC}=14x10^6$, whereas the most part of the wind tunnel data was acquired at the Reynolds number $Re_{MAC}=16x10^6$.

Results

As expected, the experimental lift curve with free transition lies between the CFD results for free transition and the fully turbulent simulations (Fig. 1). This is partly attributed to the loss of laminarity due to turbulent wedges [3]. Furthermore, a steeper gradient of the experimental results can be observed. This can be explained by static aeroelastic deformation of the forward swept wing, that is not included in the numerical simulations yet. Significant differences between experiment and simulation is apparent at angles of attack $\alpha>2.5°$. In this range, the numerical solution exhibits a side-of-body (SoB) separation that leads to a significant loss of lift. In contrast to that, the wind tunnel data reveals a nearly-linear rise of the lift curve up to $\alpha\approx3.0°$ before saturation sets in more gently compared to the CFD results.
Extensive laminar flow on the wing upper side is predicted (regions of low skin friction in Fig. 2, right). Laminar-turbulent transition occurs close to the shock for large portions of the wing span. In accordance with that, the temperature-sensitive-paint (TSP) images show large laminar areas (Fig. 2, middle). It is apparent that laminarity is reduced due to the presence of turbulent wedges present mainly at the most inboard TSP pocket.

The wind tunnel test was performed for a wide range of flow conditions. Accordingly, more comprehensive results and discussion will be presented in the full text paper.

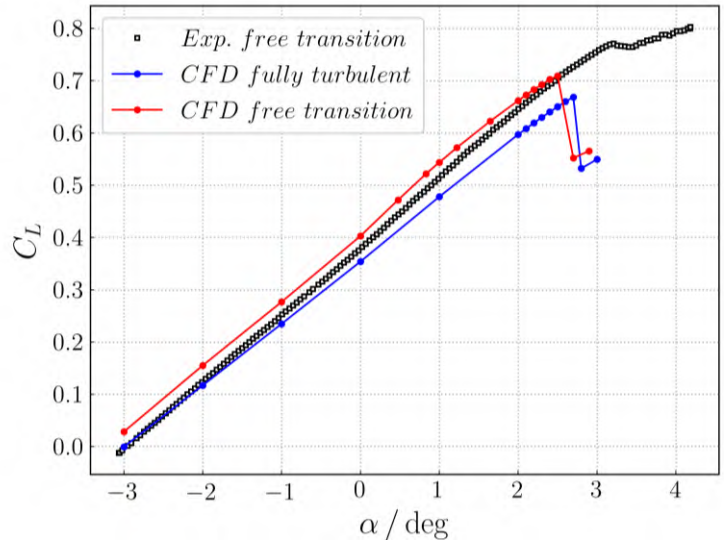

Fig. 1: Lift curve at M=0.78

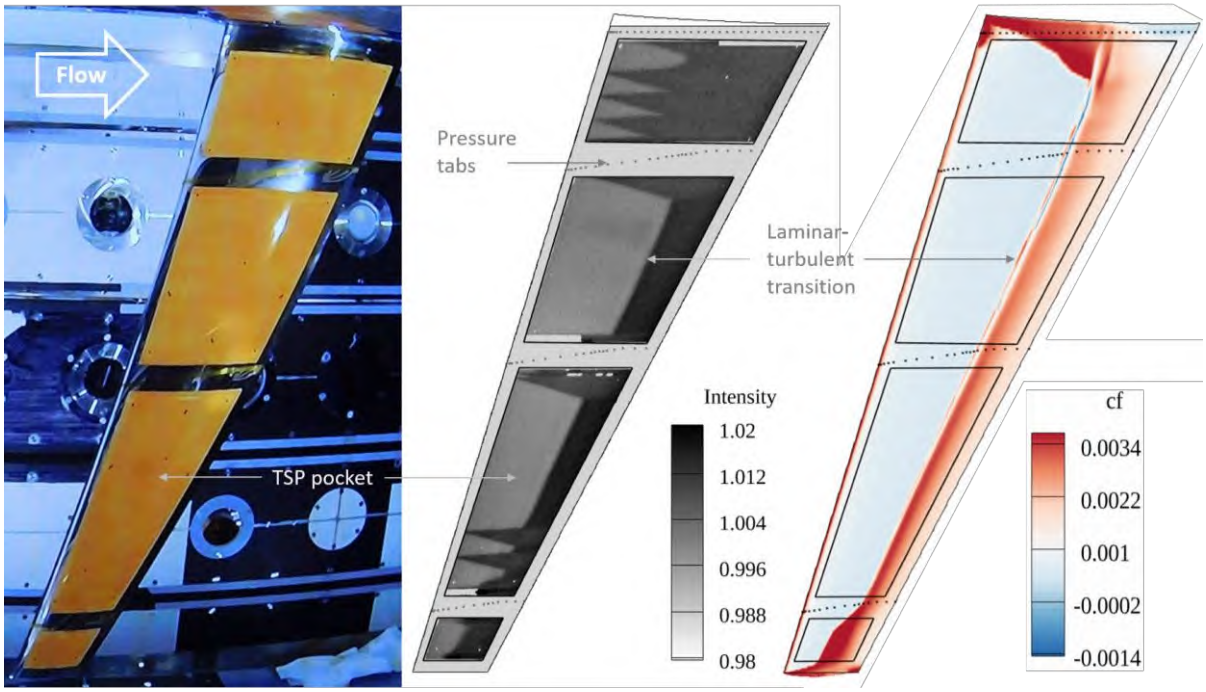

Fig. 2: NLF-ECOWING-FSW model in the ETW (left); TSP image (middle); CFD skin friction distribution (right)

Acknowledgement

The authors would like to thank the team of the ETW, the team of Airbus, the team of the DLR Department Aeroelastic Experiments and the team of the DLR Institute of Aerodynamics and Flow Technology for the provision of data.

Literature

[1] Seitz, A., Hübner, A., Risse, K.: The DLR TuLam project: design of a short and medium range transport aircraft with forward swept NLF wing. CEAS Aeronautical Journal (2019)

[2] Krumbein, A., Krimmelbein, N., Schrauf, G.: Automatic transition prediction in hybrid flow solver, part 1: Methodology and sensitivities. Journal of Aircraft, 46, pp. 1176-1190 (2009)

[3] Helm, S., Fehrs, M., Nitzsche, J.: Towards CFD-based Aeroelastic Analysis of NLF Wings. 21st STAB/DGLR Symposium on New Results in Numerical and Experimental Fluid Mechanics, 12, pp. 491-500 (2019)

Mitteilung

Fachgruppe: Turbulenz und Transition

Stochastic modeling of heat and momentum transfer in annular pipe flow:
A one-dimensional turbulence study with comparison to DNS and LES

Marten Klein Pei-Yun Tsai Heiko Schmidt

Lehrstuhl Numerische Strömungs- und Gasdynamik, Brandenburgische Technische Universität (BTU) Cottbus-Senftenberg, Siemens-Halske-Ring 15A, D-03046 Cottbus
marten.klein@b-tu.de

The predictive capabilities of numerical simulations for applications with coupled heat and momentum transport crucially depend on the fidelity of the numerical approach and the applicability of models for the unresolved scales. This concerns wall-bounded flows in general and transfer-limited applications in particular since these require an accurate representation of the scalar and momentum boundary layers. In engineering applications, such as cylindrical heat exchangers (e.g. [1,2,3]) or chemical reactors (e.g. [4]), further complications arise due to spanwise wall curvature and modification of boundary layer profiles (e.g. [5,6]). A canonical flow configuration for such devices is heated annular pipe flow, which is sketched in Fig. 1(a). Fluid is confined between two concentric coaxial cylinders and an axial mean flow is driven by a prescribed axial pressure gradient. In addition, the fluid is weakly heated by a prescribed wall heat flux q_w or, alternatively, by isothermal inner and outer cylinder walls that are held at different temperature (not shown here).

In filter-based approaches like Reynolds-averaged Navier–Stokes simulation (RANS) or large-eddy simulation (LES), the ensemble effect of turbulence is usually modeled based on gradient-diffusion closure assumptions that date back to Boussinesq [7] for RANS and Smagorinsky [8] for LES, respectively. In these approaches, it is usually not feasible to resolve small-scale turbulence in the vicinity of the wall. Instead, wall models (WM) are used [9,10]. For RANS, this means bypassing details of near-wall turbulence by prescribed wall functions. For LES/RANS near-wall turbulence is resolved in an average sense, and it is partly resolved in WMLES while an additional set of equations for the unresolved wall-shear stress and surface heat flux is solved. Unfortunately, the predictive capabilities of these approaches can be very limited when the application case differs from the calibration case. This is demonstrated in Fig. 1(b) for radial profiles of the normalized mean axial velocity in concentric annular pipe flow that have been obtained with OpenFOAM [11] (version 9) using the wall-adapting local eddy-viscosity (WALE) model with default parameters that have been calibrated for channel flow. For various radius ratios, $\eta = R_\mathrm{i}/R_\mathrm{o}$, a strong dependence on the grid resolution (here labeled as low “l” and high “h”) can be discerned.

The mentioned shortcoming in wall modeling due to spanwise curvature effects is addressed in the present study with the aid of the stochastic one-dimensional turbulence (ODT) model [12] formulated for cylindrical geometry [13]. ODT is a dimensionally reduced flow model that has been utilized recently as stand-alone tool for forward-modeling temporal boundary layers [14], differentially diffusing scalars in turbulent channel flows [15,16,17], and variable-density effects in heated pipe flow [18]. The model has recently also been used as subfilter-scale [19] and wall [20] model in LES demonstrating fidelity improvements at affordable cost. In the present study, stand-alone ODT is utilized in order to address radial transport processes by modeling turbulent stirring motions by a stochastically sampled sequence of radial mapping events that punctuate the continuous molecular-diffusive flow evolution. Fig. 1(c) demonstrates in terms of radial profiles of the normalized mean temperature profiles that ODT predictions for weakly heated annular pipe flow at moderate friction Reynolds $(Re_\tau \sim 300)$ and Prandtl $(Pr = 0.7)$ numbers are in reasonable agreement with available reference DNS. A

similar level of fidelity is obtained for the ODT mean axial velocity (not shown here). As in the case of the LES mentioned above, ODT model parameters have been kept fixed after calibration for channel flow [15,16] by making use of the model's predictive capabilities.

In the contribution, we will discuss how the heat and momentum transfer to the cylindrical domain walls depends on the geometric (radius ratio and thermal wall boundary condition) as well as physical (Reynolds and Prandtl number) control parameters. We will show that the stochastic model is able to capture radius ratio, Reynolds, and Prandtl number effects for fixed model parameters and, thus, exhibits good predictive capabilities with respect to the mean. In addition, we will analyze low-order flow statistics and fluctuation budget balance equations for the radially asymmetric boundary layers over the inner and outer cylinder, respectively. We will demonstrate that small curvature radii affect boundary layer profiles also at high Reynolds numbers suggesting that wall modeling over spanwise curvature must be done carefully and may demand advanced modeling strategies for robust predictions.

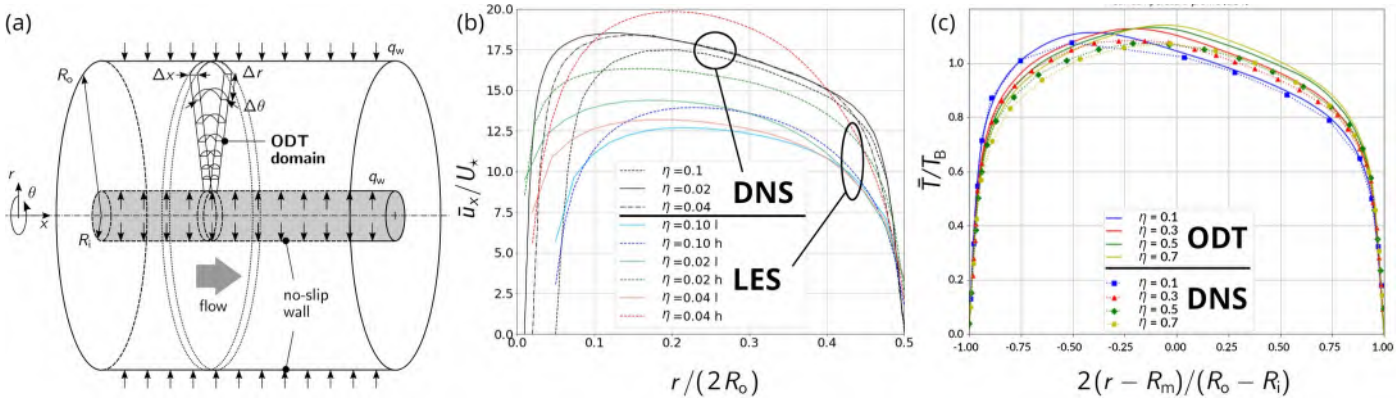

Fig. 1: (a) Sketch of the heated concentric coaxial pipe flow configuration investigated. (b) Radial profiles of the normalized mean axial velocity predicted by LES (OpenFOAM-9, WALE model) in comparison to reference DNS [6]. (c) Radial profiles of the normalized mean temperature predicted by ODT in comparison to reference DNS [3]. For both, ODT and WALE, model parameters originally calibrated for channel flow were used and kept fixed.

References

[1] S. Y. Chung, G. H. Rhee, H. J. Sung, *Int. J. Heat Fluid Flow* **23:**426–440, 2002.
[2] S. Y. Chung, H. J. Sung, *Int. J. Heat Fluid Flow* **24**(3):399–411, 2003.
[3] E. Bagheri, B.-C. Wang, *Phys. Fluids*, **33**(5):055131, 2021.
[4] E. Balestrin, S. M. Arruda Guelli Ulson de Souza, J. A. B. Valle, A. da Silva, *Chem. Eng. Res. Design*, **170**:90–106, 2021.
[5] J. M. Nouri, H. Umur, J. H. Whitelaw, *J. Fluid Mech.* **253**:617–641, 1993.
[6] B. J. Boersma, W.-P. Breugem, *Flow Turbulence Combust.* **86**:113–127, 2011.
[7] J. Boussinesq, *Théorie Analytique de la Chaleur*, Vol. II, Gauthier-Villars, 1903.
[8] J. S. Smagorinsky, *Mon. Weather Rev.* **91**:99–164, 1963.
[9] U. Piomelli, *Progress Aerospace Sci.* **44**:437–446, 2008.
[10] J. Larsson, S. Kawai, J. Bodart, I. Bermejo-Moreno, *Mech. Eng. Rev.* **3**:1500418, 2016.
[11] H. G. Weller, G. Tabor, H. Jasak, C. Fureby, *Comput. Phys.* **12**(6):620, 1998.
[12] A. R. Kerstein, *J. Fluid Mech.* **392**:277–334, 1999.
[13] D. O. Lignell, V. B. Lansinger, J. A. Medina Méndez, M. Klein, A. R. Kerstein, H. Schmidt, M. Fistler, M. Oevermann, *Theor. Comput. Fluid Dyn.* **32**:495–520, 2018.
[14] Rakhi, M. Klein, J. A. Medina Méndez, H. Schmidt, *J. Turbul.* **20**(8):506–543, 2019.
[15] M. Klein, H. Schmidt, STAB/DGLR Symposium 2020, *NNFM* **151**:47–57, 2021.
[16] M. Klein, H. Schmidt, D. O. Lignell, *Int. J. Heat Fluid Flow*, **93**:108889, 2022.
[17] M. Klein, C. Zenker, H. Schmidt, *Chem. Eng. Sci.* **204**:186–202, 2019.
[18] J. A. Medina Méndez, M. Klein, H. Schmidt, *Int. J. Heat Fluid Flow* **80**:108481, 2019.
[19] C. Glawe, J. A. Medina Méndez, H. Schmidt, *Z. Angew. Math. Mech.* **98**:1907–1923, 2018.
[20] L. S. Freire, M. Chamecki, *Comput. Fluids* **230**:105135, 2021.

Mitteilung

Fachgruppe: Turbulenz und Transition

Large Eddy Simulations Towards Industrial Relevant Flows on Graphics Processing Units

Dr.-Ing. Christian Lübon

SimIoTec GmbH
Telawiallee 2
88400 Biberach

christian.luebon@simiotec.com

Since a couple of years the feasibility of Large Eddy Simulation (LES) for industrial relevant flows has been discussed (Slotnick, et al., 2014). In order to overcome the limiting factor for LES, the required computing time, especially for wall bounded flows, Wall-Modeled Large Eddy Simulation (WMLES) has been continuously improved and new powerful HPC hardware such as graphics processing units (GPUs) is available.
To demonstrate the applicability and effectiveness this approach a number of test cases with different LES models were calculated by using the open-source GPU solver OpenCruncher and the results were investigated. This provides the basis for further developments towards industrial applications.

The solver OpenCruncher is a density based, second order explicit solver optimized for GPUs. It uses the parallel infrastructure and high flop counts of current GPUs and makes it possible to perform LES calculations on a workstation.
Various LES models are available. WMLES is an extension to the classical LES which couples the Prandtl–van Driest Reynolds Averaged Navier Stokes (RANS) model and the Smagorinsky (Smagorinsky, 1963) subgrid-scale (SGS) model. This reduces the Reynolds number dependent grid resolution requirements of classical wall-resolved LES. An alternative is the wall-adapting local eddy-viscosity (WALE) model (Nicoud & Ducros, 1999) often combined with wall functions (Kalitzin, Medic, Iaccarino, & Durbin, 2005). For some cases the generation of artificial turbulent fluctuations as an inlet condition is necessary, here a Fourier based synthetic turbulence generator is used (Bechara, Bailly, Lafon, & Candel, 1994) (Adamian & Travin, 2013).

For basic validation of the LES models we have started with very simple cases like the decaying isotropic turbulence (DIT) test and have analysed the energy spectra. The Reynolds stress components and the turbulent kinetic erergy distribution were investigated with with another case, the Volvo triangular cylinder case (Sjunnesson, Nelsson, & Max, 1991), figure 1. For wall bounded flows the turbulence lenght scale and the size of the turbulent eddies reduces close to the wall. To resolve these structures a high resolution in space and in time is required (WRLES), especially for higher Reynolds numbers this becomes very expensive in terms of computational time. When making use of wall functions (WFLES) or wall models (WMLES) this scaling behavior and the computational time can be reduced. But one has to keep in mind that we introduce additional modeling errors. Therefore careful validation of the wall functions and models with the turbulent periodic channel case (Kim, Moin, & Moser, 1987), a periodic hill flow (Fröhlich, Mellen, Rodi, Temmerman, & Leschziner, 2005) and the flat plate with synthetic turbulence at the inlet has been done.
As a high Reynolds number case a LES of the turbulent flow with a complex boundary layer past the Aérospatiale A-airfoil was performed and compared with simulations (Mary & Sagaut, 2002) and wind-tunnel experiments (Gleyzes & Capbern, 2003).

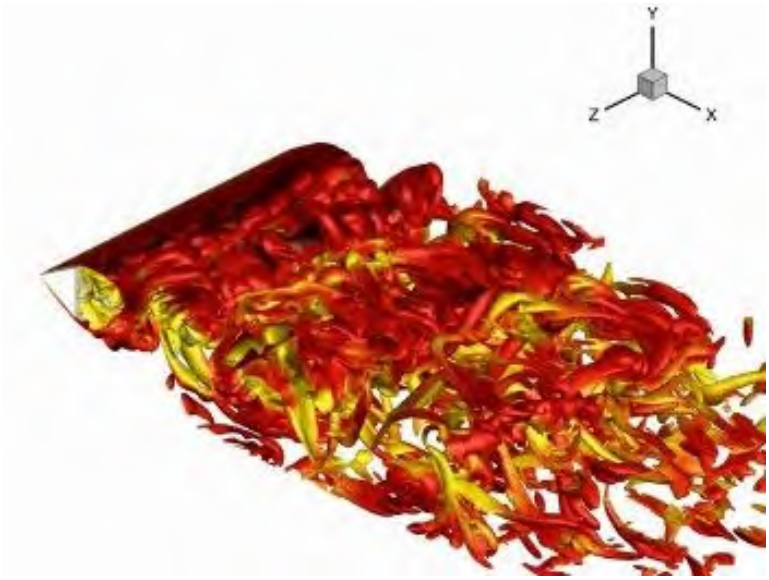

Figure 1: Turbulent flow past a triangular cylinder

We show that WMLES and synthetic turbulence delivers promising results, at least for academic cases, such as two-dimensional geometries. All these simulations were cheap in terms of computational time and hardware costs and ran on workstations equipped with consumer GPUs. The next step is to calculate more complex three-dimensional cases, starting form the Ahmed body and the DrivAer configuration to the Onera M6 wing and an NREL phase VI wind turbine rotor.

References

Adamian, D., & Travin, A. (2013). Assessment of an approach to generating inflow synthetic turbulence for large eddy simulations of complex turbulent flows. *Progress in Flight Physics 5*, S. 43–54.

Bechara, W., Bailly, C., Lafon, P., & Candel, S. (1994). Stochastic Approach to Noise Modeling for Free Turbulent Flows. *AIAA Journal 32*, S. 455–463.

Fröhlich, J., Mellen, C., Rodi, W., Temmerman, L., & Leschziner, M. (2005). Highly resolved large-eddy simulation of separated flow in a channel with streamwise periodic constrictions. *J. Fluid Mech., vol 525*, S. 19-66.

Gleyzes, C., & Capbern, P. (2003). Experimental study of two AIRBUS/ONERA airfoils in near stall conditions. Part I: Boundary layers. *Aerospace Science and Technology, vol. 7*, S. 439-449.

Kalitzin, G., Medic, G., Iaccarino, G., & Durbin, P. (2005). Near-wall behavior of RANS turbulence models and implications for wall functions. *Journal of Computational Physics 204*, S. 265–291.

Kim, J., Moin, P., & Moser, R. (1987). Turbulence statistics in fully developed channel flow at low Reynolds number. *J. Fluid Mech., vol. 177*, S. 133-166.

Mary, I., & Sagaut, P. (2002). Large Eddy Simulation of Flow Around an Airfoil Near Stall. *AIAA Journal, vol. 40, no. 6*.

Nicoud, F., & Ducros, F. (1999). Subgrid-scale stress modelling based on the square of the velocity gradient tensor. *Flow, Turbulence and Combustion 62*, S. 183–200.

Sjunnesson, A., Nelsson, C., & Max, E. (1991). LDA measurements of velocities and turbulence in a bluff body stabilized flame.

Slotnick, J., Khodadoust, A., Alonso, J., Darmofal, D., Gropp, W., Lurie, E., & Mavriplis, D. (2014). CFD Vision 2030 Study: A Path to Revolutionary Computational Aerosciences. *Langley Research Center, NASA CR-2014-218178*.

Smagorinsky, J. (1963). General Circulation Experiments with the Primitive Equations. *The Basic Experiment, Mon. Weather Rev. 91*, S. 99–165.

Mitteilung

Fachgruppe: Turbulenz und Transition

Thema/Titel des Beitrags: Contribution of Vortices to Laminar-Turbulent Transition in a Boundary Layer Disturbed by a Roughness Element

Tristan Römer, Ulrich Rist
Institut für Aerodynamik und Gasdynamik, Universität Stuttgart
Pfaffenwaldring 21, 70569 Stuttgart, roemer@iag.uni-stuttgart.de

The classical laminar-turbulent transition in boundary layers is characterized by the exponential growth of a primary instability, which is the Tollmien-Schlichting (TS) wave for small initial disturbances. If the TS wave is grown to a finite amplitude, there follows a three-dimensional (3D) secondary instability characterized by a resonance type. Common resonance types are the fundamental resonance (K-type, [1]) and the subharmonic (H-type, [2]) resonance, which differ in the aligned Λ-vortices in streamwise and spanwise direction. The secondary instability finally leads to a turbulent boundary layer [1,2].

Placing a three-dimensional (3D) roughness element in a laminar boundary layer, the boundary layer usually undergoes a premature transition. Moreover, the breakdown to turbulence differs from the classical TS breakdown. This can be demonstrated at the vortex formation downstream of a cylindrical roughness element, where two major vortices can be found: a horseshoe and hairpin type [3]. The vortices are illustrated in Figure 1 (A: hairpin; B: horseshoe) by dye streakline visualization. The horseshoe vortex wraps around the cylinder and forms low-speed and high-speed streaks in the roughness element wake. If the Reynolds number $Re_k = U_e k/\nu$, being U_e the free-stream velocity and k the cylinder roughness height, exceeds a certain value, hairpin vortices periodically separate from the top of the cylinder. Although these primary structures, which are followed by complex secondary structures, have been intensively studied (e.g. [3,4]), the decay of those structures leading to roughness-induced transition is not fully understood.

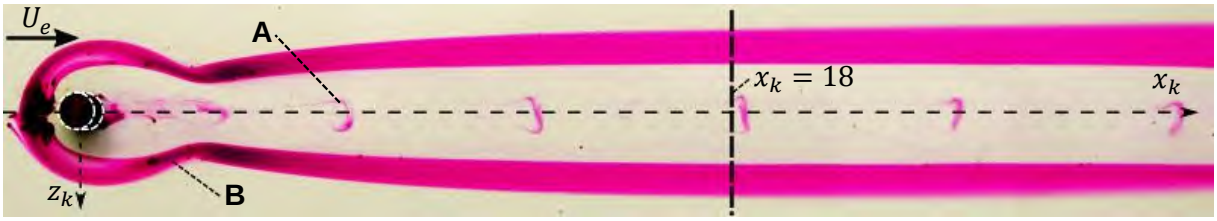

Figure 1: Overview of hairpin (A) and horseshoe (B) vortex for $Re_k = 770$

The focus of this research is on the development of secondary structures and how primary and secondary structures contribute to laminar-turbulent breakdown. For this purpose, experiments have been performed in the Laminar-Water-Channel (LaWaKa), where a flat plate forms a Blasius boundary layer. A cylindrical roughness element with height $k = 10\ \mathrm{mm}$ and diameter $d = 10\ \mathrm{mm}$ (aspect ratio $\eta = d/k = 1$) is placed $570\ \mathrm{mm}$ behind the leading edge of the flat plate. Hot-film measurements and visualizations by hydrogen bubble and dye streaklines are performed in the wake of the cylinder.

Figure 2 (left) shows hydrogen bubble snapshots at $x_k = 18$ (compare with Figure 1) for different time snapshots $t_0 < t_1 < t_2$. The origin of the x_k, y_k, z_k-coordinate system (non-dimensionalized by k) is at the roughness element, where x_k gives the distance to the cylinder in streamwise direction and y_k gives the wall-normal distance. The Reynolds number $Re_k = 770$ is higher than the transition Reynolds number $Re_{k,tr} = 666$, where $Re_{k,tr}$ is identified by hot-film measurements and is comparable with the results from Puckert et al. [5].

At t_0, the hairpin head (A) can be clearly identified in Figure 2 (left). In the next snapshot t_1, the hairpin head has passed and the hairpin legs are visible at $y_k = 1$. The hairpin is connected to a Λ-vortex (C), which has also been observed by Acarlar and Smith [3] and is comparable to the known Λ-vortex from classical boundary layer transition. At t_2, a new structure (D) can be identified, here named a V-vortex. The V-vortex is located between the Λ-vortex and the wall. It seems that the hairpin pushes the Λ-vortex in spanwise direction, as shown by the red arrows in Figure 2.

To identify the contribution of these vortices to roughness induced laminar-turbulent breakdown, the fluctuation power measured by a hot-film probe is presented in Figure 2 (right) at the same $x_k = 18$ position. Note that the measurements were taken only from the center of the cylinder, as there is a clear symmetry to the Y-axis (compare Figure 2 (left)). It is clearly visible, that the Λ-vortex (C) is the most dominant in terms of fluctuation power, while the hairpin and the V-vortex (D) have about 50% of the power of the Λ-vortex. This indicates, that the Λ-vortex contributes most to laminar-turbulent breakdown. In the full paper, visualizations of the Λ-vortex and V-vortex are shown in more detail. Moreover, further YZ-layers at different x_k positions will be presented, to demonstrate the impact of those structures to laminar-turbulent transition more quantitatively.

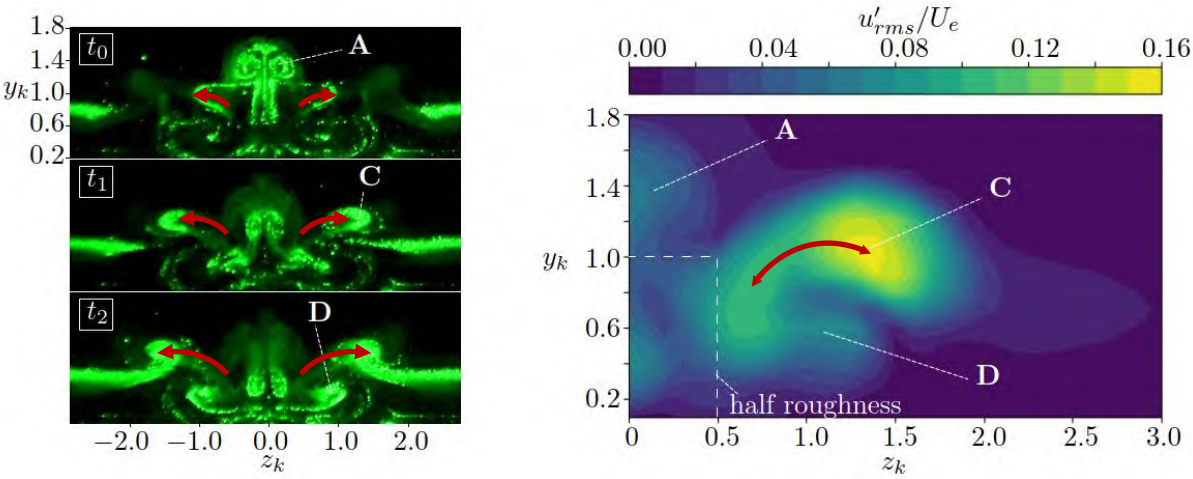

Figure 2: Hydrogen-bubble snapshots (left) and hot-film measurements (right) at $x_k = 18$ for $Re_k = 770$. The red arrows indicate the spanwise movement of the Λ-vortex.

References

[1] Klebanoff P.S., Tidstrom K.D., Sargent L.M. The three-dimensional nature of boundary-layer instability. J. Fluid Mech. 1962;12:1–34.

[2] Herbert T. Secondary instability of plane channel flow to subharmonic three-dimensional disturbances. Phys. Fluids. 1983;26:871.

[3] Acarlar M.S., Smith C.R. A study of hairpin vortices in a laminar boundary layer. Part 1. Hairpin vortices generated by a hemisphere protuberance. J. Fluid Mech. 1987;175:1.

[4] Ergin F.G., White E.B. Unsteady and Transitional Flows Behind Roughness Elements. AIAA Journal. 2006;44:2504–2514.

[5] Puckert D.K., Römer T.M., Scibelli G., Rist U. Experimental Investigation on Roughness-Induced Transition Under the Influence of Freestream Turbulence. In: Dillmann A, Heller G, Krämer E, et al., editors New Results in Numerical and Experimental Fluid Mechanics XIII; 2021; p. 205–214.

Mitteilung

Fachgruppe: Turbulenz und Transition

Rotation and Curvature Correction for Turbulent Diffusion inside a Differential Reynolds-Stress Model

P. Ströer and T. Knopp
Deutsches Zentrum für Luft- und Raumfahrt, Institute of Aerodynamics and Flow Technology,
Bunsenstraße 10, 37073 Göttingen, philip.stroeer@dlr.de

In many flow configurations, mean-streamline curvature can have a major impact on the turbulent boundary-layer or the turbulent wake. Flow features like curved surfaces, curved wakes or vortices inevitably occur in aerodynamical flows. Therefore, reliable simulation capabilities need to be provided for these kinds of flows.

For Reynolds-Stress Turbulence models (RSM) like the SSG/LRR-ω model [1] and other differential Reynolds stress models it is known that the production term captures rotation and curvature effect in a natural way. According to Zeman [2] third moments inside the turbulent diffusion terms can become important in case of curved streamlines. However, these terms are not preserved using the simple or the general gradient diffusion hypothesis (SGDH/GGDH). For this purpose, Zeman derived a corrected eddy viscosity ν_{Tr} that is eventually used inside the SGDH or GGDH, respectively, the following way (shown here for SGDH):

$$\rho D_{ij} = \nabla \cdot (\mu + \rho \nu_{Tr}) \nabla R_{ij} \tag{1}$$

The SGDH models the turbulent diffusion inside the Reynolds-stress equations:

$$\partial(\rho R_{ij})/\partial t + \partial(\rho\, u_k\, R_{ij})/\partial x_k \; = \rho P_{ij} + \rho \Pi_{ij} - \rho \varepsilon_{ij} + \rho D_{ij}, \tag{2}$$

where R_{ij} is the Reynolds-stress tensor, P_{ij} is prodcution, Π_{ij} is the pressure-strain correlation and ε_{ij} is the disspation-rate tensor. The correction might be also used inside the length scale equation. The additional term ν_{Tr} is derived utilizing the linearized equation for the fluctuating Lagrangian velocities and reads [2]:

$$\nu_{Tr} = c_1\, \tau\, \overline{v'^2}/(1 + (c_2\tau)^2 K_z^{2\prime}/(2r^3)\,) \tag{3}$$

where r is the radius (cf. Fig. 1), τ is a turbulent time scale, $\overline{v'^2}$ is the Reynolds-stress component that is normal to the mean streamline, K_z is the mean-angular momentum in z-direction and the prime denotes the radial derivation.

Applying this correction inside a general Computational Fluid Dynamics (CFD) code leads to several issues since this formulation is neither grid-point local nor general. Therefore, the current work deals with a grid-point local and general reformulation of the correction term Eq. (3) and application to verification and validation test cases. In a first step this equation is reformulated, so that only two non-local quantities remain: One is the radial gradient of the tangential velocity and one is the so-called gradient Richardson number for streamline curvature, that already includes the former quantity. That is, a local and general representative of the gradient Richardson number needs to be derived.

For verification purposes, the channel with U-turn test case was computed [3]. The advantage of this test case is that (in regions with attached flow) quantities like the radius and the radial derivative in polar coordinates can be computed exactly (cf. Fig. 1). In this way, an analytical reference solution can be provided for verification purposes.

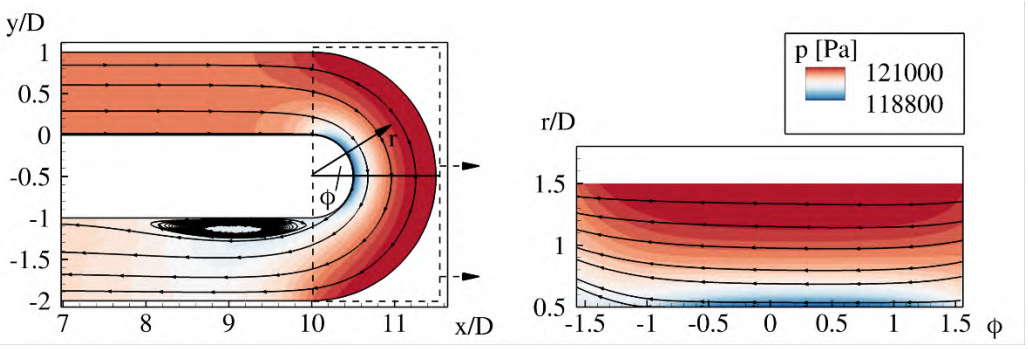

Fig. 1: Channel with U-turn test case [3] in Cartesian (*left*) and polar coordinates (*right*), $[\phi] = 1\,rad$

In the literature a reformulation of the gradient Richardson number by Hellsten [4] is available. However, this Richardson number does not match the analytical reference by Bradshaw [5] for the channel with U-turn test case. This can be seen from Fig. 2 (*right*). Performing a detailed analysis in polar coordinates a new gird-point local and general Richardson number was derived. In this context, it was found that the Richardson number of Ref. [4] neglects the effect of the angular velocity in the denominator.
Results of the verification are shown in Fig. 2 (cf. Fig. 1, *right*). The Figure on the right-hand side provides a comparison of the analytical Bradshaw definition, the Richardson number of Ref. [4] and the new formulation at a fixed angle $[\phi] = 0\,rad$ over the radius. It can be seen that the new formulation shows a significantly better agreement with the analytical reference.

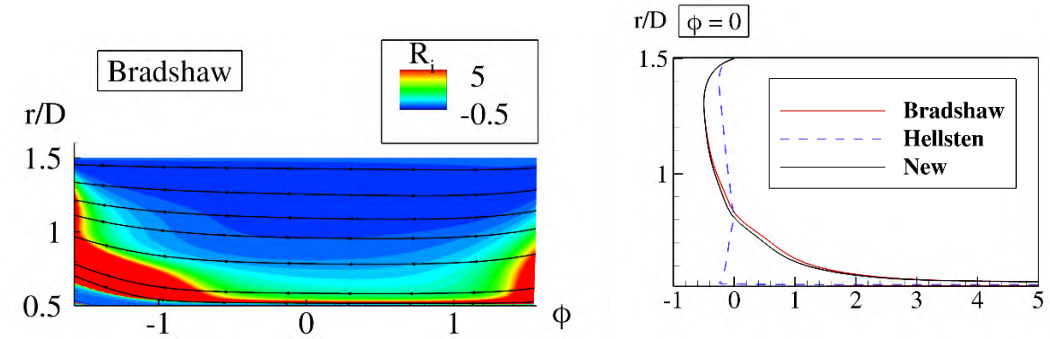

Fig. 2: Contour of the analytical Bradshaw gradient Richardson number (*left*) and comparison of different Richardson numbers at $\phi = 0\,rad$ (*right*)

For the full contribution the derivation of the correction term is presented in detail. Moreover, an in-depth verification will be presented. The final formulation of the new Richardson number is eventually used inside the correction term Eq. (3). The validation of this term inside the SSG/LRR-ω model will be done using the experimental results of Ref. [3]. In addition, another test case will be used for verification and validation purposes. Moreover, it is planned to apply the new Richardson number to further test cases in order to characterize rotation effects (e.g. the DLR/Uni Bw turbulent boundary layer experiment with convex curvature and a wake flow above the flap of a multi-element airfoil).

References:
[1] Eisfeld, B., Rumsey, C., and Togiti, V., "Verification and validation of a second-moment-closure model." AIAA Journal, Vol. 54, No. 5, 2016, pp. 1524 - 1541.
[2] Zeman, O., "The persistence of trailing vortices: a modeling study," Physics of Fluids, Vol. 7, No. 1, 1995, pp. 135 - 143.
[3] Monson,D. J., Seegmiller, H. L., McConnaughey,P. K., and Chen, Y. S., "Comparison of Experiment with Calculations Using Curvature-Corrected Zero and Two Equation Turbulence Models for a Two-Dimensional U-Duct," AIAA Paper 90-1484, 1990.
[4] Hellsten, A., "Some improvements in Menter's $k-\omega$ SST turbulence model," AIAA Paper 98-32817, 1998.
[5] Bradshaw, P., "The analogy between streamline curvature and buoyancy in turbulent shear flows," Journal of Fluid Mechanics,
Vol. 36, No. 177, 1969.

Mitteilung

Fachgruppe: Turbulenz und Transition

A surrogate-based e^N transition prediction method for three-dimensional compressible boundary layers

Alexander Theiss, Stefan Hein
DLR – Institut für Aerodynamik und Strömungstechnik
Bunsenstr. 10, D-37073 Göttingen, Germany, alexander.theiss@dlr.de

Background and Motivation

The state of the boundary layer (laminar, transitional, or turbulent) significantly affects the skin friction drag of objects moving through the air. A physics-based, commonly used transition prediction technique is the e^N method employing linear stability theory (LST) and semi-empirical transition criteria. Transition is assumed when the integrated amplification rate of a disturbance mode reaches a threshold value, the critical N-factor. Although the LST-based e^N method has been widely used for transition prediction by expert users, it is still quite complicated to handle in an automated transition prediction framework, e.g., within a RANS simulation. Difficulties include the preparation of the basic flow, the automatic selection of initial guess values for the eigenvalue computation, and selections of relevant frequencies and wavenumbers that contribute to the N-factor envelope. Therefore, efforts have been made for simplified e^N methods, such as surrogate-based e^N methods [1]. The surrogate-based e^N methods directly model the characteristics of instability modes instead of using envelope [2] or parabola [3] simplifications and are robust with no human-in-the-loop iteration to yield reasonable results. However, most surrogate-based e^N methods have been proposed for two-dimensional compressible or three-dimensional incompressible flows. This work proposes a radial basis function (RBF)-based surrogate model for three-dimensional compressible boundary layers aiming to reproduce the instability characteristics of two-dimensional (2D) Tollmien-Schlichting waves (TSI) and stationary cross-flow instabilities (CFI).

Approach and Results

The proposed surrogate-based e^N transition prediction method consists of three steps. In the first step, the instability characteristics of TSI and CFI are precomputed with LST for various three-dimensional (3D) compressible boundary layers. The 3D boundary layers are obtained from compressible Falkner-Skan-Cooke local similarity solutions [4] for Mach numbers $Ma \in [0,1.4]$ (typically encountered in boundary layers on transport aircraft). The precomputed instability results are then used to precalculate samples of RBF-based surrogate models with thin-plate spline basis functions for TSI and CFI. The 2D TSI surrogate-based model can be expressed as $(\sigma, \alpha_r) = f(Ma_e, H_{12}, Re_{\delta_1}, \omega)$, where σ represents the spatial growth rate, α_r the streamwise wavenumber, Ma_e the boundary-layer edge Mach number, H_{12} the incompressible shape factor, Re_{δ_1} the Reynolds number built with the displacement thickness, and ω stands for the nondimensional circular frequency. For stationary CFI, the surrogate model can be represented as $(\sigma, \alpha_r) = f(Ma_e, \theta_{sw}, V_{max}, Re_{CF}, \beta)$, where θ_{sw} is the local sweep angle, V_{max} the maximum cross-flow velocity, Re_{CF} the cross-flow Reynolds number, and β the transverse wave number. The time required for the calculation of the RBF interpolant and the evaluation of the surrogate model depends significantly on the number of sample points. A sample partition method is utilized to split the entire sample set into a series of sub-samples sets. Hence, the RBF interpolants are precomputed for each of these sub-sample sets. The second step of the surrogate-based e^N transition prediction method involves the evaluation of the corresponding sub-sample-set and surrogate model for given flow conditions to predict amplification rates. In the last step, the local growth rates are integrated into N-factors, and transition can be predicted at the position where the critical N-factor is reached.

To validate the proposed method, Fig. 1 shows the growth rate of stationary CFI predicted by the RBF surrogate model and LST for a 3D compressible local similarity boundary-layer profile not included in the sample set to build the surrogate model.

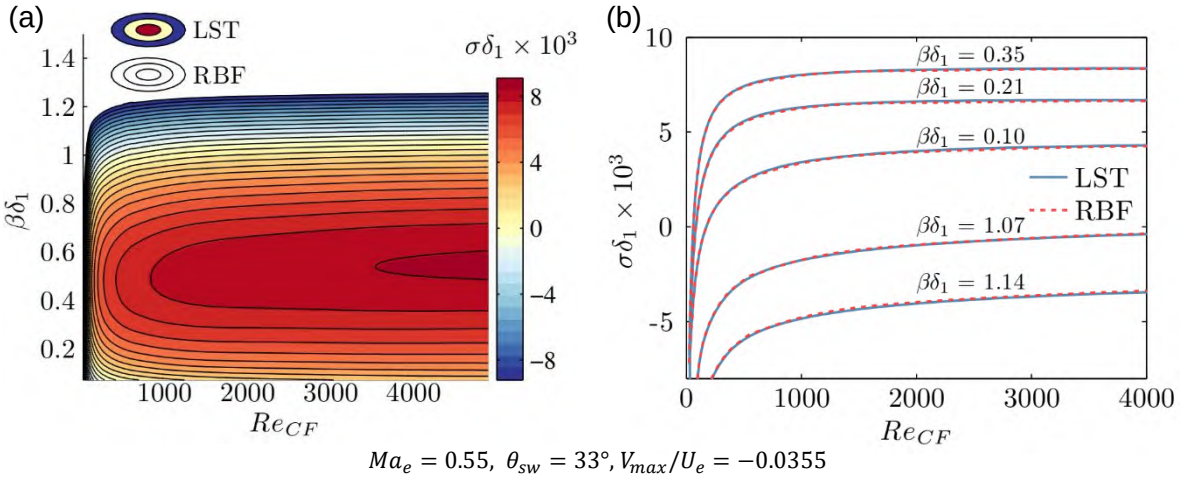

Figure 1: Comparison of LST and RBF growth rates for a 3D compressible local similarity solution.

The stationary CFI surrogate model is evaluated for a 3D flow stemming from a boundary-layer computation for a measured c_p distribution of a DLR ATTAS flight test experiment with $Ma_\infty = 0.7$ and $Re_\infty = 21.1 \times 10^6$. Figure 2 shows the evolution of the CFI N-factor curves for selected transverse wave numbers obtained from LST and RBF surrogate model. Overall, a good agreement of the N-factor results can be identified. The slight deviations of the RBF model is likely due to the non-locality of the basic flow, which can not be addressed with the local similarity solutions used to build the surrogate model.

The final paper will contain more detailed verifications of TSI and CFI RBF-based surrogate models and the compressible Falkner-Skan-Cooke local similarity solver. Moreover, the advantages and disadvantages of the proposed surrogate-based e^N transition prediction method are discussed in more detail.

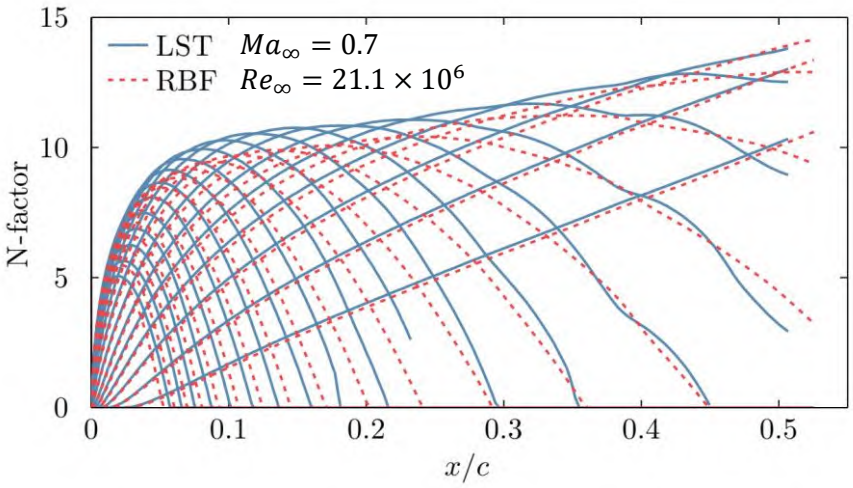

Figure 2: Comparison of CFI N-factors computed with LST and RBF surrogate model for a DLR ATTAS flight test.

References

[1] H Nie, W. Song, Z. Han, J. Chen, and G. Tu. A Surrogate-Based e^N Method for Compressible Boundary-Layer Transition Prediction. *Journal of Aircraft*, 59(1), 89-102, 2022.

[2] M. Drela. Implicit Implementation of the Full e^N Transition Criterion. AIAA Paper 2003-4066, 2003.

[3] B. Guillaume, H. Deniau, O. Vermeersch, and G. Casalis, “Database Approach for 2D Flow Transition Prediction in a RANS Code. AIAA Paper 2016-3488, 2016.

[4] Z. Liu. Compressible Falkner–Skan–Cooke boundary layer on a flat plate. *Physics of Fluids* , 33, 126109, 2021.

Mitteilung

Fachgruppe: Turbulenz und Transition

Übersicht über die Windkanalversuche mit Absaugung im DNW-NWB

R. von Soldenhoff (Richard.vonSoldenhoff@dlr.de)
Deutsches Zentrum für Luft- und Raumfahrt (DLR), Institut für Aerodynamik und Strömungstechnik
Lilienthalplatz 7, 38108 Braunschweig

Zur Erprobung neuer Absaugoberflächen werden am DLR Windkanalversuche mit Absaugung an einer modular aufgebauten ebenen Platte duchgeführt. Die ersten Versuche an diesem Modell fanden 2019 statt, es folgte eine Kampagne 2021. Das Windkanalmodell besteht aus einer aerodynamisch geformten Nase, einem 4 m langen ebenen Bereich sowie einer verstellbaren keilförmigen Klappe an der Hinterkante. Es ist modular aufgebaut, sodass sich einzelne Elemente austauschen lassen. Absaugpanels können im 500 mm breiten mittleren Bereich eingesetzt werden (vgl. Abb. 1). Deren Maße betragen wahlweise 200 x 500 mm oder 400 x 500 mm und lassen sich beliebig positionieren sowie aneinanderreihen [2].

Die Druckverteilung auf dem Modell lässt sich über den Anstellwinkel und den Hinterkantenwinkel derart einstellen, dass die Transition ohne Absaugung für alle Anströmgeschwindigkeiten von 20 m/s bis 60 m/s auf dem ebenen Bereich des Modells liegt. So ist gewährleistet, dass die Transition nicht stromauf der gewählten Absaugbereiche auftritt. Die Absaugung kann zwischen $\dot{V} = 0 \ldots 10$ l/s variiert werden, der Volumenstrom wird im sogenannten Laminar Flow Meter über den Druckverlust in laminar durchströmten Röhrchen gemessen. Auf diese Weise werden Volumenstrombeiwerte bis $c_Q = 1 \cdot 10^{-3}$ realisiert.

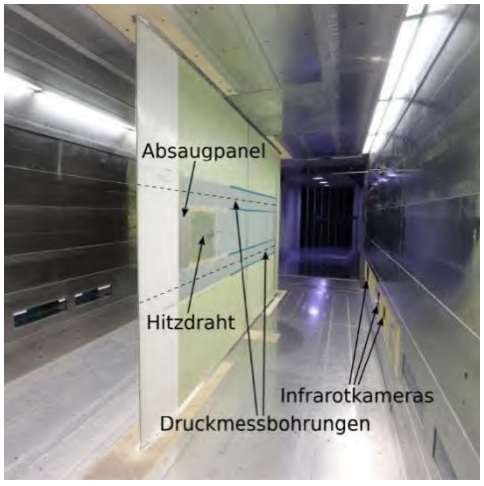

Abbildung 1: Modell im DNW-NWB, aus [1]

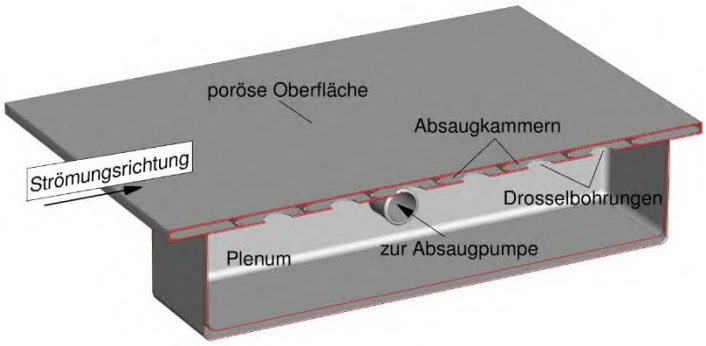

Abbildung 2: Schnittdarstellung eines Absaugpanels

Untersucht werden verschiedene Absaugoberflächen. Hierzu zählen u. a. lasergebohrte Bleche mit einer Stärke von 0,6 mm. Die Poren haben einen Durchmesser von 50 µm bei einem Abstand von 0,5 mm. Daraus ergibt sich eine Porosität von 0,785 % [2]. Darüber hinaus werden Oberflächen des TSSD-Konzepts untersucht (vgl. [3]). Diese bestehen aus einer 50 µm starken perforierten (geätzten) Metallfolie sowie einer mehrlagigen Unterstruktur aus Drahtgeweben. Hierfür wird einerseits ein Perforationsmuster analog zu den lasergebohrten Blechen verwendet, andererseits für aktuelle Versuche auch zwei verschiedene Muster aus spannweitig ausgedehnten Schlitzen. Letztere werden im August 2022 im DNW-NWB untersucht.

Die Windkanalversuche zeigen, dass alle untersuchten Oberflächen dazu geeignet sind, die laminar-turbulente Transition stromab zu verschieben. Es zeigt sich allerdings, dass diese Verschiebung geringer ausfällt, als von den Methoden der Lineraen Stabilitätstheorie vorhergesagt. Als destabilisierende Einflüsse kommen eine Interaktion zwischen den Instabilitäten in der Grenzschicht (Tollmien-Schlichting-Wellen) und der Absaugkammer sowie eine Störung durch die dreidimensionale Absaugströmung in Betracht.

Begleitend zu den Windkanalversuchen werden numerische Studien mit vollständig aufgelösten Absaugschlitzen durchgeführt. Diese sollen dazu dienen, die destabilisierenden Phänomene näher zu untersuchen. Die Interaktion zwischen Grenzschicht- und Kammerstörung wird anhand von zweidimensionalen direkten numerischen Simulationen analysiert (Abb. 3). Dabei zeigt sich ein einheitlicher Zusammenhang zwischen der akustischen Impedanz der Oberfläche und dem Zusatzwachstum der Tollmien-Schlichting-Wellen. Anhand von stationären dreidimensionalen Simulationen werden die Strömungsverhältnisse im Bereich verschiendener Absaugöffnungen untersucht (Abb. 4).

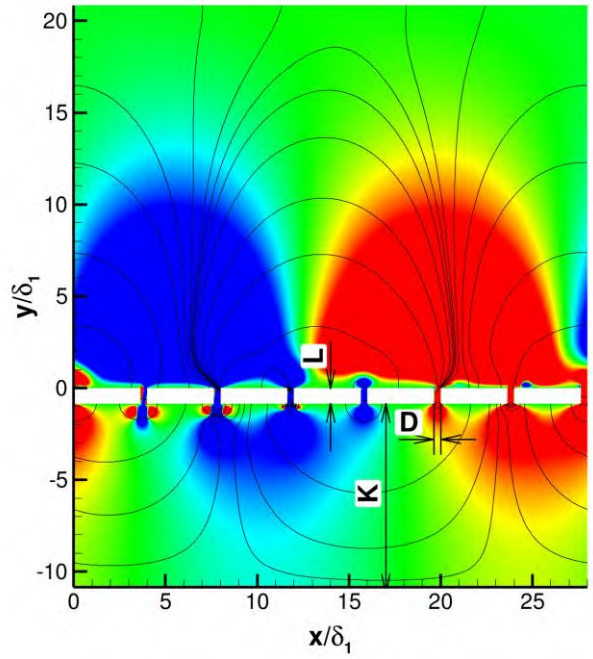

Abbildung 3: Interaktion zwischen TS-Welle und Kammer aus 2D-Simulation

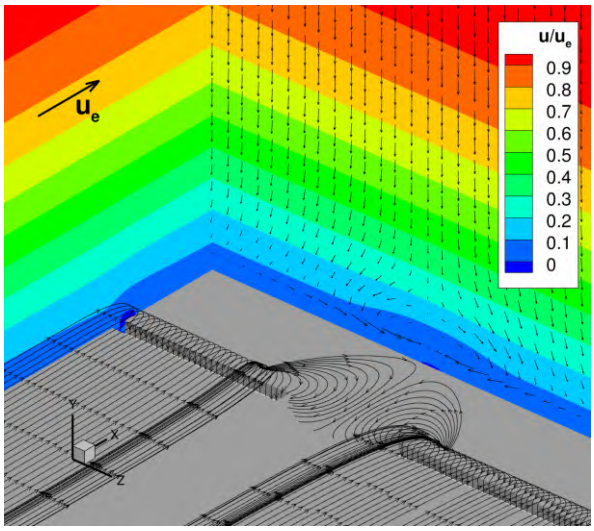

Abbildung 4: Beeinflussung der Grenzschicht durch einzelne Schlitze und Wirbelbildung hinter den Schlitzen

Gefördert durch die Deutsche Forschungsgemeinschaft (DFG) im Rahmen der Exzellenzstrategie des Bundes und der Länder – EXC 2163/1 - Sustainable and Energy Efficient Aviation – Project-ID 390881007.

Literatur:

[1] C. Breitenstein, H. Lüdeke: Auswertung experimenteller Untersuchungen einer ebenen Platte mit hybrider laminarer Strömungskontrolle. DLR Braunschweig, 2020.

[2] H. Lüdeke, C. Breitenstein: Experimental investigation of hybrid laminar flow control by a modular flat plate model in the DNW-NWB. CEAS Aeronautical Journal, 2021

[3] M. Horn, A. Seitz, M. Schneider: Cost-effective HLFC design concept for transport aircraft. DLRK, 2019.

Mitteilung

Fachgruppe:

Turbulenz und Transition

Turbulent flow in a concentric annulus with inner and outer cylinder rotation: a conventional and sensitized RANS modelling study

Xiaoyu WANG, Jeanette HUSSONG and Suad JAKIRLIĆ
Institute of Fluid Mechanics and Aerodynamics (SLA)
Alarich-Weiss-Straße 10, 64287, Technical University of Darmstadt
wang@sla.tu-darmstadt.de, hussong@sla.tu-darmstadt.de, jakirlic@sla.tu-darmstadt.de

A turbulent flow evolving in an annulus formed by two concentrically arranged cylinders is presently computed by a differential near-wall Reynolds stress model (RSM) used in a conventional Reynolds-Averaged Navier Stokes (RANS) framework, coupled with the equation governing the inverse turbulent time scale relying on the so-called 'homogeneous dissipation' rate ($\omega_h = \epsilon_h/k$). Two characteristic situations, in which the rotation of the inner cylinder by a constant angular velocity and that of the outer cylinder were considered individually, were studied in a range of rotational intensities ($N = U_{\theta,wall}/U_b$). Reference Large Eddy Simulations (LES) carried out under the conditions of an axially homogeneous flow have been performed by Chung and Sung (2005) for the inner cylinder rotation and Hadziabdic et al. (2013) for the outer cylinder rotation. The corresponding Reynolds numbers based on the hydraulic diameter and bulk velocity amount *8900* and *12500* for the inner and outer cylinder rotations, respectively. Complementary to the 'conventional' (baseline) Reynolds stress model (RSM) based on the Jakirlic and Hanjalic's (2002) formulation, its version sensitized appropriately to account for the turbulence unsteadiness was also applied. The latter eddy-resolving model, formulated by Jakirlic and Maduta (2015), is termed as Improved Instability-Sensitized RSM model (IIS-RSM). The eddy-resolving capability of the model is achieved by a selective enhancement of the turbulence production by introducing an additional production term in the length-scale determining transport equation. Its functional dependency on the second derivative of the underlying velocity field is motivated by the Scale-adaptive Simulation (SAS) strategy by Menter and Egorov (2010). Instead of the SAS-like expression of this source term, which is formulated as a 3-D generalization of the classical boundary layer definition of von Karman length, the near-original form proposed by Rotta (1972) is currently used depending only on the second derivative of the velocity field. All model equations are implemented into the Finite-Volume-Method-based code OpenFOAM® with which all computations were performed. The qualitative topology of the flow within the gap between two cylinders resembles the form found in the case of the so-called spiral Poiseuille flow (see e.g., Manna et al., 2020). Depending on the operational conditions - among others, the rotational intensity and the height of the clearance ($2\delta = R_{outer} - R_{inner}$) in terms of the curvature parameter (ratio of the inner to the outer radius: $R^* = R_{inner}/R_{outer}$) - the velocity field can be subject of patterns of different complexity. They are characterized by alternately varying velocity gradients, both in terms of intensity and sign.

A selection of the results is shown in Figures 1 and 2. Figures 1 illustrate the capability of the eddy-resolving Reynolds-stress model to adequately capture the fluctuating flow field. The instantaneous velocity fields allow insight into the fundamental differences between the influences of internal and external cylinder rotation on the overall flow topology. Whereas the results for the mean velocity and turbulence quantity profiles for the "inner-rotation" case obtained by both model versions show very good mutual agreement, following closely the reference LES (not shown here), the RANS-RSM model returns a laminar solution for the "outer rotation" flow configuration at higher rotational intensities, Figures 2. This premature relaminarization is analogous to the situation observed for flow in an axially rotating pipe, having its origin in the incorrect negative sign of the $\overline{u_z' u_\theta'}$ shear stress components, affecting a poor reproduction of the $\Phi_{z\theta}$ pressure strain term, see e.g., Jakirlic et al. (2002). The capability of the IIS-RSM model to correctly predict the instantaneous flow field remedied this anomaly and ultimately led to a corresponding turbulent solution that agrees well with the reference LES.

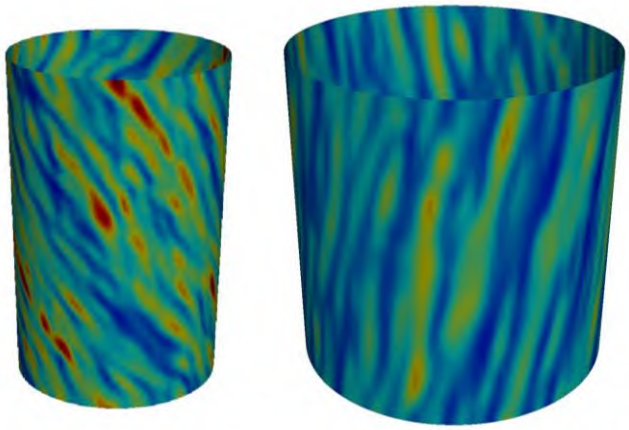

Figure 1: Instantaneous velocity field in the immediate wall vicinity of the flow in a concentric annulus with inner (left) and outer (right) cylinder rotation, obtained by the eddy-resolving RSM (IIS-RSM) at the rotational intensity of N=0.858.

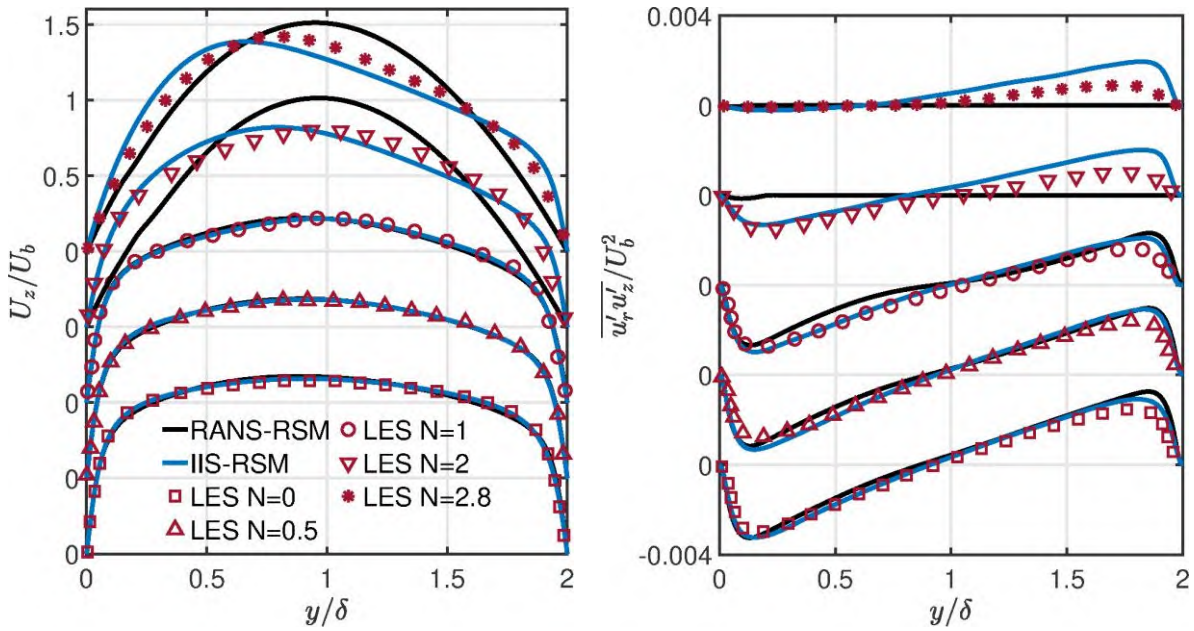

Figure 2: Mean velocity (left) and shear stress component (right) profiles in a range of rotational intensities in the flow in a concentric annulus with outer cylinder rotation obtained by both RSM versions.

Acknowledgement. The authors gratefully acknowledge the German Federal Ministry of Education and Research (BMBF) and the federal state of Hessen for supporting this project as part of the NHR4CES (*National High Performance Computing Center for Computational Engineering Sciences*) funding at TU Darmstadt and RWTH Aachen. The authors furthermore acknowledge the computing time granted on the Lichtenberg High Performance Computer of the Technical University of Darmstadt.

References

Chung, S.Y. and Sung, H.J. (2005): Large-eddy simulation of turbulent flow in a concentric annulus with rotation of an inner cylinder. *Int. J. Heat and Fluid Flow* 26:191-203

Hadziabdic, M. and Hanjalic, K. and Mullyadzhanov, R. (2020): LES of turbulent flow in a concentric annulus with rotating outer wall. *Int. J. Heat and Fluid Flow* 43:74-84

Manna, M., Vacca, A. and Verzicco, R. (2020): Pulsating spiral Poiseuille flow. *J. Fluid Mech.* 890:A21

Menter, F. and Egorov, Y. (2010): The Scale-adaptive Simulation method for unsteady turbulent flow predictions. Part 1: theory and model description. *Flow, Turbulence and Combustion* 85:113-138

Jakirlić, S., Tropea, C. and Hanjalić K. (2002): Modeling rotating and swirling turbulent flows: a perpetual challenge. *AIAA J.* 40(10):1984-1996

Jakirlić, S. and Hanjalić K. (2002): A new approach to modelling near-wall turbulence energy and stress dissipation. *J. Fluid Mech.* 439:139-166

Jakirlic, S. and Maduta, R. (2015): Extending the bounds of “steady” RANS closures: towards an instability-sensitive Reynolds stress model. *Int. J. Heat and Fluid Flow* 51:175-194

Mitteilung

Fachgruppe: Allgemeine Strömungstechnik

Einsatz von adjungierten Optimierungsmethoden zur Widerstandsminderung in Rohrströmungen

Eman Bagheri
Lehrstuhl für Strömungsmechanik, Universität Erlangen-Nürnberg,
Cauerstr. 4, 91058 Erlangen,
eman.m.bagheri@fau.de

Nicolas Gauger
Lehrstuhl fur Scientific Computing TU Kaiserslautern
Paul-Ehrlich-Str. 34, 67663 Kaiserslautern
nicolas.gauger@scicomp.uni-kl.de

Stefan Becker
Lehrstuhl für Strömungsmechanik, Universität Erlangen-Nürnberg,
Cauerstr. 4, 91058 Erlangen,
stefan.becker@fau.de

Die Leistungsfähigkeit vieler technischer Geräte ist oft von ihren geometrischen Randbedingungen abhängig. In der Vergangenheit wurde der geometrische Entwurf derartiger Geräte mit empirischen Methoden, heuristischen Ansätzen und umfangreichen Experimenten über mehrere Jahre durchgeführt. Ein Beispiel für solche Entwurfsverfahren ist die Entwicklung von Flügelprofilen, die sich bereits über Jahrzehnte erstreckt. Die genannten Methoden sind jedoch kostspielig, zeitaufwendig und garantieren keine optimale Lösung. Mit der ständig wachsenden Rechenleistung ist es nun möglich, solche langwierigen Entwurfsverfahren durch wohldefinierte Optimierungsalgorithmen zu ersetzen und damit den Entwurfsprozess vollständig zu automatisieren.

Ziel der gegenwärtigen Untersuchung war die Erstellung eines umfassenden Open-Source-Softwarepakets für die diskrete-adjungierte Formoptimierung multiphysikalischer Systeme. Die Strategie bestand darin, ein vorhandenes Open-Source-Berechnungsprogramm zu nutzen und weiterzuentwickeln, um eine Software zu schaffen, die für multidisziplinäre Simulation und Formoptimierung geeignet ist. Schließlich wurde das Berechnungstool zur Formoptimierung für den Testfall eines Rohrbogens mit relevanter technischer Anwendung eingesetzt.

Im Optimierungsprozess wurde die Software SU^2 für die Strömungssimulation, Sensitivitätsberechnungen und diskret-gelenkige Formoptimierungen mithilfe des Algorithmic Differentiation (AD) Pakets CoDiPack eingesetzt. KRATOS wurde für Strukturs imulationen und knotenbasierte Formoptimierungen benutzt. Dabei ist eine umfassende und flexible Plattform für Multiphysik-Simulationen und multidisziplinäre Formoptimierung entstanden. Mit dieser Plattform kann ein kompliziertes Optimierungsproblem mit Fluid-Struktur-Interaktion bei relativ geringen Rechenkosten für benutzerdefinierte Zielfunktionen gelöst werden.

Als Validierung dient der Testfall eines 180° gekrümmten Rohrbogens. Als Einströmrandbedingung dient eine voll ausgebildete Rohrströmung, die für konstante und pulsierende Strömungsprofile betrachtet wurde. In der Optimierung konnte über einen breiten Reynoldszahlbereich eine mehr als 60-prozentige Verbesserung des Druckverlustes im Vergleich zu der Basisgeometrie erzielt werden. In den Untersuchungen bezüglich der Optimierung zeigte sich, dass die Benutzung von eindimensionalen Strömungsberechnungsverfahren nicht zielführend war. Deshalb wurden dreidimensionale CFD-Berechnungen mithilfe eines k-ω-SST-Turbulenzmodells benutzt. Die Ergebnisse konnten durch experimentelle Untersuchungen umfangreich bestätigt und validiert werden. Es wurde ein spezieller Versuchsstand konstruiert und aufgebaut, der es ermöglicht, neben der Bestimmung der Druckverluste auch Messungen der Geschwindigkeitsverteilungen in der Rohrströmung durchzuführen. Eine weitere Besonderheit des Versuchsstandes ist die Generierung reproduzierbarer und kontrollierter Randbedingungen für eine pulsierende Strömung.

Außer der experimentellen Validierung erfolgte zusätzlich eine Berechnung mit einer hochaufgelösten DNS-Simulation. Hier galt es, noch einmal die wesentlichen physikalischen Mechanismen für die Widerstandsreduktion zu klären. Neben der viskosen Dissipation spielt die turbulente Dissipation eine maßgebliche Rolle in der Widerstandsreduktion. In den numerischen Simulationen konnte gezeigt werden, dass neben der Glättung der mittleren Geschwindigkeitsprofile auch die Relaminarisierung der Rohrströmung einen entscheidenden Einfluss auf die Optimierung der Widerstandsreduktion hat. Die Ergebnisse bei stationären Einströmbedingungen lassen sich übertragen auf pulsierende Einströmbedingungen und sind gültig für einen großen Bereich der turbulenten Rohrströmung.

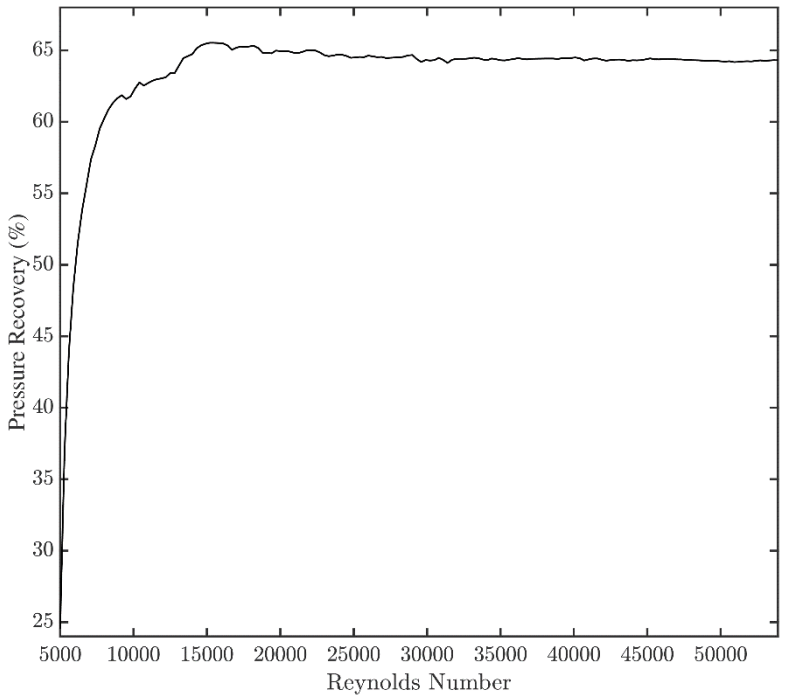

Abbildung: Druckrückgewinnung bei verschiedenen Reynoldszahlen

Mitteilung

Fachgruppe: Allgemeine Strömungstechnik

Direct Numerical Simulation of the dispersion of aerosol particles emitted in a single breath in a generic room

Ege Batmaz, Philipp Bahavar, Daniel Schmeling and Claus Wagner
Deutsches Zentrum für Luft- und Raumfahrt e.V. (DLR)
Bunsenstraße 10, 37073 Göttingen
ege.batmaz@dlr.de

A Direct Numerical Simulation (DNS) study of 'jet-like' breathing event in a generic environment is performed to quantify how respiratory droplets of different momentum and size are spreading after being emitted by a human subject in a closed room. Beside coughing and sneezing, breathing is a continuous function of human subjects and can spread aerosol droplets carrying SARS-CoV-2 and other airborne diseases. Large droplets follow ballistic trajectories, while relatively small particles are transported within the puff of air emitted by breathing. This paper focuses on the detailed analysis of the turbulent movement of respiratory particles emitted in a breath.

The considered computational domain is a rectangular prism, 1.11 m (streamwise length) x 0.37 m (spanwise length) x 0.37 m (height) in size, following the geometry used by Chong et al. [1]. A cylindrical pipe (see Fig. 1) with 50 mm in length and 23 mm in diameter is attached to the prism at mid-height to represent the mouth opening of a human subject. The computational domain is discretized with a mesh consisting of nearly 15 million cells. The uniform grid width of the mesh in the pipe section is below unity in wall units, i.e. $\Delta y+ < 1$. The grid cells are refined downstream the inlet area in the streamwise direction and are getting coarser in lateral directions. The prism boundary opposite the pipe is set as an outlet boundary. To reduce computational cost, all remaining boundaries are considered as slip walls where no shear force is acting on the flow, thus no velocity gradient occurs.

The incompressible Navier-Stokes equations are solved for the gas phase (air) using the finite-volume methods provided by OpenFOAM. Second order central differences are used for the spatial discretization. A DNS solver using explicit, second-order Euler-Leapfrog time integration scheme is implemented. The Euler-Leapfrog scheme does not suffer from false diffusion for the cases where the convective term is much larger than the diffusive term. Thus, it is more stable than, for example, the Adams-Bashforth scheme [3]. The coupling of velocity and pressure of the incompressible flow is realized with Chorin's projection method. Droplets are assumed to be spherical point-particles and described with the momentum equation combined with mass conservation. In a normal breathing event, 5000 droplets will be tracked using an Euler-Lagrangian approach. This approach considers the gas phase as continuum in the Eulerian reference frame and droplets as dispersed. The forces on each particle are considered in a Lagrangian reference frame. Since the droplet volume fraction in the domain is relatively small, droplets are assumed not to collide or coalesce. Thus, the two-way coupling strategy between fluid and particles is applied and is sufficient. Through the breathing event, the initial velocity of the particles matches the inlet velocity profile of the exhalation and the initial droplet diameters vary between 10 and roughly 1000 µm. Tang et al. [2] show that airflow parameters of nasal and mouth breathing are quite similar, with an exhalation duration of between 0.5 and 2.5 seconds and maximum velocity of 1.4 m/s and 1.3 m/s, relatively. In this study, the reference exhalation time for a single breath is considered as 1 second with a mean velocity of 1 m/s. This creates an inlet velocity profile with maximum velocity of approximately 1.3 m/s at the centerline of the pipe. Thus, the Reynolds number of the laminar pipe flow based in the pipe diameter and the peak velocity is $Re_D \approx 2000$.

In order to check the grid resolution and the boundary condition, a preliminary DNS was conducted to predicted flow field for jet-like breathing. *Fig. 1* shows an instantaneous picture of velocity contour for velocity magnitude at middle x-y plane (z = 0). This DNS was initialized with a mean flow obtained in a Reynolds-averaged Navier-Stokes (RANS) simulation with the k-epsilon model and integrated for approximately 1 second. Since for the considered $Re_D \approx$ 2000, the flow in the pipe is laminar, a transitional jet flow changing from the laminar pipe velocity to a turbulent jet develops. Since the well-revolved flow field shown in Fig. 1 was obtained in a stable simulation, we conclude that the used combination of DNS solver, grid and boundary conditions allows the prediction of a jet-like breathing.

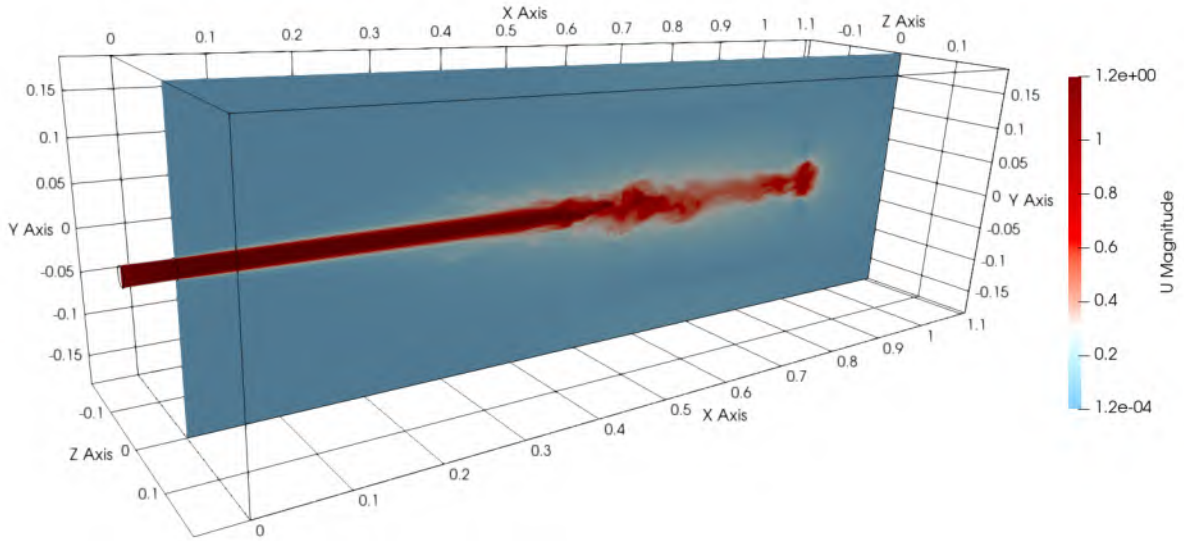

Figure 1: Velocity magnitude of DNS for the jet-like breathing after 1 s.

In the next step, aerosol particles of different size will be prescribed and tracked using the above discussed Euler-Lagrangian approach. The single breath event reflecting an exhalation phase of 1 second as reported by Tang et al. [2] will be prescribed in the DNS and the Lagrangian dynamics of the aerosol particles will be analyzed. At the Symposium quantitative results like average contamination range, maximum-reach and particle reach probability of aerosol particles will be presented and discussed to show the environmental effects on the dispersion characteristics of a breathing puff.

[1] Chong, K., Ng, C., Hori, N., Yang, R., Verzicco, R., & Lohse, D. (2021). Extended Lifetime of Respiratory Droplets in a Turbulent Vapor Puff and Its Implications on Airborne Disease Transmission. Physical Re-view Letters, 126(3)

[2] Tang, J., Nicolle, A., Klettner, C., Pantelic, J., Wang, L., & Suhaimi, A. et al. (2013). Airflow Dynamics of Human Jets: Sneezing and Breathing - Potential Sources of Infectious Aerosols. Plos ONE, 8(4), e59970. doi: 10.1371/journal.pone.0059970

[3] Shishkina, O., & Wagner, C. (2004). Stability conditions for the Leapfrog-Euler scheme with central spatial discretization of any order. Applied Numerical Analysis &Amp; Computational Mathematics, 1(1), 315-326. doi: 10.1002/anac.200310028

Mitteilung

Fachgruppe: Allgemeine Strömungstechnik

Investigations on a flow reconstruction method for urban wind field prediction

Carola Ebert, Julien Weiss
Fachgebiet Aerodynamik, Institut für Luft- und Raumfahrttechnik, TU Berlin,
Sekr. F2, Marchstrasse 12-14, 10587 Berlin, carola.ebert@tu-berlin.de

The wind field of an urban city is characterized by areas that boast strong flow separations, local vortices and large formations of shear layers due to the dynamic flow around buildings and obstacles. These dynamical and turbulent wind fields of urban areas have an intense impact on the application field of manned and unmanned aircrafts and constitute a high potential risk for safe, efficient and sustainable flight operations [1]. The knowledge of the prevailing wind conditions in an urban area provide an important and necessarily aspect of safety for UAVs operating in an urban area especially during windy conditions [2]. The use of computational fluid dynamics (CFD) to simulate the wind field in an urban environment is used by an increasing number of researchers and has proven itself as a promising solution during the last years [3, 4]. However, high resolution full-size CFD simulations of urban wind fields require very high computational costs so that real-time online calculations are not feasible. To circumvent these computational limitations, a method of real-time wind field prediction will be investigated within this contribution in order to estimate the prevailing wind conditions in an urban area. A promising method of real-time aerodynamic flow prediction constitutes the method of proper orthogonal decomposition (POD) combined with the data reconstruction method Gappy POD as a reduced order model [5].

The overall procedure of the reduced order model is shown in Fig. 1. The reduced order model is divided in an offline and an online stage. The offline stage is assumed to be calculated in advance and includes the three-dimensional full-size CFD simulations of the flow around the complex buildings of the campus of the Technical University of Berlin that will be performed for different inlet wind directions using OpenFoam®. The buildings used for the simulated area are visualized in Fig. 2a in a section of a satellite map. A result of the wind field simulation is presented in Fig. 2b for the chosen area, where the contour plot shows the wind field magnitude in the x-y plane at a constant altitude. A CFD simulation will be done for various inlet wind directions in order that a set of simulation data is computed that constitutes the snapshot basis for the proper orthogonal decomposition (POD). The POD will be applied using the singular value decomposition (SVD) that produces the POD modes which represent the coherent structures of the flow field and the energy of the system. The investigation will focus on the influence of the size of the snapshot basis used for the POD with regard to the accuracy of the wind field reconstruction by Gappy POD. In order to assess the accuracy of the wind field reconstruction a reconstruction error will be defined using the least-square error.
In the second step of the offline stage of the reduced order model, the POD modes of the system will be used to solve the sensor placement problem to find the best sensor locations that will be used to reconstruct the wind field. Within this contribution, different sensor placement problem methods will be applied and compared considering the reconstruction error. The wind field reconstruction by using a Gappy POD approach will be performed during the online stage and is assumed to be done inside of the UAV just before the UAVs flight mission. The input data of the online stage are the dominant POD modes and the wind data according to the defined sensor locations. Varying the number of dominant POD modes and the number of sensor

locations influences the accuracy of the wind field. The accuracy of the wind field reconstruction will be investigated according to the number of sensor locations that is equal to the number of POD modes.

The final paper will discuss feasible adjustments of the reduced order model method in order to achieve a higher accuracy of the reconstruction method of an aerodynamic flow field.

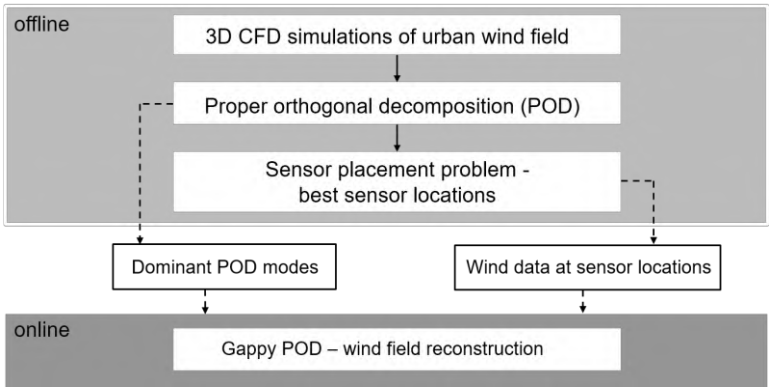

Fig 1: Procedure of the reduced order model method.

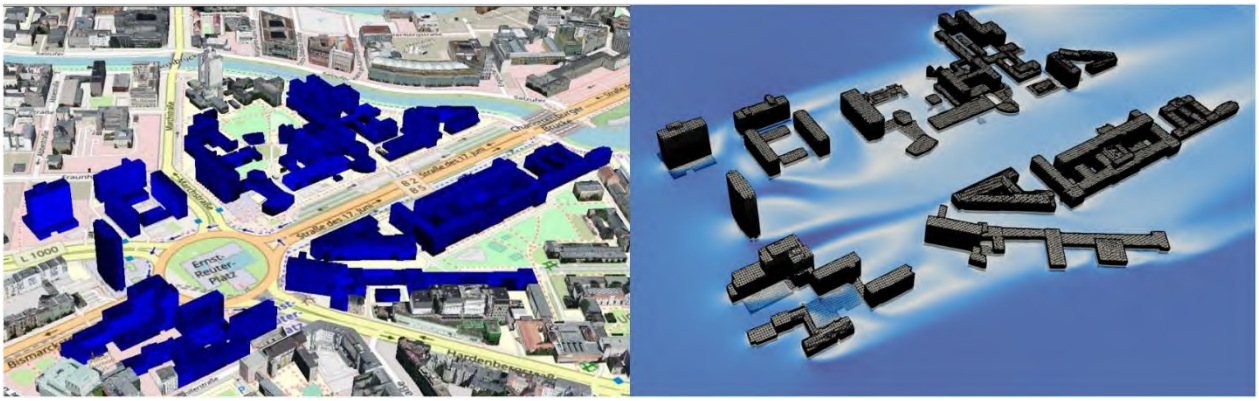

Fig 2: a) Buildings of the simulation area of the campus of TU Berlin. b) Computaional grid and flow visualization.

References:

[1] Wang, B. H., Wang, D. B., Ali, Z. A., Ting Ting, B., and Wang, H., “An overview of various kinds of wind effects on unmanned aerial vehicle,” Measurement and Control, Vol. 52, No. 7-8, 2019, pp. 731–739. https://doi.org/10.1177/0020294019847688.

[2] Kothari, M., Postlethwaite, I., and Gu, D.-W., “UAV Path Following in Windy Urban Environments,” Journal of Intelligent & Robotic Systems, Vol. 74, No. 3-4, 2014, pp. 1013–1028. https://doi.org/10.1007/s10846-013-9873-z.

[3] Blocken, B., Janssen, W. D., and van Hooff, T., “CFD simulation for pedestrian wind comfort and wind safety in urban areas: General decision framework and case study for the Eindhoven University campus,” Environmental Modelling & Software, Vol. 30, No. 1–3, 2012, pp. 15–34. https://doi.org/10.1016/j.envsoft.2011.11.009.

[4] van Hooff, T., and Blocken, B., “Coupled urban wind flow and indoor natural ventilation modelling on a high-resolution grid: A case study for the Amsterdam ArenA stadium,” Environmental Modelling & Software, Vol. 25, No. 1, 2010, pp. 51–65. https://doi.org/10.1016/j.envsoft.2009.07.008.

[5] Ebert, C. and Weiss, J., “Trajectory Planning inWindy Urban Environment – a Gappy POD Approach for Wind Field Estimates with Sparse Sensors, ” AIAA Aviation Forum 2022.

Mitteilung

Fachgruppe: Allgemeine Strömungstechnik

Towards indirect assessment of surface anomalies on wind turbine rotor blades

Daniel Feldmann[1*], Felix Oehme[2], Andreas Fischer[2] and Marc Avila[1]Universität Bremen, ZARM[1], BIMAQ[2], 28359 Bremen, Germany
*daniel.feldmann@zarm.uni-bremen.de

With 132 TW h electricity fed into the grid in 2020, wind power has become Germany's leading source of energy (27 %) outperforming any fossil source [5]. However, cost reduction is indispensable to further strengthen the competitiveness of sustainable energy production beyond initial stages of massive subsidisation and political control. Rotor blade inspection of ageing wind turbines, for example, is cost-intensive and thus offers high potential to further reduce energy production costs through more efficient maintenance procedures.

Our goal is to explore the possibility to monitor damage and contamination level of wind turbine blades (Fig. 1a) using non-invasive detection of laminar-turbulent flow transition via infrared thermography (IRT) of the blades' surface temperature (Fig. 1b). If successful, this tech-

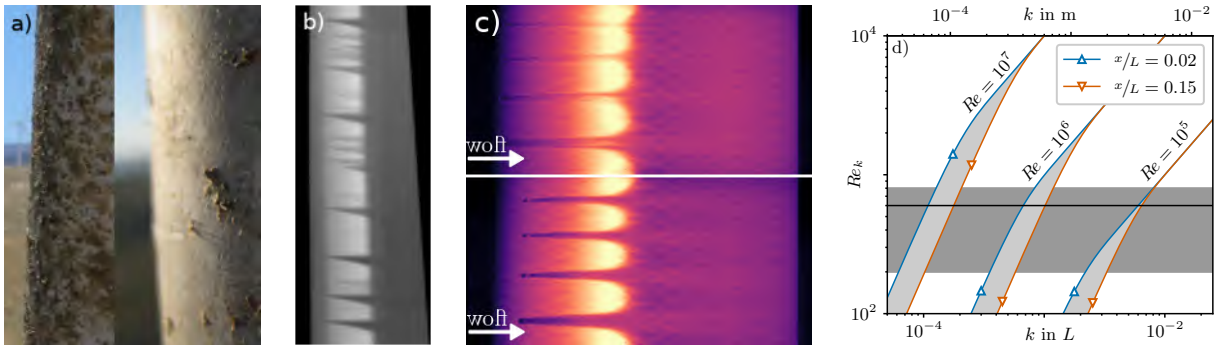

Figure 1: Problem description. a): Wind turbine rotor blade with heavy/light surface contamination in the vicinity of its leading edge [1]. b): Infrared image of the blades surface temperature indicating wedges of locally turbulent flow (dark) due to surface anomalies in contrast to the otherwise laminar flow (light) in an operating wind turbine at $Re = \mathcal{O}(10^6)$. c): Same as b), but for wind tunnel measurements at $Re = \mathcal{O}(10^5)$, where cylindrical perturbation elements of different size (k) and position (x) are used as generic surface contamination. d): Relevant parameter space in terms of element size (k), position (x), chord (Re) and roughness (Re_k) Reynolds numbers, based on the crude assumption of a Blasius boundary layer to estimate the local velocity (u_k).

nique would allow to remotely monitor the blades surface condition in the vicinity of the blades leading edge in order to detect, locate and classify anomalies in the rotor blade surface without taking the wind turbine out of service for inspection. In fact, recent studies [2, 4, 6] have shown, that it is possible to detect premature laminar-turbulent transition induced by surface anomalies in a running wind turbine remotely using IRT (Fig. 1b). For the application, however, it is not sufficient to simply detect the presence of an anomaly. Instead, it is necessary to additionally infer the position, size and shape of the geometrical perturbation in order to enable remote classification of the surface anomaly (e. g. distinguish between deposition, erosion, impact, fatigue). This poses many methodological challenges and it is currently unclear, to what extent such a classification can be inferred faithfully from an IRT image through physically informed modelling.

We aim at characterising the effect of different generic surface anomalies on early transition and the resulting (turbulent) wake in a rotor blade boundary layer, using a combination of both, extensive wind tunnel measurements and direct numerical simulations (DNS). For this purpose, simple perturbation elements act as generic surface anomalies that mimic localised deposition of e. g. dust or insects. In the long term, we aim at generating a comprehensive surface-state-flow-pattern catalogue and a deeper physical understanding of how surface irregularities affect early transition in wind turbine aerodynamics. Hopefully, this will lay the foundation for the development of a data-trained physics-informed model to reliably relate individual thermographic

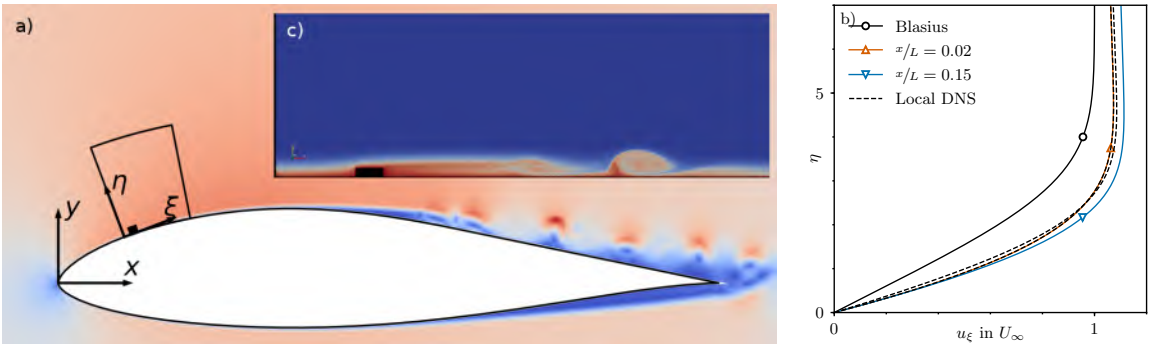

Figure 2: Local DNS ansatz. a): Colour-coded contour of the velocity magnitude in the flow field around a clean rotor blade (w/o perturbation) generated in a global 2d DNS at $Re = 10^5$. The black box indicates the local DNS domain. b): Comparison of results from local and global DNS in terms of the boundary layer velocity profile ($u_\xi(\eta)$) at different locations (x). c): Colour-coded temperature field in the flow generated in a local 2d DNS with perturbation element ($Re_k = 600$, black line in Fig. 1d) neglecting the local curvature of the airfoil.

images to particular rotor blade conditions based on machine learning and image recognition techniques.

At the symposium we will present results of our preliminary studies. First, we discuss wind tunnel measurements carried out at Deutsche Windguard. The experimental measurements indicate that it is feasible to distinguish between different elements in terms of their size (k) and location (x) by means of an IRT image of the blades' surface temperature (Fig. 1c). In the self-similar laminar Blasius boundary layer over a flat plate, the transition scenario is solely characterised by the geometry of the disturbance element and its roughness Reynolds number ($Re_k = {}^{k\,u_k}/_{\nu}$) with a critical value of roughly 400 [3]. Here, k is the height of that element, u_k is the local velocity at the element position (x) at wall-normal distance k, and ν is the fluids kinematic viscosity. Figure 1d shows in dark grey the range of Re_k realised in our preliminary campaign and indicates how these values translate to other situations; e. g. other combinations of (x, k) or higher chord Reynolds numbers ($Re = {}^{L\,u_\infty}/_{\nu}$, where u_∞ is the effective incoming wind speed and L is the local chord length of the rotor blade).

Second, we discuss DNS results generated with the spectral element code `nektar++`. The results demonstrate the feasibility of our numerical approach which is meant to complement future wind tunnel campaigns. In order to enable DNS for the intended range of control parameters ($Re \geq 10^5$, $Re_k \gg 200$), we perform our DNS exploiting a local approximation of the blade and the flow around the disturbance element (Fig. 2a). We show, that our local ansatz very well reproduces results from larger (global) DNS, when we impose the flow field generated in a global DNS as boundary conditions for the local DNS (Fig. 2b). We further show, that even if the local domain is short (w.r.t the local curvature), neglecting the local curvature of the airfoil introduces significant deviations in the boundary layer profile. Finally, we provide reasonable bounds for the minimal size of the local domain with perturbation elements and discuss first qualitative comparisons between IRT measurements and results from local DNS that also include (passive) transport of temperature in the flow field (Fig. 2c).

References

[1] R. S. Ehrmann, B. Wilcox, E. B. White, and D. C. Maniaci. Effect of Surface Roughness on Wind Turbine Performance. Technical Report October, Sandia National Laboratories, Albuquerque, 10 2017.

[2] D. Gleichauf, M. Sorg, and A. Fischer. Contactless localization of premature laminar-turbulent flow transitions on wind turbine rotor blades in operation. *Applied Sciences (Switzerland)*, 10(18), 2020.

[3] D. K. Puckert and U. Rist. Experiments on critical Reynolds number and global instability in roughness-induced laminar–turbulent transition. *Journal of Fluid Mechanics*, 844:878–904, 6 2018.

[4] T. Reichstein, A. P. Schaffarczyk, C. Dollinger, N. Balaresque, E. Schülein, C. Jauch, and A. Fischer. Investigation of Laminar–Turbulent Transition on a Rotating Wind-Turbine Blade of Multimegawatt Class with Thermography and Microphone Array. *Energies*, 12(11):2102, 6 2019.

[5] Strom-Report. Germany's Power Mix 2020 – Data, Charts & Key Findings. 2021.

[6] D. Traphan, I. Herraéz, P. Meinlschmidt, F. Schlüter, J. Peinke, and G. Gülker. Remote surface damage detection on rotor blades of operating wind turbines by means of infrared thermography. *Wind Energy Science*, 3(2):639–650, 2018.

Mitteilung

Fachgruppe: Allgemeine Strömungstechnik

Experimental and Numerical Investigation of Longitudinal Folds in Endotracheal Tube Cuffs and their Correlation to Silent Breathing

Lars Krenkel[1,2], Johanna Michel[1], Niklas Keil[1], and Jan Daschner[1]
lars.krenkel@oth-regensburg.de

1 : Technical University of Applied Sciences (OTH) Regensburg, Department of Biofluidmechanics, Galgenbergstr. 30, 93053 Regensburg, Germany

2 : Regensburg Center of Biomedical Engineering and Regensburg Center of Health Sciences and Technology, OTH and University Regensburg

Air leakage past High-Volume-Low-Pressure (HVLP) endotracheal tube (ETT) cuffs creates a potential infection risk for health care professionals during ventilation of patients suffering from contagious airborne diseases. However, unlike silent aspiration, a phenomenon where fluids enter the airways of intubated patients, the aspect of aerosol emergence through cuff folds - what we called accordingly “silent breathing” (SB)- has not been investigated in detail so far.

This study investigates air leakage past HVLP cuffs with varying cuff pressures under realistic artificial breathing scenarios experimentally and in addition numerically. The focus was laid on the parametric investigation of the occurrence and furthermore on different influencing factors of silent breathing. The morphology of the folds responsible for the leakage was captured using high-resolution 3D microcomputed tomography (µCT). For the numerical investigations (Computational Fluid Dynamics - CFD), the commercial CFD Software package FLUENT 2021 R2 (ANSYS, Inc., Canonsburg, PA, US), as well as the DLR in-house research code THETA has been used.

For all measurements, porcine tracheae were prepared and intubated using Dahlhausen Magill ETTs with HVLP cuffs. To eliminate all relative movement between cuff and trachea wall, the trachea and ETT were fixated to a surrounding setup (Figure 1). A computer-controlled linear motor pump system (LinMot) was used to simulate artificial volume-controlled ventilation according to physiological parameters. The ventilation was performed using aerosol-enriched air for visualization purposes. Additionally, the intracuff and intrapulmonary pressure were measured. Potential leakages were then visualized by a longitudinal and a cross-sectional laser light sheet. A particle sizer was used for quantifying the characteristics of emerged particles in terms of size and quantity (Palas Fidas Frog). Subsequently, without any changes to the cuff and its position, the trachea was scanned afterward using a high-resolution µCT (GE V|tome|X S). The folds responsible for leakages were then analysed and the captured fold geometry was reconstructed into a STL surface geometry. These geometries were furthermore converted into a hybrid volume mesh for CFD analysis using the mesh generator CENTAUR (CentaurSoft, Austin, TX, US).

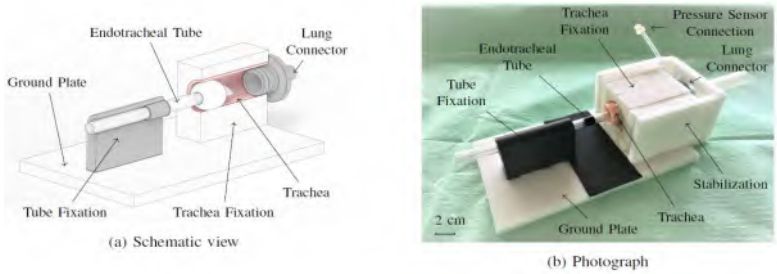

Figure 1: Experimental setup for the laser light sheet and µCT analysis.

The results of this study show that SB occurs regularly during intubation with HVLP cuffs. Overall, leakage could be detected in six out of ten investigated cases. By determining the position of exiting aerosols with help of the cross-sectional laser light analysis, it was possible to establish a relationship between leakages and specific folds in the µCT scans. In addition, leakages could also be confirmed by decreasing intrapulmonary pressure level during the ventilation cycle. However, in every case, even without observable leakage, a pressure drop ΔP_{resp} of about 30 Pa could be observed. This is presumably caused by the compliance of the entire measurement system including hoses,

trachea, tube, cuff, and artificial lung. Measurements with leaking cuffs, however, show a significant increase in ΔP_{resp}. In addition, a correlation between weak aerosol emissions and a low ΔP_{resp} and strong aerosol emissions and a high ΔP_{resp} was found. Figure 2 depicts a µCT analysis of a cuff with SB.

The morphology of individual folds, responsible for leakages, is random. However, what they have in common is their continuity over the entire length of the cuff. This seems to be the main criteria for leakage. Folds can also differ in how tightly they are compressed to form an open or a separated channel. In this case, the continuity of the channel is also decisive for its leaking properties. Folds of non-leaking cuffs are usually not continuous throughout the whole length

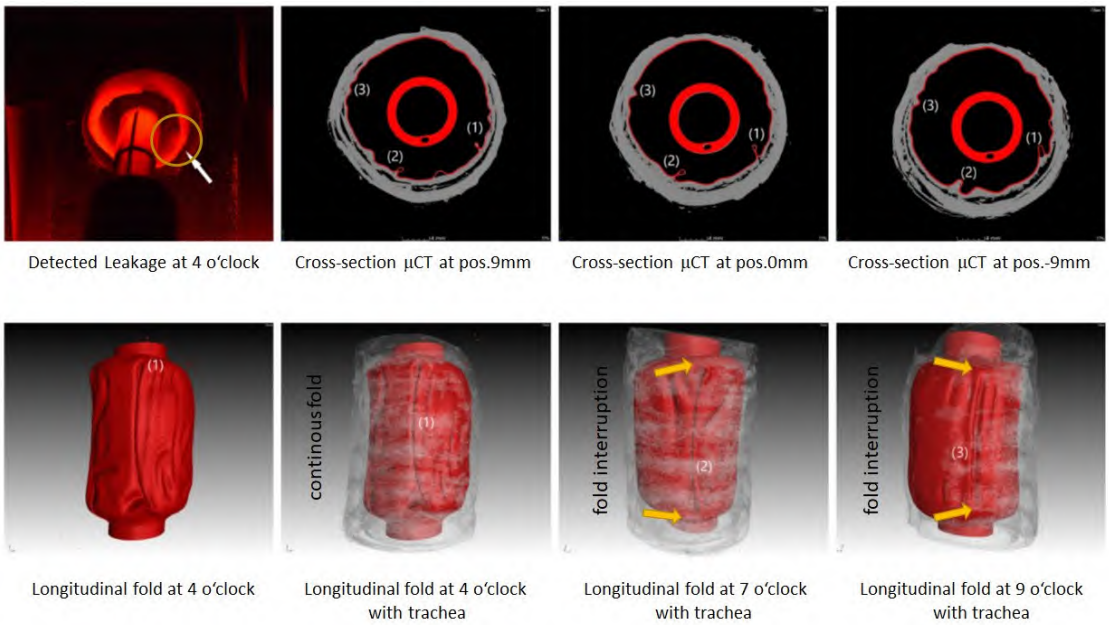

Figure 2: µCT analysis of cut-planes with silent breathing. The *upper row* shows CT cross-sections with longitudinal folds (numbered). The *lower row* shows 3D reconstructions of the distinct folds in the cuff (numbered).

of the cuff or are occluded by tracheal tissue or fluid deposits within the folds.
Furthermore, continuous folds could not only form when the cuff is initially inflated but also when a ventilation pressure is applied to a cuff with aninterrupted fold. If a fold already exists but is not permeable, a pressure peak could cause it to open. However, the opening of such a fold could be reversible as soon as the pressure is no longer applied. Especially such cases are difficult to detect with the µCT.

In addition to the experimental investigations, CFD was applied on reconstructed cuff fold geometries to gain further insights into the flow regime within the cuff folds. However, some simplifications of the rather complex system had to be made at this early stage of the project (e.g., solid walls). Since the wall of the cuff and the inside wall of the trachea could not be separated by µCT and were captured as a single wall, the outside wall of the trachea was removed, and afterward the cuff geometry was merged with a second scan of the same trachea without tube and cuff (Figure 3). As boundary conditions (BC) at the trachea, to the environment, and the tube, time-varying pressure BCs have been chosen to mimic the artificial ventilation cycle (inspiration/expiration/PEEP). Analysis of the achieved results shows a highly complex flow scenario within the trachea, the ETT, and along the continuous cuff folds. The highest amount of SB was observed at the end of expiration and positive-end-expiratory-pressure (PEEP) condition.

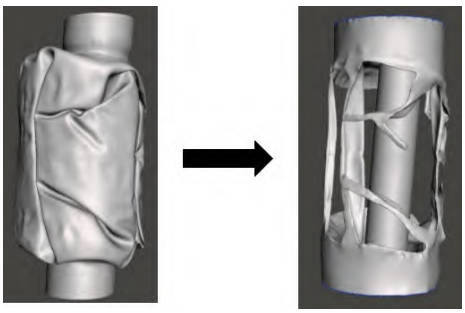

Figure 3: Reconstructed 3D cuff geometry (l) converted into a 3D fold solid with tube and tracheal segment (r) for CFD.

The existence of silent breathing was shown in this study. This may result in increased risk for health care professionals treating patients with contagious airborne diseases. However, further efforts are needed to fully understand the underlying mechanisms and the influencing factors.

Mitteilung

Fachgruppe: Allgemeine Strömungstechnik

Entwicklung eines preisgünstigen thermischen Menschmodells mit sieben Zonen zur Komforterfassung in Passagierkabinen

Daniel Schiepel, Felix Werner und Daniel Schmeling
Deutsches Zentrum für Luft- und Raumfahrt (DLR), Bunsenstr. 10, 37073 Göttingen,
Daniel.Schiepel@DLR.de

In dieser Arbeit wird die Entwicklung eines preisgünstigen thermischen Menschmodells mit sieben Zonen zur Messung des thermischen Komforts in Passagierkabinen präsentiert. Als Messgröße zur Bestimmung des thermischen Komforts kann die Äquivalenttemperatur [1] verwendet werden. Hierzu gibt es bereits verschiedene Messpuppen, welche jedoch Anschaffungskosten von mehr als 100.000 US-Doller haben. Darüberhinaus sind diese Systeme häufig sowohl sperrig als auch schwer, was insgesamt dazu führt, dass solche Systeme meist nur vereinzelt an vorab definierten Positionen zum Einsatz kommen. Somit steht die Komfortinformation nur an einem Sitzplatz zur Verfügung und nicht an vielen relevanten Plätzen. Dementsprechend ist die Datenerfassung an verschiedenen Orten nur in aufeinanderfolgenden Messungen möglich. Dies wiederum hat eine zeit- und kostenintensive Planung und Ausführung zur Folge. Daher wird bei experimentellen Untersuchungen mit mehreren Personen häufig auf die Komfortinformation verzichtet und stattdessen generische Wärmelasten, z.B Heizmatten, eingesetzt, die lediglich die absolute Wärmelast simulieren. Als Untersuchungen mit einem erhöhtem Detaillierungsgrad werden diese generischen Lasten durch beheizbare, thermische Passagiermodelle substituiert, welche neben einer realistischen Wärmeabgabe auch die geometrische Versperrung der Passagiere simulieren. Bei diesen Untersuchungen sind zudem noch eigenständige Messsysteme nötig, die die komfortspezifischen Größen erfassen und auswerten. Da das thermische Empfinden von Menschen jedoch durch die Interaktion verschiedener komfortrelevanter Strömungsgrößen, wie z. B. Lufttemperatur, Luftgeschwindigkeit und Strahlungstemperatur, beeinflusst wird ist die alleinige und punktuelle Erfassung dieser Größen für eine ganzheitlich und robuste Bewertung der thermischen Behaglichkeit oft unzureichend und kann zu einer unzureichenden Einschätzung des Komforts führen.

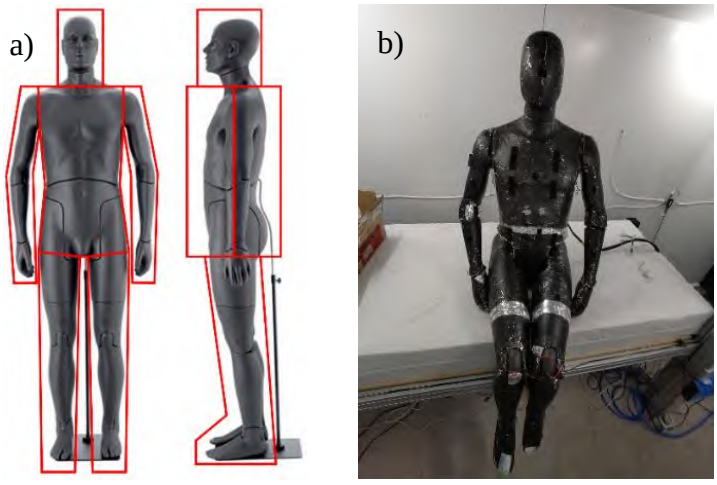

Abbildung 1: a) Illustration der sieben individuellen Zonen des thermischen Menschmodells basierend auf [2]. b) Fertiges Menschmodell mit Heizdraht und Aluminium-Außenhülle.

Daher wurde das bereits etablierte Messmittel „thermisches Menschmodell“, welches eine Erfassung der Äquivalenttemperatur nach EN ISO 14505-2 erlaubt [3], weiterentwickelt. Das Messmittel ist ein beheizbares Menschmodell, das eine realitätsnahe Wärmeabgabe eines Menschen sowie deren Versperrung simuliert und die Möglichkeit bietet mittels Infrarotthermografie gleichzeitig die Äquivalenttemperatur bestimmen zu können. Das Menschmodell kann aber nur mit einer ganzheitlichen Heizleistung betrieben werden. Jedoch gibt es eine Reihe von Anwendungen in denen eine zonale Regelung der Heizleistung von einzelnen Körperteilen notwendig ist, denn dies ist erforderlich, um den menschlichen Metabolismus regionsweise besser nachbilden zu können. Auch erlaubt die zonale Umsetzung die Erfassung der Oberflächentemperatur ohne den Einsatz von Infrarotkameras und so kann letztlich der zonale Komfort bestimmt werden.

Hierzu wurde ein Prototyp einer beheizbaren Komfortpuppe entwickelt mit dem es möglich ist, die einzelnen Körperzonen hinsichtlich eines definierten Wärmestroms zu regeln. Als Grundkörper für das thermischen Menschmodell wurde eine männliche, voll-bewegliche Schaufensterpuppe (Livelymen Volo von lideimmagine [2]) verwendet. Der Körper besteht aus expandiertem Polypropylen (EPP), welches zur Erzeugung einer homogenen Oberflächentemperatur mit einem Heizdraht umwickelt und mit einer dünnen schwarz-eloxierten Aluminiumschicht ummantelt wird.
Der Prototyp hat sieben unabhängig regelbare Zonen, welche in Abbildung 1 a) skizziert sind. Das fertige Menschmodell mit gewickeltem Heizdraht und schwarzer Aluminium-Außenhülle ist in b) dargestellt. Tabelle 1 präsentiert den gemessenen zonalen Widerstand sowie für eine Gesamtwärmeleistung von 100W zusätzlich die gewählte Zonen-Leistungen, resultierende Spannungen und Stromstärke.

Körperteil	Widerstand [W]	Leistungsanteil	Leistung [W]	Strom [A]	Spannung [V]
Kopf	2.25	17%	16.7	2.7	6.1
Vorderseite	4.35	17%	16.7	2.0	8.5
Rücken	4.75	17%	16.7	1.9	8.9
Arm rechts	3.8	8%	8.3	1.5	5.6
Arm links	3.8	8%	8.3	1.5	5.6
Bein rechts	6.5	17%	16.7	1.6	10.4
Bein links	6.5	17%	16.7	1.6	10.4

Tabelle 1: Sieben Zonen des zonalen thermischen Menschmodells. Angegeben sind gemessener Widerstand, vorgegebener Leistungsanteil, sowie Leistung, Strom und Spannung für eine Wärmeleistung von 100W.

Die Ansteuerung der einzelnen Zonen wurde mittels einer Server-ähnlichen Struktur realisiert. So gibt es ein Steuermodul und vier Leistungsmodule für je zwei Kanäle. Im Steuermodul befinden sich ein Adafruit FTDI Ft232h und ein SparkFun 8-Kanal Qwiic Mux Breakout (TCA9548A) für die Kommunikation mit den Bauteilen. Die Leistungsvorgabe erfolgt über eine Modul zur Pulsweitenmodulation (Adafruit 16-Kanal 12-bit PWM-Modul), welches die Schnittstelle zwischen den zwei Modultypen darstellt. Die Leistungsmodule nutzen zur Leistungsversorgung Cytron 10A 5-30V Zweikanal-DC-Motortreiber. Diese Motortreiber erhalten über einen PWM-Eingang die Leistungsvorgabe. Es wurde eine ausgangsseitige Leistungsmessung realisiert, um etwaige Leistungsverluste an den vorgeschalteten Bauteilen von der Leistungserfassung auszuschließen. Hier erfolgt eine Kanal-weise Erfassung der bereitgestellten Leistung mittels eines Spannungs- und Stromstärkemessmoduls (Adafruit INA260), welches die Daten an das Steuermodul überträgt. Da jedes Leistungsmodul über einen eigenen Versorgungseingang verfügt, können entsprechend Tabelle 1 die Körperzonen gemäß ihrer Versorgungsspannung gruppiert werden. So ist es möglich nur entsprechend optimal-dimensionierte Netzteile zu verwenden. Es kann allerdings auch jedes beliebige Netzteil mit einer Ausgangsspannung bis 40V und einer ausreichenden Stromstärke genutzt werden. Das sieben Zonen Menschmodell wiegt insgesamt weniger als 15 Kg und die gesamten Kosten für Steuer- und Regelungselektronik belaufen sich auf preisgünstige 150€ sowie 600€ für den Grundkörper.

Literaturverzeichnis

[1] EN ISO 14505-2, „Ergonomics of the thermal environment - Evaluation of thermal environments in vehicles - Part 2: Determination of equivalent temperature," *Beuth*, 2006.

[2] lideimmagine, „livelymen," 2020. [Online]. Available: https://www.lideimmagine.com/wp-content/uploads/2019/10/cod.00001B.jpg. [Zugriff am 20 06 2022].

[3] P. Lange, D. Schmeling, A. Westhoff und J. Bosbach, „Cost-effective human comfort manikin with realistic thermal load for studies of convection-driven ventilation systems," *Roomvent & Ventilation Konferenz,* pp. 367-372, 2018.

Mitteilung

Fachgruppe: Allgemeine Strömungstechnik

Numerical study of aerosol dispersion in the aircraft cabin

Andrei Shishkin, Daniel Schiepel, Daniel Schmeling
DLR Göttingen, Institute of Aerodynamics and Flow Technology
Bunsenstraße 10,37073 Göttingen
andrei.shishkin@dlr.de

In the present work, we study the spread of aerosol in the aircraft cabin. The measurements are conducted using well-equipped Dornier 728 (Do728) research facility of DLR (Figure 1), and therefore the numerical simulations are performed in the computational domain exactly matching the full-size Do728 cabin. This makes it possible to compare and verify mutually the results of calculations and the measurements, as well as to coordinate the numerical and experimental parts of the study. The simulations are carried out on the HPC cluster CARA of TU Dresden/DLR.

Figure 1: The Do728 research facility [2]

The study develops the results obtained earlier [1,2]. Now we address the long-term dispersion of aerosol in the cabin with various ventilation configurations and different particle sources. The main cases considered are state-of-the-art mixed ventilation (MV) and the floor-based cabin displacement ventilation (CDV) [3]. Calculations were carried out for both ventilation configurations, and the results of the computations and measurements are compared for MV. Different locations of aerosol sources are also being investigated.
The important feature of long-term aerosol propagation is that the particles are in equilibrium with the environment and the effect of particles on the air flow can be neglected. Thus, the aerosol particles are considered as non-interacting and non-changeable kinematic particles. This allows us to apply the following two-step approach. First, a steady state Navier-Stokes problem is solved for the given conditions, and then the results obtained are used for Lagrangian particle tracking. To solve these tasks, as well as for pre- and post-processing, we use tools implemented in open-source toolkit OpenFOAM.

Some results obtained for MV configuration are shown in Figures 2 and 3. Here, the permanent particle source is at position 8C indicated by the arrow in the Figure 2. The source injects 1000 parcels per second. The particle sizes are distributed uniformly from 0.5 μm to 2.5 μm. Approximately 300 seconds after starting of particle injection, the process comes to equilibrium: the number of active in-air particles remains almost unchanged. At t=1500 s the particle injection stops.
The concentration of particles in the respiration zone during the equilibrium of the system (at t=600 s) is shown in Figure 2. Only the row of seats on which the source is located and the three rows following it have a significant concentration of particles. The development of aerosol concentration in breathing area over time for these rows is depicted in Figure 3. The row located directly behind the particle source receives the most aerosol load.

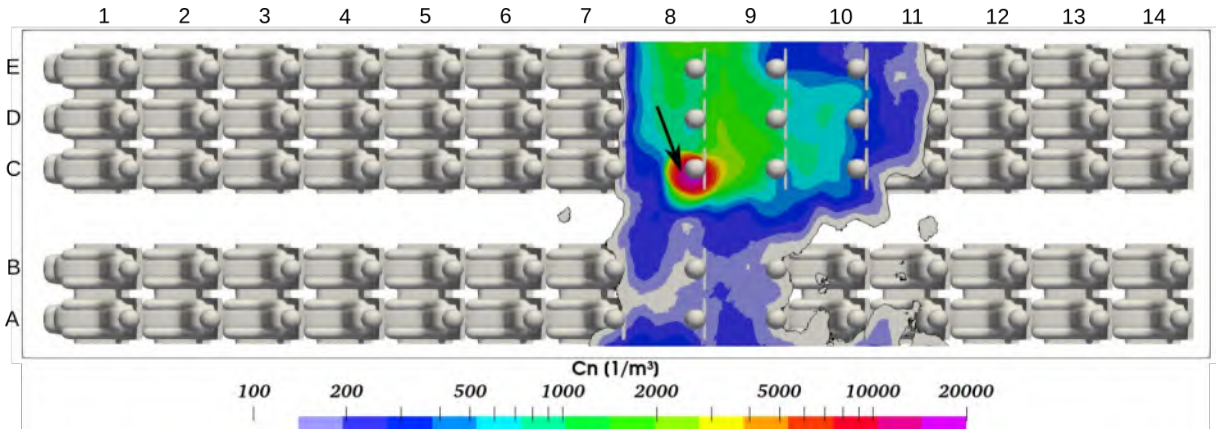

Figure 2: Numerically evaluated aerosol concentration (number of parcels per cubic meter) in the breathing zone. The particle source producing 1000 parcels per second is indicated by the arrow. The diameters of the particles are distributed uniformly from 0.5 µm to 2.5 µm.

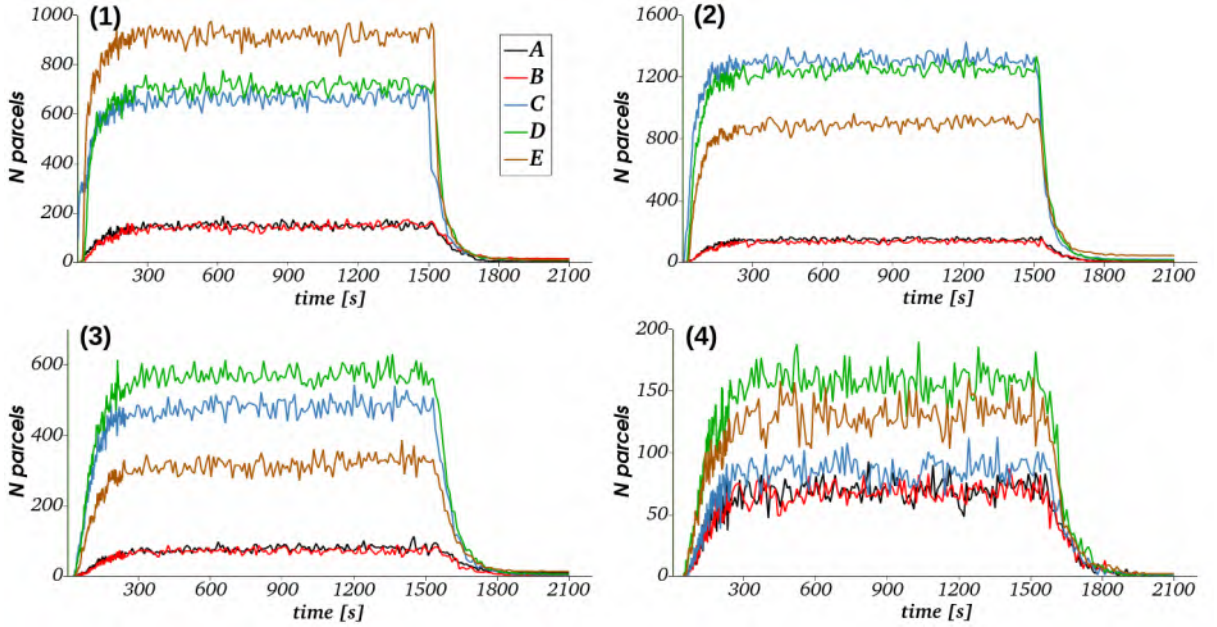

Figure 3: The history of the number of parcels in the breathing zones of different seats. The plots (1) to (4) correspond to the seat rows from 8 to 11. The notations A-E here correspond to the seats in Figure 2

Generally, the results of the numerical simulations of MV configuration show good qualitative agreement with measurements performed in the Do728 research facility.
Comparison of numerical simulations of CDV (not presented here) and MV configurations reveals certain advantages of the former. CDV provides lower aerosol concentration in the breathing zone and shorter dwell-time of particles.

References:

1.D. Schmeling, A. Shishkin, D. Schiepel, C. Wagner. Analysis of aerosol dispersion in the Do728 passenger compartment. Deutscher Luft- und Raumfahrtkongress (DLRK), 31. Aug. - 02. Sept. 2021, Bremen
2. D. Schmeling, A. Shishkin, D Schiepel, C. Wagner (2021) Aerosolausbreitung in der DO-728-Passagierkabine. Luft- und Raumfahrt (2), Seiten 20-23. Aviatic. ISSN 0173-6264.
3. J. Bosbach et al. (2013) „Alternative ventilation concepts for aircraft cabins". CEAS Aeronaut. J. 4, 301–313.

Mitteilung

Fachgruppe: Allgemeine Strömungstechnik

Generation, Distribution, and Contagiousness of Surgical Smoke during Tracheotomies

Vera Stelzer[1,2], Sandra Melina Tauwald[1,2], Veronika Vielsmeier[3], Fabian Cieplik[3], Arne Kandulski[3], Wulf Schneider-Brachert[3] and Lars Krenkel[1,2]

vera.stelzer@oth-regensburg.de

1 : Technical University of Applied Sciences (OTH) Regensburg, Department of Biofluidmechanics, Galgenbergstr. 30, 93053 Regensburg, Germany

2 : Regensburg Center of Biomedical Engineering and Regensburg Center of Health Sciences and Technology, OTH and University Regensburg,
Galgenbergstr. 30, 93053 Regensburg, Germany

3 : University Hospital Regensburg (UKR), Franz-Josef-Strauß-Allee 11, 93053 Regensburg, Germany

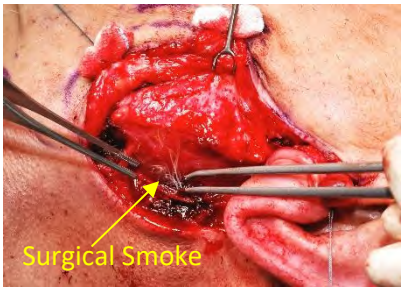

Figure 1: Generation of surgical smoke by electrocautery during surgery (here parotidectomy).

The contagiousness of surgical smoke and the associated risk for medical personnel is a very controversial topic in the literature. Surgical smoke is generated during the dissection or cauterization of tissue with heat-generating devices [1, 2]. It consists of 95 % water vapor and non-biological by-products and cellular debris (5 %) [1–3]. Various chemicals and biologically active components such as viruses and bacteria were detected in it [1]. In 1988, Garden [4] found intact bovine and human papillomavirus deoxyribonucleic acid (DNA) in the vapor of laser-treated warts and was able to detect disease transmission by viral particles [5]. Furthermore, DNA parts of viable oral poliovirus [6], human immunodeficiency virus (HIV) DNA [7], and DNA parts of hepatitis B [8] have been found in surgical smoke [3]. The viruses already detected in the smoke, as well as the equally proven disease transmission, make further investigations regarding the emergence, fluid-mechanical distribution, and contagiousness indispensable. Furthermore, the quantitative experimental determination of the aerosol number as well as the distribution of surgical smoke due to thermal convection in space is needed for the validation of the following numerical calculations. Numerical investigations are necessary to describe the real measuring situation without the measuring devices (here the particle sizers) influencing the real flow distribution.

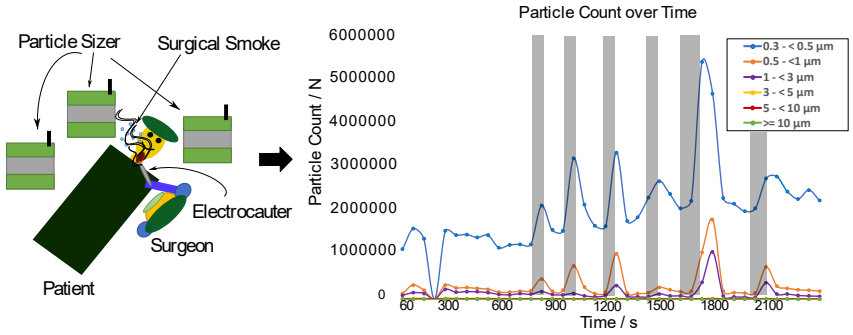

Figure 2: Measurement situation during tracheotomies. The resulting particle distribution is visible in the graph. Areas marked in gray indicate the use of the electrocautery.

Bipolar electrocoagulation is used in otorhinolaryngology, among other applications, for hemostasis and has been identified as an aerosol-generating procedure in preliminary works of our group (Figure 1). Since surgical smoke generation, particularly during tracheotomies, is thought to increase the risk to medical personnel, this study aims to determine the actual aerosol generation and distribution during tracheotomy procedures on human patients. Therefore, different particle counters (TSI Laser Particle Counter AeroTrak 9310, PC220 TROTEC, Fidas Frog) were placed at specific locations in the room during tracheotomies, and the resulting particle distribution was measured (Figure 2). To quantify the amount of aerosol produced during electrocautery under defined conditions, category 3 animal by-products (classified according to German law) were treated with electrocautery at different frequency levels in the saliva-moistened and non-moistened conditions. Therefore, the pig specimen is placed in a disinfected chamber. The resulting aerosol concentration is extracted directly from the chamber using a particle analyzer (Figure 3). In addition to the quantitative

analysis of the aerosol formation, the aerosol distribution in space during bipolar electrocoagulation is also determined. An Nd: YAG laser illuminates the resulting particles using a laser light sheet. A camera records the scattered light (Figure 3) and a programmable logic controller (PLC) triggers the system components.
Furthermore, bacteria are detected in surgical smoke to demonstrate the viability of potentially pathogenic organisms. Therefore, bacteria are applied to a porcine specimen in a disinfected chamber. The chamber is equipped with selective sedimentation plates to detect bacterial growth after subsequent incubation of the plates.

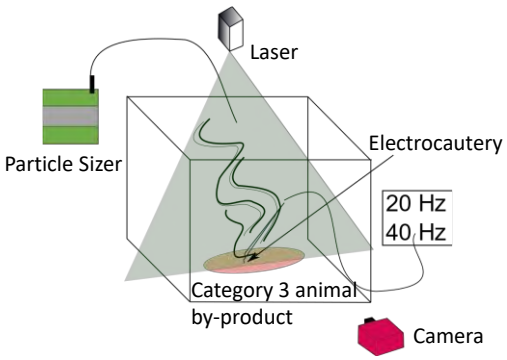

Figure 3: Quantitative measurement of the number of particles and distribution illuminated by a laser light sheet and recorded by a camera.

In all measurements during tracheotomies, there is an increase in the particle count of at least 60 % compared to the blank measurement, especially for the particle counter that was located directly by the treated patient. Figure 2 shows the particle counts over time in the channels of the particle sizer placed directly above the patient. During and after electrocautery, the particle counts rise significantly, especially in the small channels. The operating frequency of the electrocauter as well as the saliva-moisture influences the number of particles produced and their size distribution. A frequency of 40 Hz forms twice as many particles as a frequency of 20 Hz (Figure 4). After the tissue was moistened with artificial saliva, the number of particles at 20 Hz and 40 Hz doubled compared to the number of particles produced by the non-moistened tissue. At higher frequencies, more smaller particles are generated. The smaller the particles the longer they can stay airborne and also travel further in space. Therefore, they may pose a higher risk to the surgical personnel. The significant increase in particle concentration during bipolar coagulation, as well as their possible contagiousness also increases that risk. Therefore, it is important to experimentally quantify the number of produced particles under certain conditions and determine their distribution as a basis for numerical investigations. The numerical models can be used to test and implement various measures, such as the installation of an exhaust system or a filter, without interfering with the work of the medical staff.

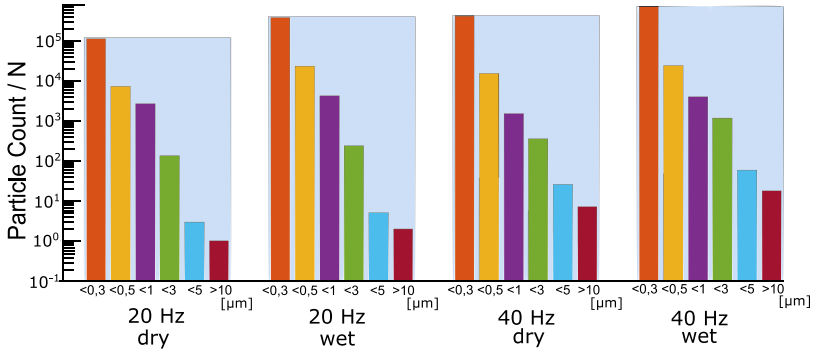

Figure 4: Maximum number of particles generated in each channel during electrocautery of category 3 animal by-products at 20 Hz, 20 Hz moistened, 40 Hz, and 40 Hz moistened. The blue area in the background marks the total maximum value during cauterization.

[1] P. Vourtzoumis, N. Alkhamesi, A. Elnahas, J. E. Hawel, and C. Schlachta, "Operating during COVID-19: Is there a risk of viral transmission from surgical smoke during surgery?," *Canadian journal of surgery. Journal canadien de chirurgie*, vol. 63, no. 3, E299-E301, 2020, doi: 10.1503/cjs.007020.

[2] B. C. Ulmer, "The Hazards of Surgical Smoke," *AORN journal*, vol. 87, no. 4, 721-738, 2008, doi: 10.1016/j.aorn.2007.10.012.

[3] K. Zakka *et al.,* "Electrocautery, Diathermy, and Surgical Energy Devices: Are Surgical Teams at Risk During the COVID-19 Pandemic?," *Annals of surgery*, vol. 272, no. 3, e257-e262, 2020, doi: 10.1097/SLA.0000000000004112.

[4] J. M. Garden, "Papillomavirus in the Vapor of Carbon Dioxide Laser-Treated Verrucae," *JAMA*, vol. 259, no. 8, p. 1199, 1988, doi: 10.1001/jama.1988.03720080033024.

[5] J. M. Garden, M. K. O'Banion, A. D. Bakus, and C. Olson, "Viral disease transmitted by laser-generated plume (aerosol)," *Archives of dermatology*, vol. 138, no. 10, pp. 1303–1307, 2002, doi: 10.1001/archderm.138.10.1303.

[6] M. J. Taravella, A. Weinberg, M. May, and P. Stepp, "Live virus survives excimer laser ablation," *Ophthalmology*, vol. 106, no. 8, pp. 1498–1499, 1999, doi: 10.1016/S0161-6420(99)90442-6.

[7] Baggish, Michael S and Polesz, Bernard J and Joret, Dale and Williamson, Patrick and Refai, Ashraf, "Presence of human immunodeficiency virus DNA in laser smoke," *Lasers in surgery and medicine*, vol. 11, pp. 197–203, 1991, doi: 10.1002/lsm.1900110302.

[8] H. D. Kwak, S.-H. Kim, Y. S. Seo, and K.-J. Song, "Detecting hepatitis B virus in surgical smoke emitted during laparoscopic surgery," *Occupational and environmental medicine*, vol. 73, no. 12, pp. 857–863, 2016, doi: 10.1136/oemed-2016-103724.

Mitteilung

Fachgruppe: Allgemeine Strömungstechnik

High Spatial Resolution Tomo-PIV of the Nasopharynx Focussing on the Physiological Breathing Cycle

Sandra Melina Tauwald[1,2], Maurizio Quadrio[3], Markus Ruetten[4], Christian Stemmer[5], Lars Krenkel[1,2]

[1]Regensburg Center of Health Sciences and Technology (RCHST), Galgenbergstr. 30, 93051 Regensburg, Germany

[2]Technical University of Applied Sciences (OTH), Department of Biofluidmechanics, Galgenbergstr. 30, 93051 Regensburg, Germany

[3]Politechnico Milano, Department Aerospace Science and Technology, Via Privata Giuseppe La Masa 34, 20156 Milan, Italy

[4]German Aerospace Center (DLR), Bunsenstr. 10, 37073 Göttingen, Germany[5]Technical University of Munich (TUM), Chair of Aerodynamics and Fluid Mechanics, Boltzmannstr. 15, 85748 Munich, Germany

melina.tauwald@oth-regensburg.de

Physicians are relying upon computational medicine to monitor emergencies, plan interventions and interpretate treatment results. Computational methods range from imaging technologies to big-data analytics [1]. Particularly in the area of respiration, computational methods can offer opportunities from both an economical and social viewpoint. Especially while linking the patient specific geometry and the physiological function of the upper airways from a fluid mechanics perspective [2–4]. To monitor patient's individual flow structures of the upper airways, numerical investigations validated by high-resolution experiments are required. Previous numerical and experimental studies assume Reynolds numbers up to 2900 in specific parts of the upper airways while linked to the breathing-cycles unsteady flow conditions [5]. The optical measurement technique Tomo-PIV provides information about velocity vectors and their derivatives in three dimensions. The in-plane and cross-plane velocity vectors give additional information about occuring vorticities. State-of-the-art time-resolved PIV with high-speed cameras is an approach to determine unsteady velocity fields. In practice, decisions concerning spatial and temporal resolution of measured flow field have to be made. Commercially affordable high-speed cameras bring a high repitition rate but with the drawback of low pixel resolution in contrast to low-repitition CCD-cameras [6]. This project aims at pseudo-time-resolved PIV measurements of unsteady nasopharyngeal flows by a trigger-shift of the flow cycle by phase-locking. A trigger-shift within the duration of the CCD-cameras double-frame-rate Δt virtually increases time resolution. While comparing measured velocity in a phase-locked way, mean velocity standard deviation enables identifications of unsteady conditions by traditional PIV-setup CCD-cameras.

The current work provides Tomo-PIV measurements on a part of the upper airways based on a patient individual geometry. A computer-tomographic scan of a patiens head builds the basis of the measurement geometry. The scan was segmented with an otorhinolarynologist and enlarged two-fold. Finally a mould for the transparent silicone model of the phantom head was build. The manufactured transparent phantom head is placed in a fishtank filled with working fluid shown in Fig. 1. Tomo-PIV, since it is an optical measurement technique, requires a precise refractive image matching (RIM) between the phantom head and the working fluid. For proper RIM, the fishtank and the phantom head is illuminated by a laser light-sheet. A camera located opposed to the laser records the light-sheet after passing the fishtank. A succesfull RIM is achieved when the light-

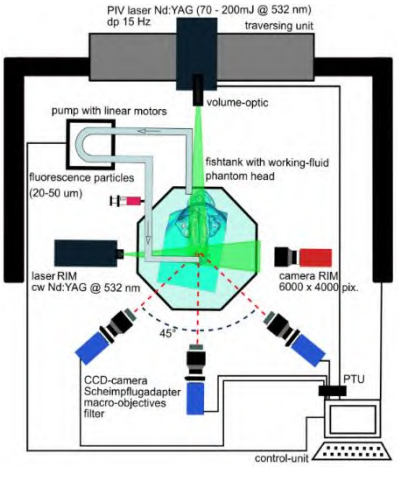

Fig. 1: *Tomo-PIV setup combined with refractive-index-matching (RIM) setup containing phantom head model.*

sheet is not distorted by the highly complex 3D geometry. RIM of 1.4140 is prooven to be most efficient. A Tomo-PIV system with three cameras (CCD-sensors, Imager Pro X 10, 1600x1200, double-frame-rate 15 Hz.) records the flow. Cameras are equipped with macro objectives (ZEISS, Milvus 2/130), Scheimpflug adapters and cut-off filters. The field of view is 52x30 mm with a scale factor of 37.05 pix/mm. A laser (Nd:Yag 70-200 mJ @ 532 nm) illuminates fluorescence tracer particles (Ø 20-50 µm, abs/emm = 560/584). The components are all centrally controlled by the software DaVis 10.2. Volumetric reconstruction and vector calculation is fullfilled with a final window size of 56 voxels and a maximum expected displacement of 8 voxels. The initial plate calibration by 3rd order polynominal function results an error of 0.38 pix. Volume-Self-Calibration minimized the error to 0.03 pix. A pump equipped with two linear motors induces the flow rate. The induced flow rate is based on data captured by a spirometer.

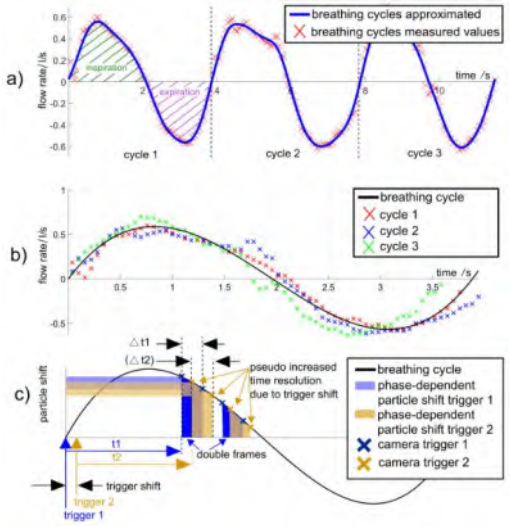

Fig. 2: a) *Spirometer data of breathing cycle* ***b)*** *averaged breathing cycle* ***c)*** *phase-locked and trigger-shift method in a breathing cycle with inter-double-frame-rate duration Δt1 and Δt2 . Pseudo-increased time resolution is shown.*

Three consecutive cycles of a test person show an averaged duration of 4 seconds (Fig. 2a). The maximum detected flow rate of inspiration is 0.7 l/s respectively 0.6 l/s of expiration. The cycles are approximated by a 3rd order polynomial function (Fig. 2b). Since the phantom head is a magnification of the physiological geometry, the experimental flow rate Q_{vitro} is adjusted to spirometer flow rate Q_{vivo} by Reynolds number. $Q_{vitro} = Q_{vivo} * M * \nu_{vitro}/\nu_{vivo}$ includes the kinematic viscosity ν_{vitro} of the working fluid, kinematic viscosity ν_{vivo} of air at BTPS (37°C, gas saturated with water vapor, 101,325 Pa) and the geometrical magnification factor M. The frequency of breathing cycles are adapted by the duration of one cycle t_{vivo} by the Womerseley number $t_{vitro} = M^2 * \nu_{vivo}/\nu_{vitro} * t_{vivo}$. Reynolds similarity results $Q_{vitro} = Q_{vivo} * 0.96$ and Womerseley similarity $t_{vitro} = 8.29 * t_{vivo}$. Averaged mean-velocity of a single breathing-cycle phase is calculated by comparing multiple measurements of the same phase in the cycle. The resulting phase-locked standard deviation of this mean-velocity can give information about unsteady flow conditions in a specific phase of the cycle. For a pseudo-increased time-resolution, a phase-adjusted trigger-shift within the double-frame-rate is applied (Fig. 2c). The comparison of the intensity of ghost-particles and real particles of the Tomo-PIV reconstruction [7] results in a signal-to-noise ratio of 2.3. The signal-to-noise ratio based on [8, 9] by comparing the number of real particles in with the number of ghost-particles results in a ratio of 1.2 in this study. The measured flow field in the trachea can be seen in Fig. 3.

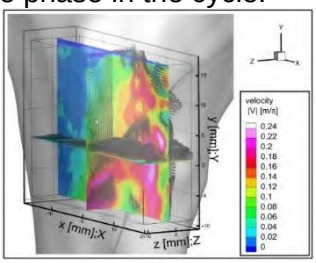

Fig. 3: *3D velocity field located in the trachea containing vectors in three dimensions.*

[1] L. Lyu, H. Cui, M. Shao, Y. Fu, R. Zhoa, and Q. Chen, "Computational Medicine: Past, Present and Future," *Chin J Integr Med*, no. 28, pp. 453–462, 2022, doi: 10.1007/s11655-021-3453-z.

[2] M. Quadrio *et al.,* "Review of computational fluid dynamics in the assessment of nasal air flow and analysis of its limitations," *Eur. Arch. Othrhinolaryngol.*, no. 271, pp. 2349–2354, 2014, doi: 10.1007/s00405-013-2742-3.

[3] A. Lintermann and W. Schröder, "A Hierarchical Numerical Journey Trough the Nasal Cavity: From Nose-Like Models to Real Anatomies," *Flow Turbulence Combust.*, no. 102, pp. 89–116, 2019, doi: 10.1007/s10494-017-9876-0.

[4] K. P. Lynch and F. Scarano, "Experimental determination of thomographic PIV accuracy by a 12-camera system," *Meas. Sci. Technol.*, no. 25, pp. 1–10, 2014, doi: 10.1088/0957-0233/25/8/084003.

[5] I. Hörschler, W. Schröder, and M. Meinke, "On the assumption of steadiness of nasal cavity flow," *J. Biomech.*, no. 43, pp. 1081–1085, 2010, doi: 10.1016/j.jbiomech.2009.12.008.

[6] D. Yifan, W. Peng, and L. Yingzheng, "Phase-locking particle image velocimetry measurement of unsteady flow behaviors: Online dynamic mode decomposition using field-programmable gate array," *Physics of Fluids*, no. 31, 2019, doi: 10.1063/1.5086907.

[7] F. Martins, J. Focaut, L. Thomas, L. Azevedo, and M. Stanislas, "Volume reconstruction optimization for tomo-PIV algorithms applied to experimental data," *Meas. Sci. Technol.*, no. 26, 2015, doi: 10.1088/0957-0233/26/8/085202.

[8] G. E. Elsinga, J. Westerweel, F. Scarano, and M. Novara, "On the velocity of ghost particles and the bias errors in Tomographic-PIV," *Exp. Fluids*, no. 50, pp. 825–838, 2011, doi: 10.1007/s00348-010-0930-0.

[9] J. Westerweel, G. E. Elsinga, and R. Adrian, "Particle image velocimetry for complex and turbulent flows," *Annu. Rev. Fluid Mech.*, no. 45, pp. 409–436, 2013, doi: 10.1146/annurev-fluid-120710-101204.

Mitteilung

Fachgruppe: Allgemeine Strömungstechnik

Automated measurement of the number and growth of water droplets in mixed convection

Marie-Christine Volk, Konstantin Niehaus, Claus Wagner
German Aerospace Center (DLR), Institute of Aerodynamics and Flow Technology, Göttingen, Germany, Marie-Christine.Volk@dlr.de

Condensation of humid air at subcooled surfaces occurs in various technical applications i.e. windows, camera lenses, windshields or headlights. Misting of these surfaces is unwanted or even poses a safety risk. Providing a better understanding of the associated mass transfer during evaporation or condensation is the requirement for solving such problems and is the aim of our work. Considering the latter, the vast majority of publications investigate condensation of steam with small fractions of non-condensable gas, while the aforementioned applications are exposed to low fractions of water vapor. The mass transfer in channel flow has been reported by i.e. Zheng et al. [1] or Westhoff et al. [2] but is rarely investigated in experimental studies with more complex flow structures.
Fig. 1 depicts a schematic of the experimental set-up. It consists of a cuboidal cell with aspect ratio 2:1:1 cooled at the front and heated at the back wall. The sample has an inlet on the left with conditioned air at relative humidity φ, volume flow $\dot{V}$, and fluid temperature T_{in} entering the cavity, while on the right side humid air may exit the sample. For a detailed description of the set-up and its boundary conditions see Niehaus et al. [3].
To study the process of condensation with a non-invasive method, three cameras are used for time-resolved recordings of the water droplets' size and growth at different viewing angles and fields-of-view. The first records the droplet size to measure the radii and contact angles of the water droplets using a far-field microscope. The second takes full view snapshots from the cooling plate to get an overview of the total water mass distribution. The last images the droplet contact lines using a far-field microscopes through the transparent cooling plate with a field of view of $4.6\,\mathrm{mm}$ by $3.9\,\mathrm{mm}$. A raw image of the third camera can be found in Fig. 2. The droplets of various sizes are indicated red. The radii probability density of Fig. 2 and at two consecutive snapshots can be seen in Fig. 3. It becomes evident that the distribution of droplet size changes with time. Having first a Gaussian-like distribution of droplet sizes, for higher condensation durations a minimum in the histogram of droplet radii is observed in the range $50 - 70\,\mu\mathrm{m}$. This indicates the border between single droplet growth and growth due to coalescence .

To understand the ongoing process of condensation, a precise observation of the droplet growth is key. For that, we need to assess the droplet radii distribution not only at few discrete times, but continuously. Having pictures with more than 2000 distinct droplets, hand labeling is not feasible. Therefore, an automated droplet detection is required. The implemented process is illustrated in Fig. 4, where a pre-processing to increase contrast is followed by an edge detection to apply a Circle Hough Transform which ultimately gives droplets positions and sizes. A more detailed description of the implementation of detection and close examination of the live cycles of droplets during evaporation and condensation will be the topic of our presentation.

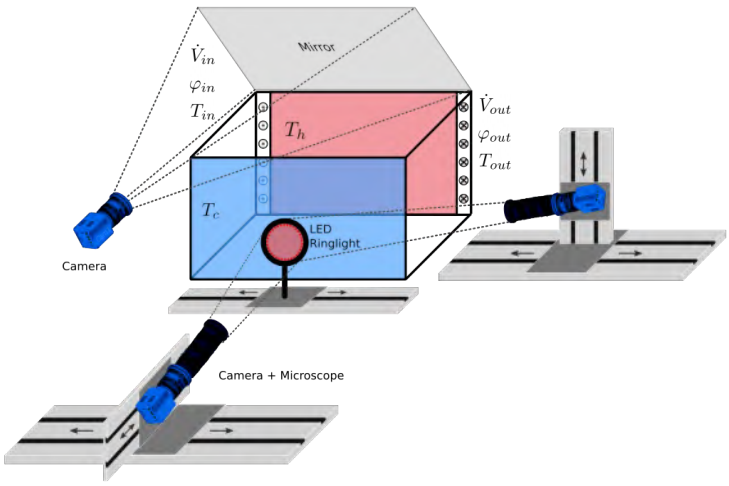

Fig. 1: Experimental set-up: The cooling plate at the front (blue) at temperature T_c and the heating plate (red) at T_h. Volume flow $\dot{V}$, relative humidity φ and dry-bulb temperature are measured at the inlet (circles) and the outlet (crosses). Three cameras - two of them with far-field microscopes - record the growth of the condensation on the front glass pane.

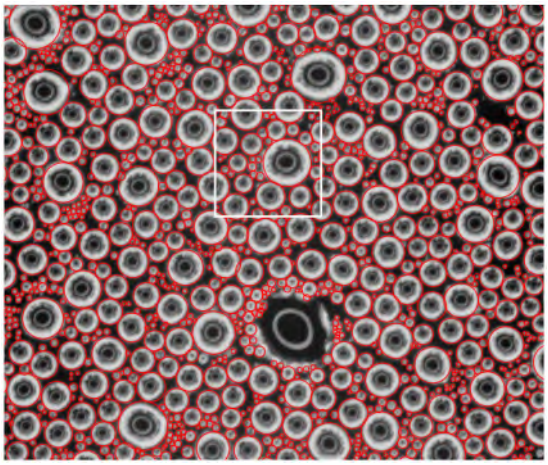

Fig. 2: Water droplets captured with the front camera using a far field microscope. The field of view is a $[2560 \times 2160]\,\mathrm{px}^2$ area corresponding to a size of $[(4.59 \pm 0.01) \times (3.89 \pm 0.01)]\,\mathrm{mm}^2$. The picture is taken after $5731\,\mathrm{s}$ of condensation with $T_c = 9\,℃$, $T_h = 25\,℃$, $\dot{V}_{in} = 100\,\mathrm{l/min}$ and a dew point of $T_{dp} = 15\,℃$. The droplets are labeled by hand to examine their size distribution (see orange curve in fig. 3).

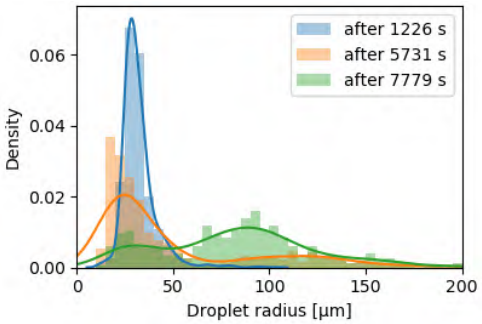

Fig. 3: The distribution of droplet radii is plotted at 3 different times during condensation.

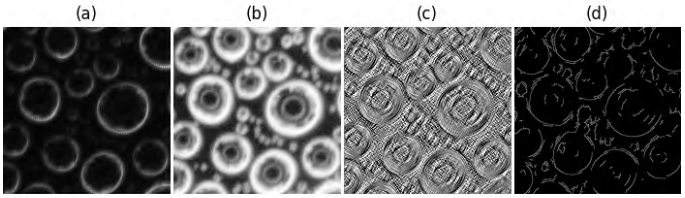

Fig. 4: Image processing steps using the section indicated white in 2 (white area): (a) raw image data from the camera. (b) the image is pre-processed by applying histogram equalization using its cumulative distribution function (cdf) and blurred. (c) shows the gradient of the image intensity obtained with the Sobel filter and (d) the detected edges with a Canny edge detector.

References

[1] Shaofei Zheng, Ferdinand Eimann, Christian Philipp, Tobias Fieback, and Ulrich Gross. Experimental and modeling investigations of dropwise condensation out of convective humid air flow. *International Journal of Heat and Mass Transfer*, 151:119349, April 2020.

[2] A. Westhoff. Experimentelle Untersuchung des Einflusses der Oberflaechenbeschaffenheit von Scheiben auf die Kondensatbildung. *FAT-Schriftenreihe*, (303), 2017.

[3] Konstantin A. Niehaus, Andreas Westhoff, and Claus Wagner. Characterization of a Mixed Convection Cell Designed for Phase Transition Studies in Moist Air. In Andreas Dillmann, Gerd Heller, Ewald Krämer, and Claus Wagner, editors, *New Results in Numerical and Experimental Fluid Mechanics XIII*, Notes on Numerical Fluid Mechanics and Multidisciplinary Design, pages 483–493, Cham, 2021. Springer International Publishing.

Mitteilung

Fachgruppe: Allgemeine Strömungstechnik

Aerosol spread in a generic train entrance: Comparison between experiment and numerical simulation

Florian Webner, Andreas Kohl, Daniel Schmeling und Claus Wagner
Deutsches Zentrum für Luft- und Raumfahrt e.V. (DLR)
Institut für Aerodynamik und Strömungstechnik
Bunsenstraße 10, 37073 Göttingen
florian.webner@dlr.de

Computational fluid dynamics (CFD) rely on models and approximations that have to be validated. Thus, the present study focuses on the comparison of steady state CFD predictions with measurements of the distribution and spreading of aerosol particles, emitted by a passenger in a ventilated full-scale geometry representing the entrance area of a passenger train. The entrance area is represented by a simplified cubic geometry (see *Fig. 1a*), where two heatedstanding thermal manikins (TMs) are opposing each other. One of the manikins is exhalingaerosol at a constant rate and a size distribution typically produced during human breathing.
Filtered and conditioned air is supplied through a rectangular panel in the ceiling, the air outlets are distributed symmetrically laterally near the floor. The simplicity of the utilized geometry allows to minimize differences between the experimental and the numerical setup, while also including all relevant mechanisms (e.g. ventilation and body heat) of a passenger cabin.

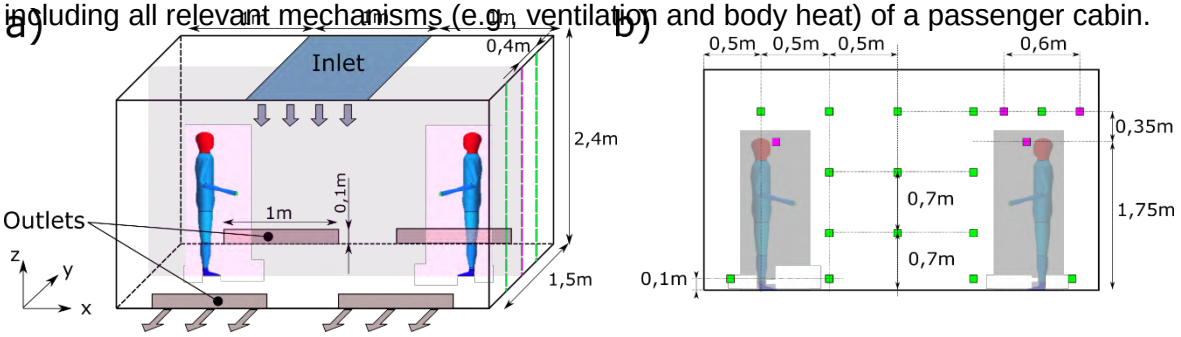

Figure 1: a) Schematic of the simplified train entrance model used for the experimental and numerical studies. b) Position of the aerosol particle sensors on the three measurement planes (green, purple dashed lines in Fig. a)). Green squares mark the particle sensor-positions on the outward planes, purple squares additional sensor-positions on the middle plane.

The air supply is positioned on the ceiling with the velocity being constant over the inlet area and over time. In the experiment, this is achieved through a membrane inlet, distributing the airflow equally over the whole area. The volumetric flow rate is 25 l/s at a temperature of 17°C. The walls are adiabatic. In the experiment, this is nearly achieved through thick layers of insulation. Both TMs simulate the geometrical dimensions and thermal influence of humans inside the model, with a constant heat flux of 100 W emitted from each of their bodies. Temperature probes are distributed in the experimental setup to measure the wall and air temperatures (not included in *Figure 1b*), for the determination of the experimental thermal boundary conditions.

For the experimental determination of the aerosol distribution, we use 49 particulate matter sensors which are well-established and used in many studies regarding aerosol spread in airplane cabins [1, 2]. Aerosol particles with diameters from 0,3 – 10 µm are recorded at around 1 Hz frequency at the positions shown by the squares in *Figure 1b* in three parallel xz-planes. For the generation and distribution of the aerosol similar to human exhalation, an aerosol

source is used [2]. It generates a total number concentration of 10^5 particles per cubic centimeter, using artificial saliva, at a constant aerosol exhalation of 12 liters per minute. As aerosol exhalation opening, a tube inlet with a diameter of 12 mm is used representing an opened generic mouth of an average opening-area of 1.13 cm². The resulting Reynolds number of the jet is in the range of 1400. To allow comparability between our measurements and the CFD simulation, we are evaluating the resulting aerosol concentration distribution, after a steady state temperature (and developed flow field) is reached in the experiment.

For the numerical simulation, the open-source software package OpenFOAM is employed to approximate solutions of the Reynolds-averaged Navier-Stokes equations (RANS). From this package, the solver buoyantSimpleFoam is chosen, which is suitable for buoyancy driven convection flows caused by TMs. Turbulence is considered by employing a k-omega SST model. The mesh is locally refined around the TMs, around the expected breathing jet as well as the thermal plume. The ventilation inlet velocity and temperature are prescribed in accordance to the values realized in the experiment. The air outlets are defined with a passive outlet boundary condition on the positions shown in *Fig. 1a*. Heat flux and heat radiation boundary conditions are specified at the surfaces of the manikins by prescribing a power of 100 W and an emissivity of ε = 0.95. An additional air inlet is defined on one of the manikins faces, mimicking the mouth for the continuous exhalation. The particles are inserted directly into the breathing jet at the mouth opening.

Fig. 2 shows blue-red streamlines through the x-orientated centerline of the air supply panel, where the color indicates the temperature in Kelvin. The streamlines reveal large, nearly symmetrical circulations that divide the room. The red colored streamlines above the heads reflect the buoyancy effects. In a steady state, the streamlines are equal to the path lines, illustrating the theoretical mean path of tracer particles that are solely affected by drag force, where gravity, inertia, and other forces are neglected. Therefore, the streamlines suggest that particles are recirculating symmetrically in the room before depositing or leaving the enclosure through the outlets near the floor. The additional gray streamlines represent the trajectories of aerosol particles emitted by the manikins' mouth reflecting the case with exhalation (right TM) and also represent the trajectories of aerosol particles, which are crossing the breathing zone (in front of the mouth) of the left TM. For the comparison with the experiment, the influence of forces neglected by streamlines are considered by reactingParcelFoam for realistic particle tracing.

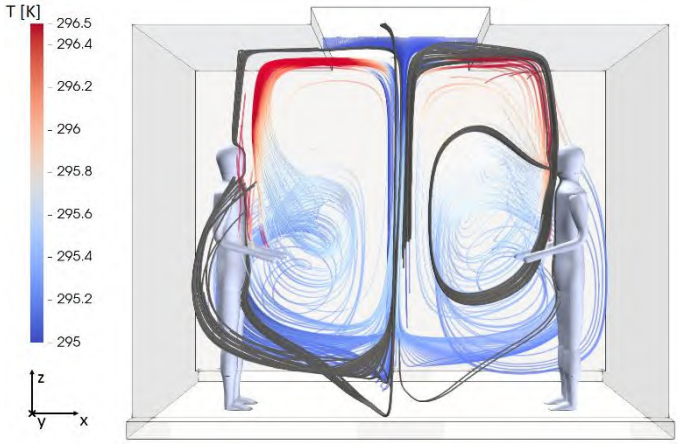

Figure 2: CFD results of the temperature field, streamlines through the air supply panel and mouth openings

The quantitative comparison presented at the Symposium will focus on temperature and particle concentration distribution measured in the experiment at selected positions. The objective is to validate CFD predictions with an experiment, addressing the aerosol spreading in a simple but relevant train geometry. The validation also serves as a basis for future prediction of the spreading of (potentially) pathogen-laden aerosols in indoor environments such as passenger compartments of trains and airplanes.

[1] Netherland Aerospace Center (NLR) and National Institute for Public Health and the Environment (RIVM) (2021) "CORSICA final report" NLR-CR-2021-232.

[2] Schmeling et al., Numerical and experimental study of aerosol dispersion in the Do728 aircraft cabin. (2022)

Mitteilung

Fachgruppe: Drehflügler

Dynamic Stall Computations of a Double-Swept Rotor Blade with Rigid and Elastic Modelling

Georg Babij
Institute of Aeroelasticity, German Aerospace Center,
Bunsenstraße 10, 37073 Göttingen, georg.babij@dlr.de

Innovative helicopter rotor blades with a combined for- and backward sweep at the outer part of the blade enable a reduction in noise emission and enhance the overall performance of a rotor. In this context, the influence of the aeroelastic behaviour in connection with the dynamic stall phenomenon is of great importance. It is accompanied by large aerodynamic load peaks, primarily seen in the lift and the pitching moment, impacting the structural integrity of the blades and adjacent control components. Double-swept model rotor blades were developed [1] and investigated experimentally in a four-bladed rotor configuration at DLR's Rotor Test Facility Goettingen (RTG) which is shown in Figure 1 [2]. They are built from multiple layers of carbon fibre reinforced polymer with an integrated foam core and measure 541 mm in blade length as well as 72 mm in chord length at the root. The rotor radius amounts to 652 mm. Due to an axial inflow to the rotor a sinusoidal variation in pitch angle is introduced to trigger the dynamic stall behaviour once per revolution. The following numerical study simulates the conducted experiments utilizing two different modelling approaches: on the one hand, an approach that incorporates aeroelasticity connected with flexible rotor blades, and on the other hand, one that considers the blades merely as rigid bodies. The corresponding computations are carried out with the use of computational fluid dynamics (CFD) and a multibody system (MBS) which is used in both cases, i.e. with rigid and flexible blades, to prescribe body motions. With the inclusion of aeroelasticity both domains are connected together by using a strong aeroelastic coupling scheme and, in addition, forces as well as displacements are exchanged between each other.

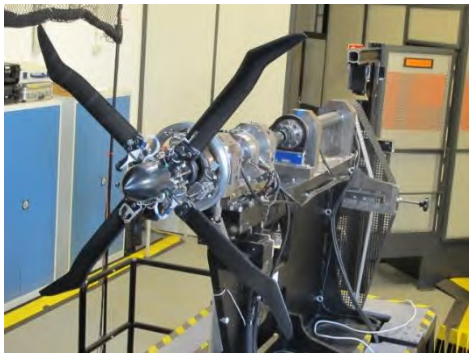

Figure 1: Rotor Test Facility Göttingen with four-bladed rotor

Numerical modelling

Simpack is used to describe the structural dynamics of the entire rotor by means of a multibody system. For the approach with flexible blades, the extension module FlexModal allows taking account of their elasticity. The structural displacements are thereby described in a modal representation with an underlying linear elastic material behaviour. Stiffening effects occurring due to centrifugal forces are considered by a geometric stiffness matrix. The entire MBS configuration of the rotor modelled in Simpack can be seen in Figure 2 [3].

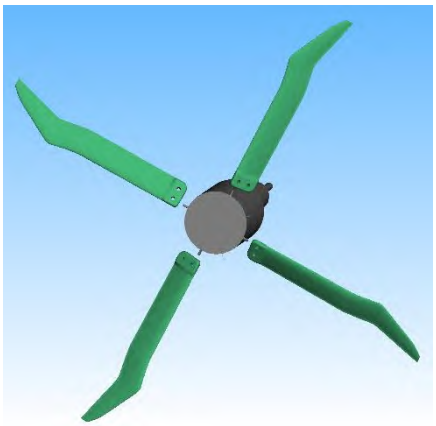

Figure 2: Modelling of structural dynamics in Simpack

TAU utilizes the Reynolds-Averaged-Navier-Stokes equations to model fluid flow by means of a finite volume method implemented for unstructured grids. Due to the unknown Reynolds stresses turbulence models are applied, such as the SST-k-ω-model according to Menter in this study. Against this backdrop, an approximate solution is sought on a dual grid being created from a user-defined primary grid. The primary grid contains approximately 13.555 million nodes and it consists of a background grid as well as four chimera grids representing the blades. Taking into account grid motion and deformation, the Chimera technique as well as the geometric conservation law were exploited.

The aeroelastic coupling is based on a sequential exchange of forces and displacements in each physical time step between both solvers. It represents in the sense of the terminology used within the rotorcraft community a strong coupling scheme. In detail, aerodynamic forces being calculated by TAU are transferred to Simpack and, vice versa, structural displacements together with rigid body motions

are transferred from Simpack back to TAU. In order to exchange this data between both differently discretized domains scattered data interpolation methods based on radial basis functions are exploited [4]. The software implementation mostly relies upon DLR's FlowSimulator and Simpack's IPC Co-Simulation which both provide powerful coupling interfaces for each simulation software, i.e. TAU and Simpack. Furthermore, the physical time step is chosen according to an azimuthal discretization $\Delta\Psi = 1°$ in this study. It results in a time step of $\Delta t \approx 1.177 \cdot 10^{-4}\ s$ for a rotational frequency $f = 23.6\ Hz$.

Numerical investigations and comparison with experiment

Several test cases with a rotational frequency $f = 23.6\ Hz$ will be presented comprising operating conditions with a solely collective pitch angle $\Theta_{\text{coll}} \in \{17°, 24°, 27°\}$ and an additionally superposed cyclic variation in pitch angle $\Theta_{cyc} \in \{6°, 8°\}$. They serve to induce the Dynamic Stall phenomenon gradually with increasing strength. Forces acting normal to the planform of a blade F_n and pitch moment M_y relative to an axis passing through the quarter chord point at the blade root, are monitored for two different modelling approaches: One that incorporates aeroelasticity connected with flexible rotor blades as well as one that considers the blades as rigid bodies. For computations including aeroelasticity, the deformations at the blade tips are additionally extracted.

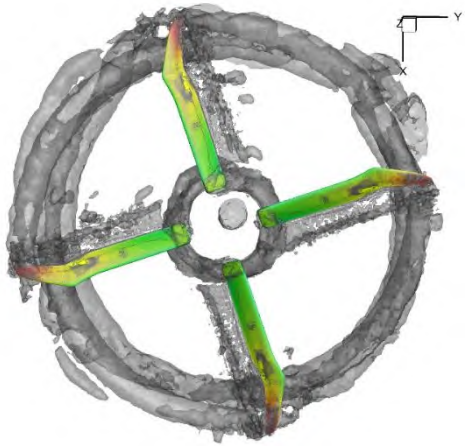

Figure 3: Simulation with elastic blades: Vortex system (grey transparent, λ_2-criterion), blade displacement (coloured)

When looking at the aerodynamic loads, particularly the normal force F_n and the pitch moment M_y, of both modelling approaches, i.e. with rigid and flexible blades, the results show differences between each other. For a test case with solely collective pitch angle $\Theta = 27° \pm 0°$ the normal force F_n is reduced under consideration of elasticity, although the magnitude of pitch moment M_y increases which acts in nose-down direction on the aerofoil. Beside the occurrence of vortices trailing at the blade tips, vortex shedding due to unsteady flow separation in the boundary layer can also be found. These characteristics in flow topology are seen for both modelling approaches, i.e. rigid and elastic blades. Insight into aeroelastic simulation is given in Figure 3 where coloured blades illustrate their displacements and, in addition, the vortex system is depicted in transparent grey by means of the λ_2-criterion. For an additional superposed cyclic pitch angle $\Theta = 27° \pm 6°$, the dynamic stall phenomenon appears. The vortex shedding in the boundary layer increases in regions near the outer kink as well as at the backward-swept part in close vicinity to the blade tip. As a consequence, a hysteresis loop with differences between the up- and downstroke motion emerge in the aerodynamic loads, shown in Figure 4 for the normal force F_n plotted against pitch angle Θ. Moreover, the inclusion of elasticity in the blade modelling influence the curves of the hysteresis loop.

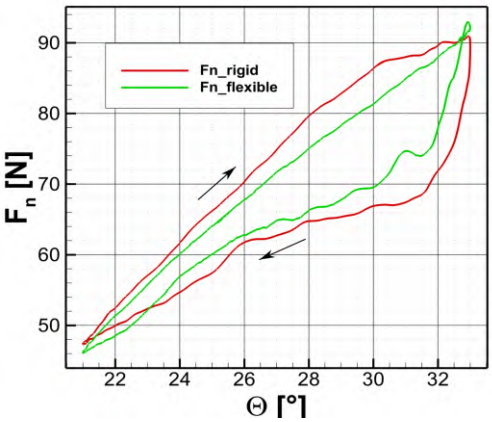

Figure 4: Normal force F_n versus pitch angle Θ for rigid and elastic blade modelling

Further investigations focusing on the dynamic stall behaviour will be continued. In order to draw conclusions about the influence of elasticity, the differences between both modelling approaches will be elaborated. Finally, experimental data which include measured blade forces and moments as well as pressure data for the numerical investigated test cases are available for comparison.

References

1. Müller, M.M., Schwermer, T., Mai, H., Stieg, C.: Development of an innovative double-swept rotor blade tip for the rotor test facility Goettingen. In: DLRK 2018 Deutscher Luft- und Raumfahrtkongress (Sep 2018), https://elib.dlr.de/122702
2. Schwermer, T., Richter, K., Raffel, M.: Development of a Rotor Test Facility for the Investigation of Dynamic Stall (2016), https://elib.dlr.de/91322
3. Arnold, J., Waitz, S.: Using Multibody Dynamics for the Stability Assessment of a New Double-Swept Rotor Blade Setup. European Rotorcraft Forum, Delft (2018)
4. Surrey, S., Ortun, B., Truong, K.V., Wienke, F.: Investigation of the structural blade dynamics and aeroelastic behavior of the 7A rotor. American Helicopter Society 72nd Annual Forum, West Palm Beach (2016)

Mitteilung

Fachgruppe: Drehflügler

Wind-tunnel experiments for a helicopter model with different blade stubs length

Ulrich Hartmann, Christian Breitsamter
Lehrstuhl für Aerodynamik und Strömungsmechanik, TUM School of Engineering and Design, Technische Universität München, Boltzmannstr. 15, 85748 Garching bei München, ulrich.hartmann@tum.de

Helicopter aerodynamics is a complex subject that continues to challenge researchers today. The rotation of the rotor and the flow around the helicopter cause noise and vibrations. Furthermore, the turbulent wake of the rotor head leads to interactions with the tail boom and the helicopter's vertical and horizontal fin [1]. Experiments in the wind-tunnel help to investigate these flow phenomena. However, full-scale testing of helicopter models is limited to only a few wind tunnels in the world, such as the National Full-Scale Aerodynamics Complex (NFAC) [2, 3]. Therefore, experimental investigations in smaller wind tunnels with a scaled helicopter model are conducted. Here, the observation of the entire rotor is usually not possible, and the rotor blades are shortened to a certain degree. There are no clear guidelines for the design of the rotor blade stubs, and different variants can be found in the literature [4]. A specific investigation of different rotor blade designs on a scaled wind tunnel model is needed to derive strategies and methods for future helicopter models.

Within the project NANNY (iNnovative AN- uNd AuftriebssYsteme für die nächste Generation leichter bis mittelschwerer Hubschrauber), wind-tunnel experiments, including forces and moments and Stereo-PIV measurements, were performed for three different blade stubs at $U_\infty = 25\ m/s$. Figure 1 shows the 1:7.333 helicopter model for the investigated configuration in the wind tunnel at the Chair of Aerodynamics and Fluid Mechanics of the Technical University of Munich (TUM). On the left side, the blades (R1) are cut at the first aerodynamic blade section, while the middle is shortened (R2). Only the inner-most blade section with the pitch horn is modeled for the smallest stub (R3) on the right side.

Figure 1: Blade stubs on the helicopter model (left: R1, middle: R2 and right: R3).

Forces and moments were determined for the helicopter while varying configuration, inflow angle, pitch angle and blade stubs. Figure 2 compares the drag α-polar (β=0) for the three different blade stubs considering a rotating rotor head with collective pitch movement. The longest blade stub generates higher drag than the medium and short stub. With higher angles of attacks, the drag difference increases. Between the medium and short blade stubs, the drag difference stays constant along the angle of attack.

Beside investigating helicopter aerodynamic loads, stereoscopic particle image velocimetry (Stereo-PIV) measurements are used to analyze the flow field. Along the tail boom, planes normal to the flow directions were evaluated. Figure 3 shows the axial flow velocity component for the three blade stubs at the collective pitch on 75% of tail boom length. The baseline blade stubs show blade tip vortices, while the hubcap dominates the flow area for the smaller blade stubs.

First results show an influence of the blade stubs on the helicopter forces and moments. Unsteady pressure measurements on the vertical fin are planned to investigate the effectiveness and excitation of the stabilizer surfaces affected by the rotor-head wake.

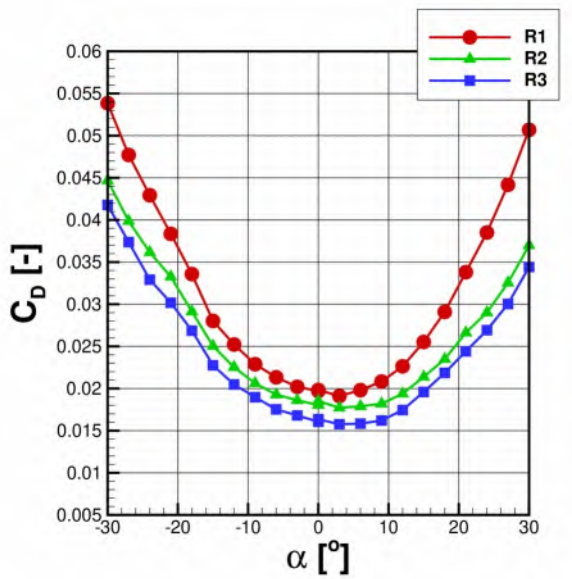

Figure 2: Drag α-polar of the blade stubs for β=0.

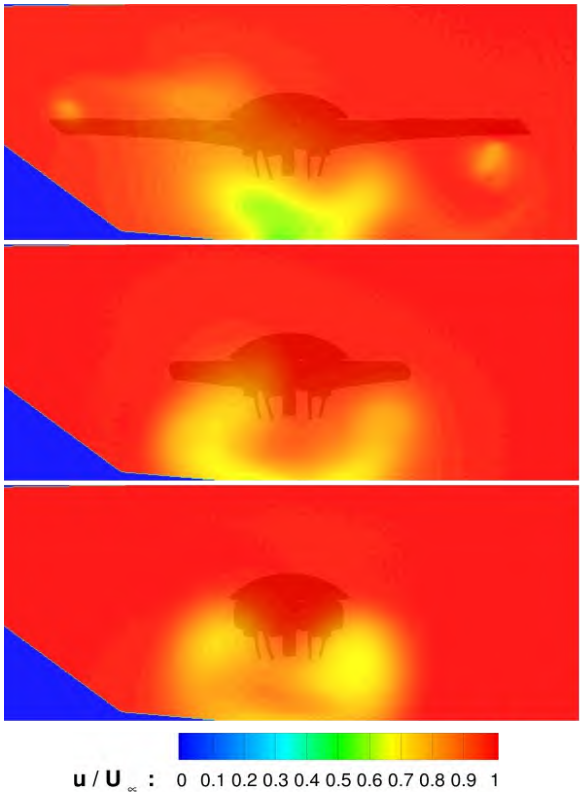

Figure 3: Axial velocity fields of the three blade stubs configurations (top: R1, middle: R2, bottom: R3).

References

[1] Leishman, G. J. Principles of helicopter aerodynamics with CD extra. Cambridge university press, 2006.

[2] Zell, P.T.: Performance and Test Section Flow Characteristics of the National Full-Scale Aerodynamics Complex 80- by 120-Foot Wind Tunnel. Technical Report, NASA Technical Memorandum 103920, Ames Research Center, Moffett Field, CA, USA, January, 1993.

[3] Norman, T.R., Shinoda, P., Peterson, R.L., Datta, A.: Full-Scale Wind Tunnel Test of the UH-60A Airloads Rotor. American Helicopter Society 67th Annual Forum, Virginia Beach, VA, May, 2011.

[4] Green, R.B., Giuni, M., Cervinka, J. Zacho, D., Austin, P., Smith, S., Desvigne, D., Alfano, D.: The Clean Sky “CARD” Project: Wind Tunnel Measurements of a Model Helicopter Rotor and Fuselage Drag. 41 st European Rotorcraft Forum, Munich, Germany, September, 2015.

Mitteilung

Fachgruppe: Drehflügler

Vortex-induced stall on an actively twisted highly loaded model rotor blade

Gunther A. Wilke, Berend G. van der Wall
German Aerospace Center, Lilienthalplatz 7, 38108 Braunschweig, Germany
gunther.wilke@dlr.de, berend.vanderwall@dlr.de
Yasutada Tanabe, Hideaki Sugawara
Japan Aerospace Exploration Agency, Japan
tan@chofu.jaxa.jp, sugawara.hideaki@jaxa.jp
Do-Hyung Kim, Hee J. Kang
Korea Aerospace Research Institute, Korea
dhkim@kari.re.kr, hkang@kari.re.kr
Sung N. Jung, Seong H. Hong
Konkuk University, Seoul, Korea
snjung@konkuk.ac.kr, shsky0721@konkuk.ac.kr
Joëlle Bailly
ONERA, The French Aerospace Lab, Meudon, France
joelle.zibi@onera.fr
George Barakos, Rinaldo Steiniger
University of Glasgow, United Kingdom
George.Barakos@glasgow.ac.uk, 2238057S@student.gla.ac.uk
Joon W. Lim
US Army, Ames Research Center, Moffett Field, California
joon.w.lim.civ@mail.mil

The aerodynamics of a helicopters are highly unsteady by nature. In cruise flight, on the advancing side of the rotor, shock waves may be encountered, while on the retreating side reverse flow exists. On top of these phenomena, the blade tip vortices interact with blades for most of the revolution. A limiting factor for helicopter rotors is the vortex induced stall, which is encountered in fast forward flight and high load. The maximum load may be traded in for speed, and is basically limited by the McHugh stall boundary of the particular rotor [1].

Due to this highly unsteady nature of rotor flows, in particular in the highly loaded forward flight, it is desirable to reduce vibrations and power requirements. An idea to alleviate these is to actively control the rotor. One technology is the higher harmonic control of the swash plate as studied in the HART I & II wind tunnel campaigns [2] [3]. Opposing this, there is the technology of actively twisting the blade through piezo-electric elements, e.g. [4]. The advantage of actively twisting the blade is that no moving complex actuators are required.

Therefore, DLR decided to further investigate this technology and re-initiated the STAR project – a consortium comprising of DLR as lead, JAXA, KARI, Konkuk University, ONERA, NASA, University of Glasgow, and the US Army. Various test cases have been studied numerically beforehand to seek out interesting flight conditions to be tested during the wind tunnel campaign. One of these flight conditions is the vortex induced dynamic stall, which is also widely researched outside the scope of active twist [5]. The group dedicated to this task operated in two stages: first, the onset of dynamic stall, but also the maximum thrust was sought by the various partners, and second, the effect of active twist was investigated for various settings of the actuation. The results of this group are the focal point of the paper.

For the prediction activities, the tools were roughly grouped into two categories: comprehensive analysis (CA) and CFD/CSD based analysis. The first group allows for quick prediction due to simplified aerodynamics. Opposing this, the second group coupled the comprehensive codes with CFD based methods to capture the stall phenomenon based on first principles approaches. The methods used by each partner will be explained in more detail in the paper. The rough categorization and general legend are given in Figure 1.

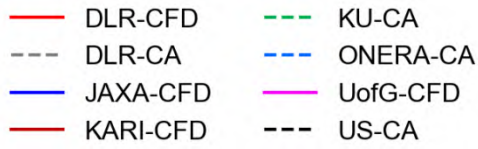

Figure 1: Legend for the line plots. CA denotes comprehensive analysis, while CFD refers to CFD/CSD coupled results.

After initial studies, it was decided to operate the rotor at half RPM to overcome wind tunnel limitations of the employed scale and motor. Exemplary results are shown in Figure 2. On the left, the required power over thrust is shown. At lower thrusts, the results agree well, but with growing thrusts it is observed the stall onset differs. On the right-hand side, the effect of the active twist actuation and the applied phase shift of the sinusoidal actuation onto the power requirements with respect to the non-actuated rotor is demonstrated. The final paper will go in more depths of these results including sectional analysis of the air loads.

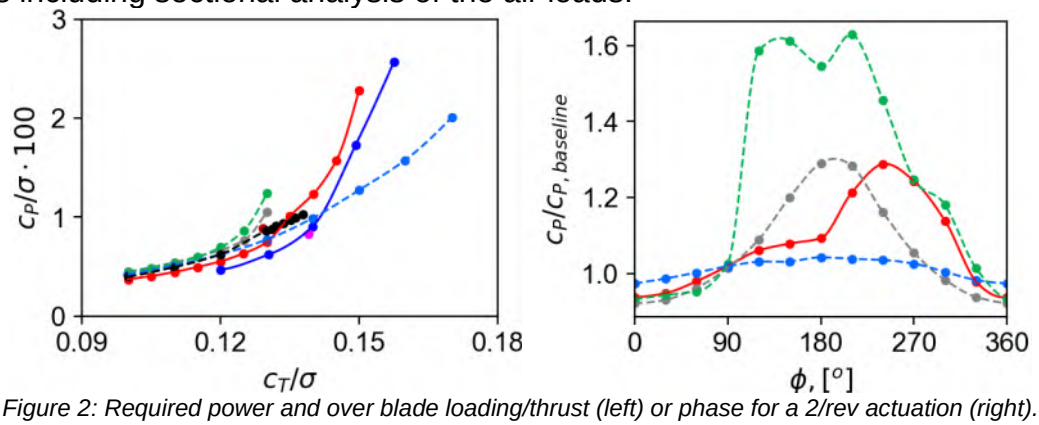

Figure 2: Required power and over blade loading/thrust (left) or phase for a 2/rev actuation (right).

The conclusions of these studies are that correctly capturing the absolute value of the maximum thrust proofs to be a challenging task. However, the mechanics of the stall are generally captured. Interesting data points for the actuation are identified based on the numerical studies, but the data from the wind tunnel test will prove invaluable for further validation of the here used codes.

References

[1] F. J. McHugh, "What are the Lift and Propuslive Force Limits at High Speed for the Conventional Rotor," in *34th Annual National Forum of the American Helicopter Society*, Washington, D.C, 1978.

[2] W. R. Splettstößer, R. Kube R, W. Wagner, U. Seelhorst, A. Boutier, F. Micheli, E. Mercker, K. Pengel, "Key results from a higher harmonic control aeroacoustic rotor test (HART)," *Journal of the American Helicopter Society 42,* vol. 1, p. 1, 1998.

[3] B. G. van der Wall, "A Comprehensive Rotary-Wing Data Base for Code Validation: The HART II International Workshop," *The Aeronautical Journal,* vol. 115, p. 91–102, 2011.

[4] S. J. Shin, C. E. S. Cesnik, and S. R. Hall, "Closed-Loop Control Test of the NASA/Army/MIT Active Twist Rotor for Vibration Reduction," *Journal of the American Helicopter Society,* vol. 50, p. 178–194, 2005.

[5] M. J. Smith, A. D. Gardner, R. Jain, D. Peters, and F. Richez, "Rotating Wing Dynamic Stall: State of the Art and Future Directions," in *Proceedings of the 76th Annual Forum*, Virtual, 2020.

Mitteilung

Fachgruppe: Hochagile Konfigurationen

Influence of the Vertical Stabilizer on the Aerodynamics and Roll Stability of a Generic Multi Delta Wing Aircraft Configuration

Katharina Alt, Andreas Schütte
DLR – Deutsches Zentrum für Luft- und Raumfahrt,
Institut für Aerodynamik und Strömungstechnik, Lilienthalplatz 7,
38108 Braunschweig, katharina.alt@dlr.de

Introduction

The aerodynamic requirements of modern fighter aircraft can be fulfilled by delta wings. The medium to high leading edge sweep angles of these configurations lead to a complex vortical flow field and challenging aerodynamic behavior. The aerodynamic requirements of such configurations include a high degree of agility, a high maneuverability, good supersonic flight characteristics, as well as low observability.

The DLR project Diabolo is looking at the design and assessment capabilities of modern fighter aircraft configurations and the understanding of the flow physics and aerodynamic behavior of fighter aircraft with a vortex-dominated flow field. The aim of Diabolo is the demonstration of the design and assessment methods by the development of a virtual DLR Future Fighter Demonstrator (DLR-FFD), see Fig. 1.

In the present work, a generic multiple delta wing aircraft configuration was derived from the wind tunnel model DLR-F22 looking at the integration of vertical tail planes to identify the influence on the flow physics and the aerodynamic behavior, with a focus on the influence to the rolling moment stability of the configuration [1], see Fig. 2 and 5.

Objectives

The aim of the present work is to analyze the influence of the vertical stabilizer on the aerodynamics and aerodynamic stability, especially roll stability, of the delta wing configuration. Planform studies established to enhance the rolling moment behavior by means of strakes and wing leading edge slats are taken as a reference for the current vertical tail plane studies [1] and should identify the differences between the configuration with and without vertical tails. The computational investigations should identify in particular the influences of the vortical flow topology (see Fig. 4) and interaction with vertical tail planes on the aerodynamic behavior, see Fig. 3 and 6. This should lead to design recommendation for the DLR-FFD within Diabolo.

Approach and Results

For the present computational investigations, the DLR RANS solver TAU has been applied [3] using the Spalart-Allmaras turbulence model with rotation correction. The computational hybrid grids are generated with the CentaurSoft [4] grid generator and for the deflection of the rudder the DLR TAU chimera approach has been applied.

In the current study, all configurations have been reviewed at a Mach number of $M = 0.5$ and a Reynolds number of $Re = 9 \cdot 10^6$ with model configurations in wind tunnel scale.

During the study of the aerodynamics and aerodynamic stability of the preliminary investigation, it was found that the configuration exhibits a roll-stable flight condition at asymmetric free stream conditions at an angle of sideslip of $\beta = 5°$. If the strake and the slat on the windward side were deflected the roll stability can be improved. Due to the integration of the vertical stabilizer, vortex breakdown is shifted to lower AoA and the rolling moment behavior can get unstable depending on the strake planform, although the vertical tail planes provide a stabilizing contribution to the overall roll stability.

The results in the final paper will provide a detailed analysis of the flow physics and aerodynamics of the studied delta wing configurations. Furthermore, comparisons between the results of the preliminary investigations and the delta wing configuration with vertical tail planes will be discussed to identify design recommendations.

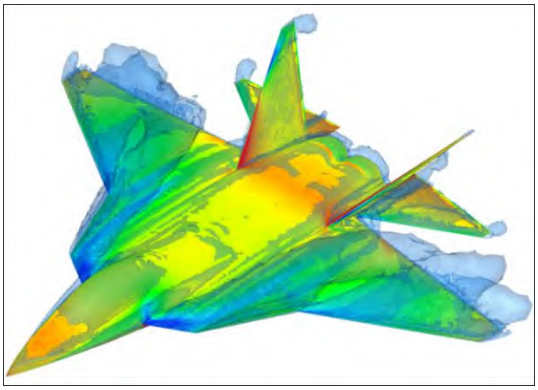

Figure 1: Flow topology of the DLR Future Fighter Demonstrator (DLR-FFD).

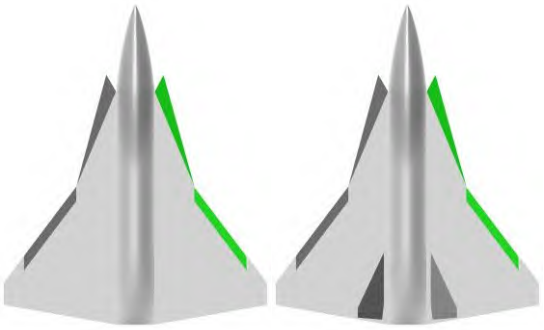

Figure 2: Planform 3: Geometry with and without fin and rudder. Left/right: $\eta_{Strake,r} = 20°$, $\eta_{Slat,r} = 20°$, right: $\eta_{Rudder(r|l)} = 10°|10°$.

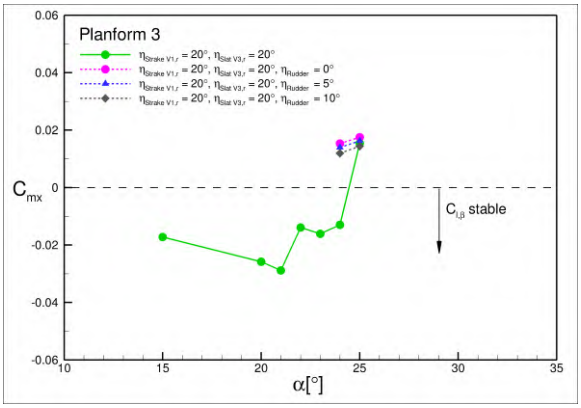

Figure 3: Planform 3: Integral data with and without fin and rudder: Rolling moment coefficient versus AoA at β = 5°, M = 0.5. No fin and η_{Rudder} = 0°, 5° and 10°.

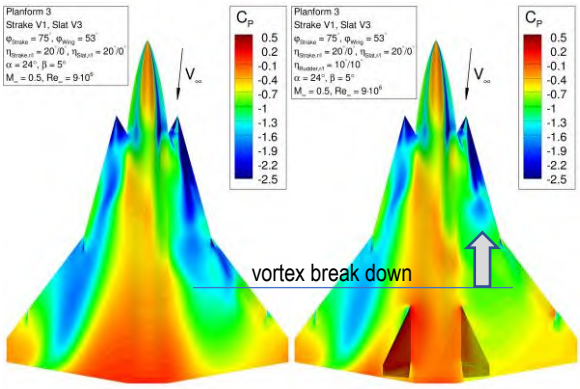

Figure 4: Planform 3: Pressure distribution with and without fin and rudder: Rolling moment coefficient versus AoA at β = 5°, M = 0.5. No fin and η_{Rudder} = 10°.

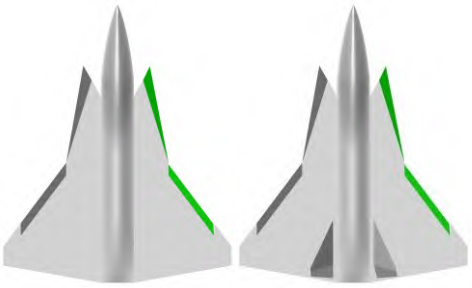

Figure 5: Planform 4: Geometry with and without fin and rudder. Left/right: $\eta_{Strake,r} = 30°$, $\eta_{Slat,r} = 30°$, right: $\eta_{Rudder(r|l)} = 10°|10°$.

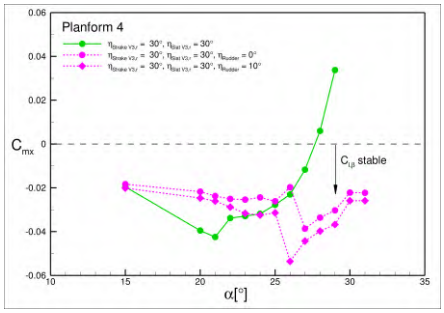

Figure 6: Planform 4 with and without fin and rudder: Rolling moment coefficient versus AoA at β = 5°, M = 0.5. No fin, η_{Rudder} = 0° and 10°.

References

[1] Alt, K.: Einfluss des Seitenleitwerks auf die Aerodynamik und Rollstabilität einer generischen Mehrfach-Deltaflügel-Flugzeugkonfiguration. DLR E-124-2022/901, Bachelorarbeit, TU Braunschweig, Febr. 2022.

[2] Schütte, A.; Hummel, D.: Impact of planform and control surfaces on the vortical flow topology and roll stability of a multi delta wing configuration. AIAA-Paper, accepted. 2022 AIAA Aviation and Aeronautics Forum and Exposition, 27 June–1 July 2022, Chicago, IL, USA.

[3] Schwamborn, D.; Gardner, A.D.; Geyr, H. von; Krumbein, A.; Lüdeke, H.: Development of the DLR TAU-Code for Aerospace Application. International Conference on Aerospace Science and Technology (2008).

[4] CentaurSoft: Centaur Version 14.1.1. *https://www.centaursoft.com/* (2021).

Mitteilung

Fachgruppe: Hochagile Konfiguration

A gradient-based adjoint aerodynamic Multi-Point Optimization of a Generic Multi Delta Wing Aircraft Configuration

Patrick Löchert
DLR – Deutsches Zentrum für Luft- und Raumfahrt,
Institut für Aerodynamik und Strömungstechnik, Lilienthalplatz 7,
38108 Braunschweig, patrick.loechert@dlr.de

Introduction

The aerodynamic requirements of modern fighter aircraft including high degree of agility, high maneuverability, good supersonic flight characteristics, low observability as well as the super cruise capability can be fulfilled by delta wings. Beside these aerodynamic requirements the demand for high range to fulfill mission requirements is given. This leads to the aerodynamic challenge of an efficient cruise and super cruise condition without declining other capabilities for agility, maneuverability, observability.

The DLR project Diabolo is looking at the multidisciplinary design and assessment capabilities of modern fighter aircraft configurations and the understanding of the flow physics and aerodynamic behavior of fighter aircraft with a vortex-dominated flow field. The aim of Diabolo is the demonstration of the design and assessment methods by the development of a virtual DLR Future Fighter Demonstrator (DLR-FFD), see Figure 1

Objectives

The aim of the present work is to establish an optimization process chain for the DLR-FFD of a multi-point optimization consisting cruise and super cruise flight conditions. Within the project Diabolo a multidisciplinary design tool VAMP Zero F will be created starting from level-0 design up to an high-fidely optimization cycle. The multidisciplinary design process is described in **Fehler! Verweisquelle konnte nicht gefunden werden.** and announce a list of requirements for fighter aircrafts. Through an iterative process a geometry is resulting fulfilling all given requirements. Further iterative cycles with higher fidelity method like a multi-fidelity aero performance map published in **Fehler! Verweisquelle konnte nicht gefunden werden.** is used to assess the flight performance and verify the desired turn rates. The gradient-based adjoint multi-point optimization process presenting in this work is part of the full multidisciplinary design process. After the level-0, level-1 and level-2 design processes of the fighter aircraft an automated aerodynamic optimization is planned to reach a higher efficiency for the cruise and super cruise condition to achieve a longer range or safe fuel capacity.

Approach

For current civil aircrafts the aerodynamic optimization is already part of the design process. Multidisciplinary optimization with high fidelity methods such as RANS-CFD for flow computation are already used and developed [3]. In the DLR Project Diabolo the DLR-FFD was designed. For the optimization the CAD Parametrization and the geometrical topology are necessary. The vortical flow field of delta wing depends mainly on the wing sweep angle. To achieve a typical vortical flow field for research the flow phenomena vortex breakdown, vortex interaction and vortex shock interaction the planform of the configuration is given by the high angle of attack aerodynamics with the sweep angles of 45°; 75°; 45°. Further aspects for structure, stability and control, engine and payload give more limitations to the aircraft design. For the aerodynamic optimization the wing and fuselage shall be optimized for the cruise and super cruise condition to achieve the long-range capability at that conditions but considering the other disciplines inside the process.

The fuselage and wing are described as a one wing configuration with 7 profiles for the description of the chordwise direction and 11 guide curves for the spanwise direction. The geometric topology is shown in Figure 2. The complete wing fuselage geometry is then given by the surfaces depending on the profiles and guide curves. In total the profiles and guide curve are described with 160 design parameters. As seen in Figure 2 internal components such as Cockpit, Canopy, Weapon Bays, etc. are considered as placeholders in the geometry.

Due to the high number of design parameters a gradient-based adjoint optimization was chosen due to time efficiency. For a gradient-based adjoint optimization one RANS-CFD Simulation with the DLR TAU Code [4] for every objective function is necessary, whereas for the gradient-based optimization one

RANS-CFD Simulation for every design parameter will be necessary. In this case the number of objective functions is much smaller than the number of design parameters.

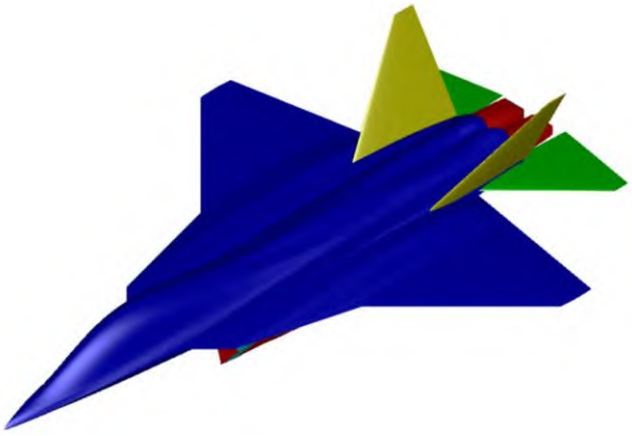

Figure 1 DLR-FFD

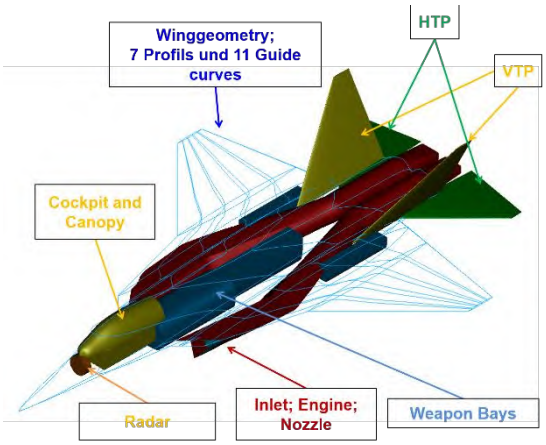

Figure 2 Geometrical Topology

The optimization process chain in shown in Figure 3. The gradient-based adjoint optimization (right part of the process chain) was developed in a past project [3] but is modified with the trimprocess and for the considered multi-points cruise and supercruise. The CAD-reduced order modell (CAD-ROM; left part of the process) have to be comitted to the optimization cycle for the mesh deformation. The CAD-ROM describs the geometrical gradients depending on the design parameters. A number of numerical discretizations of the geometry have to be done to calculate the vectors of displacements.

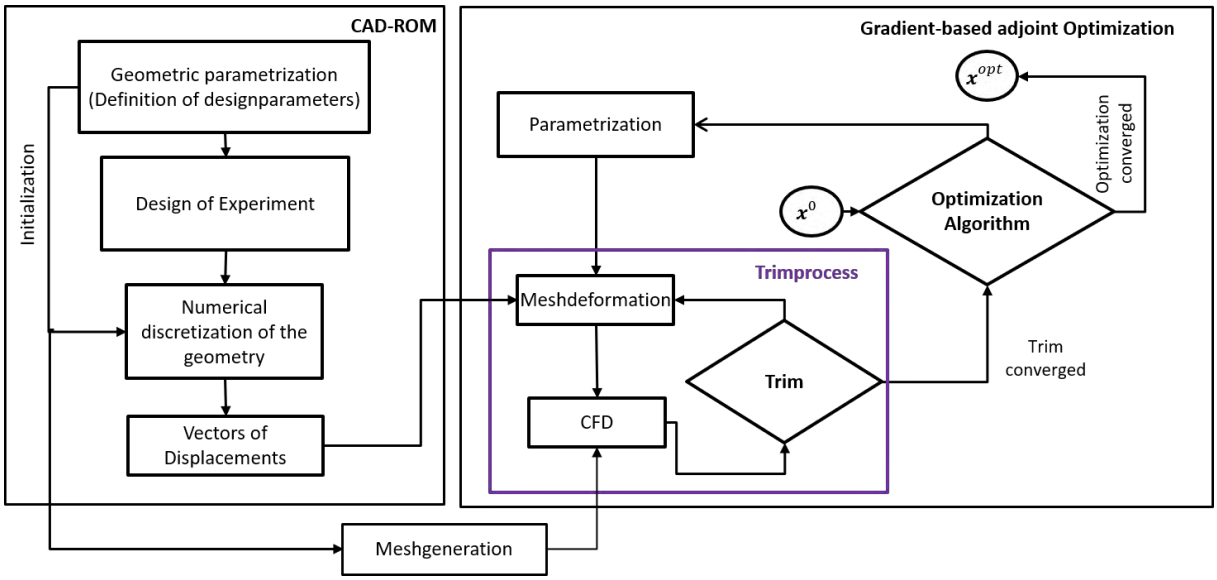

Figure 3 Optimization Process Chain

The work will present the automatically numerical discretization for the DLR-FFD in dependence of the design parameters. Additionally, the automated trim process for forces and moments with the mesh deformation of the all movable horizontal tail plan inside the optimization loop will be presented as well as the verification of the CAD-ROM will be shown with the visualization of the performed mesh deformation.

References

[1] Mancini, Andrea und Zamboni, Jacopo und Moerland, Erwin (2021) A knowledge-based methodology for the initiation of military aircraft configurations. AIAA AVIATION 2021 FORUM, 2-6 Aug 2021, Virtual Event. doi: 10.2514/6.2021-2789 <https://doi.org/10.2514/6.2021-2789>

[2] Stradtner, M.; Liersch, C. M.; Löchert, P.: *Multi-Fidelity Aerodynamic Data Set Generation for Early Aircraft Design Phases,* NATO STO AVT-366 Research Workshop on ”Use of Computational Fluid Dynamics for Design and Analysis: Bridging the Gap Between Industry and Developers”, Sibiu, Romania, 23-27 May 2022

[3] Merle, A., Ronzheimer, A., Bekemeyer, P., Görtz, S., Keye, S., and Reimer, L. Gradient-based optimization of a flexible long-range transport aircraft using a high-dimensional cad-rom parameterization. (DLRK Conference, Friedrichshafen, Germany, 2018

[4] Schwamborn, D.; Gardner, A.D.; Geyr, H. von; Krumbein, A.; Lüdeke, H.: Development of the DLR TAU-Code for Aerospace Application. International Conference on Aerospace Science and Technology (2008).

Mitteilung

Fachgruppe: Fluid- und Thermodynamik

Invariant Analysis of Vortical Delta Wing Flow using the Extended Optimal Triple Tensor Decomposition

Markus Rütten, Michael Werner, German Aerospace Center (DLR),
Institute of Aerodynamics and Flow Technology
Jonas Zastrow, German Aerospace Center (DLR), Institute of AeroelasticityBunsenstr. 10,
37073 Göttingen, Germany
markus.ruetten@dlr.de, michael.werner@dlr.de, jonas.zastrow@dlr.de

Agility, maneuverability and speed performance of new combat aircraft are realized by low-aspect-ratio highly swept wings. Such aircraft designs have to meet challenging aerodynamic requirements, since they have to operate in subsonic, transonic and supersonic speeds. The associated flow topologies feature leading-edge separations throughout most flight regimes. This results in large-scale vortices over major parts of the aircraft suction side. There, pressure is lowered by high circumferential velocities surounding the vortices, which, eventually, generates a great amount of locally concentrated lift. In order to increase further lift modern combat aircraft planforms reveal several leading edges and, therefore, create multiple leading edge primary vortices. However, maneuvers lead to complicated vortex-vortex and at transonic Mach-numbers vortex-shock interactions [1]. Furthermore, below a specific planform-dependent angle of attack (AoA) the vortical flow systems remain stable, however, as AoA increases, unsteady flow behavior and flow instabilities develop. Eventually, the so-called vortex breakdown phenomenon occurs and moves up-stream over the suction side [2] of the aircraft. Vortex breakdown can be described by a sudden widening of the vortex itself, and it is associated with a reversed flow and strong fluctuations within the vortex core. Additionally, it is not only a locally, but also globally highly unsteady process, that imprints its own time scales into to the overall flow topology [3]. Under certain conditions the vortex is completely dissolved, a vortex burst happened. As a consequence, the vortex-induced lift fluctuates heavily and even subsides throughout the process of vortex-breakdown. Thus, this flow phenomenon is of special interest in the current research and has a major impact on flight stability and control characteristics. Within the scope of the presented work a novel promising theoretical framework is applied to a flow simulation dataset generated for a DLR multi delta-wing model. Since at a low AoA case the three occurring main primary vortices are stable and only weakly interact, this work focusses on a high AoA case which demonstrates strongly interacting primary vortices. Thereto, vortex breakdown structures are analysed by applying flow invariant analysis techniques from critical point theory and flow topology research: the three invariants of the velocity gradient tensor are used to classify and analyse the flow field, i.e. see Fig. 1. The first invariant, $P = D_{ii} = div\,(\vec{v})$, is the divergence of the velocity field, whereas the second invariant, $Q = \frac{1}{2}\left(P^2 - D_{ij}D_{ji} + \Omega_{ij}\Omega_{ji}\right) = (div\,(\vec{v}))^2 - div\,(a_{conv})$, can be used to detect vortical flows, since it connects the source strength of the velocity divergence with the divergence of the convective part of acceleration [4]. Here $\Omega_{ij} = \frac{1}{2}\left(u_{i,j} - u_{j,i}\right)$ is the rate of rotation and $D_{ij} = \frac{1}{2}\left(u_{i,j} + u_{j,i}\right)$ the rate of strain tensor. The third invariant,

STAB

$R = \frac{1}{3}\left(P^3 + 3PQ - D_{ij}D_{jk}D_{ki} + 3\Omega_{ij}\Omega_{jk}D_{ki}\right)$, features the most complex structure consisting of, firstly, a cubed divergence term, secondly, a mixed term of first and second invariant, and, thirdly, it reveals a measure for the rate of strain and, at last, a measure of the rate of rotation, both terms multiplied by the strain rate. These latter two terms shall be further investigated in detail. The idea is to apply an extended version of the optimal triple tensor decomposition, originally developed by Kolár [5], on the observed flow field in order to recalculate the rate of strain and rotation tensors in an associated basic reference frame (BRF). By variation of the three Euler rotation angles of a rotation tensor operator and applying it to the velocity gradient, $\tilde{Q} \cdot grad\,(\vec{v}) \cdot \tilde{Q}^T$, the BRF is determined when $(|D_{12}\Omega_{12}| + |D_{23}\Omega_{23}| + |D_{23}\Omega_{23}|)$ is maximal in comparison to all other rotated reference frames. In this calculated BRF it is possible to further decompose and reformulate the resulting rotation and strain parts into novel pure shear and elongational flow depending straining and rotational terms of the third invariant by using $grad\,(\vec{v})^{BRF} = \tilde{D}_{sh} + \tilde{\Omega}_{sh} + \tilde{D}_{el} + \tilde{\Omega}_{rr}$. Eventually, this decomposition can be utilized to gain more information about the flow physical mechanisms during vortex breakdown by analysing shearing and elongational straining of strain and vorticity measures of the invariant R in the BRF separately.

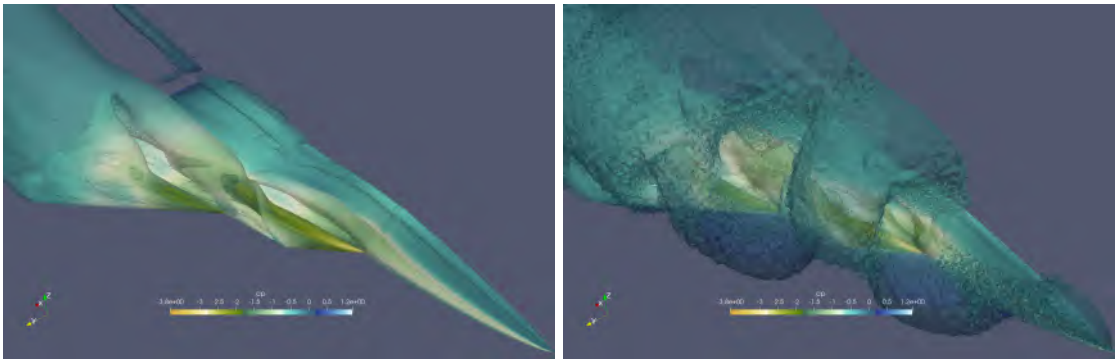

Fig. 1: Visualization of vortical flow structures above the DLR F23 delta-wing based on the second (left) and third (right) invariant of the velocity gradient tensor.

Literature:

[1] Gursul, I., Gordnier, R., and Visbal, M., Unsteady aerodynamics of nonslender delta wings, *Progress in Aerospace Sciences*, 2005.

[2] Lambourne, N. C., and Bryer, D. W., The bursting of leading-edge vortices-some observations and discussion of the phenomenon, 1961.

[3] Breitsamter, C., Unsteady flow phenomena associated with leading-edge vortices, *Progress in Aerospace Sciences*, 2008.

[4] Truesdell, C., *The kinematics of vorticity*, 2018.

[5] Kolár, V., Vortex identification: new requirements and limitations, Int. J. Heat and Fluid Flow 28, pp. 638-652, 2007.

Mitteilung

Fachgruppe: Hochagile Konfigurationen

Untersuchung des instationären Verhaltens Seitenstrahl-induzierter Steuerungskonzepte für hochfliegende Flugkörper

Christian Schnepf
DLR, Institut für Aerodynamik und Strömungstechnik (AS),Bunsenstraße 10,
37073 Göttingen, christian.schnepf@dlr.de

Einleitung

Der Flug in großen Höhen (Upper Tier) stellt für Steuerungskonzepte hochagiler Flugkörper eine besondere Herausforderung dar. Die geringen Luftdichten im Upper Tier und die damit einhergehenden kleinen Staudrücke wirken sich negativ auf die Effektivität herkömmlicher aerodynamischer Steuerungsmethoden, wie Ruder und Canards, aus. Infolgedessen besitzen in diesem Höhenbereich operierende, hochagile Flugkörper speziell angepasste, alternative Steuerungsmethoden, wie etwa eine Querschubsteuerung [1,2] (siehe Abb. 1) am Rumpf oder eine Schubvektorsteuerung [3]. Beide Steuerungskonzepte werden in dieser Studie auf numerischem Wege genauer untersucht und ihre Effektivität miteinander verglichen. Im Fall der Schubvektorsteuerung wird die Seitenstrahl-induzierte Schubvektorsteuerung [3] (SISVS) genauer betrachtet (siehe Abb. 1). Bei diesem Konzept wird ein von der Schubdüsenwand ausgehender Seitenstrahl in den Schubdüsenstrahl geblasen, wodurch es im Idealfall zu einer positiven Wechselwirkung zwischen beiden Strahlen kommt. In der vorliegenden Studie liegt hierbei ein besonderes Augenmerk auf das instationäre Verhalten der Steuerungskonzepte. Dieses wird zum einen hervorgerufen durch das Hochfahren des Seitenstrahlmassenstroms von null auf den maximalen Massenstrom und zum anderen durch die Seitenstrahl-(Stoß)-Grenzschichtwechselwirkung selbst, die bei beiden Konzepten auftritt.

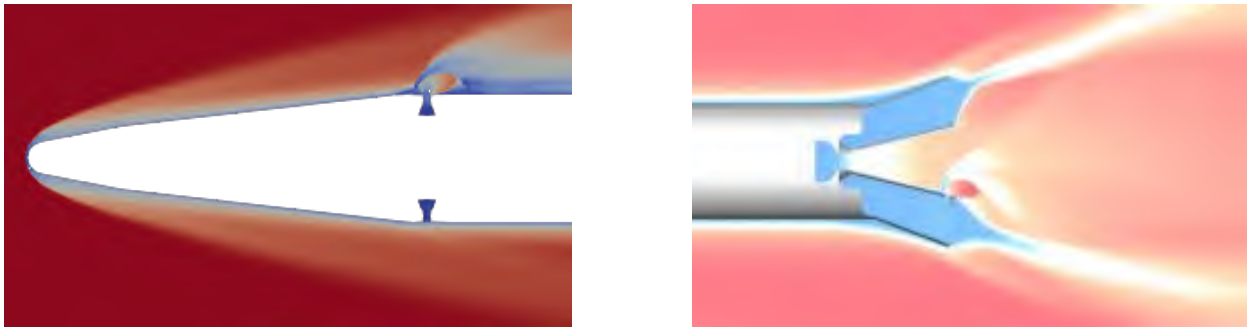

Abbildung 1: Visualisierung der Funktionsweise der Querschubsteuerung im Flugkörpernasenbereich (links) und der Seitenstrahl-induzierten Schubvektorsteuerung (rechts) anhand einer qualitativen Machzahlverteilung

Methodik

Die numerischen Simulationen wurden mit dem DLR-eigenen Finite-Volumen-Strömungslöser TAU [4] für zwei verschiedene Flughöhen 10km und 30km und für zwei verschiedene Machzahlen 6,2 (10km) und 7,0 (30km) durchgeführt. Hierbei wurde die TAU-Erweiterung zur Simulation von (nicht reaktiven) Gasgemischen verwendet. Im vorliegenden Fall ist diese Erweiterung relevant, um zum einen die Wechselwirkung zwischen dem Querschubstrahl und der ihm umgebenen Luft der freien Anströmung zu simulieren und zum anderen, um die Wechselwirkung des Seitenstrahls mit dem Haupttriebwerkstahl zu modellieren. Neben der Variation der Flughöhe wurde in den Simulationen auch der Gesamtdruck des Querschubstrahls variiert und des Weiteren der Einfluss des Zustandes der Grenzschicht (laminar / turbulent) im

Nasenbereich auf die Querschubsteuerung untersucht. Beide Parameter wirken sich auf die Größe der Querschubstrahl-induzierten Ablösung aus.

Ergebnisse

Insgesamt lässt sich feststellen, dass die SISVS ein stabileres Steuerungskraftsignal liefert als die Seitenstrahlsteuerung. Zum einen hinsichtlich der maximal zu erreichenden Kraft für verschiedene Flughöhen und zum anderen hinsichtlich des instationären Verhaltens des Kraftverlaufs. Beide Erkenntnisse liefert eine Analyse von Abbildung 2, die den Kraftverlauf mit zunehmenden Massenstrom der Seitenstrahldüse / Querschubdüse über die Zeit präsentiert. Ein instationäres Verhalten tritt vor allem für die kleinere Flughöhe (links) deutlich in Erscheinung. Die Querschubsteuerung braucht z.B. deutlich länger um die maximale Kraft zu erreichen und weist zusätzlich eine periodische Schwingung am Ende des Kraftsignals auf. Die maximale Steuerkraft ist aber für diese Flughöhe für beide Steuerungskonzepte in etwa gleich groß. Dies ändert sich deutlich mit der Zunahme der Flughöhe. Bei 30km induziert die Querschubsteuerung eine deutlich kleinere Kraft, infolge einer reduzierten Kraftkomponente durch die Seitenstrahl-Grenzschichtwechselwirkung, als die SISVS.

Der Grund für die grundsätzlich größere Sensibilität der Querschubsteuerung liegt in der Wechselwirkung des Seitenstrahls mit der Außenströmung und der Grenzschicht. Während bei der SISVS die Wechselwirkung nahezu unabhängig von der Flughöhe ist, wirken sich die von der Flughöhe abhängigen Druck- und Dichtewerte der Außenströmung deutlich auf die am Flugkörper induzierten Kräfte aus. Der Zustand der Grenzschicht besitzt einen ähnlichen Effekt, denn die Größe des Wechselwirkungsgebiets ist stark davon abhängig ob die Grenzschicht laminar oder turbulent ist.

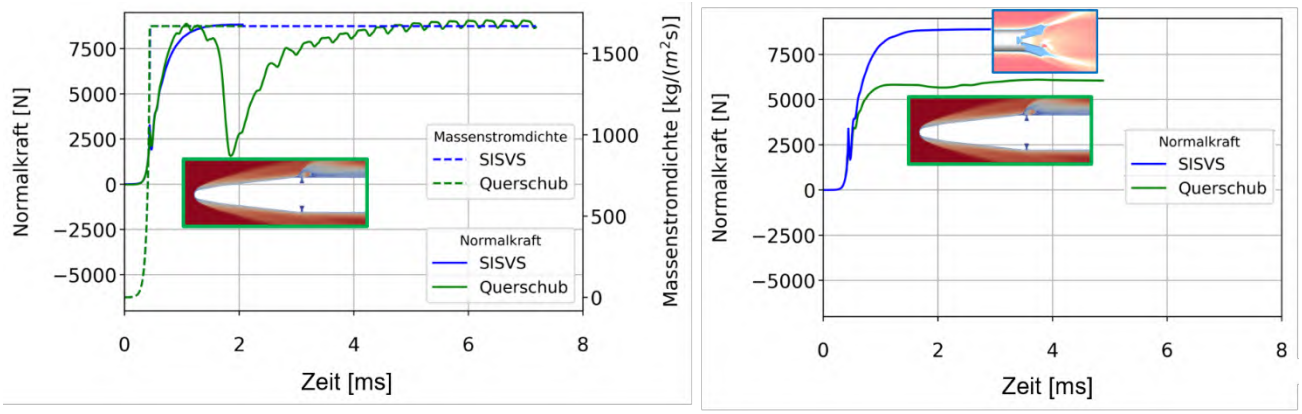

Abbildung 2: Vergleich des Normalkraftverlaufs beider Steuerungskonzepte für eine Flughöhe von 10km (links) und einer Flughöhe von 30km (rechts)

Weiteres Vorgehen:

Im endgültigen Beitrag findet eine detaillierte Analyse des Strömungsfeldes statt, unter anderem hinsichtlich der Ursache des instationären Verhaltens des Kraftsignals bei der Seitenstrahlsteuerung. Ferner wird der Einfluss der Flughöhe auf das relevante Strömungsfeld genauer untersucht. Des Weiteren wird die Wirkung des maximalen Massenstroms auf die von der Seitenstrahlsteuerung induzierte Wechselwirkung analysiert und der Aspekt des Grenzschichtzustandes auf die Wechselwirkung betrachtet.

[1] J. DeSpirito: Lateral reaction jet flow interaction effects on a generic fin-stabilized munition in supersonic crossflows. RTO-MP AVT-135, German Aerospace Center, 2013.

[2] A. Kovar and E. Schülein: Effect of side jets in a supersonic flow measured and calculated on a flat plate and a generic missile configuration. RTO-MP AVT-135, German Aerospace Center, 2013.

[3] K. A. Deere: Summary of fluidic thrust vectoring research conducted at NASA Langley research center, 21 AIAA

[4] D. Schwamborn, T. Gerhold, and R. Heinrich: The DLR TAU-code: Recent applications in research and industry. 2006

Mitteilung

Fachgruppe: **Transportflugzeugkonfigurationen**

Aerodynamic design of shock control bumps considering structural constraints

A. Goerttler[1], S. C. Künnecke[2], C. Sabater[3]
[1]Institute of Aerodynamics and Flow Technology, German Aerospace Center (DLR)
Bunsenstraße 10, 37073 Göttingen, Germany
Andreas.Goerttler@dlr.de

[2]Institute of Composite Structures and Adaptive Systems, DLR
[3]Institute of Aerodynamics and Flow Technology, DLR
Lilienthalplatz 7, 38108 Braunschweig

Introduction

During cruise flight, a shock emerges in the transonic flow field around an aircraft wing and leads to high wave drag, especially at high cruise speeds. Shock control bumps are known to be able to change the flow in the vicinity of the shock, changing the strong single shock into a weaker λ-shock characteristic, similar to the green shock system in Figure 1. This leads to a reduction in wave drag compared to the original shock, and thus to a lower overall drag. However, the reduction is very sensitive towards the shape of the bump. Especially the height and the position of the crest play a dominant role. A wrong combination of those parameters can even lead to an increase in drag compared to a wing or airfoil without bump, see two single red shocks in Figure 1. While aerodynamic optimization of the bump shape yields optimum performance, restrictions imposed due to the integration of the bump into the wing structure can limit the drag reduction significantly. In this regard, in this investigation, two-dimensional shock control bumps are designed to robustly reduce drag within given structural constraints. This includes the constructional feasibility of integrating a bump with a specific shape and height on the spoiler. The aerodynamic optimization of the shock control bump covers a variation of the height and the crest position of the bump and the position of the bump on the spoiler. Furthermore, a variation of the shape function is also investigated. The optimization goal is to diminish the overall drag at a constant lift coefficient. This optimization procedure is done for different lift coefficients to analyze the influence of different flow situations on the bump shape and the drag reduction.

Methods

The numerical computations are carried out with the DLR inhouse flow solver TAU-Code. The optimization is done with the Surrogate-Modelling for Aero-Data Toolbox (SMARTy) which is also developed by DLR. This approach has already shown successful optimization of shock control bumps under uncertainty (Sabater et al. [1]).

Results

A robust shock control bump has been optimized for a two-dimensional airfoil section at a spanwise coordinate of $\eta = 57\%$ of a flight relevant wing. The optimization considered the bump displacement only on top of the spoiler in the rear part of the airfoil to facilitate structural feasibility. The outcome of the optimization for three relevant lift coefficients is displayed in Figure 2. The shown bump shape function “LoadedBeam” is inspired by a beam loaded with an individual force. For all three optimized bumps in Figure 2, the rear end of the bump is at the rearmost location of the spoiler. It can be seen that despite this geometrical constraint the height increases with increasing lift coefficient. Furthermore, the crest position of the bump shifts, like the shock movement, in downstream direction with increasing lift coefficient.

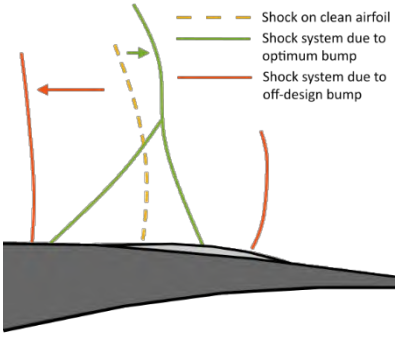

Figure 1: Sketch of shock systems on airfoil.

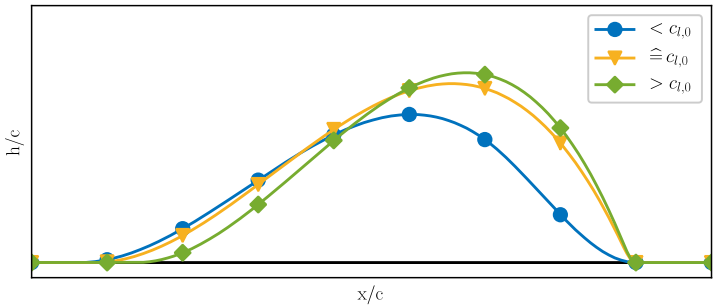

Figure 2: Optimized bump shapes for three different lift coefficients.

The bump shapes, shown in Figure 2, are the results of several optimizations at different constant lift coefficients. The corresponding drag polars are shown in Figure 3 to evaluate the bump performance at off-design conditions. Depending on whether the lift coefficient is higher or lower than the design lift coefficient (black border around colored circles), two flow characteristics occur. Above the design lift coefficient, all colored curves, representing an airfoil with an optimized bump, are above the baseline case (black dashed line). This indicates higher lift at constant drag or lower drag at constant lift. At these higher lift coefficients, the bump still induces a favorable shock system, similar to the green shock system in Figure 1. This leads to lower drag values than the baseline case. However, at lower lift coefficients the drag values are significantly higher than the baseline case due to the evolution of two strong shocks, like the red shock system in Figure 1. After the first shock, which is positioned upstream of the bump, the flow accelerates due to the curvature of the bump. The flow again reaches supersonic speeds and decelerates into the subsonic regime with a second strong shock. Those two shocks lead to a significant increase in wave drag. In order to avoid this additional drag, the bump shape must be retractable by a bump actuation mechanism for flow conditions below the design lift coefficient.

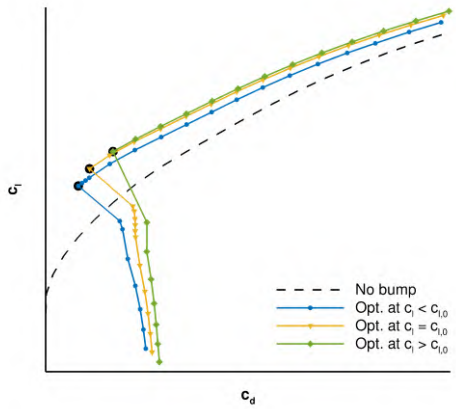

Figure 3: Drag polars of two-dimensional airfoils with bumps optimized at different lift coefficients (black dots indicate optimized lift coefficient).

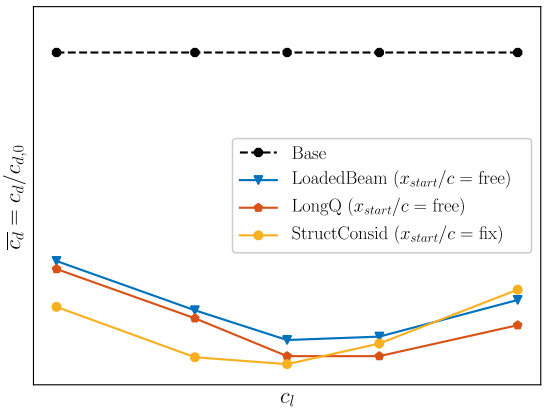

Figure 4: Normalized drag values of two-dimensional airfoils optimized with different bump shapes against different lift coefficients.

Figure 4 shows the drag reduction potential of three shape functions for bump optimization by displaying the normalized drag of an optimized 2D airfoil section for different lift coefficients. The focus is not only on aerodynamic performance, but also on structural feasibility and the quantification and evaluation of the differences of the various bump shape functions. The structural constraints originate from a possible integration of a bump actuation mechanism in the wing, which is able to attain both the clean airfoil and the optimized bump shape on the spoiler. All investigated shapes show almost similar drag reduction potential in the investigated, flight relevant, lift coefficient range.

The final paper will be more detailed and will also include the influence of suction rates in the front part of the airfoil. In addition, means of increasing the performance of the bump shapes in off-design conditions will be investigated and specific bump design guidelines will be created. And furthermore, the influence of a variable camber on the shock and an optimized bump position will be analyzed.

References

[1] C. Sabater, P. Bekemeyer and S. Görtz, “Efficient Bilevel Surrogate Approach for Optimization Under Uncertainty of Shock Control Bumps”, *AIAA Journal*, Vol. **58**, No. 12, Dec. 2020.

Mitteilung

Fachgruppe: Transportflugzeugkonfigurationen

Erhöhung der Effektivität von Shock Control Bumps zur Verzögerung des transsonischen Buffets durch Ausschlag einer Hinterkantenklappe

J. Müller[1], A. Waldmann[1], A. Goerttler[2], S. C. Künnecke[3], T. Lutz[1]
[1]Universität Stuttgart, Fakultät 6, Institut für Aerodynamik und Gasdynamik
Pfaffenwaldring 21, 70569 Stuttgart
jens.mueller@iag.uni-stuttgart.de

[2]DLR, Institut für Aerodynamik und Strömungstechnik
Bunsenstraße 10, 37073 Göttingen

[3]DLR, Institut für Faserverbundleichtbau und Adaptronik
Lilienthalplatz 7, 38108 Braunschweig

Einleitung

An konventionellen Transportflugzeugen werden Fluggeschwindigkeit und Anstellwinkel unter anderem durch das Auftreten instationärer Stoßoszillation, das so genannte transsonische Buffet, begrenzt. Aufgrund der aus dem Buffet resultierenden instationären Aerodynamik und den auftretenden Lastschwankungen ist während des Fluges ein ausreichender Abstand zur Buffetgrenze einzuhalten. Eine Erweiterung der Flugbereichsgrenzen zu höheren Machzahlen und Anstellwinkeln kann über eine aktive Beeinflussung des Verdichtungsstoßes mittels Stoßkontrollbeulen, so genannten Shock Control Bumps (SCBs), erreicht werden [1]. An heutigen Verkehrsflugzeugkonfigurationen ist der Bauraum zur Integration von SCBs begrenzt, sodass die Positionierung der SCBs starken Restriktionen unterliegt. Des Weiteren kann mittels SCBs eine ebenfalls wünschenswerte Reduktion des Wellenwiderstands im Reiseflug erreicht werden. Hierfür ist jedoch eine andere Positionierung der SCBs relativ zur Stoßlage notwendig. Beide Aspekte können somit die Wirksamkeit der SCBs zur Verschiebung der Buffetgrenze stark einschränken, wenn sich der Scheitelpunkt der Beule zu nahe an der Stoßlage befindet. Somit besteht die Notwendigkeit, bei einer im Hinblick auf die Verschiebung der Buffetgrenze nicht optimalen Positionierung des SCBs, die Lage des Verdichtungsstoßes zu verschieben, um weiterhin eine Erhöhung des Buffet Auftriebsbeiwertes C_L zu ermöglichen, ohne geometrische Restriktionen zu verletzen oder die Effektivität des SCBs zur Verbesserung der Performance im Reiseflug einzuschränken. In der vorliegenden Arbeit werden hierfür Ausschläge von Hinterkantenklappen verwendet, um die Wölbung des Profils zu verändern (Variable Camber [VC]) und somit bei gleichem C_L eine Beeinflussung der Stoßlage mit und ohne SCBs zu erreichen.

Methodik

Das Projekt, in dessen Rahmen diese Arbeit erfolgt, befasst sich mit der Auslegung von SCBs an einem hybriden Laminarflügel mit Absaugung im Reiseflug. Die Untersuchungen erfolgen an einem repräsentativen 2D Flügelschnitt, wobei Geometrie und Strömungsbedingungen in den Normalschnitt transformiert werden. Die Bestimmung der Buffetgrenze erfolgt anhand des $\Delta\alpha$-Kriteriums [2]. Die hierfür notwendigen Auftriebspolaren werden in stationären 2D RANS Profilsimulationen in FLOWer [3] ermittelt. Die Lage der SCBs ist am untersuchten Flügel auf den Spoiler beschränkt, um eine strukturelle Integrierbarkeit der Beule und Aktuatorik zu ermöglichen. Aus vorangegangen Untersuchungen im Projekt hat sich gezeigt, dass auf dem Spoiler positionierte SCBs die Buffetgrenze zu höheren C_L verschieben, das volle Potential aufgrund des nicht ausreichend stromab des Stoßes liegenden Beu-

lenscheitelpunktes jedoch nicht ausgeschöpft werden kann. Für eine Erhöhung der Buffet-SCB Wirksamkeit wird eine direkt hinter dem Spoiler befindliche Hinterkantenklappe in den 2D CFD Simulationen ausgeschlagen. Die Erzeugung des Klappenausschlags erfolgt dabei geometrieseitig vor Vernetzung des Profils und ist innerhalb der C_L-Polare konstant.

Erste Ergebnisse und Ausblick

Die Wirksamkeit der Hinterkantenklappe zur Beeinflussung der Stoßlage ist in Abb. 1 am 2D Profil ohne SCB (clean airfoil) dargestellt. Über einen breiten Anstellwinkelbereich führt ein Ausschlag der Klappe nach unten ($\eta > 0$) zu einer stromab Verschiebung der Stoßposition. Ein Ausschlag der Klappe nach oben führt entsprechend zu einer Verschiebung der Stoßlage stromauf. An der aktuell untersuchten Konfiguration wird die Buffet-SCB Wirksamkeit durch die Positionierung auf dem Spoiler begrenzt. Der Scheitelpunkt der Beule kann folglich nicht weit genug stromab verschoben werden, um die optimale Wirksamkeit der Beule zur Verschiebung der Buffetgrenze zu nutzen. Somit werden im Folgenden Ausschläge der Hinterkantenklappe nach oben und deren Auswirkungen auf die Wirksamkeit unterschiedlicher SCBs betrachtet. Es werden dabei tangentenstetige (SCB1a) und strukturell realisierbare (structural consideration) Buffet-SCBs untersucht. Zusätzlich wird eine auf Reduktion des Wellenwiderstandes optimierte Beule (performance) betrachtet, welche ohne Klappenausschlag einen negativen Effekt auf die Buffetgrenze aufweist. Die in Abb. 2 dargestellte Veränderung des Auftriebsbeiwertes ΔC_L, bei welchem Buffet relativ zum clean Profil ohne VC auftritt, dient als Bewertungskriterium. Es zeigt sich, dass sowohl am Profil ohne SCBs, als auch bei den unter geometrischen Restriktionen ausgewählten Buffet-SCBs das Buffet-C_L deutlich zu höheren Werten verschoben werden kann. Es ist ebenfalls möglich die Stoßlage über den Klappenausschlag (VC) so weit stromauf zu verschieben, dass ein auf Reduktion des Wellenwiderstandes ausgelegter SCB ebenfalls effektiv zur Verschiebung der Buffetgrenze genutzt werden kann. Somit sind auch beide Aspekte abdeckende, multifunktionale SCBs an der betrachteten Konfiguration mittels VC realisierbar. In der finalen Arbeit werden die aerodynamischen Mechanismen näher betrachtet, die zur Erhöhung des Buffet-C_L führen. Des Weiteren wird die Anwendbarkeit des Klappenausschlags für unterschiedliche Beulenformen und Positionierungen des Beulenscheitelpunktes analysiert.

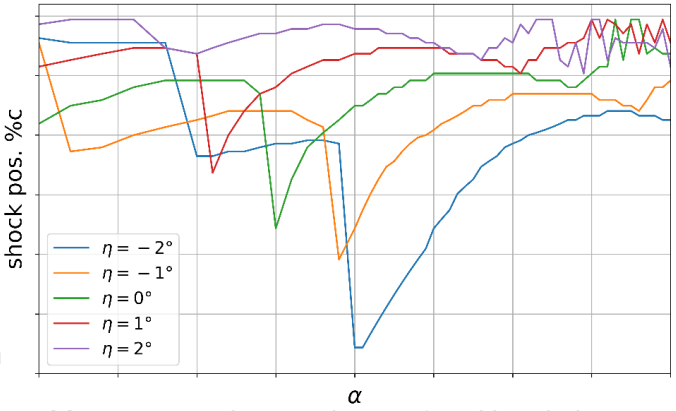

Abb. 1: *Veränderung der Stoßposition bei unterschiedlichen Ausschlägen der Hinterkantenklappe*

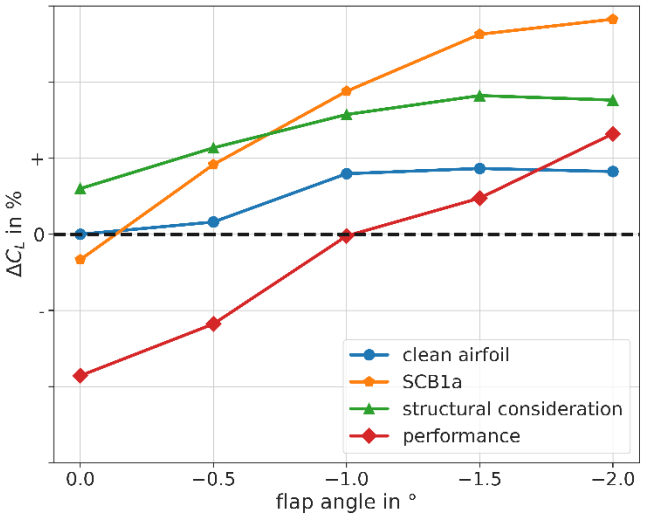

Abb. 2: *Verschiebung der Buffetgrenze durch einen Ausschlag der Hinterkantenklappe mit und ohne SCBs*

Quellen

[1] Mayer, R., Lutz, T., Krämer, E., Dandois, J.: "Control of Transonic Buffet by Shock Control Bumps on Wing-Body Configuration." Journal of Aircraft 56(2), pp. 556–568, 2019

[2] Lawson, S., Greenwell, D, Quinn, M.: "Characterisation of Buffet on a Civil Aircraft Wing." AIAA SciTech, San Diego, CA. AIAA Paper No. 2016-1309, 2016.

[3] Rossow, C.-C., Kroll, N., Schwamborn, D.: "The MEGAFLOW Project – Numerical Flow Simulation for Aircraft." Vol. 8, pp. 3-33, Springer, Berlin, 2006

Mitteilung

Fachgruppe: Transportflugzeugkonfigurationen

Stoßkontrollbeulen zur Verzögerung des transsonischen Buffets
am hybriden Laminarflügel

A. Waldmann[1], J. Müller[1], A. Goerttler[2], T. Lutz[1]
[1]Universität Stuttgart, Fakultät 6, Institut für Aerodynamik und Gasdynamik
Pfaffenwaldring 21, 70569 Stuttgart
waldmann@iag.uni-stuttgart.de

[2]DLR, Institut für Aerodynamik und Strömungstechnik
Bunsenstraße 10, 37073 Göttingen

Einleitung

Transsonisches Buffet bezeichnet ein strömungsmechanisches Phänomen, welches in einer Stoßoszillation am Profil oder am Tragflügel besteht. Es tritt bei Flugmachzahlen in Schallnähe am Flügel auf, wenn der Anstellwinkel oder die Machzahl die Buffetgrenze überschreiten. Die instationäre Strömung und die daraus resultierenden fluktuierenden Lasten sind im Betrieb unerwünscht und werden daher vermieden, indem im Normalbetrieb ein ausreichender Abstand von der Buffetgrenze gewahrt wird. Eine zeitweise Erhöhung der Fluggeschwindigkeit zu einer höheren Machzahl hin kann aus operativen Gründen jedoch wünschenswert sein. Ebenso kann im Flug durch Manöver oder atmosphärische Böen ein Anstellwinkel auftreten, der sich der Buffetgrenze annähert oder darüber liegt. Für beide Fälle werden Ansätze gesucht, um die Buffetgrenze zu verschieben.
Eine seit langem erforschte Möglichkeit der Strömungsbeeinflussung am transsonischen Flügel sind Beulen, die durch lokale Änderung der Profilgeometrie den Stoß beeinflussen. Durch solche Shock Control Bumps (SCBs) ist beispielsweise eine Wellenwiderstandsreduktion im Flug außerhalb des Auslegungspunktes möglich. Ebenso sind geeignete Beulen in der Lage, die Stoßoszillation beim Buffet zu unterbinden oder ihr Auftreten zu höheren Anstellwinkeln oder Machzahlen zu verschieben.

Methodik

Das dieser Arbeit zu Grunde liegende Projekt umfasst die Auslegung von SCBs für den Flügel einer Verkehrsflugzeugkonfiguration im Reiseflug. Es handelt sich um einen hybriden Laminarflügel mit Absaugung, so dass trotz der hohen Reynoldszahl eine lange laminare Anlaufstrecke auftritt. In der vorliegenden Arbeit werden zweidimensionale Schnitte an ausgewählten Stellen auf der Tragflügeloberseite verwendet, um die Strömung zu charakterisieren und um für die Verschiebung der Buffetgrenze geeignete Beulenformen zu bestimmen. Hierzu werden die Reiseflugbedingungen am gepfeilten Tragflügel in den Normalschnitt transformiert. Trotz des instationären Charakters des Buffetphänomens ist es möglich, die Buffetgrenze anhand einer Auftriebspolare aus einer stationären RANS-

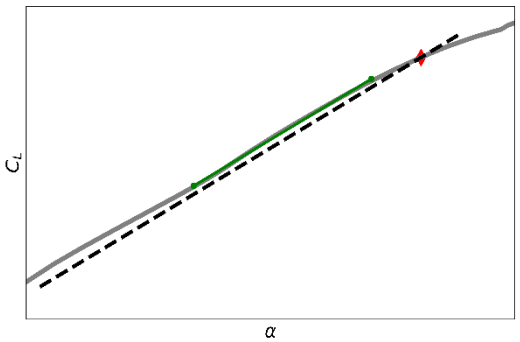

Abb. 1: Automatische Bestimmung der Buffetgrenze mittels stückweise linearem Fitting

Rechnung zu bestimmen. Dazu wird eine Vielzahl von 2D RANS Profilsimulationen mit dem Strömungslöser FLOWer [3] durchgeführt, um einen großen Parameterraum unterschiedlicher Beulenformen abzudecken. Für jede Geometrievariante wird eine vollstände Anstellwinkelpolare berechnet. Die Analyse dieser Ergebnisse erfordert ein robustes automatisiertes Verfahren. Das Δα-Verfahren (Lawson et al. [1]) findet Anwendung und ist für eine generische Polare in **Abb. 1** dargestellt. Mit dieser Herangehensweise ist es möglich, die mittels CFD bestimmten Polaren von verschiedenen Beulenformen hinsichtlich ihres Buffetverhaltens zu bewerten.

Erste Ergebnisse und Ausblick

Aus Literatur und Vorarbeiten [2] sind geeignete Positionen und Scheitelpunktshöhen für Buffet-SCBs bekannt. Die Beulengeometrie wird auf die Profilkontur mittels parametrischer Funktionen aufgeprägt, wobei verschiedene Typen von Parametrisierungen zum Einsatz kommen. So werden sowohl herkömmliche tangentenstetig in die Originalkontur übergehende Beulen verwendet, als auch eigens für das Profil angepasste realisierbare Beulen. Letztere zeichnen sich dadurch aus, dass sie mittels eines Aktuators auf dem am untersuchten Flügel vorhandenen Spoiler adaptiv realisiert werden können. Der Beulengröße, -position und -form werden damit Randbedingungen gesetzt, die das Potenzial bezüglich Buffetgrenzenverschiebung teilweise mindern.

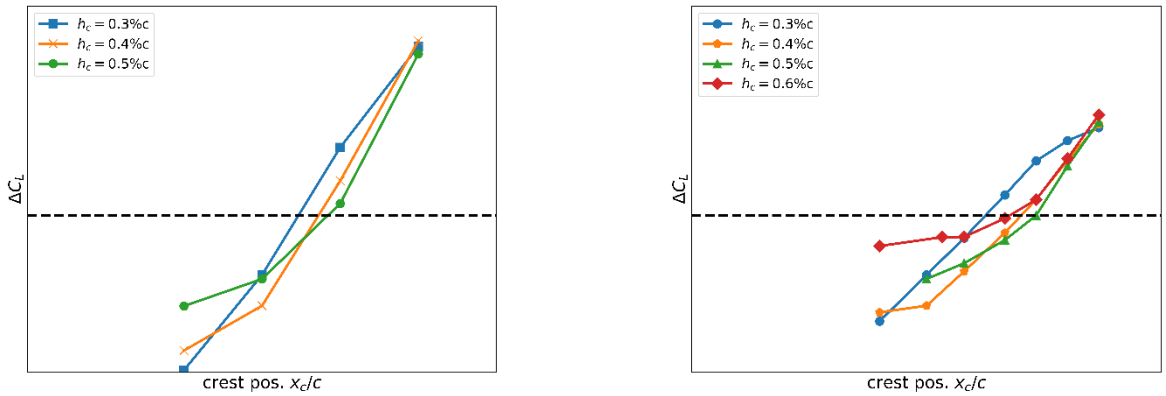

Abb. 2: Buffetgrenzenverschiebung durch Beulen mit tangentenstetigen Flanken. Gestrichelte Linie deutet $\Delta C_L = 0$ an. Links: Symmetrische Beulen variabler Position, rechts: positionsfeste asymmetrische Beulen auf einem Spoiler mit variabler Scheitelpunktsposition.

Im linken Bild von ist dargestellt, wie sich eine symmetrische tangentenstetige Beule auf die Buffetgrenze auswirkt. Die Gesamtlänge der Beule beträgt hier 15% der Profiltiefe, wobei die Position des Scheitelpunktes x_c/c sowie seine Höhe h_c/c variiert wird. Das Gütekriterium ΔC_L bedeutet hierbei die Veränderung des Auftriebsbeiwertes, bei dem Buffet detektiert wird, gegenüber dem Originalprofil ohne Beule. Es zeigt sich, dass mit ausreichender Rücklage ein deutlicher Nutzen erzielt werden kann. Im rechten Bild ist zu erkennen, dass eine Beschränkung der Beulenposition auf den Spoiler das Verbesserungspotenzial verringert, aber dennoch Beulenformen mit positivem Effekt ermöglicht. Im weiteren Verlauf der Arbeit wird anhand strukturell und systemtechnisch realisierbarer Beulen gezeigt, inwiefern sich dieses Verbesserungspotenzial tatsächlich nutzen lässt.

Quellen

[1] Lawson, S., Greenwell, D, Quinn, M.: “Characterisation of Buffet on a Civil Aircraft Wing.” AIAA SciTech, San Diego, CA. AIAA Paper No. 2016-1309, 2016.

[2] Mayer, R., Lutz, T., Krämer, E., Dandois, J.: “Control of Transonic Buffet by Shock Control Bumps on Wing-Body Configuration.” Journal of Aircraft 56(2), pp. 556–568, 2019

[3] Rossow, C.-C., Kroll, N., Schwamborn, D.: “The MEGAFLOW Project – Numerical Flow Simulation for Aircraft.” Vol. 8, pp. 3-33, Springer, Berlin, 2006

Namensverzeichnis der Autoren und Koautoren

Namensverzeichnis der Autoren und Koautoren